

# Advanced Integral Type Reactors: Passive Safety Design and Experiment

Guest Editors: Li Shengqiang, Yanping Huang,  
Luciano Burgazzi, and Annalisa Manera





---

**Advanced Integral Type Reactors:  
Passive Safety Design and Experiment**

Science and Technology of Nuclear Installations

---

# **Advanced Integral Type Reactors: Passive Safety Design and Experiment**

Guest Editors: Li Shengqiang, Yanping Huang, Luciano Burgazzi,  
and Annalisa Manera



---

Copyright © 2015 Hindawi Publishing Corporation. All rights reserved.

This is a special issue published in “Science and Technology of Nuclear Installations.” All articles are open access articles distributed under the Creative Commons Attribution License, which permits unrestricted use, distribution, and reproduction in any medium, provided the original work is properly cited.

## Editorial Board

Nusret Aksan, Switzerland  
A. C. M. Alvim, Brazil  
Won Pil Baek, Korea  
Stephen M. Bajorek, USA  
George Bakos, Greece  
Jozsef Banati, Sweden  
Ricardo Barros, Brazil  
Anis Bousbia Salah, Belgium  
Giovanni B. Bruna, France  
Nikola Čavlina, Croatia  
Xu Cheng, China  
Leon Cizelj, Slovenia  
Alejandro Clausse, Argentina  
Francesco D' Auria, Italy  
Marcos P. de Abreu, Brazil  
Giovanni Dell'Orco, France  
Juan Carlos Ferreri, Argentina  
Nikolay Fil, Russia  
Cesare Frepoli, USA  
Giorgio Galassi, Italy  
Regina Galetti, Brazil

Michel Giot, Belgium  
Valerio Giusti, Italy  
Horst Glaeser, Germany  
Satish Kumar Gupta, India  
Ali Hainoun, Syria  
Keith E. Holbert, USA  
Kostadin Ivanov, USA  
Y. Kadi, Republic of Korea  
Ahmed Khedr, Egypt  
Tomasz Kozłowski, USA  
Tomoaki Kunugi, Japan  
Mike Kuznetsov, Germany  
H.-Y. Lee, Republic of Korea  
B. Limmeechokchai, Thailand  
Jiri Macek, Czech Republic  
Annalisa Manera, USA  
Borut Mavko, Slovenia  
Oleg Melikhov, Russia  
Rafael Miró, Spain  
Josef Misak, Czech Republic  
Rahim Nabbi, Germany

Manmohan Pandey, India  
Yuriy Parfenov, Russia  
Yves Pontillon, France  
Nik Popov, Canada  
Piero Ravetto, Italy  
Francesc Reventos, Spain  
Enrico Sartori, France  
Carlo Sborchia, France  
Massimo Sepielli, Italy  
Arkady Serikov, Germany  
James F. Stubbins, USA  
Iztok Tiselj, Slovenia  
Rizwan Uddin, USA  
Eugenijus Ušpuris, Lithuania  
Richard Wright, Norway  
Chao Xu, China  
X. George Xu, USA  
Yanko Yanev, Bulgaria  
Zhiwei Zhou, China  
Enrico Zio, Italy  
Massimo Zucchetti, Italy

# Contents

**Advanced Integral Type Reactors: Passive Safety Design and Experiment**, Li Shengqiang, Yanping Huang, Luciano Burgazzi, and Annalisa Manera  
Volume 2015, Article ID 491715, 2 pages

**Single Phase Natural Circulation Behaviors of the Integral Type Marine Reactor Simulator under Rolling Motion Condition**, Hou-jun Gong, Xing-tuan Yang, Yan-ping Huang, and Sheng-yao Jiang  
Volume 2015, Article ID 815603, 10 pages

**Research and Evaluation for Passive Safety System in Low Pressure Reactor**, Peng Chuanxin, Zhuo Wenbin, Chen Bingde, Nie Changhua, and Huang Yanping  
Volume 2015, Article ID 179235, 9 pages

**Natural Circulation Characteristics of a Symmetric Loop under Inclined Conditions**, Xingtuan Yang, Yanfei Sun, Zhiyong Liu, and Shengyao Jiang  
Volume 2014, Article ID 925760, 8 pages

**An Evaluation of SMR Economic Attractiveness**, Sara Boarin and Marco E. Ricotti  
Volume 2014, Article ID 803698, 8 pages

**Procedure of Active Residual Heat Removal after Emergency Shutdown of High-Temperature-Gas-Cooled Reactor**, Xingtuan Yang, Yanfei Sun, Huaiming Ju, and Shengyao Jiang  
Volume 2014, Article ID 583597, 10 pages

**Design of the VISTA-ITL Test Facility for an Integral Type Reactor of SMART and a Post-Test Simulation of a SBLOCA Test**, Hyun-Sik Park, Byung-Yeon Min, Youn-Gyu Jung, Yong-Cheol Shin, Yung-Joo Ko, and Sung-Jae Yi  
Volume 2014, Article ID 840109, 14 pages

**Experimental Research on Passive Residual Heat Removal System of Chinese Advanced PWR**, Zhuo Wenbin, Huang Yanping, Xiao Zejun, Peng Chuanxin, and Lu Sansan  
Volume 2014, Article ID 325356, 8 pages

**Some Movement Mechanisms and Characteristics in Pebble Bed Reactor**, Xingtuan Yang, Yu Li, Nan Gui, Xinlong Jia, Jiyuan Tu, and Shengyao Jiang  
Volume 2014, Article ID 820481, 10 pages

**Experimental and Numerical Study of Stagnant Zones in Pebble Bed**, Xinlong Jia, Xingtuan Yang, Nan Gui, Yu Li, Jiyuan Tu, and Shengyao Jiang  
Volume 2014, Article ID 120640, 10 pages

**Study on Thermal-Hydraulic Behavior of an Integral Type Reactor under Heaving Condition**, Beibei Feng, Xingtuan Yang, Shengqiang Li, Yanfei Sun, Jiyuan Tu, and Shengyao Jiang  
Volume 2014, Article ID 857507, 12 pages

**Study on the Behaviors of a Conceptual Passive Containment Cooling System**, Jianjun Wang, Xueqing Guo, Shengzhi Yu, Baowei Cai, Zhongning Sun, and Changqi Yan  
Volume 2014, Article ID 358365, 8 pages



---

**Operation of Shared Systems via a Common Control System in a Multi-Modular Plant**, Jia Qianqian,  
Huang Xiaojin, and Zhang Liangju  
Volume 2014, Article ID 138693, 9 pages

**The Effect of Beam Intensity on Temperature Distribution in ADS Windowless Lead-Bismuth Eutectic Spallation Target**, Jie Liu, Lei Gao, and Wen-qiang Lu  
Volume 2014, Article ID 984971, 8 pages

**The Stress and Reliability Analysis of HTR's Graphite Component**, Xiang Fang, Haitao Wang,  
and Suyuan Yu  
Volume 2014, Article ID 964848, 8 pages

## Editorial

# Advanced Integral Type Reactors: Passive Safety Design and Experiment

**Li Shengqiang,<sup>1,2</sup> Yanping Huang,<sup>3</sup> Luciano Burgazzi,<sup>4</sup> and Annalisa Manera<sup>5</sup>**

<sup>1</sup>*Institute of Nuclear and New Energy Technology (INET), Tsinghua University, Beijing 100084, China*

<sup>2</sup>*Key Laboratory of Nuclear Engineering and Safety of MOE, Tsinghua University, Beijing 102201, China*

<sup>3</sup>*Reactor Engineering Research Division, Nuclear Power Institute of China, Chengdu 610041, China*

<sup>4</sup>*Reactor Safety and Fuel Cycle Methods Technical Unit, Italian National Agency for New Technologies, Energy and Sustainable Economic Development, 40129 Bologna, Italy*

<sup>5</sup>*Nuclear Engineering & Radiological Sciences, University of Michigan, Ann Arbor, MI 48109-2104, USA*

Correspondence should be addressed to Li Shengqiang; [sqli@tsinghua.edu.cn](mailto:sqli@tsinghua.edu.cn)

Received 26 August 2014; Accepted 26 August 2014

Copyright © 2015 Li Shengqiang et al. This is an open access article distributed under the Creative Commons Attribution License, which permits unrestricted use, distribution, and reproduction in any medium, provided the original work is properly cited.

Advanced integral type reactors are increasingly becoming a promising engineering solution for broad application of nuclear energy. A large number of prototype advanced integral reactors have been operated or are being constructed and developed in recent years, including CNP-300, KLT-40S, CAREM, mPower, IRIS, NHR-200, SMART, Westinghouse SMR, ACPRI00, SC-HTGR, IMR, NuScale, VBER-300, ENHS, and 4S. The advantages of applied flexibility, economic efficiency, staffing, waste reduction, nonproliferation, and special enhanced safety features of these integral reactors may greatly improve the public acceptance and environment compatibility in future nuclear applications. To accelerate the adoption of new research productions in future applications, a number of important issues should be addressed, such as enhanced natural circulation, passive cooling, scheduling of multimodular reactors, and advanced experimental technologies. In this special issue on advanced integral reactors, we have invited a few papers that address such issues.

The paper which is named as “Natural Circulation Characteristics of a Symmetric Loop under Inclined Conditions” in this special issue addresses the full passive cooling in the primary loop under inclined conditions. Both experiments and CFD simulations have been carried out and their products are compared. The paper, which is named as “An Evaluation of SMR Economic Attractiveness,” evaluates the economic attractiveness of small integral reactors, which can be assessed mainly from two frames: investment profitability and investment risk. A code which is based on the discounted

cash flow was applied in the study. The paper named as “Procedure of Active Residual Heat Removal after Emergency Shutdown of High-Temperature-Gas-Cooled Reactor” presents simulation for the residual heat removal with active facilities for module gas cooling reactors. A one-dimensional model was adopted in the calculation. The possible cold/heat shock in the active loop was evaluated and the optimal strategy for the operating process was provided.

Another paper, “Design of the VISTA-ITL Test Facility for an Integral Type Reactor of SMART and a Post-Test Simulation of a SBLOCA Test,” of this special issue presents a multifunction thermal-hydraulic integral effect test facility. It was designed extensively to assess the passive safety system and passive residual heat removal system for integral type reactors. Its performance and simulation capability in prototype reactors were also evaluated by MARS-KS code. Besides, the paper “Experimental Research on Passive Residual Heat Removal System of Chinese Advanced PWR” describes the serial experiments for passive residual heat removal system in Chinese advanced pressurized water reactor. A semiempirical model and a new simulation code have been developed and calibrated by experiments results. Two subsequent papers, “Some Movement Mechanisms and Characteristics in Pebble Bed Reactor” and “Experimental and Numerical Study of Stagnant Zones in Pebble Bed,” concentrate on the topic of fuel pebble movement mechanisms in the pebble bed reactors. The experiments and simulation results show mixing zone was produced from pebbles’ dispersion motions.

The geometry characteristics of the dispersion regions and stagnant zones were evaluated by both experiments and DEM simulations, respectively.

Another paper, “Study on Thermal-Hydraulic Behavior of an Integral Type Reactor under Heaving Condition,” presents the study on thermal-hydraulic behavior of the integral reactor under heaving conditions. The sensitive study on the effect of motion parameters on natural circulation was also investigated. The results were adopted for geometry characteristics optimization. Another paper, “Study on the Behaviors of a Conceptual Passive Containment Cooling System,” proposes the new design of the passive cooling system for large dry containment. It can be applied to multimodule integral reactors. The numerical studies were performed and different operating stages were classified. The feasibility of the system for integrity containment is also discussed.

Another paper, which is named as “Operation of Shared Systems via a Common Control System in a Multi-Modular Plant,” focuses on the control strategy on assemblage of integral reactors. It presents the evaluation of the module and shared control system for a group of integral type reactors in future commercial plant applications. Different characteristics of the shared system are analyzed. Different operation and control strategies are also presented. The paper “The Effect of Beam Intensity on Temperature Distribution in ADS Windowless Lead-Bismuth Eutectic Spallation Target” is more forward looking. It addresses the optimization design of spallation target for accelerator driven system, which is a promising type of future integral reactor. The nuclear physics calculation was coupled with computational fluid dynamics calculation for thermal-hydraulic study in this work. The maximum temperature and temperature distribution in the windowless target were evaluated under different beam intensity. The paper “The Stress and Reliability Analysis of HTR’s Graphite Component” addresses the mechanical analysis of graphite components in the integral gas cooling reactors under high temperature and fast neutron irradiation. Different creep models and reliability models are taken into account in the simulation.

Another paper, “Single Phase Natural Circulation Behaviors of the Integral Type Marine Reactor Simulator under Rolling Motion Condition,” presents the full natural circulation characteristics in the primary loop of integral reactors under rolling motion conditions. The experiments result and numerical simulation products were compared. A new system analysis code for integral type reactor under rolling conditions was developed. The paper “Research and Evaluation for Passive Safety System in Low Pressure Reactor” in this special issue addresses a passive safety system, which is under development, for integral small reactors. The performance of the passive safety system under LOCA and SBO conditions was evaluated by several tests and a best estimate thermal-hydraulic code.

*Li Shengqiang  
Yanping Huang  
Luciano Burgazzi  
Annalisa Manera*

## Research Article

# Single Phase Natural Circulation Behaviors of the Integral Type Marine Reactor Simulator under Rolling Motion Condition

Hou-jun Gong,<sup>1,2</sup> Xing-tuan Yang,<sup>1</sup> Yan-ping Huang,<sup>2</sup> and Sheng-yao Jiang<sup>1</sup>

<sup>1</sup>Institute of Nuclear and New Energy Technology of Tsinghua University, Beijing 100084, China

<sup>2</sup>CNNC Key Laboratory on Nuclear Reactor Thermal Hydraulics Technology, Chengdu 610041, China

Correspondence should be addressed to Xing-tuan Yang; yangxt@mail.tsinghua.edu.cn

Received 8 November 2013; Accepted 15 July 2014

Academic Editor: Shengqiang Li

Copyright © 2015 Hou-jun Gong et al. This is an open access article distributed under the Creative Commons Attribution License, which permits unrestricted use, distribution, and reproduction in any medium, provided the original work is properly cited.

During operation in the sea the reactor natural circulation behaviors are affected by ship rolling motion. The development of an analysis code and the natural circulation behaviors of a reactor simulator under rolling motion are described in this paper. In the case of rolling motion, the primary coolant flow rates in the hot legs and heating channels oscillated periodically, and the amplitude of flow rate oscillation was in direct proportion to rolling amplitude, but in inverse proportion to rolling period. The total mass flow rate also oscillated with half the rolling period, and the average total mass flow rate was less than that in steady state. In the natural circulation under a rolling motion, the flow rate oscillations in the hot legs were controlled by the tangential force; however, the mass flow rate oscillations in the total natural circulation and the heating channels were a result of the combined action of the change of inclination angle, flow resistance, and the extra force arising from the rolling motion. The extra tangential force brought about intense flow rate oscillations in the hot legs, which resulted in increasing total flow resistance; however the extra centrifugal force played a role in increasing thermal driving head.

## 1. Introduction

Apart from designed as land-based nuclear power plants, another significant application of small and medium sized LWRs is to be mounted on barges as floating nuclear power plants FNPPs (FNPPs) or as propulsion power of commercial cargo ship or icebreaker, such as SMART and KLT-40s. However, during operation in the sea, the ship inclination or rolling motion will affect the reactor thermal hydraulics, especially for natural circulation behaviors. The effects of ship motion focus on two principles. Firstly, inclination decreases the height difference between the source (core) and sink (SG) and thus decreases the thermal driving head of natural circulation. Secondly, inertial forces imparted by the ship rolling motion in addition to the gravity act upon the primary coolant, which control the natural circulation flow rate with the loop resistances together. The direction and magnitude of inertial forces depend on the position with respect to rolling axis, rolling amplitude, and period. So the natural circulation behaviors under ship motion conditions are much more complicated than those operated on the land.

Experimental studies [1–4] showed that the loop flow rates varied periodically, total mass flow rate decreased, and the heat transfer was enhanced in the case of rolling. Beside experiments, some thermal-hydraulic codes were developed to study the influence of ocean conditions. JAERI developed RETRAN-02/GRAV code, which is the modified version of RETRAN-02 code, to simulate the experimental voyages of Mutsu [5] and analyse the effects of ship motions on natural circulation of deep sea research reactor DRX [6]. Seoul National University [7] developed RETRAN-03/MOV to perform thermal-hydraulic analysis of ship reactor under multidimensional motions.

To understand the natural circulation behaviors of the integral type marine reactor under rolling motion conditions, a scaled test facility was built in Institute of Nuclear and New Energy Technology of Tsinghua University (INET) and a one-dimensional time-domain simulation program development was synchronized with test facility design. This paper describes the physical models and solution method in the program and the natural circulation behaviors of

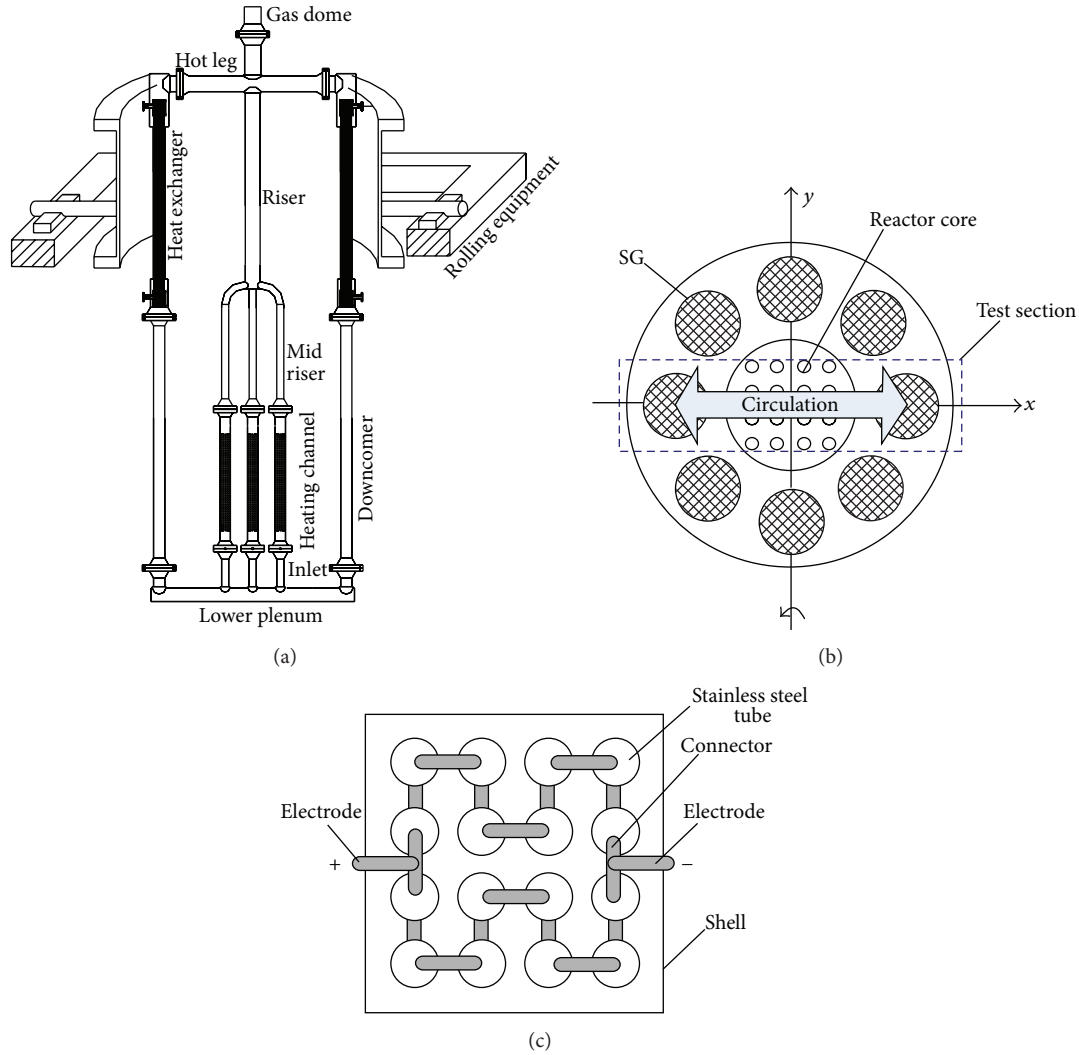


FIGURE 1: (a) Configuration of the test facility. (b) Relation between test section and real reactor system. (c) Connection of electrical heating tubes.

the reactor simulator under rolling motion condition based on the analysis results.

## 2. Test Facility

The test facility is a reactor simulator (natural circulation test loop) mounted on rolling equipment shown schematically in Figure 1(a) and the geometry parameters are listed in Table 1. To investigate the symmetric characteristics of the real reactor system as shown in Figure 1(b) with a comparable simple structure, the primary loop is designed to have two symmetrical circuits. Each circuit contains a heat exchanger and a downcomer connecting to hot legs and lower plenum. Three electrical heating channels are connected to lower plenum, playing the role of the reactor core and each of them consists of 16  $\Phi 10 \times 1$  mm and 1080 mm long stainless steel tubes with the arrangement shown in Figure 1(c). During circulation, fluid flows from the lower plenum to the electrical heater and is heated to be with higher temperature and lower

TABLE 1: Geometry parameters of test facility.

Items	Number	Length (m)	Flow area (m <sup>2</sup> )
Inlet section	3	0.306	0.00237
Heating channel	3	1.08	0.00178
Mid riser	3	0.575	0.00126
Riser	1	1.59	0.0104
Hot leg	2	0.67	0.0113
Heat exchanger	2	1.6	0.00246
Downcomer	2	1.951	0.00594
Lower plenum	1	1.34	0.0113

density and then flows up and separates in hot legs; in the heat exchanger of each circuit, the fluid is cooled down and flows back into the lower plenum through the downcomer finishing a complete circulation. The primary loop is installed on rolling equipment and the rolling axis is perpendicular to primary loop.

### 3. Code Development

3.1. *Physical Model.* Be similar to study the fluid mechanics of rotating machinery that is often best analyzed in a rotating frame of reference, a noninertial frame of reference with the same rolling motion of test facility was chosen in our study. In a noninertial frame of reference, the continuity and energy equations are unchanged but the momentum equation must be modified. The extra body force term that arises from the motion of the noninertial frame must be added to the right of momentum equation to take account of the motion of the frame.

One-dimensional single phase conservation equations of hydrodynamic component can be written as follows:

mass continuum equation:

$$\frac{\partial \rho}{\partial t} + \frac{\partial (\rho u)}{\partial z} = 0, \quad (1)$$

momentum continuum equation:

$$\frac{\partial (\rho u)}{\partial t} + \frac{\partial (\rho u^2)}{\partial z} = -\frac{\partial p}{\partial z} - \rho g_z + \rho f_{ex,z} - \frac{\lambda}{D_e} \frac{\rho u^2}{2}, \quad (2)$$

energy continuum equation:

$$\frac{\partial (\rho h)}{\partial t} + \frac{\partial (\rho u h)}{\partial z} = \frac{q'' P_H}{A_s}. \quad (3)$$

The extra acceleration  $\mathbf{f}_{ex}$  arising from rolling was obtained in this general expression,

$$\mathbf{f}_{ex} = \dot{\boldsymbol{\omega}} \times \mathbf{r} + \boldsymbol{\omega} \times (\boldsymbol{\omega} \times \mathbf{r}) + 2\boldsymbol{\omega} \times \mathbf{U}, \quad (4)$$

where  $\boldsymbol{\omega}$  is angular velocity of noninertial frame,  $\dot{\boldsymbol{\omega}}$  is angular acceleration of noninertial frame,  $\mathbf{r}$  is radial vector of fluid particle in noninertial frame, and  $\mathbf{U}$  is velocity of fluid particle in noninertial frame.

The three terms in the right side of (4) may each be significant. The first term  $\dot{\boldsymbol{\omega}} \times \mathbf{r}$  is the acceleration caused by angular acceleration of the noninertial frame, so it is of little importance for geophysical flows or for flows in machinery that rotate at a constant rate about a fixed axis. However, it does play an important role in rolling motion. The second term  $\boldsymbol{\omega} \times (\boldsymbol{\omega} \times \mathbf{r})$  is the centripetal acceleration, depending strongly on the rotation rate and the distance of the fluid particle from the axis of rotation. The final term  $2\boldsymbol{\omega} \times \mathbf{U}$  is the Coriolis acceleration, depending on the fluid particle's velocity, not on its position. Because Coriolis acceleration is perpendicular to main stream, it is omitted in the code.

Figure 2 shows a control volume with three-dimensional position in noninertial frame of reference; the center of control volume is  $p = (x, y, z)$  and unit vector of main flow direction is  $n = (\cos \alpha, \cos \beta, \cos \gamma)$ . In the simulation of rolling motion, the X-axis overlapped rolling axis, and motion parameters of the noninertial reference system were the same as rolling, so coordinate of control volume was unchanged and the one-dimensional flow was always along the main direction of control volume in the noninertial reference system.

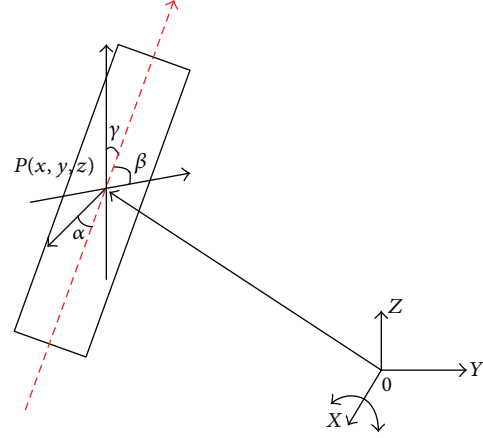


FIGURE 2: Three-dimensional spatial information of a control volume in noninertial frame of reference.

The parameters of rolling motion were defined as follows:

rolling angle:

$$\varphi = \varphi_m \sin(\omega_d t), \quad (5)$$

rolling angle speed:

$$\omega = \varphi_m \omega_d \cos(\omega_d t), \quad (6)$$

rolling angle acceleration:

$$\dot{\omega} = -\varphi_m \omega_d^2 \sin(\omega_d t). \quad (7)$$

The component of extra acceleration along main flow direction in our test facility was described by the following equation:

$$f_{ex,z} = (\omega^2 \gamma + \dot{\omega} z) \cos \beta + (\omega^2 z - \dot{\omega} y) \cos \gamma. \quad (8)$$

During rolling,  $g_z$  was changed with the angle between flow channel and vertical direction. Rolling is in some sense a rotation with varying speed around a fixed axis;  $g_z$  at the rolling angle  $\varphi$  can be obtained as

$$g_z = g [\cos \beta (\sin \varphi - \cos \varphi) + \cos \gamma \cos \varphi]. \quad (9)$$

3.2. *Constitute Correlations.* The friction factor model used in the code was simply an interpolation scheme linking the laminar, laminar-turbulent transition, and turbulent flow regimes. The laminar friction factor was calculated as

$$\lambda_L = \frac{64}{Re}, \quad \text{for } 50 \leq Re \leq 2200. \quad (10)$$

The friction factor in the transition region between laminar and turbulent flows was computed by reciprocal interpolation as

$$\lambda_{L,T} = \left( 3.75 - \frac{8250}{Re} \right) (\lambda_{3000} - \lambda_{2200}) + \lambda_{2200}, \quad (11)$$

for  $2200 < Re < 3000$ .

The turbulent friction factor is given by the Zigrang-Sylvester [8]:

$$\lambda_T = \left\{ -2 \log_{10} \left[ \frac{\varepsilon}{3.7 D_e} + \frac{2.86}{\text{Re}} - \frac{5.02}{\text{Re}} \log_{10} \left( \frac{\varepsilon}{D_e} - \frac{21.25}{\text{Re}^{0.9}} \right) \right] \right\}^{-0.5} \quad (12)$$

for  $\text{Re} \geq 3000$ .

The wall heat transfer coefficient  $h_{wl}$  was obtained:

$$h_{wl} = \frac{k_l}{D_h} \text{Nu}. \quad (13)$$

In the code, Nu was taken as the maximum of the values for laminar and turbulent forced convection and natural convection. That was,

$$\text{Nu} = \max(\text{Nu}_{\text{lam}}, \text{Nu}_{\text{turb}}, \text{Nu}_{\text{nc}}), \quad (14)$$

where  $\text{Nu}_{\text{lam}}$  is Nusselt number for laminar forced convection,  $\text{Nu}_{\text{turb}}$  is Nusselt number for turbulent forced convection, and  $\text{Nu}_{\text{nc}}$  is Nusselt number for natural convection.

The Nusselt number for laminar flow was set to the analytical value for fully developed flow with a constant heat flux boundary condition. Thus,

$$\text{Nu}_{\text{lam}} = 4.36. \quad (15)$$

The Nusselt number for fully developed turbulent flow was that of Weisman [9]; it was given by

$$\text{Nu}_{\text{turb}} = 0.023 \text{Re}^{0.8} \text{Pr}^n C_w, \quad (16)$$

where Pr is liquid Prandtl number and  $n$  equals 0.4 for heating and 0.3 for cooling. Heat transfer correction factor  $C_w$  for rods bundle is a function of bundle pitch  $P_b$  and rod diameter  $D_R$  as

$$C_w = 0.042 \frac{P_b}{D_R} - 0.024. \quad (17)$$

The Nusselt number for natural circulation was given by

$$\text{Nu}_{\text{nc}} = \max(\text{Nu}_{\text{nc,lam}}, \text{Nu}_{\text{nc,turb}}), \quad (18)$$

where

$$\text{Nu}_{\text{nc,lam}} = 0.59 (\text{Gr} \cdot \text{Pr})^{1/4} \quad (19)$$

was used for laminar natural convection, and

$$\text{Nu}_{\text{nc,turb}} = 0.1 (\text{Gr} \cdot \text{Pr})^{1/3} \quad (20)$$

was used for turbulent natural convection.

The constitute correlations discussed above were widely used in analysis codes. Although these accuracy for real cases of the test loop should be verified, it was the best choice in our studies before deep experimental studying.

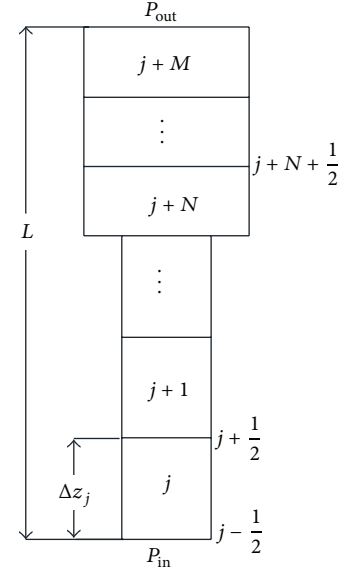


FIGURE 3: Nodalization of a flow channel.

3.3. *Solution Method.* To solve (1)–(3) and calculate the accurate density distribution along the test loop, a flow channel with abrupt area change was divided into a group of control volumes shown in Figure 3.

For single phase flow, during a small time interval, we can assume

$$\frac{\partial \rho}{\partial t} = 0. \quad (21)$$

Then (1) transforms into

$$\frac{dW}{dz} = 0. \quad (22)$$

Integrating (3) over control volume  $j$ , we can obtain

$$A_j \Delta z_j \left( \rho \frac{\partial h}{\partial t} + h \frac{\partial \rho}{\partial t} \right)_j + W \left( \dot{h}_{j+1/2}^n - \dot{h}_{j-1/2}^n \right) = (q_j^n)^{n+1} P_{H,j} \Delta z_j. \quad (23)$$

Fluid enthalpy at the joint of control volumes was obtained by using upwind scheme as

$$\dot{h}_{j+1/2} = 0.5 (h_j + h_{j+1}) + 0.5 \frac{|W_{j+1/2}|}{W_{j+1/2}} (h_j - h_{j+1}). \quad (24)$$

In the code, temperature  $T$  was chosen as independent state variable. Omitting the effect of pressure on density and enthalpy, we can obtain

$$\frac{\partial \rho}{\partial t} = \left( \frac{\partial \rho}{\partial T} \right)^n \frac{\partial T}{\partial t}, \quad \frac{\partial h}{\partial t} = \left( \frac{\partial h}{\partial T} \right)^n \frac{\partial T}{\partial t}. \quad (25)$$

For simplicity, the long expressions were replaced by single variables:

$$X_{j,1} = A_j \Delta z_j \left[ \rho_j^n \left( \frac{\partial h}{\partial T} \right)_j^n + h_j^n \left( \frac{\partial \rho}{\partial T} \right)_j^n \right], \quad (26)$$

$$X_{j,2} = (q_j^n)^{n+1} P_{H,j} \Delta z_j.$$

Combining (23) and (26), we can obtain

$$\frac{T_j^{n+1} - T_j^n}{\Delta t} = \frac{X_{j,2} - W \left( \dot{h}_{j+1/2}^n - \dot{h}_{j-1/2}^n \right)}{X_{j,1}}. \quad (27)$$

Integrating (2) along flow channel, we can obtain

$$\begin{aligned} \int_L \frac{1}{A} \frac{\partial W}{\partial t} dl + \frac{W_{\text{out}}^2}{A_{\text{out}} \rho_{\text{out}}} - \frac{W_{\text{in}}^2}{A_{\text{in}} \rho_{\text{in}}} &= - (P_{\text{out}} - P_{\text{in}}) - \int_L \rho g_z dl \\ + \int_L \rho f_{\text{ex},z} dl - \int_L \frac{\lambda}{D_h} \frac{|W|W}{2\rho A^2} dl - H\text{Loss}. \end{aligned} \quad (28)$$

And the integrating can be solved approximately as follows:

$$\begin{aligned} \int_L \frac{1}{A} \frac{\partial W}{\partial t} dl &= \sum_{j=1}^M \frac{\partial W^{n+1}}{\partial t} \frac{\Delta z_j}{A_j}, \\ \int_L \rho g_z dl &= \sum_{j=1}^M \rho_j^{n+1} g_{z,j}^{n+1} \Delta z_j, \\ \int_L \rho f_{\text{ex},z} dl &= \sum_{j=1}^M \rho_j^{n+1} f_{\text{ex},z,j}^{n+1} \Delta z_j, \\ \int_L \frac{\lambda}{D_h} \frac{|W|W}{2\rho A^2} dl &= \sum_{j=1}^M \frac{\Delta z_j \lambda_j^n \left( |W_j| W_j \right)^n}{D_{h,j} 2\rho_j^n A_j^2}, \\ H\text{Loss} &= k \frac{|W|W}{2\rho A_j^2}. \end{aligned} \quad (29)$$

Integrating (2) along four close loops shown in Figure 4, we can obtain the following:

loop 1 composed of left heating channel, middle risers, right heating channel, and part of lower plenum,

$$\begin{aligned} \frac{-\Delta W_1}{\Delta t} \left( \frac{L_1}{A_1} + \frac{L_2}{A_2} + \frac{L_3 + L_9}{A_3} \right) + \frac{\Delta W_2}{\Delta t} \left( \frac{L_1}{A_1} + \frac{L_2}{A_2} + \frac{L_3}{A_3} \right) \\ + \frac{\Delta W_4 - \Delta W_1}{\Delta t} \frac{L_9}{A_9} \\ = \int_{\text{loop1}} \left( -\rho g_z + \rho f_{\text{ex},z} - \frac{\lambda}{D_h} \frac{|W|W}{2\rho A^2} \right) dl - \sum_{\text{loop1}} H\text{Loss}, \end{aligned} \quad (30)$$

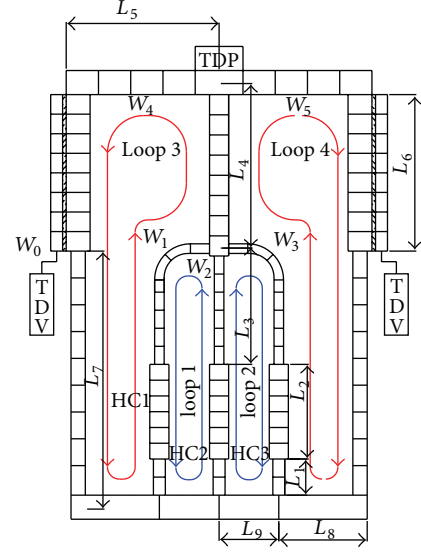


FIGURE 4: Nodalization of test facility.

loop 2 composed of right heating channel, middle risers, heating channel 2, and part of lower plenum,

$$\begin{aligned} \frac{-\Delta W_3}{\Delta t} \left( \frac{L_1}{A_1} + \frac{L_2}{A_2} + \frac{L_3 + L_9}{A_3} \right) + \frac{\Delta W_2}{\Delta t} \left( \frac{L_1}{A_1} + \frac{L_2}{A_2} + \frac{L_3}{A_3} \right) \\ + \frac{\Delta W_5 - \Delta W_3}{\Delta t} \frac{L_9}{A_9} \\ = \int_{\text{loop2}} \left( -\rho g_z + \rho f_{\text{ex},z} - \frac{\lambda}{D_h} \frac{|W|W}{2\rho A^2} \right) dl - \sum_{\text{loop2}} H\text{Loss}, \end{aligned} \quad (31)$$

loop 3 composed of left heating channel, riser, left hot leg, left heat exchanger, downcomer, and part of lower plenum,

$$\begin{aligned} \frac{\Delta W_1}{\Delta t} \left( \frac{L_1}{A_1} + \frac{L_2}{A_2} + \frac{L_3 + L_9}{A_3} \right) + \frac{\Delta W_1 + \Delta W_2 + \Delta W_3}{\Delta t} \frac{L_4}{A_4} \\ + \frac{\Delta W_4}{\Delta t} \left( \frac{L_5}{A_5} + \frac{L_6}{A_6} + \frac{L_7}{A_7} + \frac{L_8}{A_8} \right) \\ = \int_{\text{loop3}} \left( -\rho g_z + \rho f_{\text{ex},z} - \frac{\lambda}{D_h} \frac{|W|W}{2\rho A^2} \right) dl - \sum_{\text{loop3}} H\text{Loss}, \end{aligned} \quad (32)$$

loop 4 composed of right heating channel, riser, right hot leg, right heat exchanger, downcomer, and part of lower plenum,

$$\begin{aligned} \frac{\Delta W_3}{\Delta t} \left( \frac{L_1}{A_1} + \frac{L_2}{A_2} + \frac{L_3 + L_9}{A_3} \right) + \frac{\Delta W_1 + \Delta W_2 + \Delta W_3}{\Delta t} \frac{L_4}{A_4} \\ + \frac{\Delta W_5}{\Delta t} \left( \frac{L_5}{A_5} + \frac{L_6}{A_6} + \frac{L_7}{A_7} + \frac{L_8}{A_8} \right) \\ = \int_{\text{loop4}} \left( -\rho g_z + \rho f_{\text{ex},z} - \frac{\lambda}{D_h} \frac{|W|W}{2\rho A^2} \right) dl - \sum_{\text{loop4}} H\text{Loss}. \end{aligned} \quad (33)$$

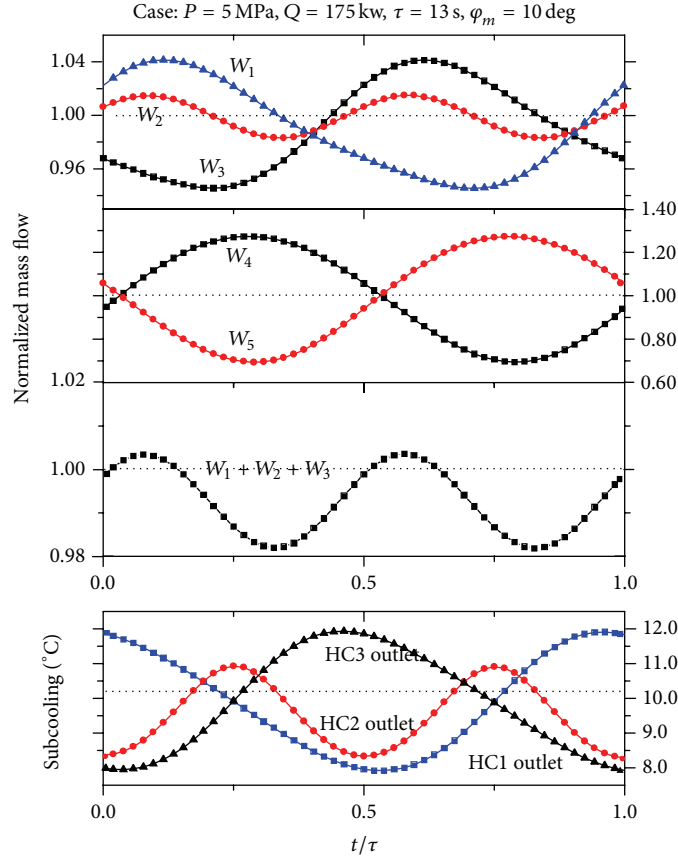


FIGURE 5: Natural circulation behavior under rolling condition.

$W_1$ ,  $W_2$ ,  $W_3$ ,  $W_4$ , and  $W_5$  are the mass flow rates of left heating channel, mid heating channel, right heating channel, left hot leg, and right hot leg, respectively, and their positive directions are identical with those in steady natural circulation.

Applying the mass continuity, we can obtain

$$\Delta W_1 + \Delta W_2 + \Delta W_3 = \Delta W_4 + \Delta W_5. \quad (34)$$

In the code, Gaussian elimination is used to solve (30)–(34), and final  $W^{n+1}$  is obtained by using

$$W^{n+1} = W^n + \Delta W. \quad (35)$$

#### 4. Results and Discussion

The node model for test facility is shown in Figure 4, and the distance from rolling axis to bottom of test loop was 3.2 m. The coordinates of hydrodynamic volumes' center and unit vector of main stream in the noninertial frame were added when establishing the input card. Boundary condition of the analysis was that the feed water properties (temperature, pressure, and enthalpy) and the pressure of feed water outlet were constants. The initial condition of transient simulation corresponds to vertical steady state, with the pressure of gas space being 5 MPa and the subcooling of heating channel inlet being 44 K. The mass flow rate  $W_0$  of feed water was

determined by a control system in the code. The function of the control system was to satisfy the balance of energy during steady state. If the total heat of heat exchanger transfer exceeded the total heating power, the mass flow rate  $W_0$  was decreased and vice versa.

The transient simulation began with the variation of body force due to rolling motion. During the transient simulation, the feed water mass flows and total heating power kept being identical with those in steady state. Analyses were carried out for 3 s, 8 s, 13 s, 18 s, and 23 s rolling periods and 5°, 10°, 22.5°, and 45° rolling amplitude with heating power 175 kw, operating pressure 5 MPa.

A case of natural circulation mass flow rates and subcooling of heating channels outlet under rolling motion was shown in Figure 5. As was observed, the heat and flow symmetry between heating channels and hot legs were broken. The mass flow rates of heating channels began to oscillate when starting the transient simulation, the oscillation periods of left and right heating channels were the same as rolling motion, but the oscillation period of middle heating channel was half the rolling motion. The same oscillations were also observed in mass flow rates of hot legs with rolling period, but oscillation amplitudes were much larger than those of heating channels. Total natural circulation mass flow rate also oscillated with half the rolling period, and the average within a period was smaller than that of steady state. The oscillation

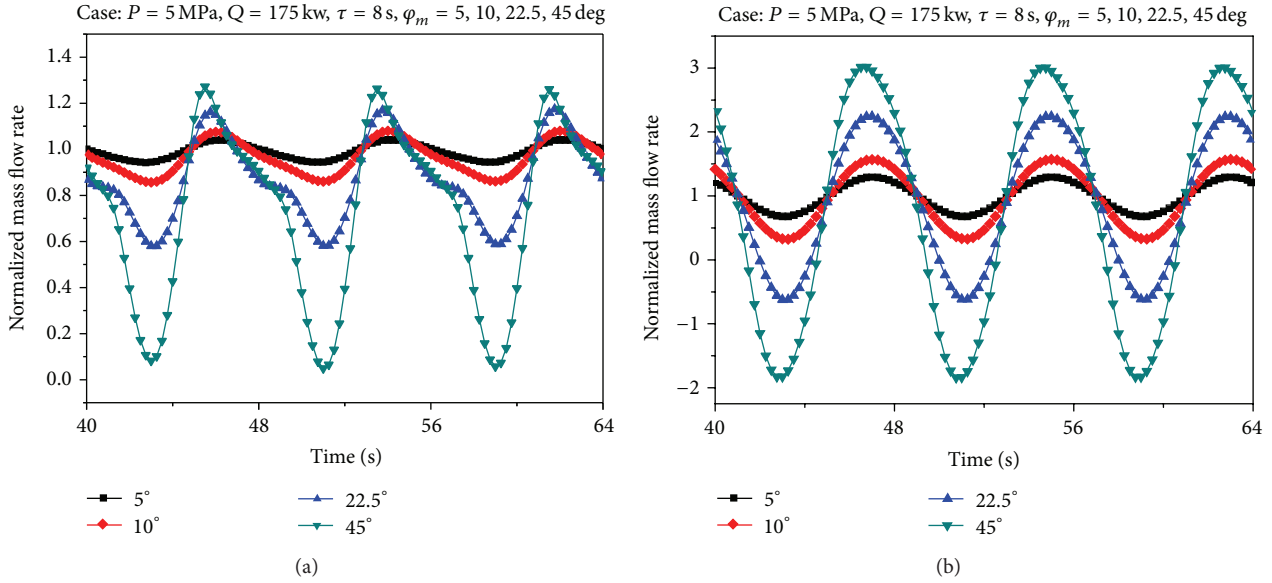


FIGURE 6: Mass flow rate under the same rolling period, different rolling amplitude, (a) left heating channel, (b) left hot leg.

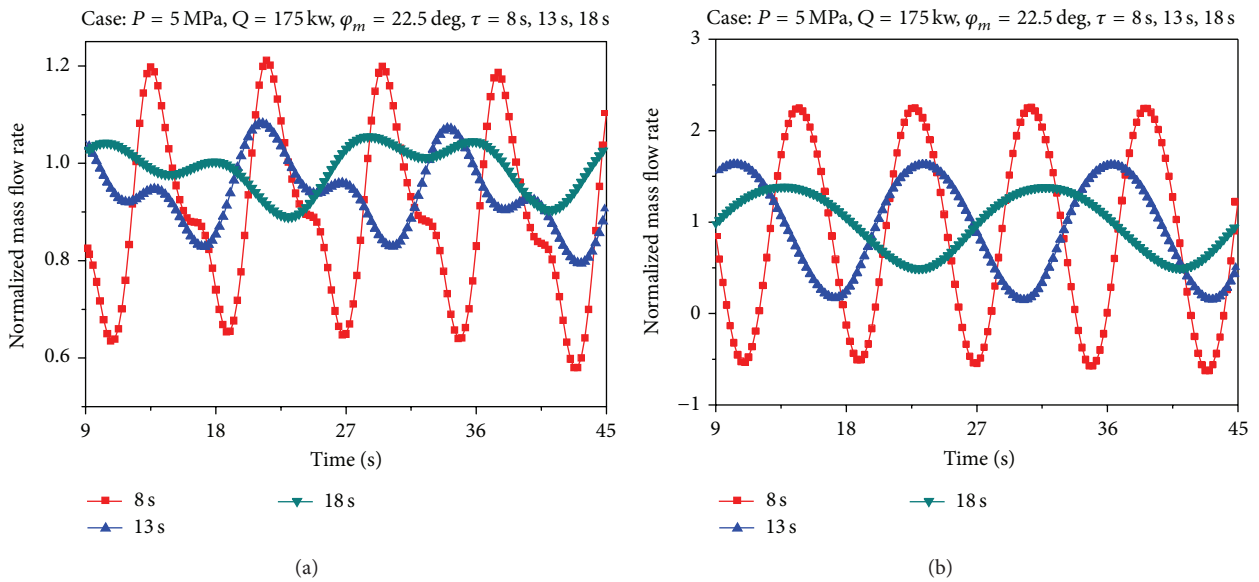


FIGURE 7: Mass flow rate under the same rolling amplitude, different rolling period, (a) left heating channel, (b) left hot leg.

of subcooling of heating channels outlets corresponded to the oscillation of mass flow rates, but the subcooling varied lag related to mass flow rate because of the time needed for water to flow through heating channel. The phenomenon was similar to that found by Murata et al. [2].

Figure 6 shows the mass flow rate under same rolling period 8 s, different rolling amplitude. Obviously, the oscillation amplitude of mass flow rate increased as the rolling amplitude increased. When the rolling amplitude equaled 45°, the mass flow rate left heating channel was only 10% of that in vertical steady state. This situation was very harmful and CHF may occur at high power level for a real reactor. When the rolling amplitude was greater than 22.5°, the fluid

of hot leg changed the velocity direction in a small range near the trough, which can degrade the quality of steam generator. So it was a great challenge to use natural circulation in primary circuit under severe ocean conditions.

Figure 7 shows the mass flow rate under the same rolling amplitude 22.5°, different rolling period. As was observed, the oscillation amplitude decreased as the period increased. An interesting phenomenon was also observed that the mass flow rate oscillation waveform of left heating channel deviated from sine wave more and more as rolling period increased. However the oscillation waveform of hot legs was very close to sine wave. The clearer phenomenon can be seen in Figure 8. Although the oscillation period of left and right heating

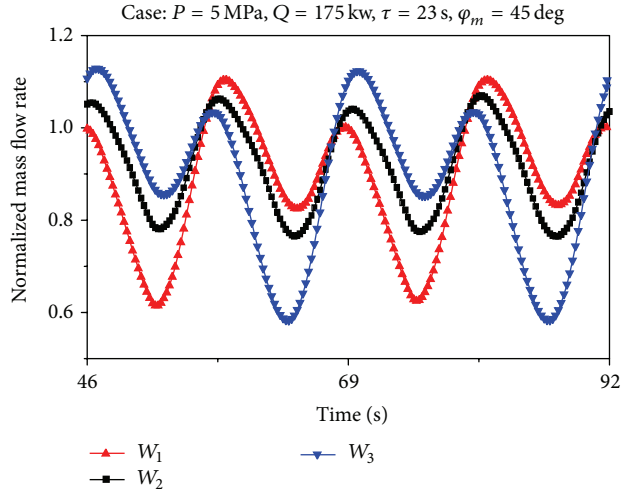


FIGURE 8: Mass flow rate of heating channels under rolling period 23 s, rolling amplitude  $45^\circ$ .

channels was equal to that of rolling motion, there were two maximum and minimum in one period and the oscillation period had the trend to be half of rolling period. A discussion of the causes of these forms is given later in this paper.

Natural circulation flow rates under rolling motion were affected by extra forces, thermal driving head, and flow resistance. The extra force varied with the rolling angle. On the other hand, the thermal driving head also varied with the inclination angle, and flow resistance varied with velocity. Therefore, it was difficult to judge how much do these three factors contribute to overall thermal hydraulic behaviors ostensibly. If the natural circulation was only affected by thermal driving head decrease due to inclination, the normalized total natural circulation mass flow was always less than unit. However, as shown in Figure 5, the peak value of normalized total mass flow was greater than unit, so there was influence of rolling motion on natural circulation without doubt.

The mechanisms of influence of rolling motion can be interpreted by the analysis of extra forces. Figure 9 shows the extra forces induced by rolling motion; the vectors only denote the direction of extra forces; they do not denote the modulus. As was observed, the extra tangential forces  $F_e$  along the pipes were in two circles, which were thought to generate theoretical flows along outer and inner loops marked in Figure 9. The tangential force varied periodically with the same period of rolling motion; thus the theoretical flows oscillations were approximate to sine wave. Therefore, the oscillations of  $W_1$ ,  $W_3$ ,  $W_4$ , and  $W_5$  were the superposition of theoretical flows and flows driven by density difference. The integration of tangential force along outer loop was greater than that of inner loop, and that was why flow rate oscillation amplitude of hot legs was larger than that of heating channels. Due to the intense flow rate oscillation of hot legs, the total flow resistance was larger than that in steady state. The extra centrifugal force  $F_r$  was parallel to radial vector, because the rolling axis was higher than

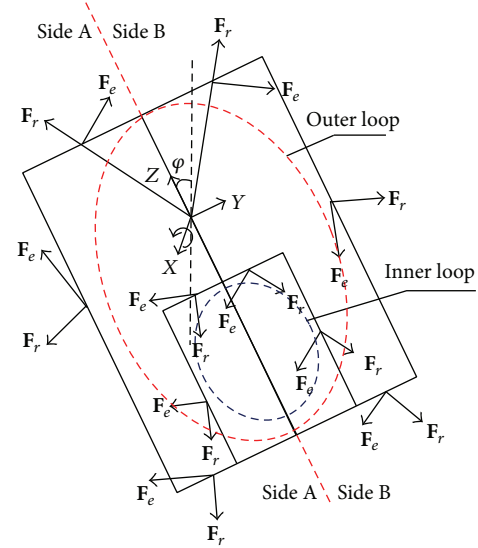


FIGURE 9: Analysis of extra forces arising from rolling.

the geometric center; thus the effect of centrifugal force was similar to gravity, which caused the peak value of total mass flow to be greater than unit. The centrifugal force and thermal driving head varied periodically with half the rolling period, thus the total mass flow oscillation with half rolling period. Under large rolling period and large rolling amplitude condition, ratio the variation of thermal driving head and tangential force along inner loop become large, that was why the oscillation waveform deviated from sine wave.

From above discussion, it was concluded that in the natural circulation under rolling motion, the flow rates oscillations in hot legs were controlled by tangential force; however, the mass flow rate oscillations of total natural circulation and heating channels were a result of the combined action of the change of inclination angle, flow resistance, and extra force due to rolling motion. The centrifugal force and thermal driving head varied periodically with half the rolling period, and the tangential force varied periodically with the same rolling period, so the oscillation waveforms of left and right heating channels depended on the quantity of the centrifugal force, the tangential force, and thermal driving head, that was why there were two maximum and minimum in one period shown in Figure 8.

Figure 10 shows the average of normalized total mass flow rates of different rolling cases. The average total mass flow rate was less than unit in rolling condition and was in direct proportion to rolling period but was in inverse proportion to rolling amplitude.

## 5. Conclusions

A transient system analysis code was developed to study natural circulation under motion condition. The momentum equation was modified and it adopted the fluid mechanics in noninertial frame of reference. The natural circulation

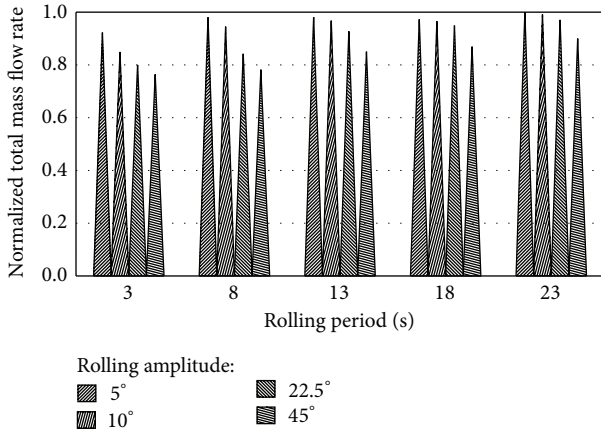


FIGURE 10: Average normalized total mass flow rates of different rolling cases.

behavior of integral type marine reactor simulator under rolling condition can be concluded as follows.

- (1) The heat and flow symmetry between heating channels and hot legs were broken. The flow rates of hot legs and left and right heating channels oscillated periodically with the same rolling period; however, the flow rates of middle heating channel and total mass flow rate oscillated with half rolling period. The average total mass flow rate in rolling motion was less than that in steady state.
- (2) The tangential forces along the pipes were in two circles, which generate theoretical flows in outer and inner loops. The superposition of theoretical flows and flows driven by density difference resulted in the oscillation of hot legs and left and right heating channels.
- (3) Natural circulation behaviors in rolling motion were results of the combined action of the variation of inclination angle, flow resistance (extra tangential force), and extra centrifugal force. Extra tangential force caused intense flow rates oscillation of hot legs, which resulted in increasing total flow resistance; however extra centrifugal force played a role in increasing the thermal driving head.

## Nomenclature

$A_s$ : Area of cross section,  $m^2$   
 $C_w$ : Heat transfer correction factor  
 $D_e$ : Hydraulic equivalent diameter, m  
 $D_h$ : Thermal equivalent diameter, m  
 $D_R$ : Rod diameter, m  
 $F_e$ : Extra tangential force  
 $F_r$ : Extra centrifugal force  
 $f_{ex}$ : Extra acceleration,  $m/s^2$   
 $f_{ex,z}$ : Extra acceleration component along axial,  $m/s^2$   
 $Gr$ : Grashof number

$g$ : Gravity acceleration =  $-9.8 m/s^2$   
 $g_z$ : Gravity acceleration component along axial,  $m/s^2$   
 $H_{Loss}$ : Pressure drop, Pa  
 $h$ : Enthalpy, J/kg  
 $k_i$ : Thermal conductivity, W/m  
 $Nu$ : Nusselt number  
 $Nu_{lam}$ : Nusselt number for laminar flow  
 $Nu_{turb}$ : Nusselt number for turbulent flow  
 $Nu_{nc}$ : Nusselt number for natural convection  
 $P_H$ : Thermal perimeter, m  
 $Pr$ : Prandtl number  
 $u$ : Velocity, m/s  
 $W$ : Mass flow rate, kg/s

## Greek letters

$\alpha$ : Intersection angle between main stream and  $x$ -axis, rad  
 $\beta$ : Intersection angle between main stream and  $y$ -axis, rad  
 $\gamma$ : Intersection angle between main stream and  $z$ -axis, rad  
 $\rho$ : Density,  $kg/m^3$   
 $\lambda$ : Friction factor  
 $\lambda_L$ : Friction factor for laminar flow  
 $\lambda_T$ : Friction factor for turbulent flow  
 $\varphi$ : Rolling angle, rad  
 $\varphi_m$ : The maximum rolling angle, rad  
 $\omega$ : Angle velocity, rad/s  
 $\tau$ : Rolling period, s  
 $\dot{\omega}$ : Angle acceleration,  $rad/s^2$   
 $\omega_d$ : Rolling frequency ( $= 2\pi/\tau$ )  
 $\varepsilon$ : Roughness.

## Conflict of Interests

The authors declare that there is no conflict of interests regarding the publication of this paper.

## References

- [1] T. Ishida, T. Yao, and N. Teshima, "Experiments of two-phase flow dynamics of marine reactor behavior under heaving motion," *Journal of Nuclear Science and Technology*, vol. 34, no. 8, pp. 771–782, 1997.
- [2] H. Murata, K. Sawada, and M. Kobayashi, "Natural circulation characteristics of a marine reactor in rolling motion and heat transfer in the core," *Nuclear Engineering and Design*, vol. 215, no. 1-2, pp. 69–85, 2002.
- [3] S. Tan, G. H. Su, and P. Gao, "Experimental and theoretical study on single-phase natural circulation flow and heat transfer under rolling motion condition," *Applied Thermal Engineering*, vol. 29, no. 14-15, pp. 3160–3168, 2009.
- [4] B. H. Yan and L. Yu, "The experimental and theoretical analysis of a natural circulation system in rolling motion," *Progress in Nuclear Energy*, vol. 54, no. 1, pp. 123–131, 2012.
- [5] T. Ishida, T. Kusunoki, M. Ochiai, T. Yao, and K. Inoue, "Effects by sea wave on thermal hydraulics of marine reactor system,"

*Journal of Nuclear Science and Technology*, vol. 32, no. 8, pp. 740–751, 1995.

- [6] T. Ishida and T. Yoritsune, “Effects of ship motions on natural circulation of deep sea research reactor DRX,” *Nuclear Engineering and Design*, vol. 215, no. 1-2, pp. 51–67, 2002.
- [7] J. H. Kim and G. C. Park, “Developemt of RETRAN-03/MOV code for thermal hydraulic analysis of nuclear reactor under moving conditions,” *Journal of the Korean Nuclear Society*, vol. 28, no. 6, pp. 542–550, 1996.
- [8] D. J. Zigrang and N. D. Sylvester, “Review of explicit friction factor equations,” *Journal of Energy Resources Technology, Transactions of the ASME*, vol. 107, no. 2, pp. 280–283, 1985.
- [9] J. Weisman, “Heat transfer to water flowing parallel to tube bundles,” *Nuclear Science and Engineering*, vol. 6, pp. 78–79, 1959.

## Research Article

# Research and Evaluation for Passive Safety System in Low Pressure Reactor

**Peng Chuanxin, Zhuo Wenbin, Chen Bingde, Nie Changhua, and Huang Yanping**

*Nuclear Power Institute of China, Chengdu 60041, China*

Correspondence should be addressed to Peng Chuanxin; [xingxing322@163.com](mailto:xingxing322@163.com)

Received 6 December 2013; Revised 23 March 2014; Accepted 15 July 2014

Academic Editor: Shengqiang Li

Copyright © 2015 Peng Chuanxin et al. This is an open access article distributed under the Creative Commons Attribution License, which permits unrestricted use, distribution, and reproduction in any medium, provided the original work is properly cited.

Low pressure reactor is a small size advanced reactor with power of 180 MWt, which is under development at Nuclear Power Institute of China. In order to assess the ability and feasibility of passive safety system, several tests have been implemented on the passive safety system (PSS) test facility. During the LOCA and SBO accident, the adequate core cooling is provided by the performance of passive safety system. In addition the best-estimate thermal hydraulic code, CATHARE V2.1, has been assessed against cold leg LOCA test. The calculation results show that CATHARE is in a satisfactory agreement with the test for the steady state and transient test.

## 1. Introduction

The use of passive safety systems eliminates the costs associated with the installation, maintenance, and operation of active safety systems that require multiple pumps with independent and redundant electric power supplies [1]. As a result, passive safety systems are being considered for numerous reactor concepts, such as AP600/API1000 [2], APRI400 [3], APWR+ [4], SMART [5], IRIS [6], and MASLWR [7].

The AP600 was the first passively safe nuclear plant to be certified in the United States. It employs passive safety systems that rely on gravity (core make-up tank, in-containment refueling water storage tank), compressed gas (accumulator), natural circulation (passive residual heat removal heat exchanger), and evaporation to provide for long-term cooling in the event of an accident.

The certification of AP600/API1000 was based on comprehensive integral system and separate effects testing conducted by Westinghouse and the US Department of Energy at the SPES test facility in Italy and at the APEX test facility at Oregon State University. The purpose of SPES-2 tests was to simulate AP600 response to postulated accident events and to validate safety analysis codes [8]. The second integral facility APEX emphasized the depressurization, IRWST injection, and long-term cooling during small break LOCA [9]. Besides, US NRC conducted independent integral test programs at

ROSA in Tokai-mura, Japan, focusing on the high pressure and depressurization phase, the initiation of IRWST injection [10], and the passive residual heat removal [11].

Low pressure reactor is a small size advanced reactor with power of 180 MWt, which is under development at Nuclear Power institute of China. The primary system of reactor consists of a reactor pressure vessel, four loops, and the tank. Each loop is made up of heat exchanger and reactor coolant pump, hot leg and cold leg, and so forth. The reactor produces 200,000 m<sup>3</sup>/day of hot water (90°C) for low temperature seawater desalination. The low pressure reactor operates at low temperature (temperature at the outlet is 98°C) and atmospheric pressure (pressure at the top of tank is 0.1 MPa). It follows that the consequences of accidents are less severe than typical PWR. In addition, it adopts passive engineered safety systems such as emergency core cooling system and passive residual heat removal system to mitigate consequences of accidents. Figure 1 shows the schematic diagram of the low pressure reactor. The tank is a significant component of low pressure reactor, which is a very large pool filled with cold borated water with a volume of 1310 m<sup>3</sup>. During the normal operation, the tank is used to maintain the primary system pressure. And during the shutdown or non-LOCA, tank is treated as heat sink for the core decay heat. Another important role of the tank is to provide water source for core injection if LOCA occurs. As the operational

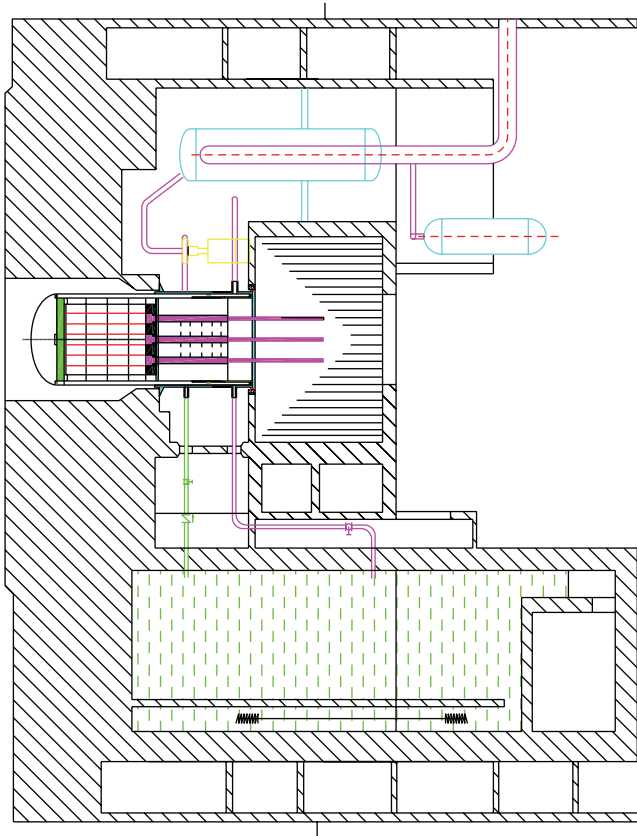


FIGURE 1: Schematic diagram of low pressure reactor.

pressure is about 0.4 MPa, the head pressure of the water in the tank is adequate for core injection. Therefore the design of Accumulator and Automatic Depressurization System is not necessary for the low pressure reactor.

In order to assess the ability and feasibility of low pressure reactor passive safety system, several tests have been implemented on the passive safety system (PSS) test facility [12]. In this paper the experimental investigations on the characteristics of the passive safety systems under LOCA and SBO are reported in detail. In addition the experimental data are used to assess CATHARE simulating the cold leg LOCA test.

## 2. Passive Safety System Test Facility

The passive safety system test facility is employed to simulate various accidental scenarios (such as loss-of-coolant accident and station black-out accident) that might occur in the low pressure reactor. To preserve the similar thermal hydraulic transients, the PSS facility has a geometrical scaling ratio of 1/1 in length and height and 1/45 in volume, and it operates at full pressure and temperature conditions of prototype [13]. Table 1 shows the scaling ratios of the facility to the low pressure reactor for some major geometrical and thermal hydraulic parameters. The schematic diagram of PSS facility is shown in Figure 2. And its main features are summarized as follows.

- (1) The reactor vessel is simulated by the core simulation vessel and downcomer annulus simulation vessel. A total number of 96 electrically heated rods with a maximum total power of 600 kW are installed in the core simulation vessel. The break simulating system consists of a quick open valve, a venturi flow meter, and the core external cavity simulation vessel. The break flow rate was directly measured with a venturi flow meter. The venturi flow meter was installed at the upstream of the break nozzle for the break flow location. The accumulated water in the core external cavity simulation vessel shows good agreement with the break flow rate measured by venturi flow meter.
- (2) The PSS test facility is designed to be operated by a combination of manual and automatic operations. The controlled components include the electrically heated rod, the primary coolant pump, the primary loop flow control valve, and the heat exchanger cooling water flow control valve. All the safety related accidents should be initiated and controlled by automatic control logics as they require automatic reactor trip logics to initiate the passive core cooling systems and the passive residual heat removal system. The corresponding trip logics, tables, and set points are programmed to control a sequence of events.
- (3) The data acquisition system involves 55 instruments to measure system pressure, differential pressure, fluid temperature, water level, and flow rate. The precision of nickel-chrome and nickel-silicon thermocouples is within  $\pm 1.5^{\circ}\text{C}$ . The pressure of the system is measured by the pressure transducer, whose precision is within  $\pm 0.5\%$ . The flow rate is measured by wide range venturi flow meters, the precision of which is within  $\pm 1\%$ .

## 3. Description of the Tests

A series of tests devoted to validate the efficiency of low pressure reactor passive safety system were performed in the recent years. The experimental program includes two series with altogether eighteen experiments. The experimental series and conditions are listed in Table 2. The first series focus on validation and research of passive core cooling behaviour, such as cold leg LOCA, hot leg LOCA, and the influence of sensitive parameters. The second series study SBO accident and the influence of sensitive parameters on the passive residual heat removal behaviour [5]. In this paper the cold leg LOCA and SBO test results are presented.

**3.1. Cold Leg LOCA Test.** The passive system is designed to cool the reactor in more than 48 h, and the fluid temperature in the tank should be less than  $80^{\circ}\text{C}$ , when the LOCA accident occurs. The motivation of cold leg LOCA test (PSS-11) is to evaluate the safety features of low pressure reactor.

The postulated cold leg LOCA is the one initiated by opening the break simulation valve, causing the system pressure to decrease. Thereafter, the check valve of injection line

TABLE 1: Major scaling ratios of PSS.

Parameters	Scaling ratio	PSS	Parameters	Scaling ratio	PSS
Length (height)	$l_{OR}$	1:1	Diameter	$d_{OR}$	1:6.71
Area	$d_{OR}^2$	1:45	Volume	$l_{OR} d_{OR}^2$	1:45
Core temperature rise	$T_{OR}$	1:1	Velocity	$l_{OR}^{1/2}$	1:1
Time	$l_{OR}^{1/2}$	1:1	Power/volume	$l_{OR}^{1/2}$	1:1
Heat flux	$l_{OR}^{1/2}$	1:1	Core power	$l_{OR}^{1/2} d_{OR}^2$	1:1
Diameter of rod	1	1:1	No. of rods	$d_{OR}^2$	1:45
Flow rate	$l_{OR}^{1/2} d_{OR}^2$	1:45	Pressure drop	$l_{OR}$	1:1

TABLE 2: Typical test matrix.

Experiment	Condition (Break location, break size, and water level and temperature in tank)	Objectives
First series		
PSS-11	Cold leg, 22 mm, 23 m, 32°C	Validation of passive core injection
PSS-12	Hot leg, 22 mm, 23 m, 32°C	Validation of passive core injection
PSS-13	Cold leg, 18 mm, 23 m, 32°C	Break size effect
PSS-14	Cold leg, 14 mm, 23 m, 32°C	Break size effect
PSS-15	Cold leg, 10 mm, 23 m, 32°C	Break size effect
PSS-16	Hot leg, 18 mm, 23 m, 32°C	Break size effect
PSS-17	Hot leg, 14 mm, 23 m, 32°C	Break size effect
PSS-18	Hot leg, 10 mm, 23 m, 32°C	Break size effect
PSS-19	Cold leg, 22 mm, 18 m, 32°C	Water level effect
PSS-110	Cold leg, 22 mm, 13 m, 32°C	Water level effect
PSS-111	Cold leg, 22 mm, 23 m, 22°C	Water temperature effect
PSS-112	Cold leg, 22 mm, 23 m, 42°C	Water temperature effect
Experiment	Condition (Resistance*, startup mode*, and water temperature in tank)	Objectives
Second series		
PSS-21	100% of prototype, cold startup, 32°C	Validation of passive residual heat removal
PSS-22	120% of prototype, cold startup, 32°C	Resistance effect
PSS-23	150% of prototype, cold startup, 32°C	Resistance effect
PSS-24	100% of prototype, hot startup, 32°C	Startup mode effect
PSS-25	100% of prototype, cold startup, 22°C	Water temperature effect
PSS-26	100% of prototype, cold startup, 42°C	Water temperature effect

\* Resistance includes.

Startup mode includes cold startup and hot startup.

Cold startup: the fluid in the PL is cold before the natural circulation is established.

Hot startup: the fluid in the PL is warm before the natural circulation is established.

is actuated automatically. Then the coolant in the tank was injected into reactor through the surge line. The discharge of coolant in the tank causes liquid level to decrease. A scram signal trips, when the pressure at the core outlet is less than 350 kPa. Following the S-signal, the reactor is tripped; the reactor coolant pumps coasted down; the feedwater supply of heat exchanger is terminated; the passive residual heat removal line and injection line isolation valves are open.

According to the characteristics of the test, the overall transients of the cold leg LOCA test can be roughly characterized by typical two stages: injection stage and natural circulation stage.

The typical results of cold leg LOCA test are shown in Figures 3~6. Figure 3 shows the core pressure. As the break occurs at the cold leg, the system pressure decreases. The top of tank is open to atmosphere, and the initial liquid level is

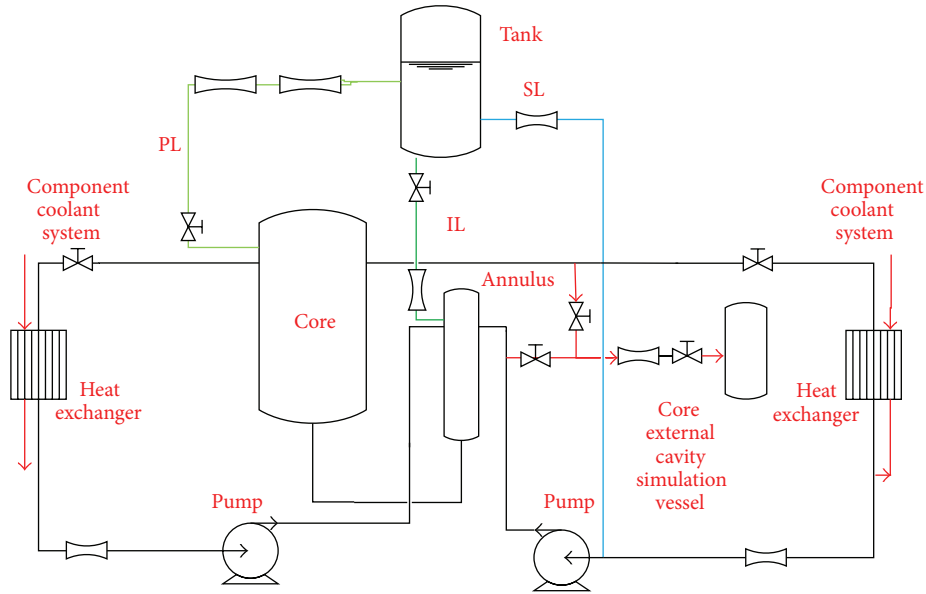


FIGURE 2: Schematic diagram of PSS test facility.

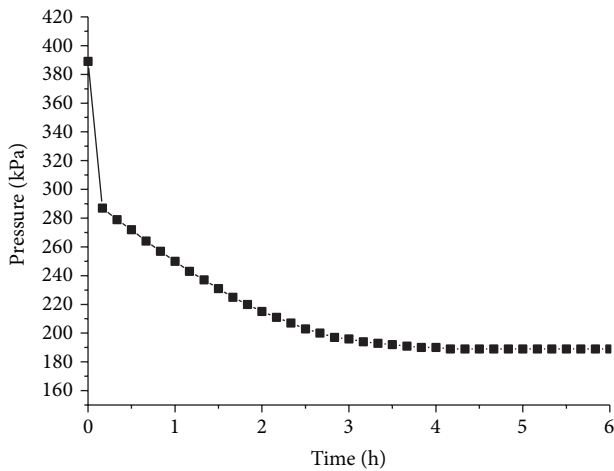


FIGURE 3: The system pressure.

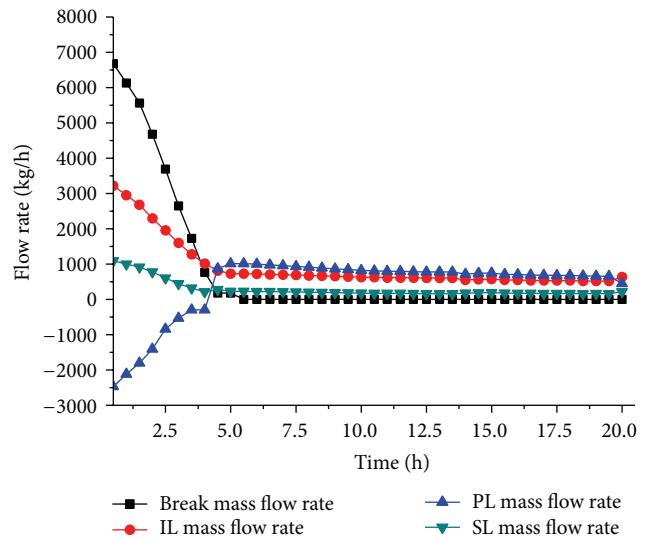


FIGURE 4: The mass flow rate of the main lines.

23 m (the bottom of tank is 0.15 m higher than the top of reactor vessel). Therefore the water in the tank can be injected into reactor vessel by gravity.

Figure 4 shows the flow rate of some lines. As the liquid level in the tank descends, the mass flow rate of break, IL, SL, and PL decreases. When the level in the tank is equal to that in the core external cavity simulation vessel, the break flow stops and the natural circulation stage begins.

The temperature of fluid in the core is illustrated in Figure 5. At the initial period, the fluid temperature drops quickly, and the core outlet temperature is lower than that in the inlet. Because most of injection of SL and IL bypasses the core simulation vessel, however the cold water from PL can be injected into the upper plenum. As a result, the reverse flow happens in the core simulation vessel. As the flow rate injected into the core decreases, the temperature begins to

rise after 2.8 h. When the fluid in the core is stagnant, the temperature in the core inlet and outlet rises to 52.4°C and 69.4°C, respectively. The fluid temperature in the core does not rise until the stable natural circulation is established.

In the natural circulation stage, cold water in the tank is injected into the core through SL and IL. Hot water from the core outlet rises along PL and returns to the tank, which is driven by buoyancy. The core residual heat is removed into the tank by natural circulation. Figure 6 shows the fluid temperatures in tank. When the natural circulation begins (about 4.1 h after accident happens), the fluid temperature at the top of tank rises. After 48 h, the fluid temperature in the tank is less than 60°C. Therefore, the adequate core cooling

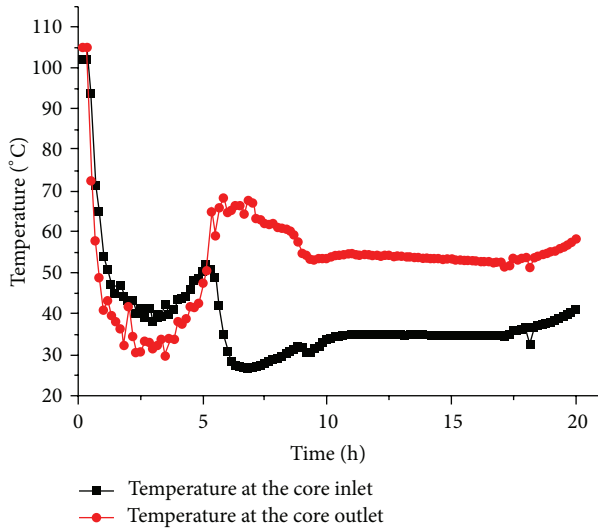


FIGURE 5: Temperature at the core inlet and outlet.

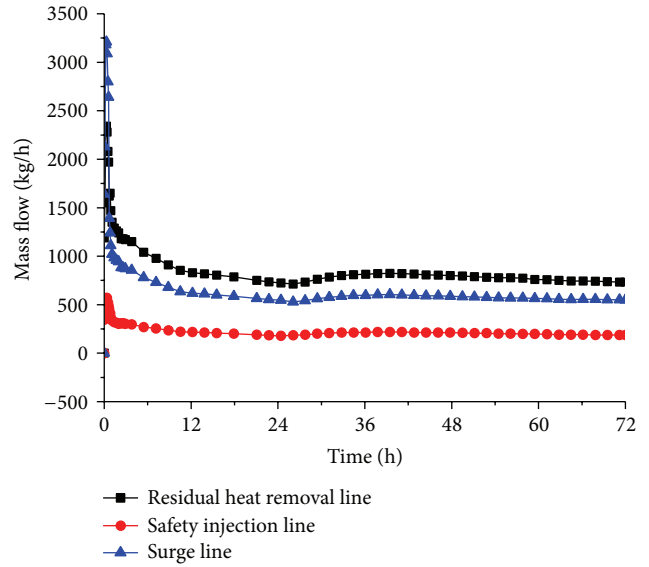


FIGURE 7: Natural circulation flow rate.

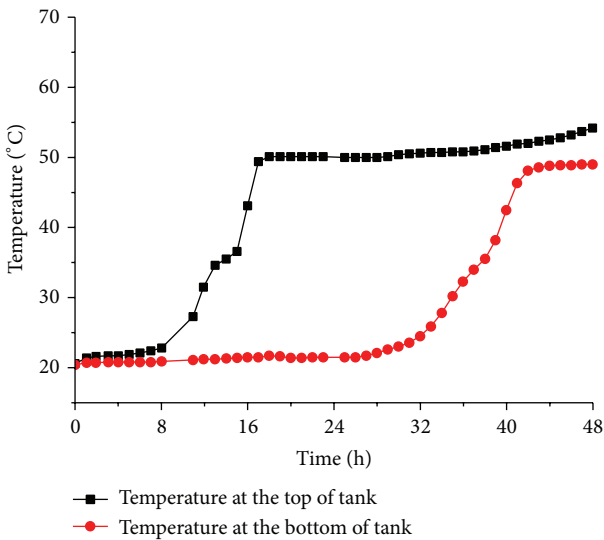


FIGURE 6: Fluid temperatures in tank.

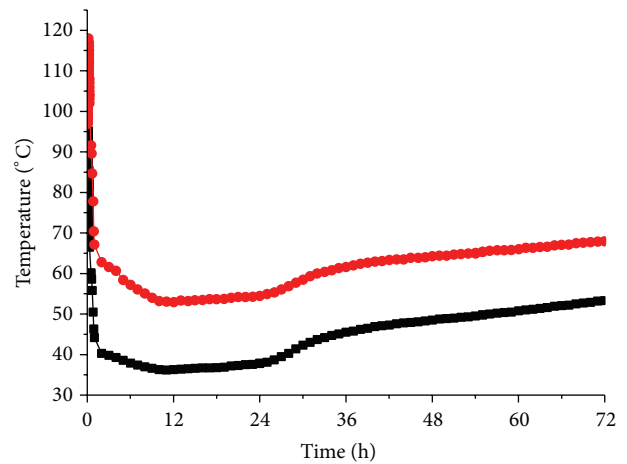


FIGURE 8: Core inlet and outlet fluid temperatures.

is provided by passive safety system dominantly, during the cold leg LOCA.

3.2. *Station Black-Out Accident.* The passive residual heat removal system is designed to remove the decay heat in more than 72 h, and the fluid temperature in the tank should be less than 80°C, when the station black-out accident occurs. The motivation of station black-out accident (PSS-21) is to validate the ability of the passive residual heat removal system.

The postulated station black-out accident is the one initiated by stopping the reactor coolant pumps. Following the accident, the reactor is tripped; only the passive safety systems are operational to remove the core decay heat or to mitigate the consequence of the accident.

The typical results of station black-out accident test are shown in Figures 7~9. Figure 7 shows the flow rate in the two parallel natural circulation paths. When the station black-out accident is initiated, the natural circulation begins at the time of reactor coolant pumps coastdown. The two parallel natural circulations “core—residual heat removal line—tank—safety injection line—core” and “core—residual heat removal line—tank—surge line—core” remove the core decay heat to the tank.

Figure 8 shows the temperature of fluid at the core inlet and outlet. At the beginning of the accident, the natural circulation is unable to remove the core decay heat effectively. And a small portion of coolant at the core outlet evaporates. The two-phase mixture flows into the residual heat removal line, resulting in the increase of natural circulation. The measurements of the flow in the PL line, considered just

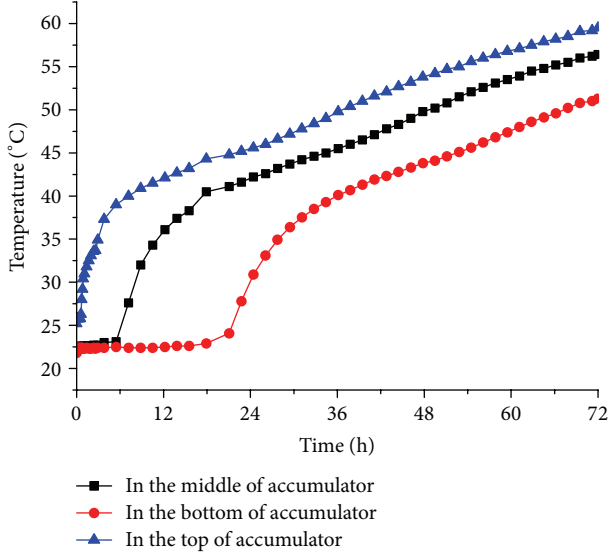


FIGURE 9: Fluid temperatures in tank.

for single-phase flow, are corrected by flow rate of IL and SL. When the natural circulation comes to being stable, the temperature in the core drops rapidly.

Figure 9 shows the temperature of coolant in the tank. The residual heat removal line connects to the top of tank; therefore, the water in the top becomes hot firstly. As the core decay heat is taken to the tank constantly, the cold water in the tank is replaced by hot water gradually. After 72 h, the coolant in the core is still lower than 60°C. Therefore the experimental results show that the single-phase natural circulation flows steadily into the two parallel loops that it effectively removes the decay heat from the core to tank in more than 72 hours.

## 4. Computer Code Simulations

**4.1. Code Description.** CATHARE is a system code developed by CEA, EDF, FRAMATOME-ANP, and IRSN for pressurized

water reactor (PWR) safety analysis. CATHARE is designed to perform best-estimate analyses of LOCA, operational transients, and other accident scenarios in pressurized water reactor. It can also model phenomena occurring in experimental facility designed to simulate transients in reactor systems. CATHARE modules are based on a six-equation two-fluid model (mass, energy, and momentum equations for each phase), with additional optional equations for non-condensable gases and radiochemical components. A specific treatment of the residual phases exists in order to manage their appearance and disappearance while minimizing convergence problems and with a quasiperfect mass and energy conservation [14]. The version of the code used in this paper is CATHARE V2.1.

**4.2. System Model.** CATHARE has a flexible modular structure for the thermal-hydraulic modeling in applications ranging from simple experimental test facilities to large and complex installations like nuclear power plants. The main hydraulic components or elements are pipes (1D), volumes (0D), 3D vessel, and boundary conditions, connected to each other by junctions. These models except 3D vessel are based on the 6-equation model, which are two mass balance equations, two momentum balance equations, and two energy balance equations. In CATHARE, the critical flow rate is also determined by the some characteristic of the 6-equation model. The physical closure laws play a dominant role in the calculation of critical flow rate. The critical flow rate for nonhomogeneous nonequilibrium two-phase flow is obtained by solving the Jacobian matrix at each time step. The liquid and vapour velocity, obtained by solving the 6-equation system, are then compared with the choking criterion (known as the GROS D'AILLON correlation) [15]. This method is qualified using the results of experimental facilities, such as MOBY DICK facility, BETHSY BREAK NOZZLE characterization tests, and MARVIKEN facility [16]. These facilities are high pressure experiments. In this paper, the break flow rate is validated by experimental data from low pressure:

$$\begin{aligned}
 G_{CR} &= S \times \sqrt{\frac{20 \times 0.456^2 \times \rho_m \times (P - P_{sat}(T_L))}{(\alpha + 10 \times 0.456^2 \times (1 - \alpha)) \times (1 + 0.012 \times (L/D) + k_{\Delta Ps})}}, \\
 \rho_m &= \alpha \times \rho_g + (1 - \alpha) \rho_L, \\
 &(P - P_{sat}(T_L)) \\
 &= \begin{cases} P - 0.9 \times 10^5 \times \left( \frac{T_{Leq} + 17.95}{117.8} \right)^{1/0.223}, & \text{if } T_L < T_{sat}(P), \\ \frac{P}{10}, & \text{if } T_L > T_{sat}(P), \end{cases} \\
 T_{Leq} &= T_L + \frac{(H_V - H_L) \times \alpha \times \rho_V}{\rho_m \times CP_L},
 \end{aligned}
 \tag{1}$$

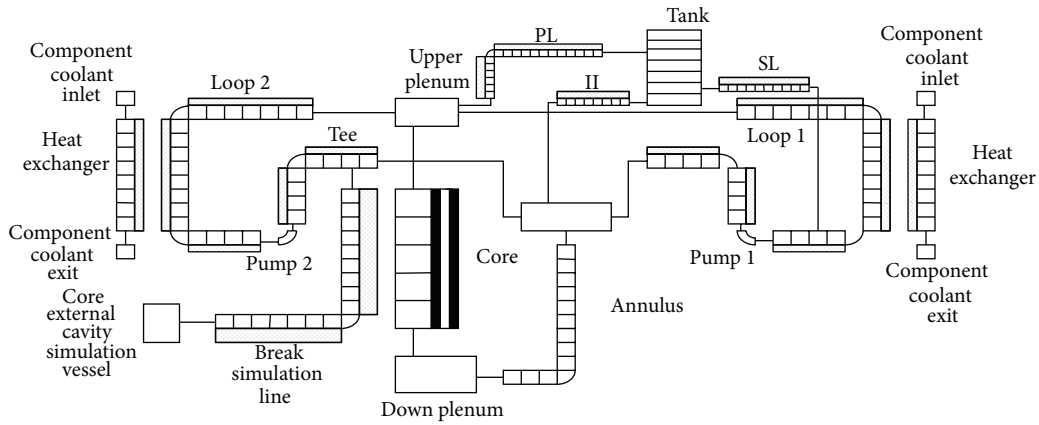


FIGURE 10: CATHARE nodalization diagram of the PSS facility.

where  $G_{CR}$  is the critical flow rate choking criterion,  $S$  is the break area,  $\rho_m$  is the mean density,  $\rho_g$  is the gas density,  $\rho_L$  is the liquid density,  $T_{Leq}$  is the equilibrium temperature (after steam condensation),  $T_L$  is liquid temperature,  $T_g$  is the gas temperature,  $P$  is the pressure,  $H_L$  is the liquid enthalpy,  $H_g$  is the gas enthalpy,  $\alpha$  is void fraction, and  $CP_L$  is the liquid specific heat.

In this paper the core and bypass are modeled with 1D pipes, and the WALL is used to model the power produced by the electrically heated rods and the heat loss of test facility. The upper plenum, lower plenum, and tank are modeled by 0D volume. TEE + AXIAL+ BCONDIT is used to model the break. Figure 10 illustrates a schematic nodalization of the major elements of the PSS test facility for CATHARE simulation.

### 4.3. Calculation Results

**4.3.1. Calculation of the Initial Steady State.** At first, a steady state calculation with constant boundary conditions was performed for each test. With help of these calculations, the temperature and pressure distribution, the heat losses, the pressure losses, and the water level were adjusted. When the stable conditions are reached, the steady state calculation is stopped. The main parameters obtained at the end of steady state calculation are compared with the experimental data shown in Table 3. The small difference between the calculation result and the experimental data remains below the sensors uncertainties. Therefore, we can consider that there is a good agreement between CATHARE code predictions for the initial steady state.

**4.3.2. Calculation of Transient State.** The transient calculation results of cold leg LOCA test are compared with experimental data in Figures 11~13. The comparison of break flow rate is shown in Figure 11. We can see that the calculated break flow rate is in acceptable agreement with experimental data. For low pressure and highly subcooled inlet conditions, the

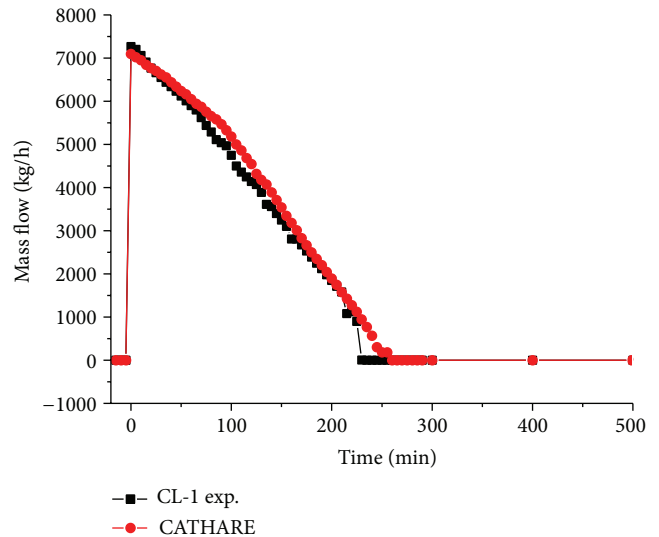


FIGURE 11: The break flow rate.

break flow rate is obtained by solving the Bernoulli equation, and CATHARE can predict it accurately. There is a little discrepancy, which occurs at the end of injection stage. As for the instrumental error, the small break flow rate cannot be monitored by the wide range venturi flow meter.

Figure 12 illustrates the calculated system pressure, which shows reasonable agreement with the experimental data, owing to the good predicted break mass flow rate. During the transition between injection stage and natural circulation stage, the main phenomenon is that the flow reverses in passive residual heat removal line. It is also predicted well by CATHARE as shown in Figure 13. In addition, the other calculated system parameters, such as the temperature of coolant at the core inlet and outlet, the IL mass flow rate, SL mass flow rate, and water level in tank, are in accordance with experimental data.

TABLE 3: Measured and calculated initial conditions.

Parameter	Unit	Test	Calculation	Error %
Core power	kW	600	600.5	0.02
Pressure	kPa	398.0	396.3	-0.43
Loop 1 flow rate	kg/s	4.339	4.396	1.3
Loop 2 flow rate	kg/s	4.354	4.401	1.1
Core inlet fluid temperature	°C	91.2	91.0	-0.22
Core outlet fluid temperature	°C	98.0	98.6	0.61
Water level in tank	m	23.0	22.8	-0.87

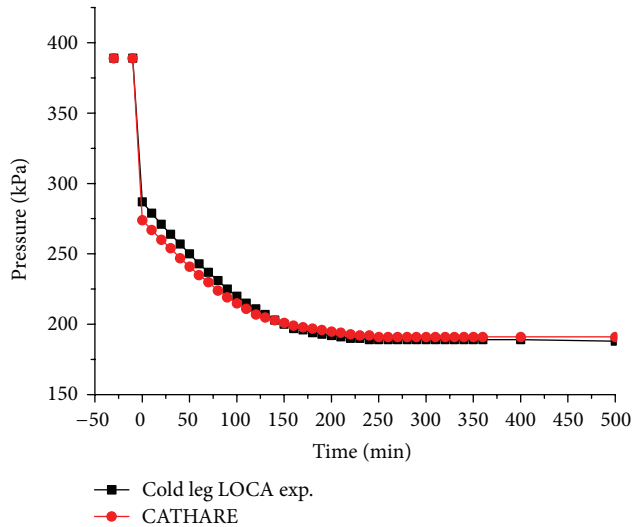


FIGURE 12: The system pressure.

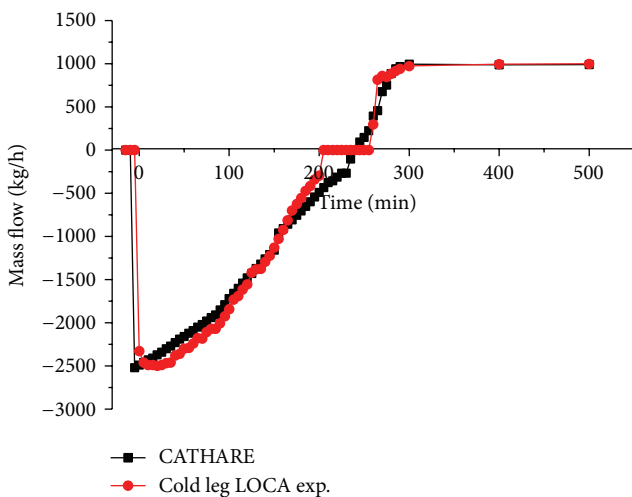


FIGURE 13: The PL flow rate.

## 5. Conclusions

The designed passive engineered safety systems are an important part of the low pressure reactor. The passive safety characteristics of the reactor following several safety related events have been experimentally investigated in the

PSS test facility. In case of LOCA and SBO accident, the transient trend of the reactor primary loop, emergency core cooling system, and passive residual heat removal system are studied. In the cold leg LOCA test, the water level is enough for passive injection driven by gravity. After the injection stage stops, the natural circulation is established to remove the decay heat to tank continuously. During the station black-out accident, the natural circulation effectively removes the decay heat from the core to tank in more than 72 hours. In addition, the best-estimate thermal hydraulic code, CATHARE V2.1, has been assessed against cold leg LOCA test. The calculation results show that CATHARE predicts the break flow rate accurately for low pressure and highly subcooled inlet conditions. And CATHARE is fully able to calculate the overall scenario observed in the cold leg LOCA test. The calculated parameters are in acceptable agreement with the experimental data.

## Nomenclature

PSS: Passive safety system  
 LOCA: Loss-of-coolant accident  
 SBO: Station black-out  
 PL: Passive residual heat removal line  
 SL: Surge line  
 IL: Injection line.

## Conflict of Interests

The authors declare that there is no conflict of interests regarding the publication of this paper.

## References

- [1] International Atomic Energy Agency, "Passive Safety Systems and Natural Circulation in Water Cooled Nuclear Power Plants," IAEA-TECDOC-1624.
- [2] L. Enchavarri, A General Description of AP1000 Advanced Passive Nuclear Power Plant.
- [3] Korea Hydro & Nuclear Power Corporation, "Standard safety analysis," Tech. Rep. APRI400, Korea Hydro & Nuclear Power Corporation, Seoul, South Korea, 2002.
- [4] Y. Tujikura, T. Oshibe, K. Kijima, and K. Tabuchi, "Development of passive safety systems for Next Generation PWR in Japan," *Nuclear Engineering and Design*, vol. 201, no. 1, pp. 61-70, 2000.
- [5] H. C. Kim, Y.-J. Chung, K. H. Bae, and S. Q. Zee, "Safety analysis of SMART," in *Proceedings of the International Conference*

- on Global Environment and Advanced Nuclear Power Plants (GENES4/ANP '03)*, Kyoto, Japan, September 2003.
- [6] J. M. Collado, "Design of the reactor pressure vessel and internals of the IRIS integrated nuclear system," in *Proceedings of the International Congress on Advanced Nuclear Power Plants*, Cordoba, Spain, 2003.
  - [7] J. N. Reyes Jr., J. Groome, B. G. Woods et al., "Testing of the multi-application small light water reactor (MASLWR) passive safety systems," *Nuclear Engineering and Design*, vol. 237, no. 18, pp. 1999–2005, 2007.
  - [8] M. T. Friend, R. F. Wright, R. Hundal, L. E. Hochreiter, and M. Ogrins, "Simulated AP600 response to small-break loss-of-coolant-accident and non-loss-of-coolant-accident events: analysis of SPES-2 integral test results," *Nuclear Technology*, vol. 122, no. 1, pp. 19–42, 1998.
  - [9] R. F. Wright, "Simulated API000 response to design basis small-break LOCA events in APEX-1000 test facility," *Nuclear Engineering and Technology*, vol. 39, no. 4, pp. 287–298, 2007.
  - [10] Y. Kukita, T. Yonomoto, H. Asaka et al., "ROSA/AP600 testing: facility modifications and initial test results," *Journal of Nuclear Science and Technology*, vol. 33, no. 3, pp. 259–265, 1996.
  - [11] T. Yonomoto, Y. Kukita, and R. R. Schultz, "Heat transfer analysis of the passive residual heat removal system in ROSA/AP600 experiments," *Nuclear Technology*, vol. 124, no. 1, pp. 18–30, 1998.
  - [12] L. Xun and P. Chuanxin, "Low Pressure Reactor Passive Safety System integrated simulation," Test Analysis Report, NPIC, 2009.
  - [13] M. Ishii and I. Kataoka, *Similarity Analysis and Scaling Criteria for LWRs Under Single Phase and Two-Phase Natural Circulation*, NUREG/CR-3267, ANL-83-32, Argonne National Laboratory, 1983.
  - [14] G. Lavialle, "CATHARE2 V2.5.1: User Guidelines, DER/SSTH/LDAS/EM/2005-034," 2005.
  - [15] G. Lavialle, *CATHAREV2.5.1: User Manual DER/SSTH/LDAS/EM/2005-035*, 2005.
  - [16] F. Barre and M. Bernard, "The CATHARE code strategy and assessment," *Nuclear Engineering and Design*, vol. 124, pp. 257–284, 1990.

## Research Article

# Natural Circulation Characteristics of a Symmetric Loop under Inclined Conditions

**Xingtuan Yang, Yanfei Sun, Zhiyong Liu, and Shengyao Jiang**

*Key Laboratory of Advanced Reactor Engineering and Safety, Ministry of Education, Institute of Nuclear and New Energy Technology of Tsinghua University, Beijing 100084, China*

Correspondence should be addressed to Xingtuan Yang; [yangxt@mail.tsinghua.edu.cn](mailto:yangxt@mail.tsinghua.edu.cn)

Received 10 November 2013; Revised 28 June 2014; Accepted 15 July 2014; Published 14 August 2014

Academic Editor: Shengqiang Li

Copyright © 2014 Xingtuan Yang et al. This is an open access article distributed under the Creative Commons Attribution License, which permits unrestricted use, distribution, and reproduction in any medium, provided the original work is properly cited.

Natural circulation is an important process for primary loops of some marine integrated reactors. The reactor works under inclined conditions when severe accidents happen to the ship. In this paper, to investigate the characteristics of natural circulation, experiments were conducted in a symmetric loop under the inclined angle of  $0\sim 45^\circ$ . A CFD model was also set up to predict the behaviors of the loop beyond the experimental scope. Total circulation flow rate decreases with the increase of inclined angle. Meanwhile one circulation is depressed while the other is enhanced, and accordingly the disparity between the branch circulations arises and increases with the increase of inclined angle. Circulation only takes place in one branch circuit at large inclined angle. Also based on the CFD model, the influences of flow resistance distribution and loop configuration on natural circulation are predicted. The numerical results show that to design the loop with the configuration of big altitude difference and small width, it is favorable to reduce the influence of inclination; however too small loop width will cause severe reduction of circulation ability at large angle inclination.

## 1. Introduction

Natural circulation is widely used in nuclear systems because of its advantages over the forced flow process, such as the elimination of the pump, improved safety and reliability, and the reduction of maintenance costs [1, 2]. Certain ship-mounted integrated type nuclear power plants also use the natural circulation process for portable desalination [3, 4]. However, the thermohydraulic characteristics of natural circulation in ship-mounted plants are far more complex than land-based plants due to the influence of ship motions such as heaving, rolling, and inclination [5–9] (Figure 1). In the event of incidents such as collision, sinking, or stranding, the reactor will work under inclined conditions. An understanding of natural circulation behavior under different inclined angles is crucial because inclination causes a reduction in the driving force and also a break in the thermohydraulic symmetry of the reactor, where the steam generators annularly surround the core.

Different groups have conducted experimental and numerical studies on specific systems in order to predict

the influences of inclination. Iyori [10] used a model of an integrated type marine reactor to investigate the effect of inclination on single-phase natural circulation. Results showed that the temperature distribution from the steam generator at an inclined attitude was primarily dependent on elevation. Kim [11] performed steady-state natural circulation experiments on the test facility of the system-integrated modular advanced reactor (SMART) mounted on leaning equipment for inclination. The experiments investigated asymmetric flow patterns in the upper pressure header, steam generator cassettes, and downcomer during feed water isolation and inclination. Kim [12] also developed a CFD model and investigated the 3D effects of inclination for the same system. Ishida [13] investigated the effects of inclination on thermal-hydraulic behavior of a DRX (deep-sea reactor) using the RETRAN-02/GRAV code. The numerical results showed that ship inclination, even at  $60^\circ$ , induced the core flow to decrease, but the reactor power recovered to initial power levels due to the inherent characteristics of the DRX core. Gao [14] developed a simple mathematical model to

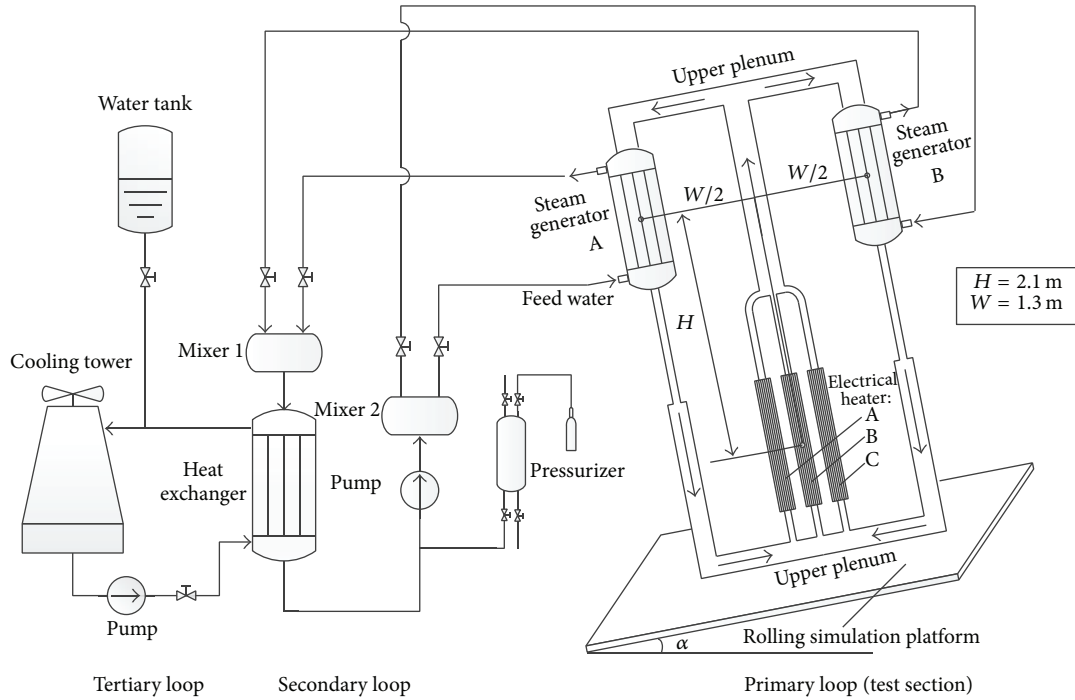


FIGURE 1: Test apparatus.

predict the circulation characteristics under inclined conditions, but asymmetric effects were not considered in that model. In principle, these results are all restricted to specific systems. The mechanisms of inclination influence are still not comprehensively and quantitatively presented for different systems.

This paper presents research on the natural circulation process in a symmetric two-circuit test loop under inclined conditions. Experiments were conducted under inclined angles of  $0\sim 45^\circ$ . A CFD model was built, based on which the thermodynamics characteristics of natural circulation under inclined angles of  $45\sim 90^\circ$  were also analyzed. Additionally, this paper discusses the variations in overall circulation ability, disparity in branch circulation, and the influence of loop configuration and resistance distribution.

## 2. Test Apparatus

The test loop consisted of three subloops (Figure 1). The primary loop was the test section, designed as a symmetric two-circuit loop in order to simulate the symmetric characteristics of an actual plant. Three electric heaters (EH), located at the shared part of the two circuits, supplied the heat source. Each heater consisted of 16  $\Phi 10 \times 1$  mm and 1080 mm long stainless steel heating tubes. A direct current was applied to the electric heater during operation, with a voltage up to 75 V and total current of 2000 A. The heat sink was two steam generators (SG) that were symmetrically installed on the upper part of each circuit. Heat generated by EH was finally emitted into the environment through the SG, the secondary

loop, and the third loop, in order to establish the energy balance. The effective altitude difference between the heat source and heat sink,  $H_0$ , was 2100 mm. The distance between the steam generator centers,  $W$ , was 1255 mm. The primary loop was installed on a ship motion simulation platform, which inclined about the  $x$ -axis and  $y$ -axis with maximum angles of  $45^\circ$  and  $20^\circ$ , respectively. The working fluid of the primary loop was demineralized water with a pressure of 4.0 MPa.

The secondary loop consisted of a pump, a heat exchanger, two mixers, and a pressurizer. The coolant for the secondary loop was water driven by a pump rather than natural circulation. The mixer and control valves were used to equally set the coolant temperature and flow rates of the two circuits in order to avoid an unbalanced load. The secondary loop was kept at high pressure (4.0 MPa) to prevent the occurrence of two-phase flow due to the simplicity of the equipment. The pressurizer was filled with high-pressure nitrogen gas in order to adjust and maintain the pressure. The main equipment for the third loop was the cooling tower, through which heat input from the secondary loop was finally emitted into the environment with the coolant circulation.

Ultrasonic flow meters measured the flow of natural circulation at the outlets of each electric heater module and steam generator. The meters had an accuracy 0.5% over the measured flow rate value and did not bring extra resistance to the circulation. The flow rates of the secondary and third loop were measured by orifice-type flow meters. Temperature was measured by thermocouples with an accuracy 1% over the temperature range (according to manufacturer specifications). A total of 36 thermocouples were installed at crucial

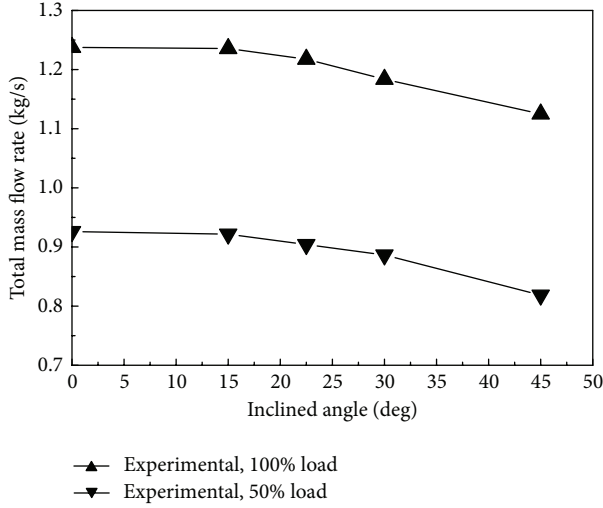


FIGURE 2: Total mass flow rates under different inclined angle.

positions throughout the entire test loop, including the inlets and outlets of EH, SG, and the heat exchanger.

### 3. Experimental Results

A series of experiments were conducted under inclined angles of  $0^\circ$ ,  $15^\circ$ ,  $22.5^\circ$ ,  $30^\circ$ , and  $45^\circ$ . The maximum inclined angle is  $45^\circ$  because of the restriction of the ship motion simulation platform. Power input from the electric heater controlled the load from 50 to 100%. The flow rates of the secondary and third loop were kept constant during the experiments. The testing was conducted over 2 hours for each inclined angle in order to obtain a steady state.

The volume flow rate of each steam generator outlet was recorded. The total mass flow rate was obtained by multiplying the density computed by the local pressure and temperature. The results showed that an increase in the inclined angle gradually weakened the circulation. An inclined angle of  $45^\circ$  had a mass flow rate approximately 10% less than an inclined angle of  $0^\circ$  (Figure 2). The average temperature difference,  $\overline{\Delta T}$ , between the hot leg and the cold leg increased as the inclined angle increased (Figure 3). Here  $\overline{\Delta T}$  is defined by

$$\overline{\Delta T} = \frac{\Delta T_A \dot{m}_A + \Delta T_B \dot{m}_B}{\dot{m}_A + \dot{m}_B}. \quad (1)$$

Both the flow rate decrease and the temperature difference increase indicated that the circulation ability was inhibited when the inclined angle was increased.

Asymmetry of the steam generator load may cause variations in steam properties and mechanical problems. However, the altitude difference between the cold legs occurs under inclined conditions and leads to a disparity of circulation ability. If the system inclines anticlockwise, the circulation in right branch was always stronger than the left. The flow rate of the right branch increased approximately 2% when  $\alpha = 45^\circ$  (compared to  $\alpha = 0^\circ$ ), while the flow rate of the left circuit decreased 26%, as shown in Figure 4.

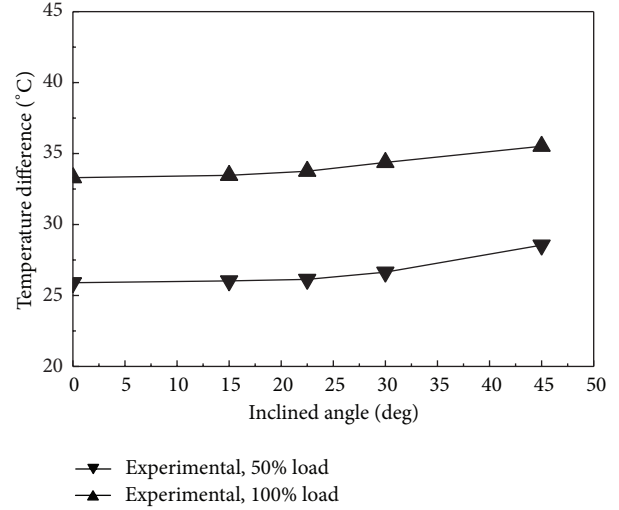


FIGURE 3: Average temperature differences under different inclined angles.

### 4. Numerical Model

Numerical analysis of natural circulation in the test section was carried out using CFD package ANSYS FLUENT. The whole meshes were structured and were created using ICEM. A total of 15 interfaces exist in the mesh system, which divided the test section into separated parts. Meshes were created for the parts individually and connected by the interfaces. A boundary layer mesh was generated for all the flow channels. The mesh used for this analysis is shown in Figure 5.

Variation of water properties with temperature was neglected in this analysis. The Boussinesq assumption was employed in calculating the buoyancy force.

The realizable  $k-\varepsilon$  turbulence model was used in these computations. This scheme is ideal for flows involving rotation, boundary layers under strong adverse pressure gradients, separation, and recirculation. Power law scheme of discretization is used for turbulent kinetic energy and dissipation rate equations. Pressure velocity coupling was done using the SIMPLEC scheme. Momentum equations were discretised using QUICK scheme. Convergence criterion used was  $1.0e-3$  for continuity,  $1.0e-5$  for velocities, energy,  $k$ , and  $\varepsilon$ .

We adopted porous medium model in simulating the flow and heat transfer in steam generators and electrical heater. In this model the flow resistance is calculated through a coefficient that is an input parameter to FLUENT. Electrical heating power was represented by a source term of the energy equation. Heat transfer in steam generator was calculated by the average heat transfer coefficient and temperature difference between the primary and secondary loop's fluids and added to the energy equation as a source term through UDF (user defined function) programming.

The numerical model was verified through comparing with the experimental results, as shown in Table 1. It can be seen that the numerical results show good agreement with

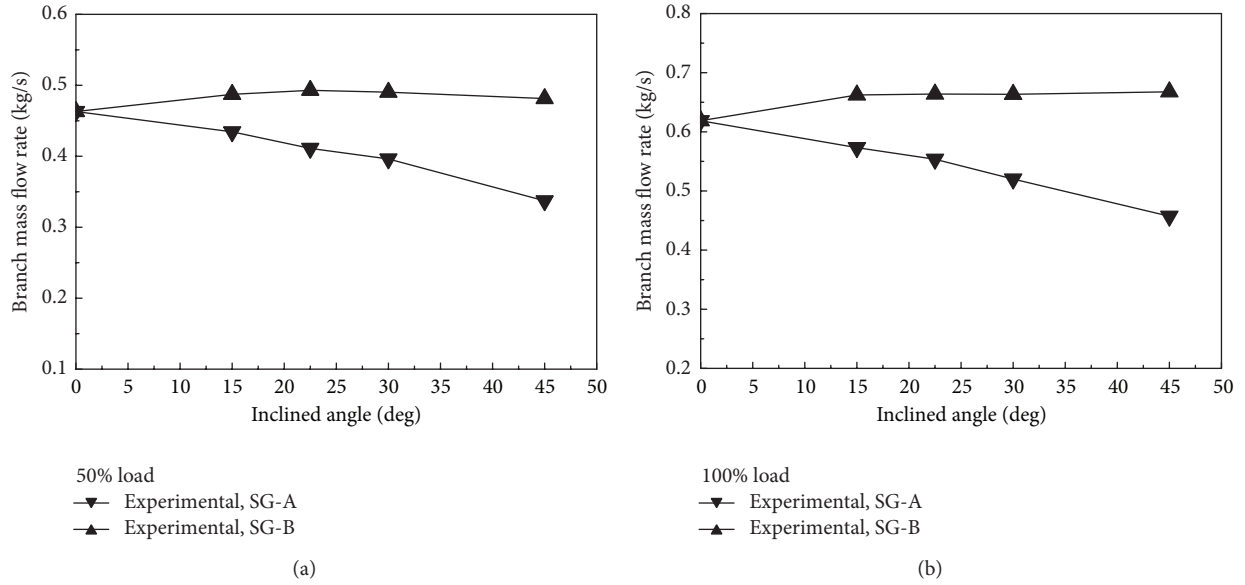


FIGURE 4: Branch flow rates under different inclined angles—(a) 50% load; (b) 100% load.

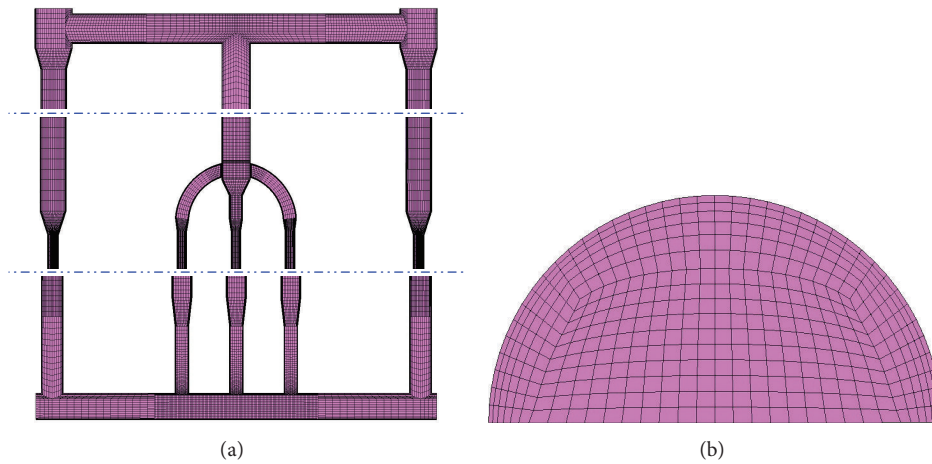


FIGURE 5: Meshes of test section used in computation: (a) whole test section; (b) cross section of flow channel.

TABLE 1: Comparison of numerical results and experimental results (noninclination).

Parameters	Experimental	Numerical
Mass flow rate of SG-A	0.61	0.62
Mass flow rate of SG-B	0.62	0.62
Inlet temperature of SG-A	181.10	180.50
Outlet temperature of SG-A	144.63	145.55
Inlet temperature of SG-B	181.71	180.50
Outlet temperature of SG-B	147.38	145.55

the experimental results. The temperature distribution and velocity fields are shown in Figure 6.

## 5. Numerical Results

5.1. *Flow Patterns at Large Inclined Angle (45~90°)*. The temperature fields and velocity fields were obtained through

CFD simulation (Figure 7). In comparing with no-inclination condition, obvious disparities arise under inclined condition. The lower branch circulation was nearly suspended when inclined angle increases to nearly 90°.

Total mass flow rate decreases with the increase of inclined angle continuously (Figure 8), in accordance with the analysis in Section 3. At large inclined angle the circulation mainly occurs in the higher circuit. The effective altitude difference is reaching the minimum value, which is half of the loop width ( $W/2$ ). The total mass flow rate decreases 58% under inclined angle of 90°.

The branch flow of SG-B decreases rapidly when inclined angle increases. When the inclined angle reaches 75° the flow rate of SG-B vanishes (Figure 9). The flow rate of EH-A also decreases which causes the outlet temperature of EH-A to increase (Figure 7). If the inclined angle enlarged to 90°, the temperature of EH-A will exceed the saturated temperature

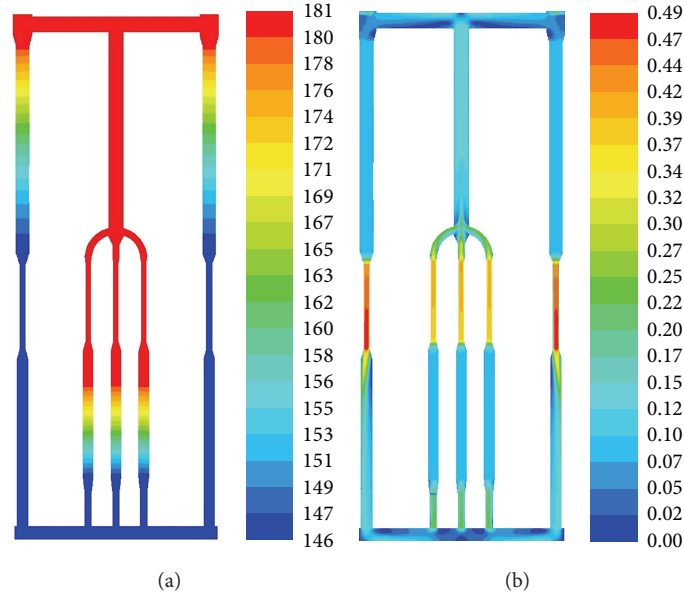


FIGURE 6: Flow fields in the test section: (a) temperature field; (b) velocity field.

(250°C) (Figure 10) and boiling will occur. This is dangerous to the reactor.

**5.2. Effect of Configuration.** The previous analysis showed that inclination caused the decrease of overall circulation ability and a disparity in branch circulation abilities. Optimizing the configuration of the loop may reduce these unwanted effects.

In order to reduce the disparity of different branch circulation ability, the outer force circuit (Figure 11) should be inhibited, while the inner force circuit should be enhanced. The ratio of the two driving forces is as follows:

$$\phi = \frac{Wg \sin \alpha}{H_0 g \cos \alpha} = \frac{2 \tan \alpha}{\tan \beta}. \quad (2)$$

Equation (2) shows that an increase in  $\beta$  reduced the relative importance of the outer circuit driving force and then reduced the disparity in the branch circulation abilities (Figure 12). The difference between the mass flow rates of the two cold legs rapidly increased with the increase of inclined angle  $\alpha$  for small values of  $\beta$ . This indicates that in order to control the influence of inclination, a long and thin reactor core is a better loop configuration for a reactor design.

**5.3. Effect of Flow Resistance Distribution.** The ratio between pressure drops of hot leg and cold leg also affected the magnitude of the disparity in the branch circulation (Figure 12). The disparity reduced with the decrease of  $\Delta p_{HL}/\Delta p_{CL}$  (Figure 13). Therefore it is favorable to decrease the flow resistance coefficient,  $f$ , of hot leg (or increase,  $f$ , of cold leg) as well as increase the cross section area of flow channel,  $A$ , of hot leg (or decrease,  $A$ , of cold leg).

## 6. Conclusion

This paper experimentally and numerically investigated steady-state single-phase natural circulation under inclined conditions. Both experimental and numerical results showed that under inclined conditions the circulation ability was inhibited—the total mass flow rate decreased and  $\Delta T$  increased. This was caused by the decrease of the average effective altitude. Furthermore, the driving force along the outer circuit of the loop had an opposite effect on the branch circulation and caused disparity in the branch mass flow rates. An increase in loop angle  $\beta$  (a reduction in width  $W$ ) reduced the disparity in branch circulation and alleviated the decrease of the overall circulation ability. Furthermore, a decrease in the value of  $\Delta p_{HL}/\Delta p_{CL}$  was also helpful for reducing the branch circulation disparity. The electrical heater elements will be overheated under large inclined condition because of the severe reduction of circulation flow rate.

## Nomenclature

- $A$ : Cross section area [ $\text{m}^2$ ]
- $c_p$ : Specific heat capacity [ $\text{J}/(\text{kg} \cdot \text{K})$ ]
- $g$ : Gravity [ $\text{m}/\text{s}^2$ ]
- $H$ : Altitude [ $\text{m}$ ]
- $k$ : Natural circulation ability [ $\text{W} \cdot \text{K}^{-3/2}$ ]
- $m$ : Mass flow rate [ $\text{kg}/\text{s}$ ]
- $N$ : Cold leg number
- $Nc$ : Loop component number
- $f$ : Resistance coefficient
- $T$ : Temperature [ $^\circ\text{C}$ ]
- $W$ : Loop width [ $\text{m}$ ].

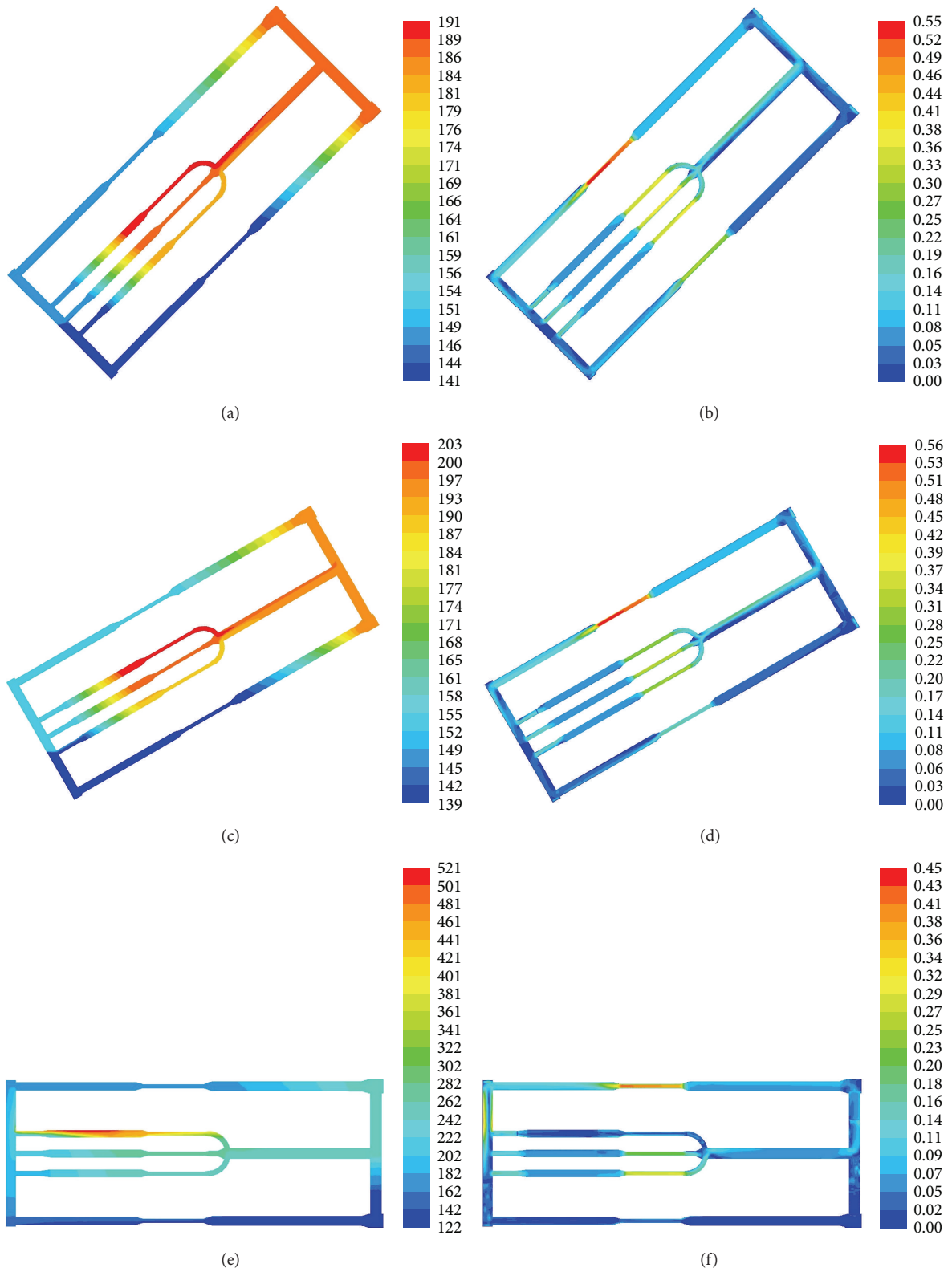


FIGURE 7: Flow fields in the test section: (a) 45°, temperature field; (b) 45°, velocity field; (c) 60°, temperature field; (d) 60°, velocity field; (e) 90°, temperature field; (f) 90°, velocity field.

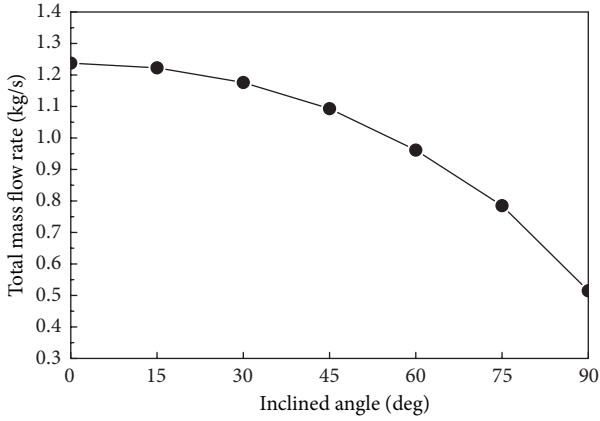


FIGURE 8: Total mass flow rate variation with inclined angle.

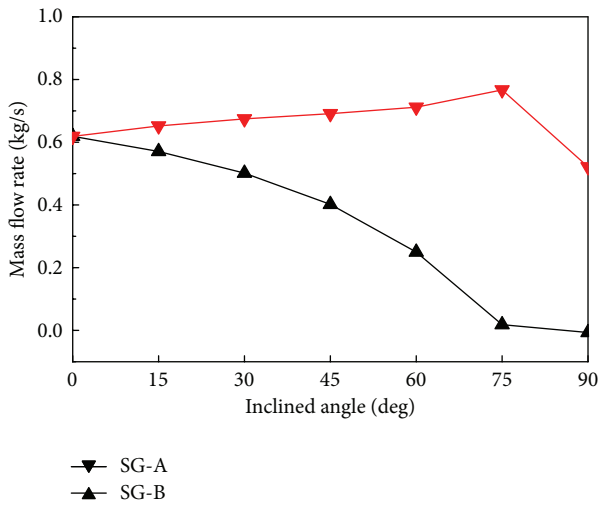


FIGURE 9: Branch mass flow rate variation with inclined angle.

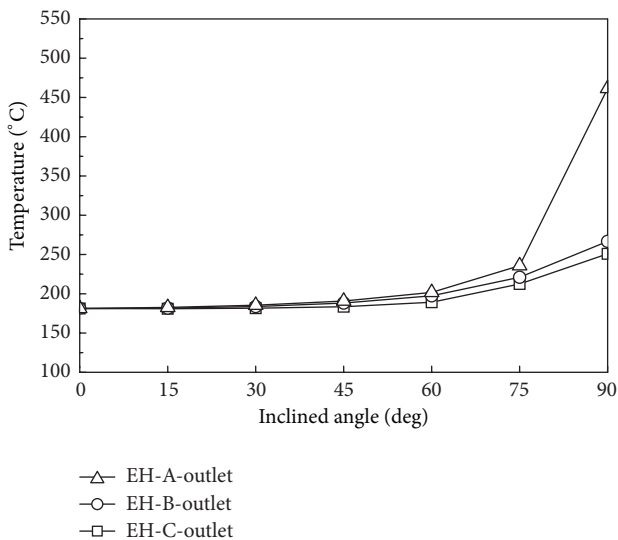


FIGURE 10: Outlet temperature of electrical heaters with inclined angle.

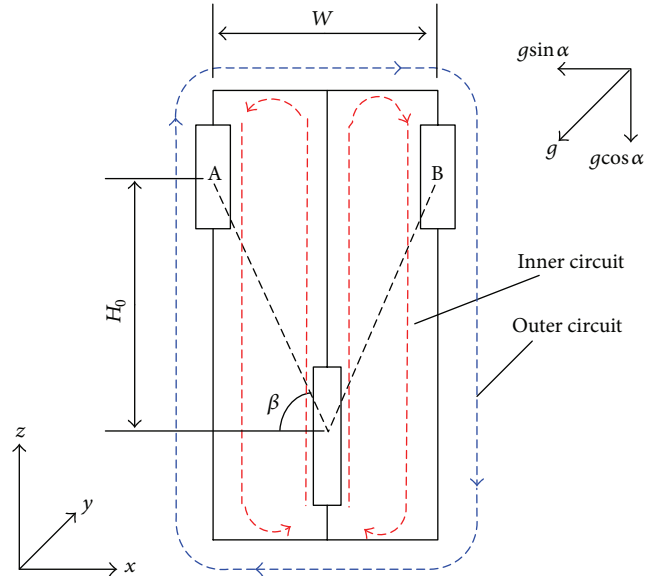


FIGURE 11: Mechanism of disparity of natural circulation ability.

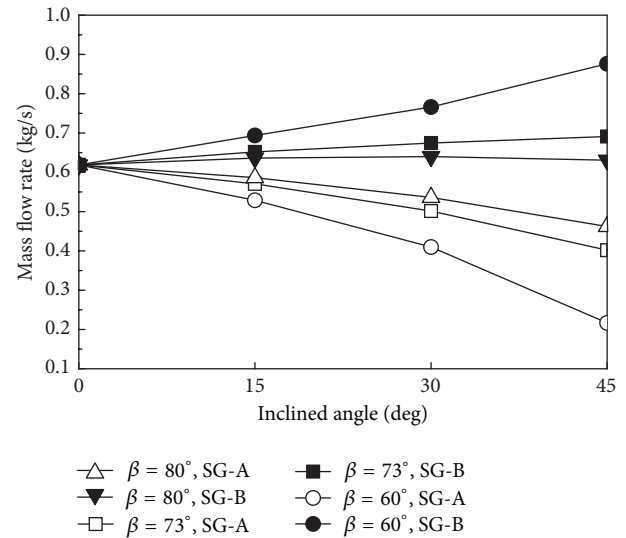


FIGURE 12: Effect of flow resistance distribution (experimental results).

Greek Letters

- $\alpha$ : Inclined angle [degree]
- $\beta$ : Configuration angle [degree]
- $\gamma$ : Thermal expansion coefficient [ $K^{-1}$ ]
- $\delta$ : Mass flow rate ratio
- $\rho$ : Density [ $kg/m^3$ ]
- $\phi$ : Driving force ratio.

Conflict of Interests

The authors declare that there is no conflict of interests regarding the publication of this paper.

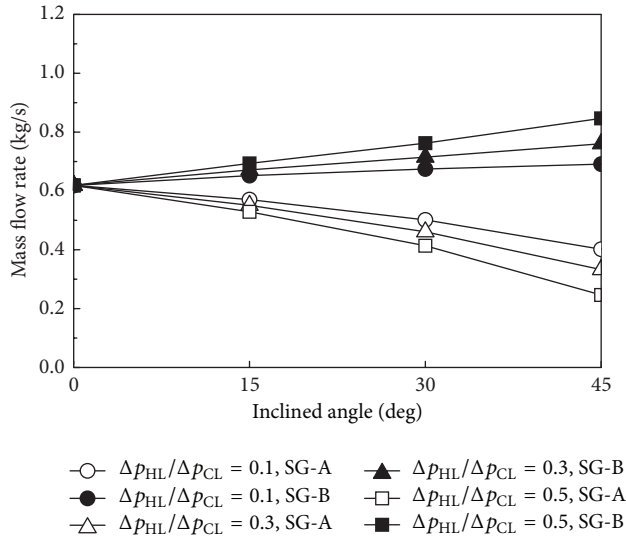


FIGURE 13: Effect of flow resistance distribution (experimental results).

## Acknowledgments

This work was supported by Ph.D. Program Foundation of Ministry of Education of China (no. 20100002120036) and Research Project of Tsinghua University (no. 2012Z02145).

## References

- [1] International Atomic Energy Agency, *Natural Circulation in Water Cooled Nuclear Power Plants*, IAEA-TECDOC-1474, IAEA, 2005.
- [2] International Atomic Energy Agency, "Passive safety systems and natural circulation in water cooled nuclear power plants," IAEA-TECDOC-1624, IAEA, 2009.
- [3] J. R. Humphries and K. A. Davies, "Floating desalination/co-generation system using the KLT-40 reactor and Canadian RO desalination technology," in *Proceedings of the Advisory Group Meeting on Small Power and Heat Generation Systems on the Basis of Propulsion and Innovative Reactor Technologies*, vol. 1172, pp. 41-52, International Atomic Energy Agency, Vienna, Austria, 1998.
- [4] Y. K. Panov, V. I. Polunichev, and K. V. Zverev, "Nuclear floating power desalination complexes," in *Nuclear Heat Applications: Design Aspects and Operating Experience. Proceedings of Four Technical Meetings Held between December 1995 and April 1998*, 1998.
- [5] H. Murata, K. Sawada, and M. Kobayashi, "Experimental investigation of natural convection in a core of a marine reactor in rolling motion," *Journal of Nuclear Science and Technology*, vol. 37, no. 6, pp. 509-517, 2000.
- [6] R. Pendyala, S. Jayanti, and A. R. Balakrishnan, "Convective heat transfer in single-phase flow in a vertical tube subjected to axial low frequency oscillations," *Heat and Mass Transfer*, vol. 44, no. 7, pp. 857-864, 2008.
- [7] S. Tan, G. H. Su, and P. Gao, "Experimental and theoretical study on single-phase natural circulation flow and heat transfer under rolling motion condition," *Applied Thermal Engineering*, vol. 29, no. 14-15, pp. 3160-3168, 2009.

- [8] J. Ma, L. Li, Y. Huang, J. Huang, and Y. Wang, "Progress in investigations on thermo-hydraulic characteristics of ship nuclear reactors under ocean conditions," *Nuclear Power Engineering*, vol. 32, no. 2, pp. 91-96, 2011.
- [9] B. H. Yan, H. Y. Gu, and L. Yu, "The flow and heat transfer characteristics of turbulent flow in typical rod bundles in ocean environment," *Progress in Nuclear Energy*, vol. 53, no. 5, pp. 487-498, 2011.
- [10] I. Iyori, I. Aya, H. Murata, M. Kobayashi, and H. Nariai, "Natural circulation of integrated-type marine reactor at inclined attitude," *Nuclear Engineering and Design*, vol. 99, pp. 423-430, 1987.
- [11] J. Kim, T. Kim, S. Lee, and G. Park, "Study on the natural circulation characteristics of the integral type reactor for vertical and inclined conditions," *Nuclear Engineering and Design*, vol. 207, no. 1, pp. 21-31, 2001.
- [12] T. W. Kim, G. C. Park, and J. H. Kim, "Numerical study on the natural circulation characteristics in an integral type marine reactor for inclined conditions," *Journal of the Korean Nuclear Society*, vol. 33, pp. 397-408, 2001.
- [13] T. Ishida and T. Yoritsune, "Effects of ship motions on natural circulation of deep sea research reactor DRX," *Nuclear Engineering and Design*, vol. 215, no. 1-2, pp. 51-67, 2002.
- [14] P. Z. Gao, F. G. Pang, S. Y. Liu, and M. J. Peng, "Effects of listing upon forced circulation and natural circulation," *Chinese Journal of Nuclear Science and Engineering*, vol. 17, pp. 179-183, 1997.

## Research Article

# An Evaluation of SMR Economic Attractiveness

**Sara Boarin and Marco E. Ricotti**

*Department of Energy, Nuclear Engineering Division-CeSNEF, Politecnico di Milano, Via La Masa 34, 20156 Milano, Italy*

Correspondence should be addressed to Marco E. Ricotti; [marco.ricotti@polimi.it](mailto:marco.ricotti@polimi.it)

Received 27 February 2014; Accepted 16 July 2014; Published 5 August 2014

Academic Editor: Shengqiang Li

Copyright © 2014 S. Boarin and M. E. Ricotti. This is an open access article distributed under the Creative Commons Attribution License, which permits unrestricted use, distribution, and reproduction in any medium, provided the original work is properly cited.

The nuclear “renaissance” that is taking place worldwide concerns the new build of GW size reactor plants, but smaller GenIII+NPP (Small Modular Reactors, SMR) are on the verge to be commercially available and are raising increasing public interest. These reactor concepts rely on the pressurized water technology, capitalizing on thousands of reactor-years operations and enhancing the passive safety features, thanks to the smaller plant and equipment size. On the other hand, smaller plant size pays a loss of economy of scale, which might have a relevant impact on the generation costs of electricity, given the capital-intensive nature of nuclear power technology. The paper explores the economic advantages/disadvantages of multiple SMR compared to alternative large plants of the same technology and equivalent total power installed. The metrics used in the evaluation is twofold, as appropriate for liberalized markets of capital and electricity: investment profitability and investment risk are assessed, from the point of view of the plant owner. Results show that multiple SMR deployed on the same site may prove competitive with investment returns of larger plants, while offering, in addition, unique features that mitigate the investment risk.

## 1. Introduction

Some GenIII advanced designs that are planned for deployment or currently under construction have emphasized their passive safety features and design simplifications [1]; nevertheless, further enhancements in passive safety are possible by reducing the plant scale below the GW power size. Following IAEA definition, the category of small and medium sized reactors encompasses the designs below 700 MWe [2], but novel design layout and concepts are made possible by smaller sizes (i.e., from 350 MWe downwards) [3–5]. The interest by the investors community for the Small Modular Reactors (SMR) option [6] and the proactive development effort by vendors recommend an in-depth analysis of the economics of this reactor category.

Currently only two SMR class reactors are under construction in the world: the Russian KLT-40s and the Argentinian CAREM, but other projects are in an advanced stage of development or under licensing, with some sites already identified for their deployment.

For the purpose of the economic evaluation, this paper excludes those cases where SMR are the only technically viable deployment option, such as scattered population, remote areas, and sites with physical limitation to the overall

power installed (e.g., limited water resources and grid capacity).

On the contrary, when SMR are considered as an alternative option to GW-scale NPP, economic analysis shall investigate the rationale of such an investment case. For a correct comparison, the same total power installed on the same site is considered: LR shall be compared with multiple SMR with equivalent overall capacity at site level. In this case, SMR exploit the so-called “Economy of Multiples,” that counterbalances the loss of “Economy of Scale.” The latter is the economic paradigm that drove the design evolution towards larger and larger power capacity along the civil nuclear era, up to the current French EPR (1,600 MWe). Economy of scale holds as a hard fact in the nuclear capital-intensive industry (Figure 1). With this considered, SMR must be able to bring new specific benefits able to recover economic competitiveness and to offer attractive or protective conditions to investors.

In this study, the assessment of the economic competitiveness of SMR is approached with a twofold perspective:

- (i) investment profitability: the value created by the investment project, given specific scenario conditions, is measured and related to the investment effort;

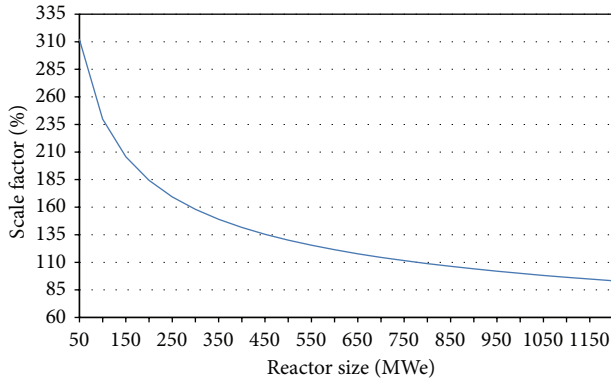


FIGURE 1: Economy of scale curve.

- (ii) investment risk: the risk-mitigation features of SMR and LR are considered and analysed.

## 2. Method and Tool

The economic competitiveness of SMR has been assessed by means of a software simulation tool developed by Politecnico di Milano—Nuclear Reactors Research Group: the integrated model for competitiveness assessment of SMR (INCAS) [7]. INCAS is a MATLAB-based code able to calculate investment scenarios in NPP deployment. The INCAS code is based on a discounted cash flow (DCF) analysis that is performed over a given investment scenario. Results provide the calculation of key economic performance indicators.

Internal rate of return (IRR) and Profitability Index (PI) have been assumed as a key indicators of investment profitability. The levelized cost of electricity (LCOE) that represents the unit generation cost of electricity attained by a specific LR or SMR plant measures cost effectiveness. In a DCF model, LCOE is calculated as the minimum electricity price that is able to grant a threshold investment profitability (in terms of IRR); this means that, by selling electricity at LCOE, the plant manager is able to cover all operating and capital costs, including a target capital remuneration (IRR).

The INCAS code is able to account for a self-financing capability of the project: if a multiple NPP fleet is deployed through a staggered schedule, the cash flows from the sale of electricity by early units may be reinvested in the construction of late NPP units. This self-financing capability allows decreasing the up-front capital requirements and may be relevant when total power installed is fractioned into multiple smaller units.

In this work, a stochastic approach is used to include the scenario uncertainties in the analysis. The statistical estimate of probability distributions of the relevant output is calculated by means of Monte Carlo simulation.

## 3. Input and Assumptions

Among the economic benefits of multiple, smaller NPP units, some apply in the construction cost mitigation [10].

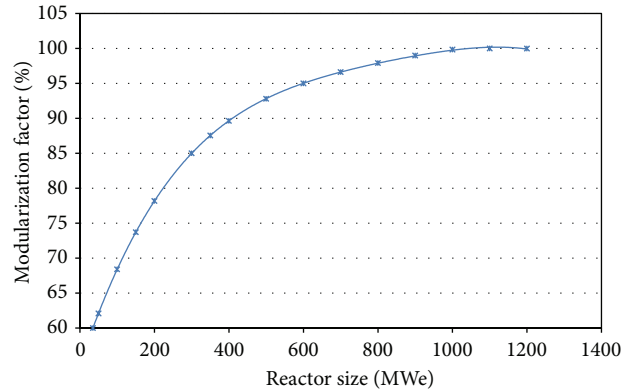


FIGURE 2: Modularization factor depending on the NPP size in terms of output power.

- (i) Modularization: the NPP is conceived for the fabrication of separate modules. This fosters standardization and factory fabrication, and parallelization of activities is enabled. A smaller plant equipment size enhances the scope of modularization. A number of SMR units in backlog enable a miniserial production. Expected benefits are higher quality and cost savings of shop-build as compared to stick-build.
- (ii) Learning effect: the higher the number of NPP built on the same site is, the higher the cost effectiveness of construction and assembling activities on site is, due to learning accumulation and best practice achievement by the manpower.
- (iii) Cositing economies: economy of scale increases the unit cost of output product because it allocates the fixed costs on the first plant unit. Cositing economies account for the redistribution of site-related fixed costs on the whole SMR fleet.
- (iv) Design savings: unique design and layout features are enabled by the smaller physical size of plant equipment. SMR design may result leaner and be simplified, with lower active components. On a stand-alone basis, the mere plant design should represent a cost-saving feature of SMR as compared to LR.

In Figures 2, 3, and 4 the above-mentioned features are represented against the power size of a single NPP. On the contrary, “Design savings” are strictly related to a specific reactor concept: for this reason they can be quantified based on the detailed engineering of a specific plant layout and are not applicable to different design with the same size. No design saving curve can therefore be sketched. On the contrary, with a reverse approach, design saving factors of different SMR sizes have been estimated in order to bring their profitability in line with LR. It has been calculated [20] that this factor strongly depends on the reference unit overnight cost assumed [€/MWe], because the higher the loss of economy of scale to recover, the higher the design enhancements and simplifications (i.e., “Design saving factor”) to recover the investment profitability. It may be calculated that,

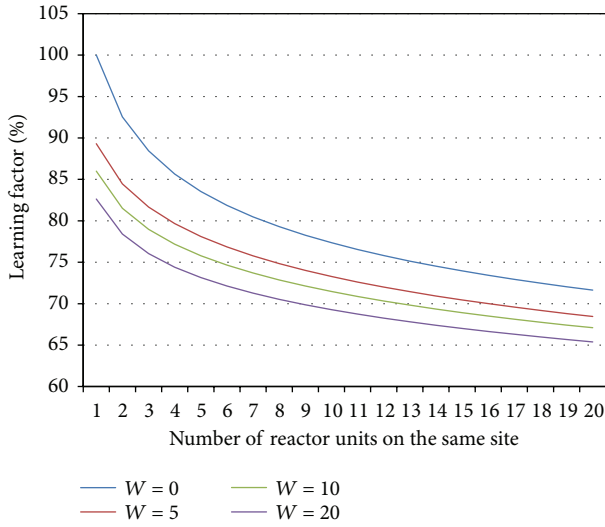


FIGURE 3: Learning factor depending on number of reactors built on site (learning on site) and parametric to the number of reactor plants of the same type built worldwide (worldwide learning,  $W$ ).

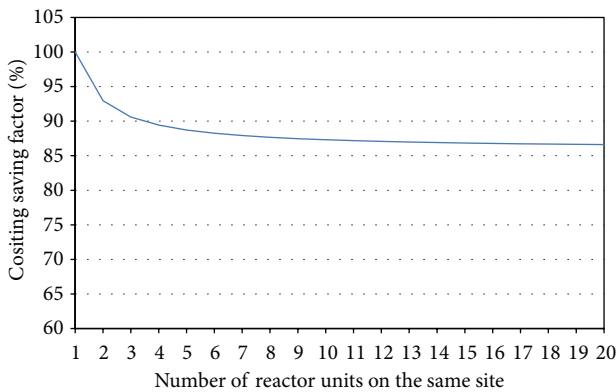


FIGURE 4: Cositing economies: site-related, fixed cost sharing by multiple units on the same site.

with construction costs ranging in 3000–5000 €/KWe, 350–150 MWe plants need design savings up to 10% in order to be competitive with larger units lays, while for the smallest plants (e.g., 50 MWe) this factor must increase up to 17%. Design saving factors of this order should be achievable [21]. In this work, a design saving factor of 10% has been allowed to a 300–350 MWe SMR over the unit construction cost of a LR.

All of the above-mentioned economic features are assumed as a framework model for the economic analysis of SMR and allow decreasing the construction costs of multiple SMR, thus recovering the loss of economy of scale.

In the following, case-study scenarios with a single, stand-alone LR and multiple power-equivalent SMR are analysed, in order to assess the economic rationale of smaller scale NPP with commercially available large scale NPP of the same technology.

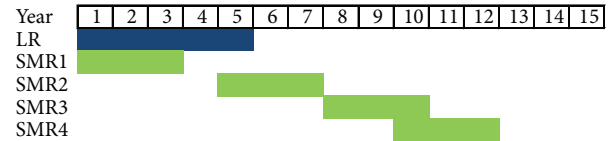


FIGURE 5: Construction schedules: reference scenario.

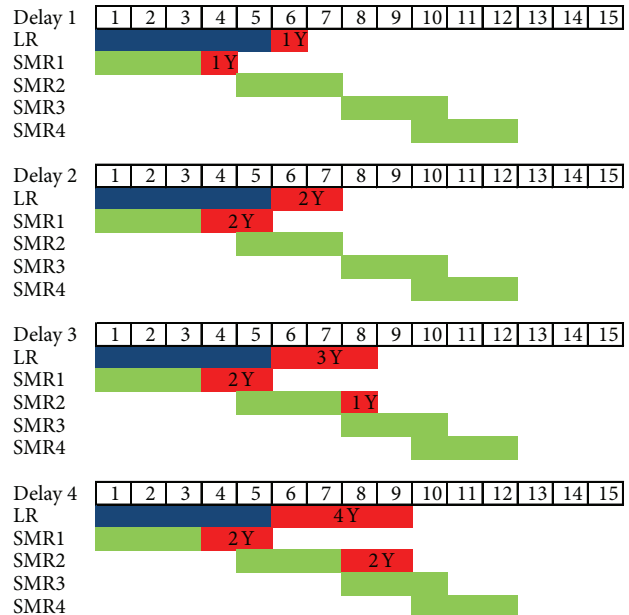


FIGURE 6: “Intrinsic” delay in the construction schedule considered in the sensitivity analysis: in red, the years of delay in the construction.

Key technical and economic assumptions are listed in Table 1, while deployment schedules considered in the analysis are represented in Figures 5 to 7, with a reference scenario and 6 possible construction delay case studies.

Static scenario analysis does not allow catching the complexity of dynamics that drives the relevant variables nor the uncertainty about their evolution and the forecast capability over a very long time horizon. Sensitivity analysis allows assessing the impact of relevant input parameters on the economic performance. This is the case of possible delay in the construction schedule. A construction delay is an event capable of deeply puzzling the economics of a NPP investment project. For this reason, SMR competitiveness versus equivalent LR has been tested against four possible construction delay scenarios, each of them with the same delay, in terms of total number of years on the project (from 1 to 4 years).

As shown in Figure 6, the construction delay on each SMR unit is shorter and/or it applies on the first SMR units only: in other words, it does not affect the whole investment cost, as it does in the case of the single LR. This is reasonable to argue that the construction delay must in some way be proportional to the construction duration and that it is considered very improbable that mistakes and project management mismatches—causing the delay—would

TABLE 1: Scenario input data to INCAS test cases.

Input	LR	SMR	Notes
Plant operating lifetime (years)	60	60	Same technology enhancement and reliability [8] assumed for LR and SMR.
Estimated construction period (years)	5 [9]	3	Reduced construction time for SMR due to reduced size and assuming design simplification [10].
Overnight construction cost (€/kWe)	4000	Estimated from LR capital costs [10]	LR [11–13].
Operation and maintenance cost (€/MWh)	9 [14]	10.8	SMR O&M cost estimated from LR [15] (SMR/LR ratio = 1.2x).
Fuel cycle cost (€/MWh)	6.7 [8]	6.7	Same fuel cost for SMR: longer core life, but higher enrichment and poorer neutron economy (leakages).
Decontam. & decommissioning sinking fund (€/MWh)	3	5.9	SMR decommissioning cost estimated from LR cost [16, 17] (SMR/LR ratio = 2x).
Electricity price (€/MWh)	80	80	
Plant availability	93%	95%	Based on estimations for GenIII/GenIII+ LR [1] and SMR [18].

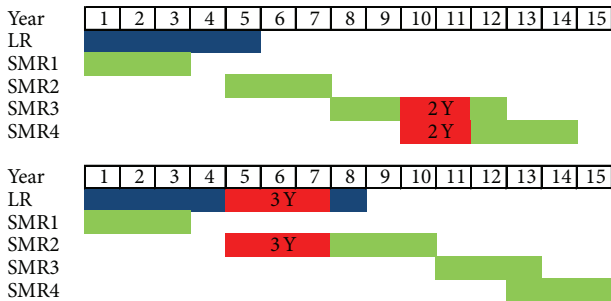


FIGURE 7: Two examples of how “external” delays may affect the construction schedule of LR/SMR: in red, the years of delay in the construction.

replicate in the same manner on all the units of a fleet made of NPP of the same type. Generally, it may be assumed that a sort of learning process might improve, correct, and optimize the information and the operations in the construction process, in a way that the possible delay might decrease from the early to the later deployed units. The same effect would apply to a LR fleet, but, given a total generation capacity installed on a site, the number of SMR units would always be higher than equivalent LR. These considerations apply as far as “intrinsic” delay events are concerned, that is to say delay events that may arise from the procurement, the project management, the assembly, and construction activities.

Unexpected “external” events may also be the cause for construction delays. These events may happen randomly in time and cause a stop in the NPP construction. This is the case, for example, of a political climate change, the withdrawal of a public support to the investment project, a political halt due to adverse public opinion, and the consequence of a natural disaster (like the recent Fukushima event). This kind of delay is not proportional to the construction duration of a NPP and happens randomly in time, with a random duration.

In this work, the effect of “intrinsic” construction delay has been investigated by means of a sensitivity analysis, while “external” delay events have been analysed by means of a Monte Carlo simulation.

It has been considered that one of such delay events may happen randomly during the investment period, producing a delay in the schedule of a NPP under construction and shifting onwards the construction of NPP that have not been started yet. Whenever it begins, the “external” delay event may affect one or more SMR units, depending on the specific construction plan and staggered units. The maximum duration considered for the “external” delay event is three years.

Along with construction delay, Monte Carlo analysis is a suitable tool to investigate the impact of general scenario uncertainty on the economic competitiveness. The key investment-case parameters have been considered stochastic and distributed according the probability distribution functions (PDF) indicated in Table 2.

## 4. Results and Discussion

**4.1. Cost Effectiveness.** In the reference case, with 7% cost of debt and 10% cost of equity, cost effectiveness of LR is sensibly higher than SMR in terms of LCOE (i.e., lower LCOE).

The reason lies in the fact that economy of scale is not fully recovered by the benefits and cost savings of multiple SMR. The overnight cost of the SMR fleet shows a decrease on the back of learning and cositing economies that brings the construction cost of the last unit in line with the cost of a single LR (Figure 8), but, on average, the whole SMR fleet bears higher construction cost on a unit base that affects its LCOE.

Nevertheless, if the target remuneration for the equity capital (i.e., cost of capital) is increased to 15%, the cost effectiveness of the two alternative investment options is brought in line with each other. The same trend is confirmed with increasing cost of debt, meaning that multiple SMR are more cost effective with high cost of capital (Figure 9).

The rationale of this outcome lies in the shorter construction period of each SMR module, that accounts for lower financial interests capitalization. Interest during Construction (IDC) is accounted over the invested capital during

TABLE 2: Scenario input data for Monte Carlo simulation.

Input	PDF	LR	SMR
Overnight construction cost (€/kWe)	Triangular	2000; 4000; 3000 (min; max; most likely)	Estimated from LR capital costs [10]
“External” delay in construction schedule	Uniform	0; 36; 18 months (min; max; mean)	0; 36; 18 months (min; max; mean)
Plant availability	Triangular	80%; 95%; 95% (min; max; most likely)	80%; 95%; 95% (min; max; most likely)
Operation and maintenance cost (€/MWh)	Uniform	6.3; 11.7; 9.0 (min; max; mean)	120% of LR
Fuel cycle cost (\$/MWh)	Uniform	4.7; 8.6; 6.7 (min; max; mean)	4.7; 8.6; 6.7 (min; max; mean)
Decontam. & decommissioning sinking fund (\$/MWh)	Uniform	1.4; 2.6; 2 (min; max; mean)	200% of LR
Electricity price (€/MWh)	Triangular	50; 90; 70 (min; max; most likely)	50; 90; 70 (min; max; most likely)
Financial interest rate	Uniform	6.0%; 8.0%; 7.0% (min; max; mean)	6.0%; 8.0%; 7.0% (min; max; mean)

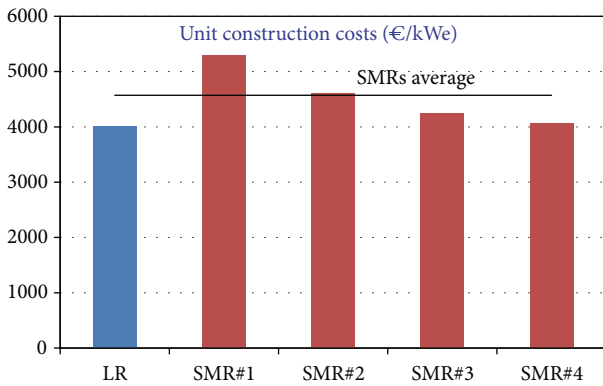


FIGURE 8: Unit construction costs in reference scenario [22].

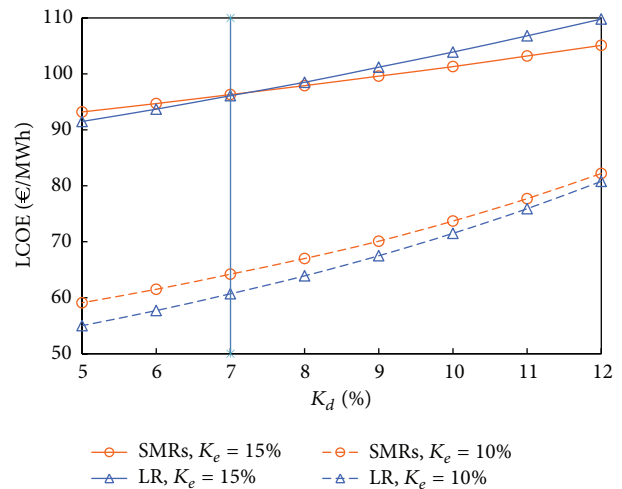


FIGURE 9: LCOE trend with increasing cost of debt ( $K_d$ ) and different cost of equity ( $K_e$ ) (adapted from [23]).

the construction period and may end up by representing a relevant part of the Total Capital Investment Cost. If construction period is shorter for SMR, then the incidence of financial interests accumulated during the construction period on overnight construction costs is lower. Financial interests are included as a component in the electricity generation cost and thus the higher the interest expenses, the higher the LCOE and the longer the payback time of the NPP investment. In other words, SMR show a better financial behaviour and for this reason, their performance improves on LR when capital costs are higher (Figure 9 with  $K_d > 7\%$  and  $K_e = 15\%$ ). This feature is particularly valuable in liberalized (capital and energy) market conditions, where capital costs are higher, compensating for higher investment risk.

4.2. Risk and Returns. Sensitivity analysis over possible delays in the construction schedule shows that multiple SMR are a robust investment project in terms of cost effectiveness, towards this kind of events.

While the cost of equipment is fixed, other construction costs are sensitive to time increase: for example, workforce on the site yard, financial costs, cranes and auxiliary equipment rent fees, and so forth.

As said, based on the assumptions, in the case of multiple SMR, delay and consequent extra-costs affect only a portion of the Total Capital Investment Cost, since only some but not all the SMR units may be concerned. In the case of LR, the whole capital investment cost is affected by the construction delay, in its sensitive cost items. As a consequence, in case of construction delay, the increase in the LCOE is sharper for LR, while multiple SMR are an intrinsically safer investment option towards this unfavourable event (Figure 10).

The economic competitiveness of multiple SMR versus LR has been investigated under uncertain scenario conditions and tested against construction delays of “external” nature.

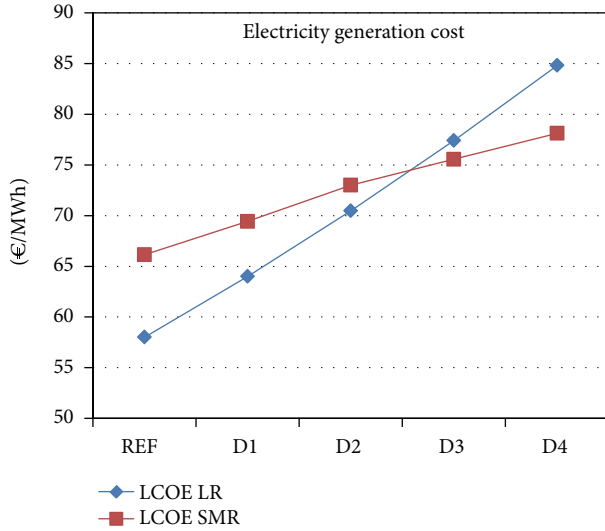


FIGURE 10: LCOE sensitivity with increasing delay in construction schedule [22].

TABLE 3: Profitability Index (PI) for multiple SMR and stand-alone LR in deterministic/stochastic scenarios [19].

	Deterministic scenario		Stochastic scenario	
	LR	SMR	LR	SMR
PI [%]	1.31	1.23	1.06	1.12
(min; max)			(0.23; 2.36)	(0.17; 2.90)
Std deviation of PI	—	—	0.29	0.37

The values of PI of the two alternative investment projects are the same magnitude and are substantially in line with each other (Table 3). Given the uncertainty span over the cost/price estimates for input parameters, it may be concluded that the two projects grant the same level of investment profitability. This result is a very significant one, if one considers the effect of economy of scale on smaller NPP: it means that multiple SMR have features able to partially compensate for the loss of economy of scale.

Nevertheless it is interesting to notice that, compared to deterministic scenario, results are reversed in stochastic simulation, where investment profitability of SMR appear better than LR (Table 3). In deterministic scenario, the value of Profitability Index is higher for the LR project, but it is lower than SMR under stochastic conditions. This result is interesting as far as it highlights a trend and shows the robustness of multiple SMR against uncertain scenario conditions. This behavior is mainly due to an intrinsic lower exposure of multiple NPP to an “external” delay event: staggered deployment grants the possibility to defer the construction of later units after the end of the “external” delay event, without incurring in cost overruns. Multiple SMR represent an intrinsic investment modularization in a way that only a fraction of the total investment (some of the units) might be affected by a random delay event. Figure 11 shows that the cost overruns in stochastic scenario are more limited for multiple

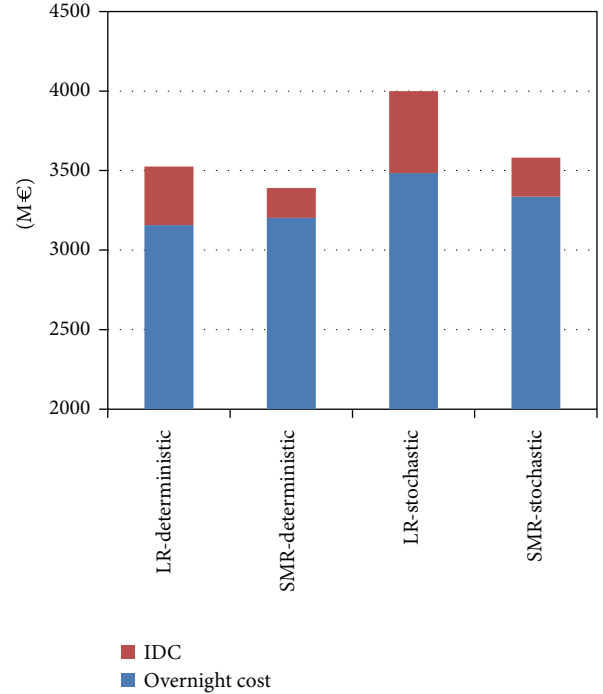


FIGURE 11: Total Capital Investment Cost (overnight cost + IDC) of SMR and LR under deterministic and stochastic scenario conditions.

SMR, accounting for lower capital expenditures. Financial interest (Interest during Construction, IDC) of SMR are half than LR’s IDC. Considering the Total Capital Investment Cost (overnight construction cost + IDC), the gap between the four SMR and the stand-alone LR reduces in stochastic conditions as compared to deterministic scenario.

In addition, self-financing capability of multiple NPP and lower financial interest escalation during construction mitigate the possibility of a financial default in case of unfavorable scenario evolution (e.g., very low electricity price).

## 5. Conclusions

The premise of this work is the opportunity to investigate the economic competitiveness of SMR, considering the impact of a loss of economy of scale over the construction cost in a capital-intensive business, like nuclear power generation. Specific features of multiple GenIII+ SMR are analysed in order to understand at what extent they are able to compensate for this loss of economy of scale.

An investment case has been defined and simulated with the comparison of four SMR, deployed with a staggered schedule, and a stand-alone LR with equivalent power on site. The economic competitiveness of multiple SMR has been tested against a single equivalent LR under deterministic and stochastic scenario conditions, accounting for the possible uncertainty embedded in the market conditions or in the capability to estimate and forecast the cost/price values. Reasonable values for key investment parameters have been

assumed and stochastic distributions have been considered to run Monte Carlo simulation of the possible investment scenarios.

In particular, specific assumptions have been elaborated to simulate possible delay events in the construction schedule of SMR and LR.

Results confirm that cost effectiveness of SMR, along with investment profitability, is in line and of the same order with LR's, provided that multiple units on the same site are deployed to exploit benefits from learning on construction process and cositing economies on fixed costs. On the other side, design modularization and simplification account for the cost reduction of each single SMR unit and help in meeting an acceptable investment return/LCOE targets.

Sensitivity analysis shows a better behaviour of multiple SMR versus LR against higher capital costs and construction delays. This "robustness" of the economic performance is confirmed by the Monte Carlo analysis. The rationale lies in the following.

- (i) Protection against construction delays:
  - (a) the possibility to learn from the past reduces the probability of an "intrinsic" delay in later SMR deployment;
  - (b) investment modularization of SMR decreases the exposure of the whole SMR project to "external" delay events.
- (ii) Better financial behaviour: shorter construction periods of SMR limit the financial cost escalation and allow to better cope with high capital costs and, in general, with construction delays and unfavourable scenario conditions.

Future developments of the SMR economic and financial analysis, to thoroughly investigate the competitiveness of such a new technology, will be devoted in addressing other important aspects of the SMR deployment path, such as the licensing process [24], the environmental implications, for example, the emergency planning zone reduction [25], and the impact on energy security [26]. In particular the licensing item will deserve specific attention, since it will be one of the first, key, and critical aspects in the deployment path also in terms of economic and market risks, due to potential delays and extra-costs.

## Conflict of Interests

The authors declare that there is no conflict of interests regarding the publication of this paper.

## References

- [1] T. L. Schulz, "Westinghouse AP1000 advanced passive plant," *Nuclear Engineering and Design*, vol. 236, no. 14–16, pp. 1547–1557, 2006.
- [2] IAEA, "Approaches for assessing the economic competitiveness of small and medium sized reactors," IAEA Nuclear Energy Series NP-T-3.7, IAEA, Vienna, Austria, 2013.
- [3] B. Petrovic, M. Ricotti, S. Monti, N. Čavlina, and H. Ninokata, "Pioneering role of IRIS in the resurgence of small modular reactors," *Nuclear Technology*, vol. 178, no. 2, pp. 126–152, 2012.
- [4] J. Reyes and P. Lorenzini, *NuScale: A Modular, Scalable Approach to Commercial Nuclear Power*, Nuclear News, 2010.
- [5] *Current Status, Technical Feasibility and Economics of Small Modular Reactors*, OECD-NEA, Paris, France, 2011.
- [6] R. Smith, "Small reactors generate big hopes," *The Wall Street Journal*, 2010.
- [7] S. Boarin, M. Massone, and M. E. Ricotti, *INCAS: INtegrated Model for the Competitiveness Analysis of Small-Medium Sized Reactors, Ver. 2.0-b0—User Manual*, Politecnico di Milano, 2012.
- [8] Y. Du and J. E. Parsons, "Update on the cost of nuclear power," MIT-CEEP Report, 2009.
- [9] "Study of construction technologies and schedules, O&M staffing and Cost, decommissioning costs and funding requirements for advanced reactor designs," Dominion Energy, Bechtel Power Corporation and TLG Report, 2004.
- [10] M. D. Carelli, P. Garrone, G. Locatelli et al., "Economic features of integral, modular, small-to-medium size reactors," *Progress in Nuclear Energy*, vol. 52, no. 4, pp. 403–414, 2010.
- [11] D. Kennedy, "New nuclear power generation in the UK: cost benefit analysis," *Energy Policy*, vol. 35, no. 7, pp. 3701–3716, 2007.
- [12] US DOE, "Assumptions to the Annual Energy Outlook 2009," DOE/EIA Report, 2009.
- [13] H. Khatib, "Review of OECD study into 'Projected costs of generating electricity-2010 Edition,'" *Energy Policy*, vol. 38, no. 10, pp. 5403–5408, 2010.
- [14] J. Koomey and N. E. Hultman, "A reactor-level analysis of busbar costs for US nuclear plants, 1970–2005," *Energy Policy*, vol. 35, no. 11, pp. 5630–5642, 2007.
- [15] M. Carelli, C. W. Mycoff, P. Garrone et al., "Competitiveness of small-medium, new generation reactors: a comparative study on capital and O&M costs," in *Proceedings of the 16th International Conference on Nuclear Engineering*, Paper no. ICONE16-48931, Orlando, Fla, USA, May 2008.
- [16] "Decommissioning Nuclear Power Plants: Policies, Strategies and Costs," OECD Nuclear Energy Agency Report, 2003.
- [17] G. Locatelli and M. Mancini, "Competitiveness of small-medium, new generation reactors: a comparative study on decommissioning," *Journal of Engineering for Gas Turbines and Power*, vol. 132, no. 10, Article ID 102906, 1 page, 2010.
- [18] M. D. Carelli, L. E. Conway, L. Oriani et al., "The design and safety features of the IRIS reactor," *Nuclear Engineering and Design*, vol. 230, no. 1–3, pp. 151–167, 2004.
- [19] S. Barenghi, S. Boarin, and M. E. Ricotti, "Investment in different sized SMRs: economic evaluation of stochastic scenarios by INCAS code," in *Proceedings of the International Congress on Advances in Nuclear Power Plants (ICAPP '12)*, Chicago, Ill, USA, June 2012, Paper 12322.
- [20] S. Boarin and M. E. Ricotti, "Multiple nuclear power plants investment scenarios: economy of multiples and economy of scale impact on different plant sizes," in *Proceedings of the International Congress on Advances in Nuclear Power Plants (ICAPP '11)*, Nice, France, May 2011, Paper 11193.
- [21] M. D. Carelli, B. Petrovic, C. W. Mycoff, P. Trucco, M. E. Ricotti, and G. Locatelli, "Smaller sized reactors can be economically attractive," in *Proceedings of International Congress on Advances in Nuclear Power Plants (ICAPP '07)*, Nice, France, May 2007, paper 7569.

- [22] S. Boarin and M. E. Ricotti, "Construction delays and extra-costs on large and small nuclear projects," in *Proceedings of the 16th International Conference on Emerging Nuclear Energy Systems (ICENES '13)*, Madrid, Spain, May 2013.
- [23] S. Boarin, G. Locatelli, M. Mancini, and M. E. Ricotti, "Financial case studies on small- and medium-size modular reactors," *Nuclear Technology*, vol. 178, no. 2, pp. 218–232, 2012.
- [24] M. V. Ramana, L. B. Hopkins, and A. Glaser, "Licensing small modular reactors," *Energy*, vol. 61, pp. 555–564, 2013.
- [25] F. C. V. Mancini, E. Gallego, and M. E. Ricotti, "Revising the emergency management requirements for new generation reactors," *Progress in Nuclear Energy*, vol. 71, pp. 160–171, 2014.
- [26] I. N. Kessides and V. Kuznetsov, "Small modular reactors for enhancing energy security in developing countries," *Sustainability*, vol. 4, no. 8, pp. 1806–1832, 2012.

## Research Article

# Procedure of Active Residual Heat Removal after Emergency Shutdown of High-Temperature-Gas-Cooled Reactor

Xingtuan Yang, Yanfei Sun, Huaiming Ju, and Shengyao Jiang

*Key Laboratory of Advanced Reactor Engineering and Safety, Ministry of Education,  
Institute of Nuclear and New Energy Technology of Tsinghua University, Beijing 100084, China*

Correspondence should be addressed to Xingtuan Yang; yangxt@mail.tsinghua.edu.cn

Received 10 November 2013; Accepted 13 June 2014; Published 7 July 2014

Academic Editor: Yanping Huang

Copyright © 2014 Xingtuan Yang et al. This is an open access article distributed under the Creative Commons Attribution License, which permits unrestricted use, distribution, and reproduction in any medium, provided the original work is properly cited.

After emergency shutdown of high-temperature-gas-cooled reactor, the residual heat of the reactor core should be removed. As the natural circulation process spends too long period of time to be utilized, an active residual heat removal procedure is needed, which makes use of steam generator and start-up loop. During this procedure, the structure of steam generator may suffer cold/heat shock because of the sudden load of coolant or hot helium at the first few minutes. Transient analysis was carried out based on a one-dimensional mathematical model for steam generator and steam pipe of start-up loop to achieve safety and reliability. The results show that steam generator should be discharged and precooled; otherwise, boiling will arise and introduce a cold shock to the boiling tubes and tube sheet when coolant began to circulate prior to the helium. Additionally, in avoiding heat shock caused by the sudden load of helium, the helium circulation should be restricted to start with an extreme low flow rate; meanwhile, the coolant of steam generator (water) should have flow rate as large as possible. Finally, a four-step procedure with precooling process of steam generator was recommended; sensitive study for the main parameters was conducted.

## 1. Introduction

In China, a commercial modular high-temperature-gas-cooled reactor pebble-bed module (HTR-PM) nuclear power plant entered its conceptual design phase in the year 2002 and aimed to complete a demonstration plant in 2012 [1]. Like other high-temperature-gas-cooled reactors (HTGR), HTR-PM has inherent negative temperature coefficient of reactivity of the core, which makes it have the unique characteristic of being able to remove the residual heat through the reactor vessel surface to the ultimate heat sink entirely by passive heat transfer mechanisms (radiation, convection, and conduction) [2]. However, the duration of passive heat transfer process will be hundreds of hours [3], which is too long to meet the requirement of rapid restart of the reactor after accident elimination. In the case of accidents (may be any kind that is able to induce the reaction of emergency system and cause shutdown of the core, such as loss of total electricity, earth quake, disabling of instruments, even false signals, etc.) happening in the nuclear part of the plant, the electric supply for both helium circulators of primary loop and feed water

pump of secondary loop is available, and the steam generators (SG) and condenser are still functioning. These conditions make it feasible to remove the residual heat of reactor core actively via SG and secondary loop rather than through passive natural heat transfer, in order to shorten the cooling process and reduce the time cost. This meets the economic consideration, which is one of the main design philosophies of HTR-PM [4].

For HTR-PM, the active residual heat removal process (ARHRP) can be accomplished by SG and start-up loop (STL), while the latter is designed for start process of the plant. After the shutdown of the core in emergency, SG will be switched to connect with STL and insulated from the main steam loop (MSL). Residual heat of the core can be transferred to STL through SG in an active manner by the coolant circulation.

However, the situation becomes very complex after core is shut down. First of all, the temperature distribution of boiling tubes of SG has a configuration with low temperature (205°C) at water inlet and high temperature (600°C) at steam outlet. Any inappropriate coolant flow into SG will cause heat/cold



TABLE 1: Design parameters of HTR-PM.

Parameters	Design value
<b>Primary loop</b>	
Helium pressure	7.0 MPa
Helium temperature at reactor outlet	750°C
Helium temperature at reactor inlet	250°C
Helium flow rate	176 kg/s
<b>Secondary loop</b>	
Steam pressure at SG outlet	13.9 MPa
Steam temperature at SG outlet	570°C
Feed water temperature	205°C
Feed water flow rate	155.4 kg/s
<b>Start-up loop</b>	
Coolant pressure	1.0 MPa
Steam at electrical boiler outlet	140~200°C
Maximum steam flow rate	9.7 kg/s

a closed loop which also has many other pieces of equipment including heat exchangers, deaerator, and control valves. These pieces of equipment were eliminated from Figure 1 since the system is too complicated to be completely shown and do not have direct relevance with the active cooling process.

**2.2. Criteria for ARHRP.** The principal criterion of ARHRP is safety. First of all, for the core, the inlet temperature and flow rate of helium need to be controlled to avoid too fast cooling. However, the major risk comes from SG where the flow states of primary loop and STL should be designed appropriately in order to avoid heat/cold shock to the positions shown in Figure 2. The preliminary criteria for ARHRP are listed in Table 2. Only when all these criteria are fulfilled can we take further measures to accelerate ARHRP.

### 3. Numerical Model

**3.1. Mathematical Representation.** The mathematical representation of SG and STL is shown in Figure 3, which models both helium and water/steam flow as one-dimensional channel flow. In SG the node numbers of helium channel, boiling tube wall channel, and water/steam channel are identical ( $N = 100$  and  $M = 50$ , for this paper's calculation, after grid independence analysis) and for each channel the node dimension is a constant equal to the channel length divided by node number. Heat transfer happens on the boundary of corresponding nodes of two adjacent channels, and the heat transfer coefficient and pressure drop are calculated by correlations.

The core is simulated by a simple lumped parameter method and treated as a boundary condition of helium flow, despite its complicated structures. Detailed analysis of the core is beyond the scope of this paper. However, this model is reasonable for the transient analysis for SG and STL, for the

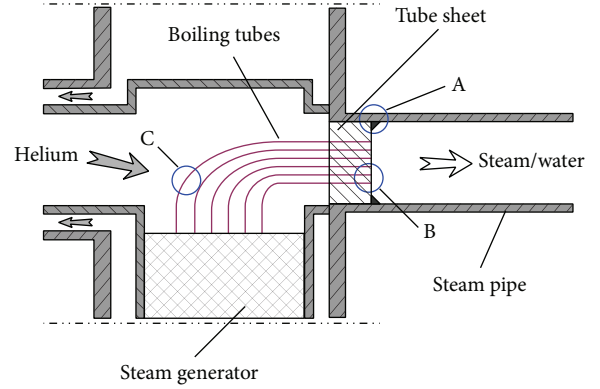


FIGURE 2: Damageable positions of SG (A: weld of tube sheet with steam pipe; B: joint of boiling tube with tube sheet; C: boiling tubes at steam outlet of SG).

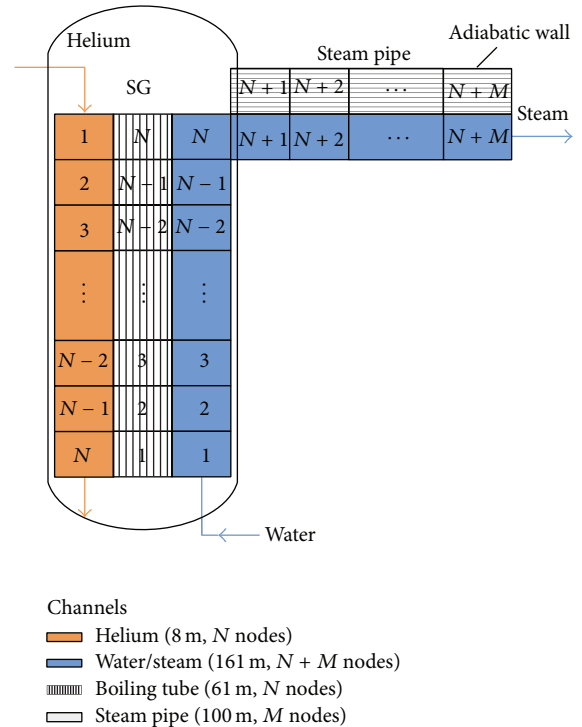


FIGURE 3: Nodalization of SG and STL.

helium temperature at core outlet is stable because of the large heat capacity of core structures and low flow rate of helium.

**3.2. Governing Equations and Solution Method.** A quasi-one-dimensional homogeneous model is used for water/steam flow, which includes governing equations as below:

Continuity equation:

$$\frac{\partial(\rho_m A)}{\partial t} + \frac{\partial}{\partial x}(\rho_m u_m A) = 0. \quad (1)$$

TABLE 2: Criterion for ARHRP.

Position	Description	Value
Core	Helium flow rate	<10% design value
	Inlet helium temperature	>100°C
SG (A)	Temperature difference between tube sheet and steam pipe	<100°C
	Temperature variation rate	<5°C/min
SG (B)	Temperature variation rate	<5°C/min
SG (C)	Temperature variation rate	<5°C/min
	Maximum temperature	<650°C

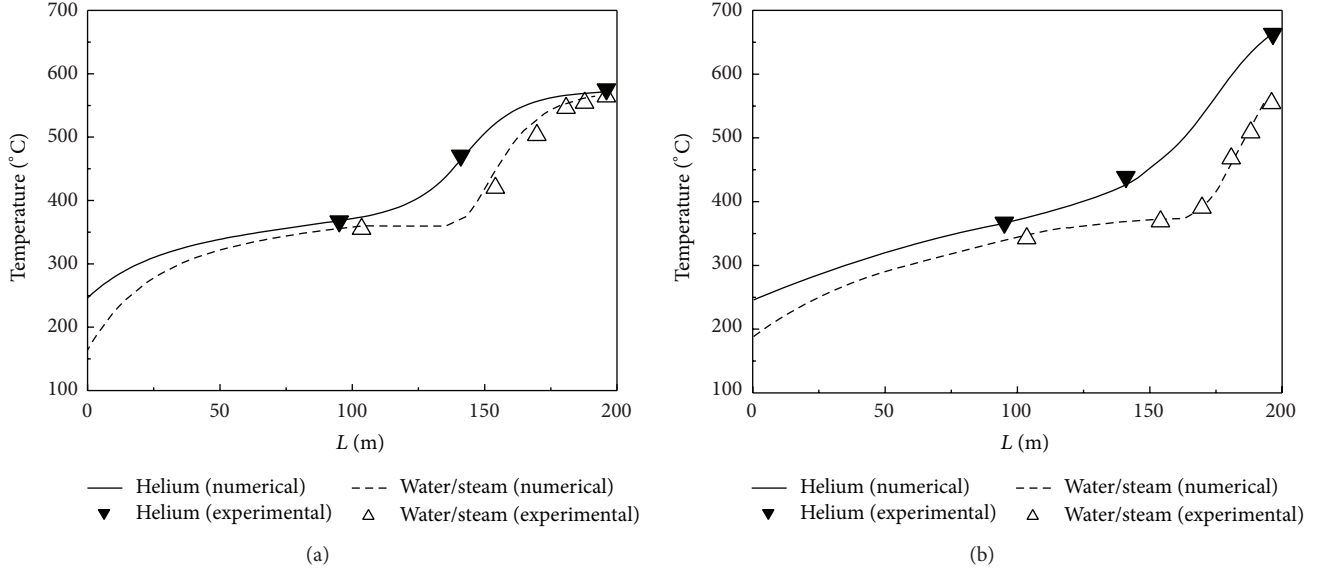


FIGURE 4: Validation of numerical model by THTR-300 experiments: (a) temperature distribution under 40% power load and (b) temperature distribution under 100% power load.

Momentum equation:

$$\frac{\partial(\rho_m u_m A)}{\partial t} + \frac{\partial(\rho_m u_m^2 A)}{\partial x} = A \left( -\frac{\partial p_m}{\partial x} - \rho_m g_m - \frac{f_m}{2D_m} \rho_m u_m^2 \right). \quad (2)$$

Energy equation:

$$\frac{\partial(\rho_m h_m A)}{\partial t} + \frac{\partial(\rho_m h_m u_m A)}{\partial x} = A \left( \frac{Dp_m}{Dt} - \frac{4q_m}{D_m} \right), \quad (3)$$

where  $\rho_m$ ,  $u_m$ ,  $p_m$ , and  $h_m$  are density, velocity, pressure, and enthalpy, respectively;  $A$  is the cross area of the channel, which is included in this model because it has different value for boiling tube and steam pipe;  $D_m$  is diameter of flow channel;  $q_m$  is heat flux; and  $f_m$  is friction factor. Void fraction,  $\alpha_g$ , is computed by state equations as we assume thermal equilibrium between liquid phase and gas phase. Subscript  $m$  denotes the fluid is water if  $\alpha_g < 0$ , steam if  $\alpha_g > 1$ , or two-phase mixture if  $0 \leq \alpha_g \leq 1$ .

A compressible flow model is used for helium flow, whose governing equations are

Continuity equation:

$$\frac{\partial \rho_h}{\partial t} + \frac{\partial}{\partial x} \rho_h u_h = 0. \quad (4)$$

Momentum equation:

$$\frac{\partial \rho_h u_h}{\partial t} + \frac{\partial}{\partial x} (\rho_h u_h^2) = -\frac{\partial p_h}{\partial x} - \rho_h g_h - \frac{f_h}{2D_h} \rho_h u_h^2. \quad (5)$$

Energy equation:

$$\frac{\partial(\rho_h h_h)}{\partial t} + \frac{\partial}{\partial x} (\rho_h h_h u_h) = \frac{Dp_h}{Dt} - \frac{4q_h}{D_h}, \quad (6)$$

where  $\rho_h$ ,  $u_h$ ,  $p_h$ , and  $h_h$  are density, velocity, pressure, and enthalpy, respectively;  $D_h$  is diameter of flow channel;  $q_h$  is heat flux;  $f_h$  is friction factor.

Both water/steam and helium are modeled as compressible flow according to the governing equations mentioned above. However, divergency will arise in the solving process if regular solution method is used, because the Mach numbers of water/steam and helium are much lower than unity. Therefore, a pressure-correction method devised for low

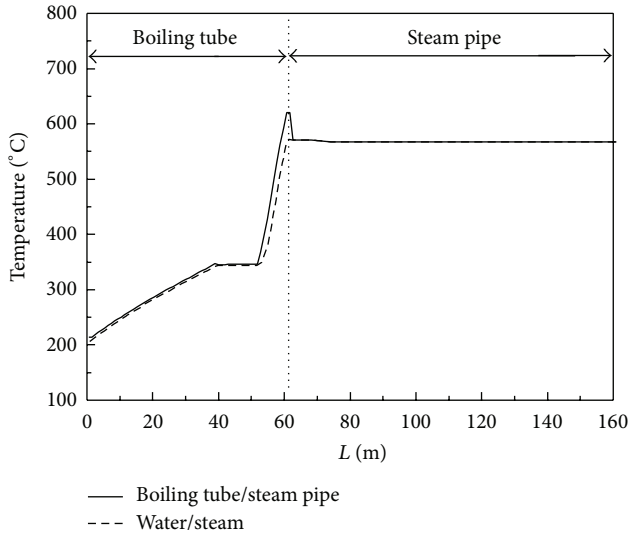


FIGURE 5: Temperature distribution of boiling tube and steam pipe after shutdown of the core.

Mach number compressible problems is used in this paper, which was developed from the famous SIMPLE method of Patankar and Spalding [6]. Additionally, staggered grid system and backward Euler implicit scheme for momentum equation and energy equation discretization are adopted to improve the convergency. The code was validated by the experimental results of THTR-300 steam generator, as shown in Figure 4. The predicted temperature distribution for both helium side and water side meet well with the experiments.

#### 4. Transient Analysis of ARHRP

**4.1. ARHRP without Precooling.** As mentioned in Section 1, the temperature of SG tubes and steam pipe will be maintained after the core is shutdown if without any further operation, as shown in Figure 5. It is straight forward to run primary loop and STL directly and simultaneously without any preconditioning of SG and STL, with the water/steam staying in the boiling tube; for if flow parameters are designed appropriately, no obvious change would appear in the temperature distribution of SG and STL and consequently the heat/cold shock to structures due to the shift of flow states will be minimized.

However, in practice there must be a delay between the starts of STL and primary loop. The feed water pump should be started first in order to eliminate the risk of heat shock caused by the high-temperature helium and overheating of boiling tubes of SG (position C in Figure 2). This makes the delay time be a crucial parameter, during which the temperature of SG tubes decreases rapidly, as shown in Figure 6. For feed water flow rate being 10% design value, the temperature of tubes at SG outlet will decrease from 570°C to 340°C within only 3 minutes, and with the increase of feed water flow rate this process will be accelerated further. This phenomenon is caused by boiling. After shutdown of the core, water occupies downside of the boiling tube and steam occupies upside; at the interface of them water and steam are

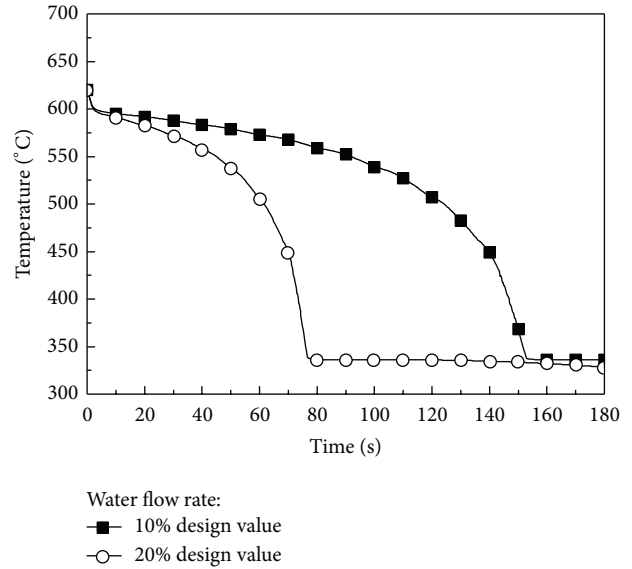


FIGURE 6: Temperature transient of boiling tube (steam outlet) during delay time; helium flow rate: 0; feed water temperature: 105°C; and pressure: 13.9 MPa.

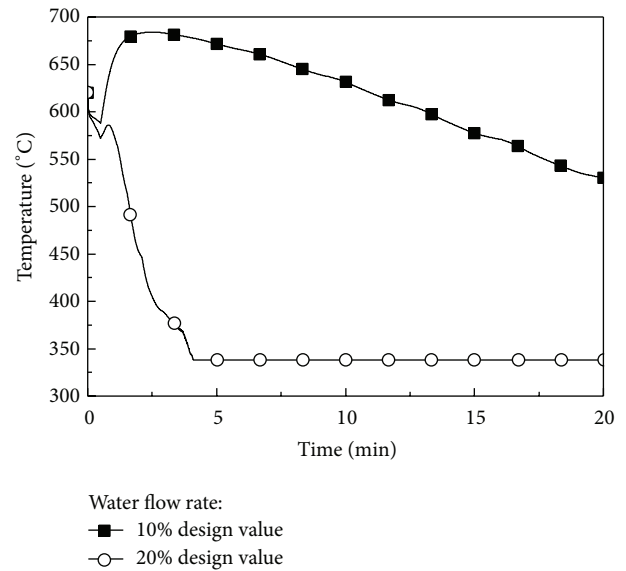


FIGURE 7: Temperature transient of boiling tube (steam outlet), with 30 s delay of helium circulation; helium flow rate: 10% design value; feed water temperature: 105°C; and pressure: 13.9 MPa.

still saturated and boiling will occur when water is heated by the tube during proceeding upward (toward the hot end) driven by the pump. Tube's temperature in the boiling area will experience a sharp decrease because of the large heat transfer coefficient. Thus a cold shock is introduced, which proceeds as fast as water/steam interface.

To decrease the feed water's flow rate is helpful to postpone the cold shock. However, the minimum flow rate of feed water is limited to be not less than 10% of design value to avoid two-phase flow instabilities. The only way to exclude the cold shock when water exists in the boiling

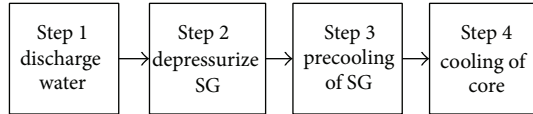
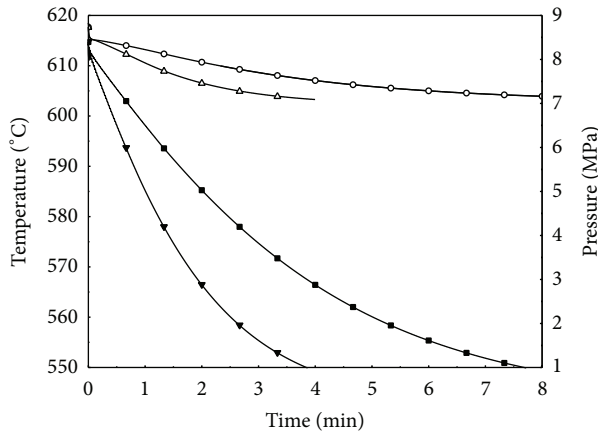


FIGURE 8: ARHRP with precooling of SG.



Temperature (tube sheet of SG)      Pressure  
 —○— Valve is opened 50%      —■— Valve is opened 50%  
 —△— Valve is opened 100%      —▼— Valve is opened 100%

FIGURE 9: Temperature and pressure transient during depressurization.

tubes is to shorten the delay time as much as possible. This is a rigid demand for the reliability of controls system and helium circulator. Even though the circulator is started in the permit time, the temperature variation of boiling tubes is still difficult to control, as shown in Figure 7. It is in a dilemma that large feed water flow rate aggravates the cold shock and low feed water flow rate makes the boiling tube be overheated. Furthermore, if helium circulator fails to start in a short time, this process must be interrupted and cannot be repeated because the permit delay time was already passed. Therefore this process is not reliable.

**4.2. ARHRP with Precooling.** To cool down boiling tubes and steam pipe before the coolant enters SG is a fundamental way to eliminate the risk of cold shock. Therefore we considered including a precooling process and presented a four-step ARHRP as shown in Figure 8. Boiling will occur if water stays in boiling tubes of SG, which is unfavorable as analyzed for ARHRP without precooling in Section 4.1. Hence we choose to discharge water from SG in the first step and then use steam as coolant to cool down SG and STL slowly. As the steam is supplied by the electrical boiler of STL with a pressure of about 1 MPa, the SG and STL should be depressurized in the second step. In the following, each step of ARHRP will be analyzed in detail.

**Step 1.** Discharge liquid water from SG. This step is accomplished by discharge system, which can remove the water entirely in no more than one minute, which occupies 2/3 space of boiling tube after shutdown of reactor core. At the

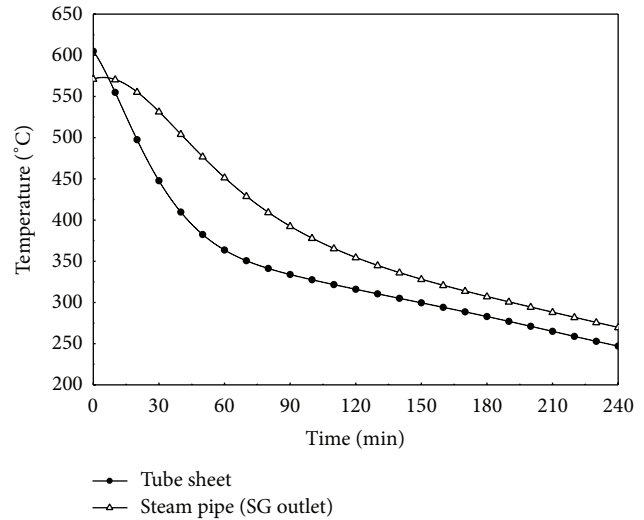


FIGURE 10: Temperature variation of SG outlet during precooling using steam as coolant; steam temperature: 190°C; pressure: 1.0 MPa; and flow rate: 0.74 kg/s.

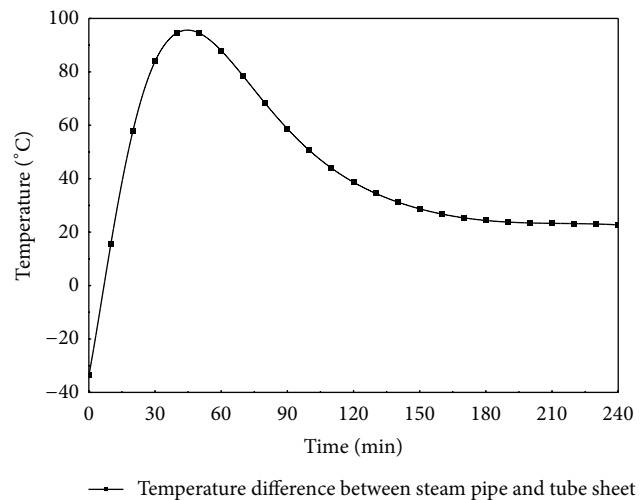


FIGURE 11: Temperature difference of steam pipe and tube sheet during precooling using steam as coolant; steam temperature: 190°C; pressure: 1.0 MPa; and flow rate: 0.74 kg/s.

end of this step the pressure in SGs boiling tube and STL will be reduced to about 8 MPa, while the temperature variation of SG tubes and tube sheet is neglectable for the water is discharged from bottom (cold end) of SG and the duration is very short.

**Step 2.** Depressurize SG and STL. Through the discharge valve on the steam pipe, steam in SG and STL can be discharged to the ambient directly, until the pressure decreases to be lower than 1 MPa. The speed of depressurization can be controlled through adjusting the valve's open degree, as shown in Figure 9. The temperature decreased about 15°C in this step and the speed meets the demands listed in Table 2 even when the valve is fully opened.

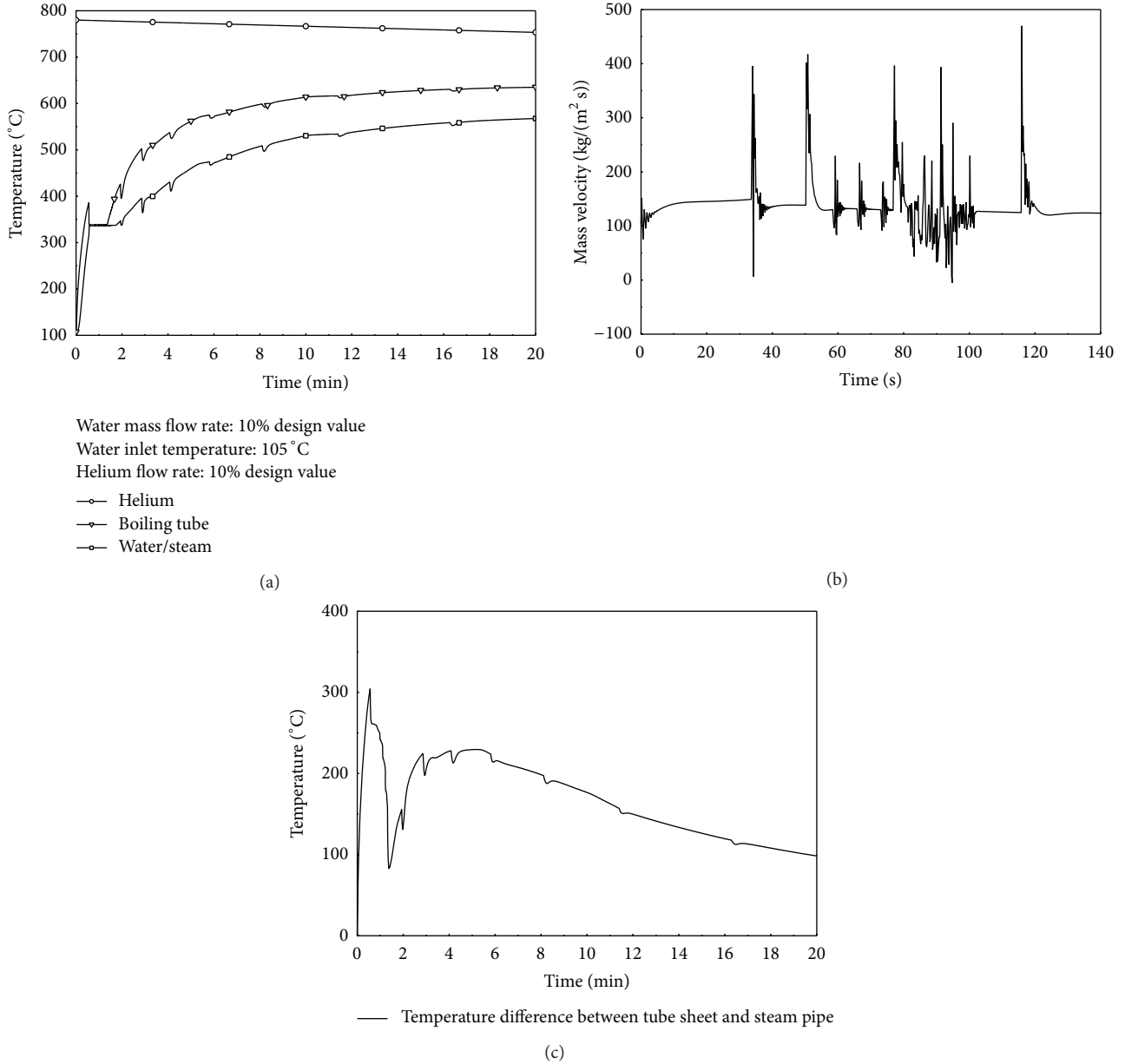


FIGURE 12: Temperature transient of SG outlet during cooling of reactor core; water mass flow rate: 10% design value; inlet temperature: 105 °C; pressure: 13.9 MPa; and helium mass flow rate: 10% design value: (a) temperature of SG outlet; (b) flow oscillation; and (c) temperature difference between tube sheet and steam pipe.

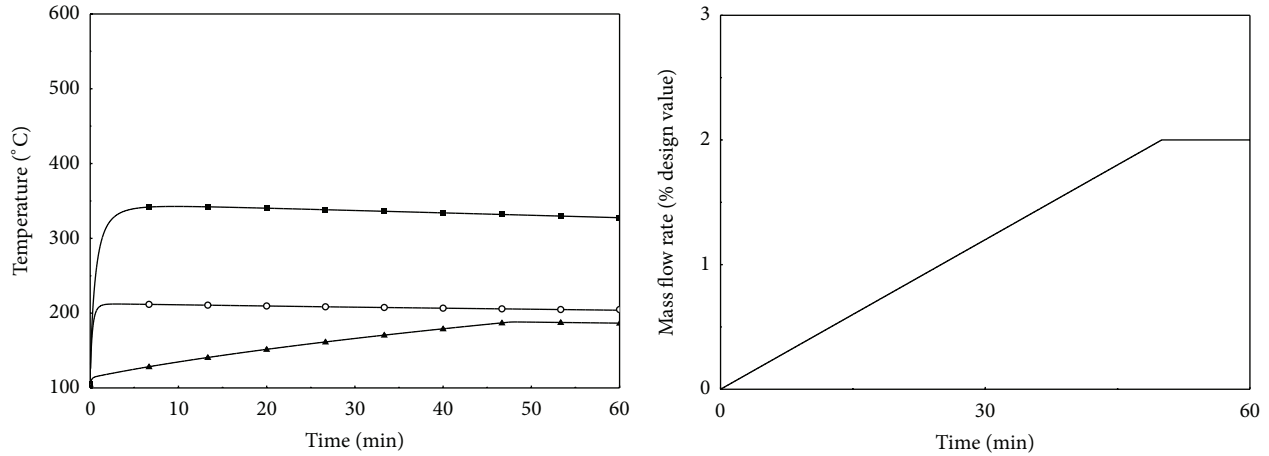
*Step 3. Precool SG and STL.* In this step steam produced by the electrical boiler of STL is fed to SG directly, with temperature of 190 °C and pressure of 1 MPa. The flow rate of steam needs to be controlled to keep the temperature variation rate less than 5 °C/min to meet the demands of Table 2. Figure 10 shows the temperature transient of boiling tubes at SG outlet with steam flow rate of 0.74 kg/s. The temperature varies with a speed close to 5 °C/min in the first hour and slows down in the following. This profile suggests that steam flow rate should be increased after the first hour to accelerate the process.

It is noticeable that an obvious delay exists between the temperature variations of boiling tube and steam pipe,

despite the fact that their positions are very close. Under lumped parameter analysis, this phenomena is caused by the difference between the time constant of SG tubes and steam pipe, which represent the response time of an object's temperature to boundary convection and is expressed as

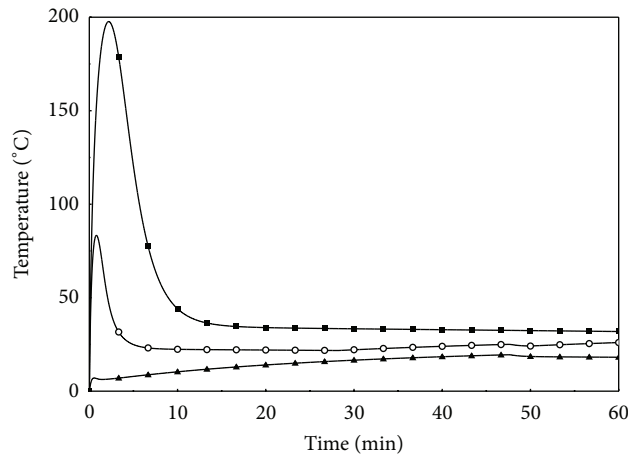
$$\tau = \frac{\rho c_p V}{hS}, \quad (7)$$

where  $\rho$  is the density,  $c_p$  the heat capacity,  $h$  the convection heat transfer coefficient,  $V$  the volume, and  $S$  the surface area for convection. For SG boiling tubes the ratio of  $V$  and  $S$  is 0.004, while for steam pipe it is 0.032; this is the principal reason that makes the time constant of steam pipe be much



Helium flow rate: 2% design value  
 Water flow rate:  
 —▲— 10% design value  
 —○— 30% design value  
 —■— 30% design value (helium flow gradually increased)

(a) (b)



Helium flow rate: 2% design value  
 Water flow rate:  
 —▲— 10% design value  
 —○— 30% design value  
 —■— 30% design value (helium flow gradually increased)

(c)

FIGURE 13: Temperature transient of SG outlet during cooling of reactor core; water inlet temperature: 105°C; pressure: 13.9 MPa; helium mass flow rate: 2%; and design value: (a) temperature at SG outlet; (b) mass flow rate of helium; and (c) temperature difference between tube sheet and steam pipe.

bigger than that of boiling tubes. This temperature delay caused a remarkable temperature difference between steam pipe and tube sheet, as shown in Figure 11, which is dangerous to the weld at position A of Figure 2 although the maximum value is less than 100°C and still meets the demands. To lower this temperature difference the steam flow rate should be reduced.

After maximum temperature of the system decreases to 200°C, the electrical heater of start-up loop will be shifted to supply water with pressure of 13.9 MPa and temperature of 105°C to cool SG and STL further to about 105°C.

*Step 4.* Cool the core. In the final step the coolant of SG is feed water with temperature of 105°C and pressure of 13.9 MPa. After Step 3, boiling tubes and steam pipe all have temperature of 105°C, which is much lower than that of helium in the core (nearly 750°C). Therefore a heat shock may be introduced to position C in Figure 2 when helium enters SG if the flow rate of helium and feed water are designed inappropriately.

Figure 12 shows the temperature transients at SG outlet when the flow rates of helium and water are set to be 10%

of design value, respectively. In the first minute boiling tube's temperature rises rapidly to nearly 400°C due to the sudden load of hot helium and then decreases to 340°C abruptly when water began to boil. After that, a staggered temperature profile arises and lasts about 10 minutes, accompanied with the oscillation of mass flow rate of steam at boiling tube outlet. The oscillation was caused by the two-phase flow instabilities because of the low mass flow rate of water. Meanwhile the maximum temperature difference between tube sheet of SG and steam pipe enlarges to 300°C. Obviously this process is unacceptable.

This series of problems is caused by big helium flow rate combined with small water flow rate. Figure 13 shows the temperature transient of SG steam outlet with helium flow rate being 2% of design value. Compared with Figure 12(a) the heat shock is alleviated and reduced further with the increase of water flow rate. However, this is still not sufficient to eliminate the heat shock. The helium flow must be controlled to increase slowly from a tiny flow rate as shown in Figure 13(b). Under such operation the temperature difference of SG tube sheet and steam pipe can be confined within 25°C. Therefore the combination of big water flow rate and gradual increase of helium flow from tiny flow rate is the optimum option for this step. However, the present helium circulator may have difficulties to work under so small flow rate. To accomplish this step a smaller circulator should be supplemented to this system.

## 5. Conclusion

In the present work the ARHRP of HTR-PM has been studied theoretically based on a one-dimensional mathematical model. Transient analysis was carried out for the whole process and following conclusions were obtained.

- (1) Boiling is unfavorable for ARHRP, due to both the cold shock to the hot structures induced by large heat transfer coefficient and potential two-phase flow instabilities when feed water flow rate is low. Actually, safety is principal for ARHRP which demands to exclude any fast heat transfer process.
- (2) Tube sheet at steam outlet of SG is one of the most damageable positions during ARHRP, for its welds with boiling tubes and steam pipe will suffer thermal stress caused by the temperature differences. Particularly, according to the fact that the time constant of tube sheet is much smaller than that of steam pipe, an obvious delay of temperature variation appears and makes the temperature difference between these two objects remarkable.
- (3) For ARHRP without precooling of SG and STL, boiling and cold shock are inevitable when water begins to proceed in the hot boiling tubes before helium begins to circulate. Although the cold shock can be alleviated through shortening the start time of helium circulator, this type ARHRP is not robust.

- (4) A four-step ARHRP with precooling of SG and STL can eliminate the cold shock fundamentally. In precooling process steam is used as the coolant to make sure no cold shock will be introduced. After that, the main consideration is to avoid the heat shock to boiling tubes and tube sheet at steam outlet when the hot helium enters SG. A combination of large feed water flow and gradually increased helium flow can eliminate the hot shock and confine the temperature difference between tube sheet and steam pipe effectively. This type ARHRP is recommended in this paper, although a new helium circulator which can supply small helium flow rate should be supplemented to this system.

This work is instructive to the engineering design of ARHRP for HTR-PM, which can shorten the cooling time of reactor core and improve the economic performance of the plant. However, more detailed calculations are needed to specify the flow parameters for each step of ARHRP.

## Nomenclature

$A$ : Cross area [m<sup>2</sup>]  
 $c_p$ : Specific heat capacity [J/(kg·K)]  
 $D$ : Diameter [m]  
 $f$ : Friction factor  
 $g$ : Gravity [m/s<sup>2</sup>]  
 $h$ : Specific enthalpy [J/kg]  
 $M$ : Node number of steam pipes  
 $N$ : Node number of boiling tube  
 $p$ : Pressure [Pa]  
 $q$ : Heat flux [W/m<sup>2</sup>]  
 $S$ : Surface area [m<sup>2</sup>]  
 $V$ : Volume [m<sup>3</sup>].

### Greek Letters

$\alpha_g$ : Void fraction  
 $\rho$ : Density [kg/m<sup>3</sup>]  
 $\tau$ : Time constant [s].

### Subscripts

$g$ : Vapor  
 $m$ : Mixture of liquid phase and vapor phase  
 $h$ : Helium.

## Conflict of Interests

The authors declare that there is no conflict of interests regarding the publication of this paper.

## Acknowledgments

This work was supported by Ph.D. Program Foundation of Ministry of Education of China (no. 20100002120036) and Research Project of Tsinghua University (no. 2012Z02145).

## References

- [1] Z. Zhang, Z. Wu, Y. Sun, and F. Li, "Design aspects of the Chinese modular high-temperature gas-cooled reactor HTR-PM," *Nuclear Engineering and Design*, vol. 236, no. 5-6, pp. 485–490, 2006.
- [2] H. Niessen and S. Ball, "Heat transport and afterheat removal for gas cooled reactors under accident conditions," Tech. Rep. IAEA-TECDOC-1163, International Atomic Energy Agency, Vienna, Austria, 2000.
- [3] Y. Qingliao, X. Zhao, W. Xinxin, H. Shuyan, and S. Yuliang, "Design of pre-stressed concrete pressure vessel residual heat removal system for modular high-temperature gas-cooled reactor," *Atomic Energy Science and Technology*, vol. 41, no. 1, pp. 74–78, 2007.
- [4] Z. Zhang and Y. Sun, "Economic potential of modular reactor nuclear power plants based on the Chinese HTR-PM project," *Nuclear Engineering and Design*, vol. 237, no. 23, pp. 2265–2274, 2007.
- [5] R. Breitenfelder, W. Wachholz, and U. Weicht, "Accident analysis and accident control for the THTR-300 power plant," in *Proceedings of the Specialists Meeting on Gas-Cooled Reactor Safety and Licensing Aspects*, Lausanne, Switzerland, 1980.
- [6] J. J. McGuirk and G. J. Page, "Shock capturing using a pressure-correction method," *AIAA journal*, vol. 28, no. 10, pp. 1751–1757, 1990.

## Research Article

# Design of the VISTA-ITL Test Facility for an Integral Type Reactor of SMART and a Post-Test Simulation of a SBLOCA Test

**Hyun-Sik Park, Byung-Yeon Min, Youn-Gyu Jung, Yong-Cheol Shin,  
Yung-Joo Ko, and Sung-Jae Yi**

*Thermal Hydraulics Safety Research Division, Korea Atomic Energy Research Institute, 989-111 Daedeokdaero,  
Yuseong, Daejeon 305-353, Republic of Korea*

Correspondence should be addressed to Hyun-Sik Park; [hspark@kaeri.re.kr](mailto:hspark@kaeri.re.kr)

Received 11 October 2013; Revised 25 February 2014; Accepted 22 May 2014; Published 26 June 2014

Academic Editor: Annalisa Manera

Copyright © 2014 Hyun-Sik Park et al. This is an open access article distributed under the Creative Commons Attribution License, which permits unrestricted use, distribution, and reproduction in any medium, provided the original work is properly cited.

To validate the performance and safety of an integral type reactor of SMART, a thermal-hydraulic integral effect test facility, VISTA-ITL, is introduced with a discussion of its scientific design characteristics. The VISTA-ITL was used extensively to assess the safety and performance of the SMART design, especially for its passive safety system such as a passive residual heat removal system, and to validate various thermal-hydraulic analysis codes. The VISTA-ITL program includes several tests on the SBLOCA, CLOF, and PRHRS performances to support a verification of the SMART design and contribute to the SMART design licensing by providing proper test data for validating the system analysis codes. A typical scenario of SBLOCA was analyzed using the MARS-KS code to assess the thermal-hydraulic similarity between the SMART design and the VISTA-ITL facility, and a posttest simulation on a SBLOCA test for the shutdown cooling system line break has been performed with the MARS-KS code to assess its simulation capability for the SBLOCA scenario of the SMART design. The SBLOCA scenario in the SMART design was well reproduced using the VISTA-ITL facility, and the measured thermal-hydraulic data were properly simulated with the MARS-KS code.

## 1. Introduction

An integral effect test (IET) program was conducted by the Korea Atomic Energy Research Institute (KAERI) using the VISTA (experimental verification by integral simulation of transients and accidents) integral test loop (VISTA-ITL). The VISTA-ITL is a modified version of an existing VISTA facility [1] that has been modified to have the capability to simulate a small-break loss of coolant accident (SBLOCA) for the SMART (system-integrated modular advanced reactor) design [2]. The VISTA-ITL was used extensively to improve the safety and performance of the SMART design and to validate various thermal-hydraulic analysis codes such as the TASS/SMR-S [3] and MARS-KS [4].

The reference plant of the VISTA-ITL is a 330 MW (thermal) class integral type reactor, SMART [2], which was developed by KAERI and licensed by the Korean regulatory body, nuclear safety, and security commission (NSSC) in June 2012. The SMART reactor is characterized by the introduction of simplified and improved safety systems such as the passive residual heat removal system (PRHRS) and its integral

arrangement of the reactor vessel assembly, which makes it possible to remove the large pipe connections between the major components. It excludes the occurrence of a large break loss of coolant accidents (LBLOCA), but an SBLOCA is still a major concern for a safety analysis.

The VISTA-ITL is a reduced-height integral effect test facility based on the design features of SMART. The VISTA-ITL is used to investigate various thermal-hydraulic phenomena during the SBLOCA. The break flow rate, safety injection flow rate, and thermal-hydraulic behaviors of the major components for a typical break size and break locations are measured. The acquired data were used to validate the related thermal-hydraulic models of the safety analysis code, TASS/SMR-S [3], which can assess the capability of SMART to cope with the SBLOCA scenario. As the VISTA-ITL is capable of simulating various transient and accident conditions for the SMART design, it will greatly contribute to the enhancement of the SMART reactor's safety and performance. Recently, an experimental investigation of the SBLOCA scenario was also performed with a scaled integral test facility for a small-sized integral PWR of REX-10 [5], and

a thermal-hydraulic system code of TAPINS was developed to confirm the design decisions and analyze the transient responses of integral PWRs such as REX-10 [6].

Several tests were conducted using the VISTA-ITL facility in support of SMART standard design approval (SDA) and technology validation from 2009 through 2011 [7]. This paper presents an overview of the VISTA-ITL test program for the SMART design. The main focus is on the scientific design characteristics of the VISTA-ITL, its ability to simulate an SBLOCA scenario of the SMART design, and a brief introduction on the tests conducted. A pretest analysis of an SBLOCA was also performed to quantify the effects of possible scaling distortion and to assess the similarity between the VISTA-ITL and the SMART design. In addition, a posttest analysis of an SBLOCA test was performed to understand the general behavior of the VISTA-ITL and to assess the MARS-KS models to simulate the VISTA-ITL test data.

## 2. Scientific Design of the VISTA-ITL

*2.1. Existing VISTA Facility.* The existing VISTA facility [2] is an integral effect test facility to simulate the primary and secondary systems as well as the major safety-related systems of the SMART-P. The reactor core is simulated by electric heaters with a capacity of 818.75 kW, which is about 120% of the scaled full power. The scaled full power is 682.29 kW. Unlike the integrated arrangements of the SMART-P, the VISTA primary components including a reactor vessel, a main coolant pump (MCP), a steam generator, and three pressurizers are connected to each other by pipes to facilitate the easy installation of the instrumentation and simple maintenance. The secondary system with a single train of a feed water supply tank (FWST), feed water line, steam generator (SG) secondary side, and steam line was simply designed to remove the primary heat source. A single train of the PRHRS is also installed. In addition to these major systems, a make-up water system and a feed water system are installed to control the feed water supply and its temperature.

The VISTA facility was designed to operate with a combination of manual and automatic operations. The controlled components include an electrical heating rod, a main coolant pump, a feed water control valve, a steam pressure control valve, an FWST heater, and a make-up pump. All safety-related accidents should be initiated and controlled by automatic control logics as they require automatic reactor trip logics to initiate the PRHRS. The corresponding trip logics, tables, and set points are programmed to control the sequence of events.

A set of experiments was performed for the SMART-P using the existing VISTA facility, which includes parametric studies on the thermal-hydraulic characteristics of the transient operation of an integral reactor [8] and experiments on the performance sensitivity of the passive residual heat removal system of an advanced integral type reactor [9].

*2.2. Design Concept and Scaling Methodology of VISTA-ITL.* In formulating the design concept, we had to consider the existing VISTA facility, which had been operated to simulate the SMART-P design. In the VISTA facility, the available core

TABLE 1: Major scaling parameters and ratios of the VISTA-ITL.

Parameters	Scale ratio	Value
Length, $l_{OR}$	$l_{OR}$	1/2.77
Diameter, $d_{OR}$	$d_{OR}$	1/21.746
Area, $a_{OR}$	$d_{OR}^2$	1/472.9
Volume, $V_{OR}$	$d_{OR}^2 \cdot l_{OR}$	1/1310
Time scale	$l_{OR}^{1/2}$	1/1.664
Velocity	$l_{OR}^{1/2}$	1/1.664
Power/volume	$l_{OR}^{-1/2}$	1.664
Heat flux	$l_{OR}^{-1/2}$	1.664
Core power	$a_{OR} \cdot l_{OR}^{1/2}$	1/787
Flow rate	$a_{OR} \cdot l_{OR}^{1/2}$	1/787
Pump head	$l_{OR}$	1/2.77
Pressure drop	$l_{OR}$	1/2.77

heater power is 818.75 kW and the flow rates of the primary and secondary loops are 3.54 and 0.25 kg/s, respectively. Therefore, the VISTA facility was proven to have sufficient electrical and pumping capacities to simulate the operating conditions of the SMART design. The existing VISTA facility [2] was modified to have the simulation capability of an SBLOCA by installing a steam pressurizer, a safety injection system, a break simulation system, and so forth.

Finally, we chose the 1/2.77 height and 1/1310 volume-scale design for SMART, as summarized in Table 1. The reference scale ratios of the length and area are based on the elevation difference between the core and steam generator centers (1/2.77) and the core flow area (1/472.9), respectively. Table 1 shows the major scaling parameters of the VISTA-ITL and its scaling ratios. The rationale for adopting the reduced-height design is similar to that for the ATLAS design [10]. As there is no absolute superiority between full-height and reduced-height designs, a decision could be made by considering the test objectives, prototype design characteristics, budget, and so forth. In the VISTA-ITL facility, the main reason for the adoption of the reduced-height design is to use the existing VISTA facility, which has a reduced-height geometry compared with the SMART design, and it was proven through various scoping analyses using best-estimate safety analysis codes that the VISTA-ITL facility can properly simulate the major sequence of events expected to occur in the SMART design. As the scale ratio of length is 1/2.77, the time for the VISTA-ITL is 1.664 times faster than that for the SMART design. The scale ratios of both the core power and the flow rate are 1/787, and the scale ratio of the pressure drop is 1/2.77.

*2.3. Scientific Design of the Systems and Components.* The VISTA-ITL has been designed following the three-level scaling methodology of Ishii and Kataoka [11], which consists of integral scaling, boundary flow scaling, and local phenomena scaling. Figure 1 shows a schematic diagram of the VISTA-ITL facility. The major components of the reactor pressure vessel, steam generator, PRHRS, and secondary system are

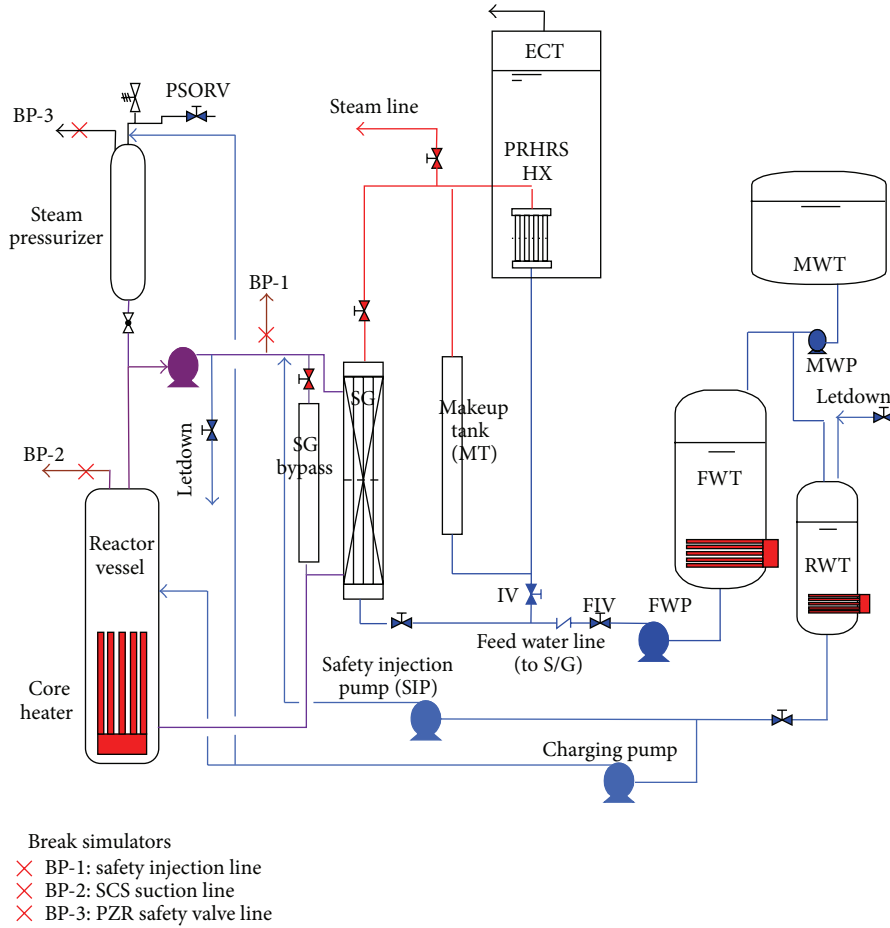


FIGURE 1: Schematic diagram of the VISTA-ITL facility.

preserved, which were described by Yi et al. [1], but some changes were made to simulate the SBLOCA behavior of the SMART design. They include a steam pressurizer, safety injection system, steam generator bypass, hot leg, cold leg, PRHRS makeup tank, break simulator, and break measuring system. These were designed to match the scaling ratios given in Table 1.

**RPV and Core Heater.** The primary loop of the VISTA-ITL facility is a single loop and is composed of a reactor pressure vessel (RPV) with a core heater, a main coolant pump (MCP), a steam generator (SG), and an interconnecting hot leg and a down-comer. In the VISTA-ITL facility, the core heater and MCP were proven to have sufficient electrical and pumping capacities to simulate the scaled full power and flow rate conditions of the SMART design, respectively. The SG bypass volume is added using a separate vessel to simulate the design characteristics of the SMART reactor. In addition, the volumes of the pump discharge line (so-called hot leg) and SG outlet region (so-called cold leg) are expanded to have scaled-down values of SMART.

**Steam Pressurizer.** The steam pressurizer is installed instead of the self-pressurized pressurizer of the existing VISTA facility.

The steam pressurizer of the SMART design was scaled-down following the scaling ratios in Table 1, and its bottom is connected to the upper part of the RPV before the RCP suction.

**Steam Generator.** The steam generator is composed of 12 helically coiled tubes, an outer vessel, and a SG bypass. The primary coolant enters the inlet of the SG and flows down through the shell side, forming a countercurrent flow with respect to the secondary feed water flow inside the tube. The secondary feed water enters the inlet of the SG tubes from the bottom, flows up through the helical tubes, and becomes a superheated steam at the outlet of the SG tubes.

**PRHRS.** The PRHRS of the VISTA-ITL facility is composed of a single train for the cooling system, which includes an emergency cooldown tank (ECT), a heat exchanger (HX), a makeup tank (MT), several valves, and the related piping. It is connected to both the feed water and the steam lines of the secondary system to provide a flow path for the natural circulation. The PRHRS is designed to have the same pressure drop and heat transfer characteristics and is arranged to have the same elevation and position as those of the reference system.

The PRHRS makeup tank functions to make up the PRHRS inventory loss during the PRHRS operation. It was scaled down following the scaling ratios in Table 1 and was newly installed between the secondary system steam line and the PRHRS condensate line in parallel with the RRHRS heat exchanger.

**Safety Injection System.** The safety injection system was scaled down following the scaling ratios in Table 1 and was additionally installed in the VISTA-ITL facility. It included a refueling water tank (RWT), a safety injection pump (SIP), a charging pump, and the related piping, valves, and instruments.

**Break Simulation System (BSS).** The line breaks of SIS, SCS, and PSV were simulated by installing a break spool piece. The configuration of the spool piece is shown in Figure 2. It consists of a quick opening valve, a break nozzle, a case holding the break nozzle, and a few instruments. A pressure transducer and two thermocouples were installed both upstream and downstream of the break nozzle. The detailed geometry of the break nozzle for the present SBLOCA tests is shown in Figure 3. The break nozzle was designed according to the scaling law so that the coolant escapes from the primary system at the scaled-down break flow rate. The break nozzle was installed horizontally at the discharge line of the break points of the SIS, SCS, and PSV. The quick opening valve was opened within 0.5 s by the operators when the test was initiated. The break flow was discharged to the break measuring system (BMS). When a SBLOCA occurs, a choking is expected to occur at the break location during the whole SBLOCA scenario. The inner diameter of the break nozzle is determined to be 1.77 mm, which corresponds to 1/787 of a 2-inch break area. The break nozzle has a well-rounded entrance and its length is fixed to 70 mm including the entrance region to comply with the long pipe requirement that the length-to-diameter ratio should be above 12.

**Break Measuring System (BMS).** The break flow was discharged into a BMS, which consists of a separating vessel (SV-1) and two measuring vessels (MV-1 and MV-2). The overall configuration of the break measuring system is shown in Figure 4. The separating vessel is used to divide the break flow from the break points into steam and water flows. The steam, which is separated in the separating vessel, was discharged through a silencer into the atmosphere. The steam flow rate was measured by a vortex-type flow meter at the discharge line. The water, which was separated in the separating vessel, was drained to one of two measuring vessels. A load cell was installed on the bottom of each measuring vessel to weigh the water mass. The separated water was first introduced to MV-01. When MV-01 is full of water, the flow direction is switched from MV-01 to MV-02 by a 3-way valve. While MV-02 is used to measure the water mass, MV-01 is drained for the next usage and vice versa. The separating vessel is also designed to simulate a containment backpressure by controlling its pressure using a pressure control valve.

**2.3.1. Instrumentation, Control, and Data Acquisition Systems.** Figure 5 shows the schematics of the instrumentation and

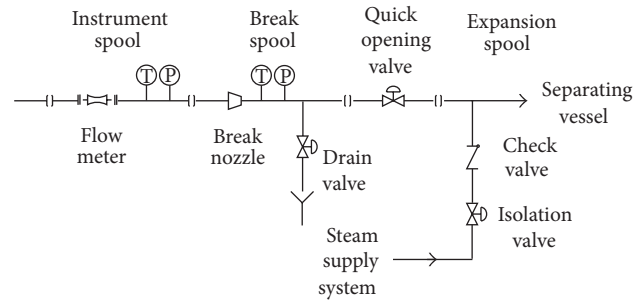


FIGURE 2: Configuration of the break simulation system.

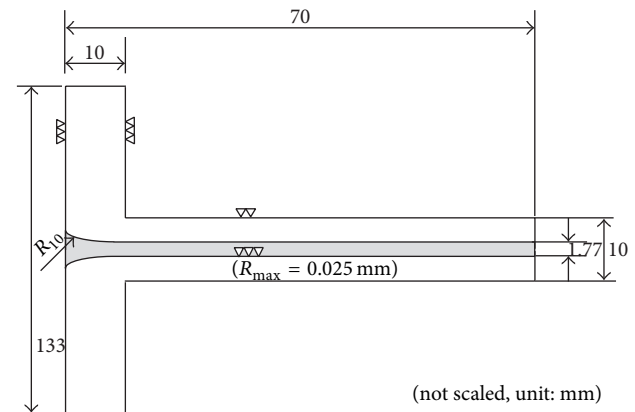


FIGURE 3: Detailed geometry of the break nozzle.

data acquisition system. The instrument system comprises a total of 246 measurement channels. It allows the measurement of all relevant thermal-hydraulic quantities of fluid systems such as a reactor pressure vessel, steam generators, a secondary system, and auxiliary systems. The instrument signals of the VISTA-ITL consist of an AI (analog input), an AO (analog output), a TC (thermocouple), a DI (digital input), a DO (digital output), and an SR (serial communication). They can also be categorized according to the instrument type such as the temperature, static pressure, differential pressure, water level, flow rate, mass, and power.

The VISTA-ITL was designed to be operated by a combination of manual and automatic operation. Several initial operations such as the inventory filling, startup, and cooldown are operated manually by an operator. Once the major thermal-hydraulic parameters reach a steady-state condition, they can be switched over to be controlled automatically by PID feedback control logics so as to maintain the achieved steady-state condition. The controlled components include an electrical heating rod, a main coolant pump, a feed water control valve, a steam pressure control valve, a feed water storage tank heater, and a makeup pump. A special combination of three heater groups is used to prevent the maximum heater surface temperature from exceeding the safety limit. The control system allows the simulation of time- or pressure-dependent parameters such as the core decay heat release and safety injection flow rates, respectively.

A high-performance data acquisition system is installed to acquire data from the instrument system. This system

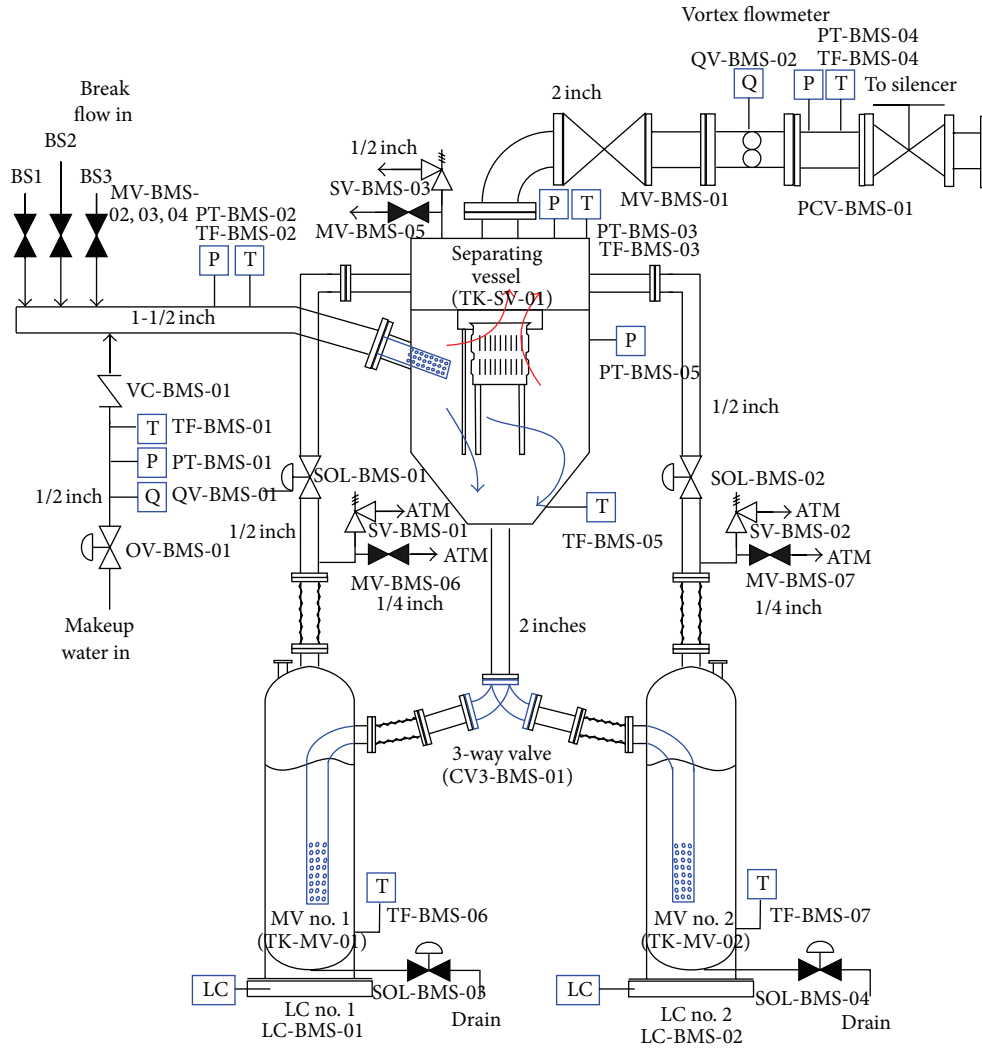


FIGURE 4: Schematic diagram of the break measuring system.

consists of two parts, a computer and display terminal, and the VXI C-size mainframe and terminal panels residing in the control room. These two parts are connected using an industry standard IEEE 1394 (Firewire) serial control and data interface. The data acquisition system is isolated from the control system using several types of signal distributors. The computer collects and saves data from various instruments measuring the pressure including the differential pressure, water level, flow rate, pump speed, and temperature.

### 3. VISTA-ITL Program

Several tests were conducted using the VISTA-ITL facility in support of the SMART design verification. Table 2 shows the brief summary of the test matrix of the VISTA-ITL program. All of them were done in the cause of the SMART standard design approval and technology validation program from 2009 through 2011. A set of tests for SBLOCAs, CLOF, and PRHRS performance were performed to understand the general behavior and assess the safety of the SMART design

using the VISTA-ITL facility [7]. The test results were used to validate the TASS/SMR-S code.

Three SBLOCA tests were successfully performed and provided for validating the TASS/SMR-S code. The break types are guillotine breaks, and their break locations are at the safety injection system (SIS) line (nozzle part of the RCP discharge), at the suction line of the shutdown cooling system (SCS) (nozzle part of the RCP suction), and at the pressurizer safety valve (PSV) line connected to the pressurizer top. Additional SBLOCA tests were performed for various initial and boundary conditions with some facility modifications.

An integral effect test was successfully performed to provide data to assess the simulation capability of the TASS/SMR code for a complete loss of reactor coolant system (RCS) flow rate (CLOF) scenario for the SMART design. The steady-state conditions were achieved to satisfy the initial test conditions presented in the test requirement; its boundary conditions were accurately simulated, and the CLOF scenario in the SMART design was reproduced properly using the VISTA-ITL facility.

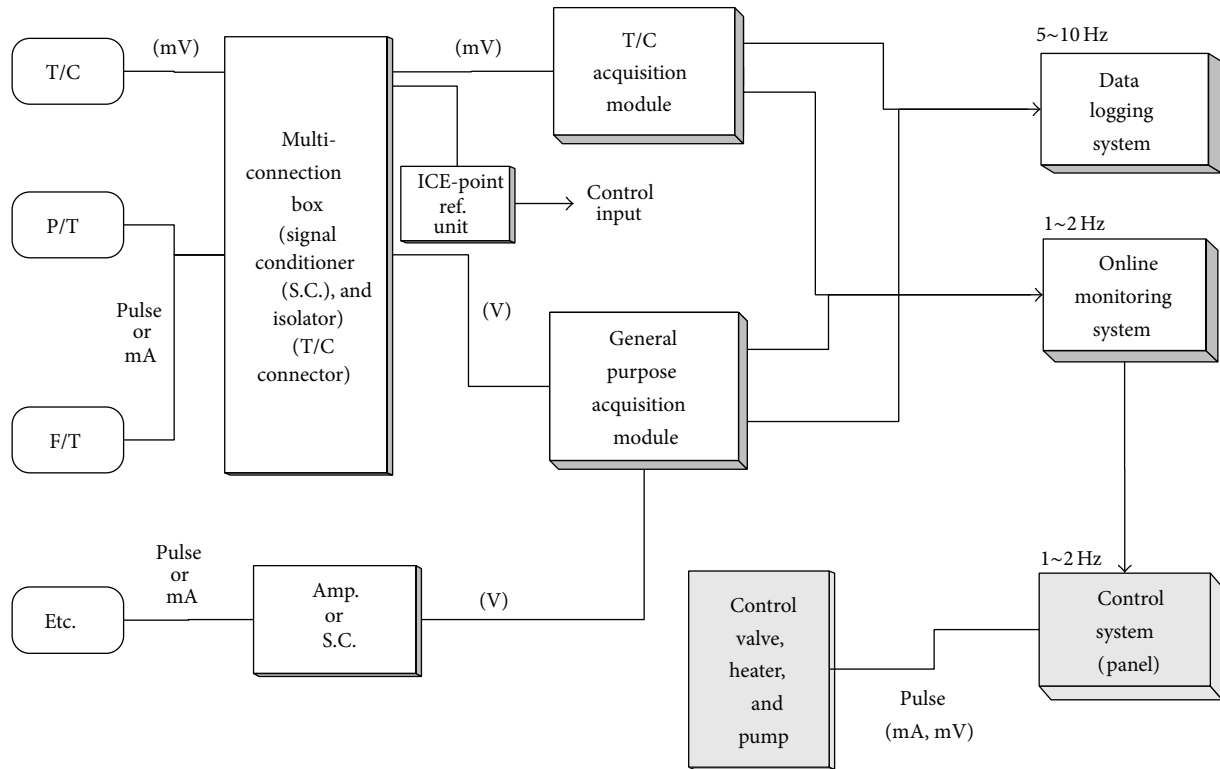


FIGURE 5: Schematics of the instrumentation and data acquisition system.

PRHRS performance verification tests were performed for 100% scaled power, 20% scaled power, and hot standby condition. It was demonstrated that two-phase natural circulation in the PRHRS was properly achieved at different initial powers and feed water flow rates. The PRHRS performance was also investigated for SBLOCA conditions. The experimental results show that the steady-state conditions were operated to satisfy the initial test conditions presented in the test requirement, and its boundary conditions were properly simulated. With the operation of PRHRS, a two-phase natural circulation flow formed inside the two-phase PRHRS natural circulation loop.

The VISTA-ITL program includes the test results on the SBLOCA, CLOF, and PRHRS performances and the analysis results on SMART and VISTA-ITL using the MARS-KS and TASS/SMR-S codes. The VISTA-ITL program contributed to the SMART SDA by providing proper test data for validating the TASS/SMR-S code.

#### 4. MARS-KS Simulation on a SBLOCA Scenario

**4.1. MARS Nodalization.** Figures 6 and 7 show the MARS-KS [4] nodalization schemes used for the SMART design and VISTA-ITL, respectively. The nodalization schemes of both the SMART design and the VISTA-ITL include all the reactor coolant systems, a safety injection system, a secondary system, PRHRS, and auxiliary systems. While the SMART design has four loops, the VISTA-ITL has a single loop. The

overall nodalization was configured to provide consistency between them.

**4.2. Pretest Analysis of a SBLOCA Scenario on SMART and VISTA-ITL.** A SBLOCA scenario for both the reference plant SMART and the VISTA-ITL has been analyzed using the best-estimate system code, MARS-KS [4].

**4.2.1. Steady-State Calculation Results.** Table 3 shows the design parameters and calculated major design parameters of the SMART design, SMART calculation, and VISTA-ITL calculations under a steady-state condition. In the VISTA-ITL facility, the actual design values are different from the ideally scaled-down values. The main source of the distortion is considered to be caused by a large heat structure owing to the inherent nature of a small-scale integral effect test facility such as VISTA-ITL. To assess the scaling distortion owing to the restraints of the actual VISTA-ITL design, three calculations were performed. One is a case in which the actual design of the VISTA-ITL was simulated (VISTA-Actual), the second one was a case in which the ideally calculated design of the VISTA-ITL was simulated (VISTA-Ideal), and the last one was a case in which the actual design values of the VISTA-ITL were simulated except for the ideally scaled-down heat structure (VISTA-Ideal HS). The MARS calculation results showed good agreement with the SMART design within an allowable uncertainty bound, as shown in Table 3.

**4.2.2. Transient Calculation Results.** The safety injection line break is considered to be a typical SBLOCA scenario. The

TABLE 2: Test matrix of the VISTA-ITL program.

Test type	Test ID	Date	Objectives
SBLOCA phase I	SB-SIS-06	December 2010	Safety injection system (SIS) line break SBLOCA and RCP discharge
	SB-SCS-01	December 2010	Shutdown cooling system (SCS) line break SBLOCA and RCP suction
	SB-PSV-01	December 2010	Pressurizer safety valve (PSV) line break SBLOCA and pressurizer top
PRHRS performance	PRHRS-SS-N1	April 2011	PRHRS actuation during the steady state operation with 100% power
	PRHRS-SS-N2	April 2011	PRHRS actuation during the steady state operation with 20% power
	PRHRS-SS-N3	April 2011	PRHRS actuation during the steady state operation under hot standby condition
	PRHRS-TR-A3	May 2011	PRHRS actuation during the transient operation of SBLOCA
Complete loss of RCS flow rate	CLOF-01	July 2011	Complete loss of RCS flow rate
	CLOF-02	July 2011	Complete loss of RCS flow rate (repetition)
SBLOCA phase II (after hardware modification)	SB-SIS-07	April 2011	Safety injection system (SIS) line break SBLOCA and RCP discharge (repetition)
	SB-SCS-04	November 2011	Shutdown Cooling System (SCS) line break SBLOCA and RCP suction (repetition)
	SB-PSV-02	October 2011	Pressurizer safety valve (PSV) line break SBLOCA and pressurizer top (repetition)

TABLE 3: Comparison of the major parameters under a steady state condition.

Parameter	SMART design value		MARS results for VISTA-ITL			
	SMART	VISTA-Ideal	SMART	VISTA-Actual	VISTA-Ideal	VISTA-Ideal HS
	Primary side					
Power [MWt]	330	0.419	330.0	0.419	0.419	0.419
PZR pressure [MPa]	15.0	15.0	15.0	15.0	15.0	15.0
1st flow rate [kg/s]	2090	2.66	2079.2	2.66	2.66	2.66
SG 1st inlet temp. [°C]	323	323	323	323	323	323
SG 1st outlet temp. [°C]	295.7	295.7	295	296	296	296
	Secondary side					
SG 2nd inlet press. [MPa]	6.0	6.0	6.0	6.0	6.0	6.0
SG 2nd outlet press. [MPa]	5.2	5.2	5.2	5.2	5.2	5.2
Feed water flow rate [kg/s]	160.8	0.204	160.8	0.201	0.204	0.204
Feed water temp. [°C]	200.0	200.0	200.0	200.0	200.0	200.0
Steam temp. [°C]	298.0	298.0	291.0	307.2	298.7	298.7

broken safety injection line was assumed to be one of the available safety lines, and only one of the four safety injections is active for the transient calculation based on a single failure assumption. The safety injection flow rate of the VISTA-ITL is scaled down by applying the appropriate scaling ratios to the SMART design. The break area was set to be reduced according to the scale ratio of the flow rate since the break flow would be choked during the SBLOCA simulation.

Table 4 shows the major sequence of events observed during the present analysis. The thermal-hydraulic behavior occurs 1.664 times faster in the VISTA-ITL than in the SMART design, as shown in Table 1. Based on the simulation results for the SMART design, the major sequence of events can be explained as follows. When one of four safety injection

lines was broken, the RCS began to be depressurized. As the pressurizer pressure reached the low pressurizer pressure (LPP) trip set point ( $P_{LPP}$ ) 285.5 s after the break, the reactor tripped with the reactor trip signal, which was generated 1.1 s after the LPP signal. Concurrently with the reactor trip signal, the injection of the feed water stopped and the main steam isolation valves were closed. A PRHRS actuating signal was generated at 287.7 s after the break. The PRHRS isolation valves were opened 292.7 s after the break with a 5 s delay. The main steam isolation valves were closed 15 s after the PRHRS actuation signal, which corresponds to 302.7 s after the break. With the operation of PRHRS, a two-phase natural circulation occurred inside the PRHRS. The decay heat generated from the reactor core was transferred through

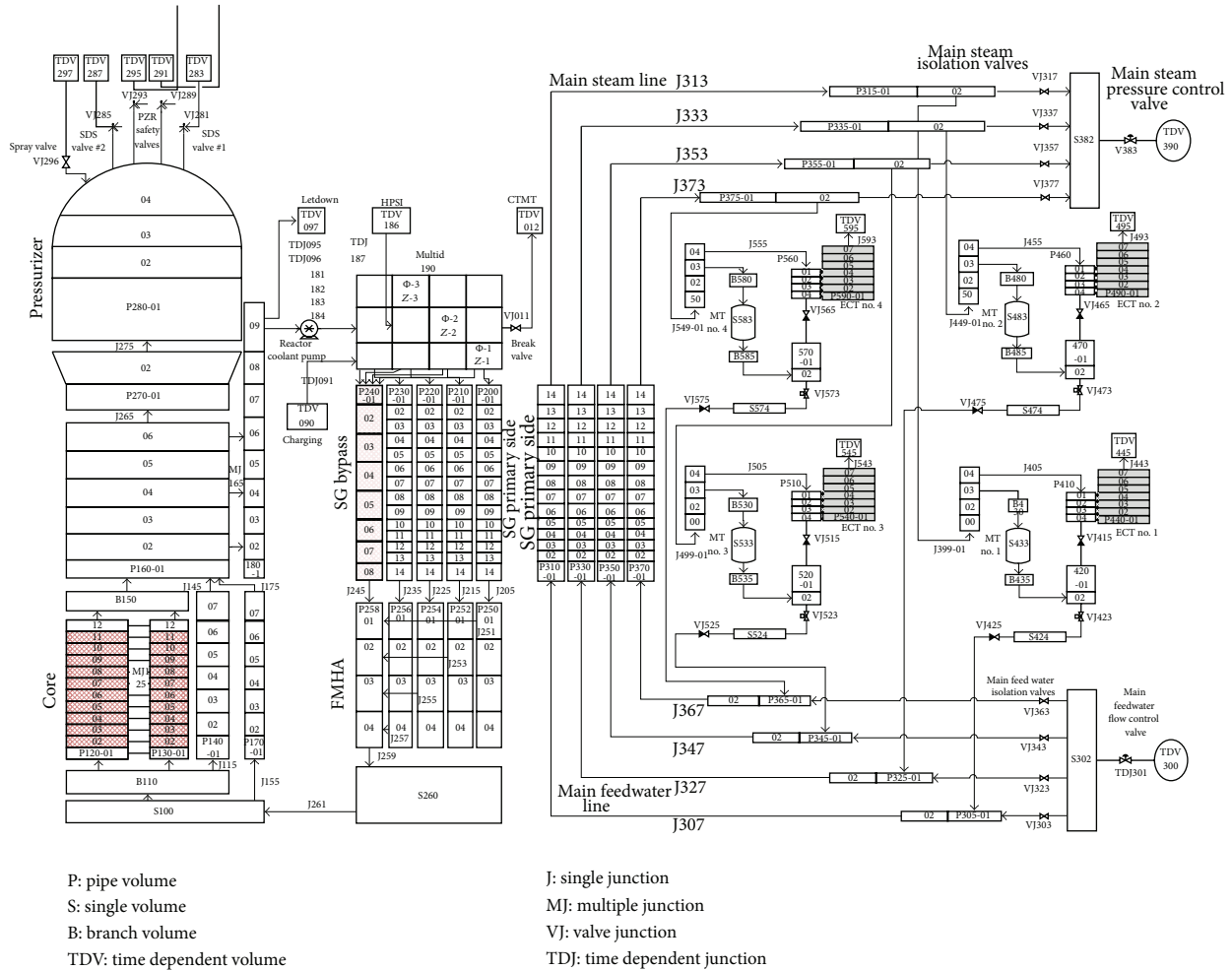


FIGURE 6: MARS nodalization for the SMART design.

the SG and was eventually removed by the PRHRS heat exchanger located in a water-filled ECT. After that, the safety injection actuation signal (SIAS) was generated 489.2 s after the break, and the safety injection water was injected 30 s after the SIAS.

When the calculation results of the SMART design are compared with those of the VISTA ITL, the SMART calculation time should be divided by 1.664 for a comparison. For all three calculations of VISTA-ITL, the sequence progressed very similarly compared with that of the SMART design during the initial sequence of events, as shown in Table 4.

Figure 8 show comparison results of the pressurizer pressure during the safety injection line break accidents, which is a typical SBLOCA scenario. The same core power curve was applied in all four calculations, and the safety injection water was supplied according to the order of the pressure reduction. Compared with the SMART design calculation, the pressures of all three VISTA-ITL calculations were reduced faster at an earlier period, and their behavior was very similar in the three calculations. About 450 s (based on the VISTA-ITL time scale) after the break, the calculated pressure of VISTA-ITL-Actual design decreased more slowly than the SMART

design calculation. This is because the VISTA ITL facility has a relatively large heat structure compared to the SMART design. When the heat structure was scaled down ideally in the VISTA ITL-Ideal HS, the calculation results showed a very good agreement with those calculations in the VISTA ITL-Ideal. The safety injection signal was actuated when the RPV pressure became lower than the safety injection set point of  $P_{SIAS}$ . As shown in Table 4, the pressure reduction of the reactor vessel was the fastest (287.0 s after the break) during the VISTA ITL-Actual calculation, followed by VISTA ITL-ideal HS calculation (313.2 s after the break), VISTA ITL-Ideal calculation (317.5 s after the break), and the SMART design calculation (398.8 s after the break). The pressure tendency of the reactor pressure vessel was similar to the pressure changes of the pressurizer. In addition, it should be noted that the safety injection flow rates of the VISTA ITL-Actual design calculation was less than that in the other calculations owing to higher system pressures during the latter period.

From the present similarity analysis, the thermal-hydraulic similarity between the SMART design and the VISTA-ITL facility was ascertained. In addition, the similarity analysis calculations provided a good insight into the unique features

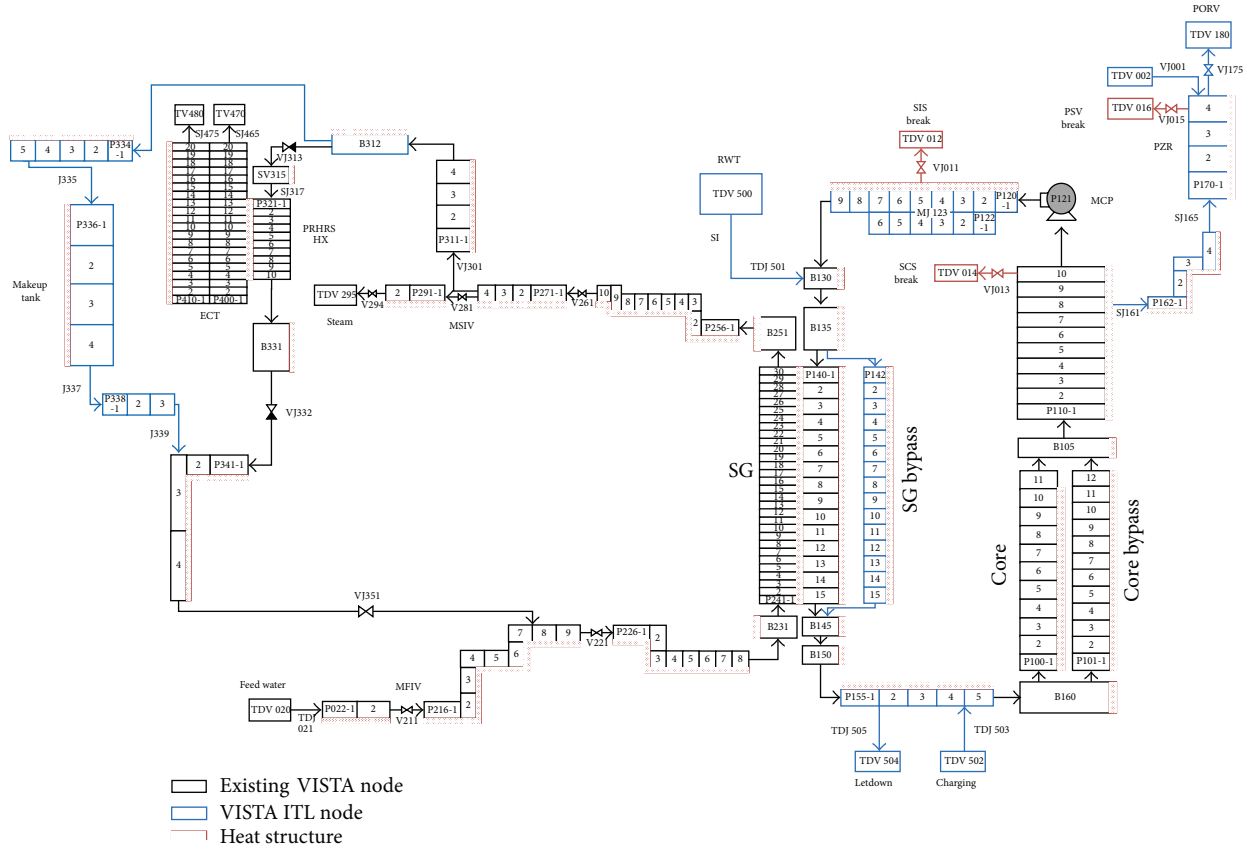


FIGURE 7: MARS nodalization for the VISTA-ITL facility.

TABLE 4: Major sequence of events for SBLOCA.

Event	Set points/time delay		Time (seconds)			
	SMART	VISTA ITL-Ideal	SMART (VISTA-equivalent)	VISTA-Actual	VISTA-Ideal	VISTA-Ideal HS
Break	—	—	0	0	0	0
Reach LPP set point	PZR pres. = $P_{LPP}$	PZR pres. = $P_{LPP}$	285.5 (171.6)	129.0	142.1	140.2
LPP reactor trip signal						
(i) FW Stop	1.1 s delay	0.66 s delay	286.6 (172.3)	129.7	142.7	140.9
(ii) Pump coast down						
Reactor trip-curve start	1.6 s after LPP	0.96 s after LPP	287.1 (172.6)	130.0	143.0	141.2
PRHR actuation signal (PRHRSAS)	2.2 s after LPP	1.32 s after LPP	287.7 (172.9)	130.3	143.4	141.5
PRHRS IV open	5 s delay	3 s delay	292.7 (175.9)	133.3	146.4	144.5
MSIV/FIV close	15 s delay	9.01 s delay	302.7 (181.9)	139.0	152.4	150.6
Safety injection signal (SIAS)	BPV pres. = $P_{SIAS}$	BPV pres. = $P_{SIAS}$	663.6 (398.8)	287.0	317.5	313.2
Safety injection start	30 s delay	18.03 s delay	693.6 (416.8)	305.0	335.5	331.2
Test end	—	—	7000 (4206.7)	4300	4300	4300

TABLE 5: Comparison of the major parameters under a steady-state condition.

Parameter	SMART (design value)	VISTA-ITL (ideal value)	VISTA-ITL (test data)	VISTA-ITL (MARS)
Power [MWt]	330.0	0.432	0.4504	0.4504
PZR pres. [MPa]	15.0	15.0	14.98	14.98
1st flow rate [kg/s]	2090.0	2.65	2.613	2.6216
SG 1st inlet $T$ . [K]	596.15	596.15	596.75	598.96
SG 1st outlet $T$ . [K]	568.85	568.85	568.85	571.62
FW flow rate [kg/s]	160.8	0.204	0.152	0.153
FW temp. [K]	473.15	473.15	326.45	325.15
SG 2nd inlet $P$ [MPa]	6.0	6.0	5.95	5.98
SG 2nd outlet $P$ [MPa]	5.2	5.2	5.19	5.22

of the VISTA-ITL and the thermal-hydraulic characteristics of the SMART design.

**4.3. Posttest Simulation of a SBLOCA Test Using VISTA-ITL.** A posttest simulation on a SBLOCA test for the shutdown cooling system line break (SB-SCS-04) has been performed with the MARS-KS code to assess its simulation capability for the SBLOCA scenario of the SMART design.

**4.3.1. A Typical SBLOCA Test (SB-SCS-04).** As a shutdown cooling system (SCS) line is broken in the SMART design, the primary system pressure decreases with the discharge of the coolant through the break. When the primary pressure reaches the low pressurizer pressure (LPP) set point, the reactor trip signal is generated with a 1.1 s (in VISTA-ITL: 0.66 s) delay. As the turbine trip and loss of off-site power (LOOP) are assumed to occur consequently after the reactor trip, the LOOP occurs, the feed water is not supplied, and the RCP begins to coast down. With an additional 0.5 s (in VISTA-ITL: 0.3 s) delay, the control rod is inserted. When the PRHRS actuation signal is generated by the low feed water flow rate 2.2 s (in VISTA-ITL: 1.32 s) after the LPP, the SG is isolated from the turbine by the isolation of the main steam and feed water isolation valves and is connected to the PRHRS. The safety injection actuation signal was generated when the RCS pressure reaches below the safety injection actuation signal, and the SI water is injected with a time delay of 30 s (in VISTA-ITL: 18.03 s). The break nozzle diameter is 50 mm in the SMART design and the scaled-down value is 1.77 mm in the VISTA-ITL. The set points of LPP and SIAS were 12.3 and 10.0 MPa, respectively.

**4.3.2. Steady-State Calculation Results.** Table 5 shows a comparison of the major parameters of the SMART design, the ideal value, test data, and MARS-KS calculation results of VISTA-ITL at 103% rated power condition. The simulation results show that most of the thermal-hydraulic parameters agree well with one another. The heat loss of about 19 kW was estimated and added during the test. The feed water flow rate is lower during the test than the ideal value owing to the low injected feed water temperature to match the heat balance.

**4.3.3. Transient Calculation Results.** Table 6 shows the major sequence of events for the SB-SCS-04 test, and Figure 9

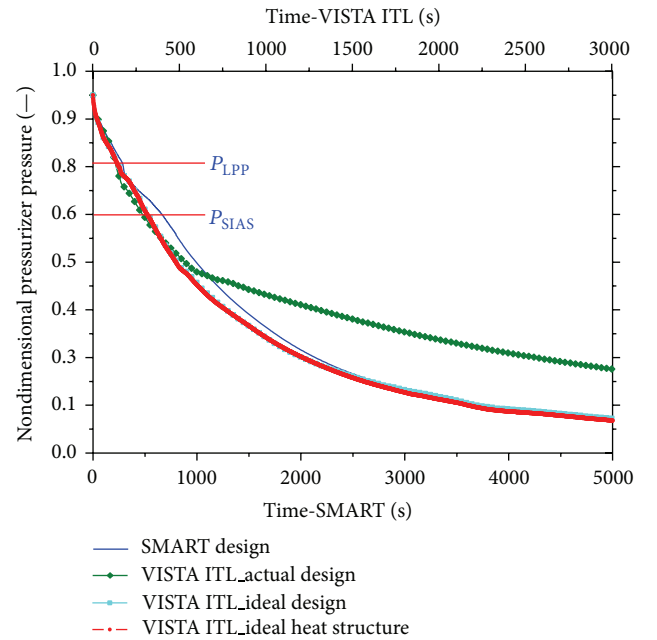


FIGURE 8: Comparison of calculated pressurizer pressures during the pretest simulation.

through Figure 15 show the variations of the major parameters of the core power, pressurizer pressure, and flow rates of the reactor coolant system (RCS) and break. The decay power curve and safety injection flow rate are successfully given for both the test and the simulation.

The core power was well simulated as a boundary condition during the MARS-KS calculation, as shown in Figure 9. The primary pressure decreased rapidly during the single-phase blow-down period, as shown in Figure 10. As the depressurization is faster in the MARS-KS simulation, the LPP-related events occur about 15 s earlier than in the test. The overall trend of the primary pressure behavior is well simulated during the initial period and the plateau region. However, the decreasing rate becomes higher after the plateau. After a certain interval of abrupt pressure drop, the decreasing rate slows down and becomes higher at the later period after 938 s. As the pressure decreased rapidly during the initial period before the safety injection signal, the safety injection signal was generated about 102.2 s earlier in

TABLE 6: Major sequence of events for SBLOCA.

Event	Time	Time	Time (s)	Time (s)
	SMART design	VISTA-ITL	Measured VISTA-ITL	Calculated VISTA-ITL
Break occurrence	0.0	0.0	0.0	0.0
LPP set point	LPP	LPP	131	116.1
LPP reactor trip signal	LPP + 1.1 s	LPP + 0.66 s	132	118.1
Reactor trip signal—urve start	LPP + 1.6 s	LPP + 0.96 s	132	118.4
PRHRS actuation signal	LPP + 2.2 s	LPP + 1.32 s	133	118.8
PRHRS IV full open	PRHRSAS + 5.0 s	PRHRSAS + 3 s	136	121.1
SI signal	SIAS	SIAS	475	372.8
SI start	SIAS + 30 s	SIAS + 18 s	502	395.8

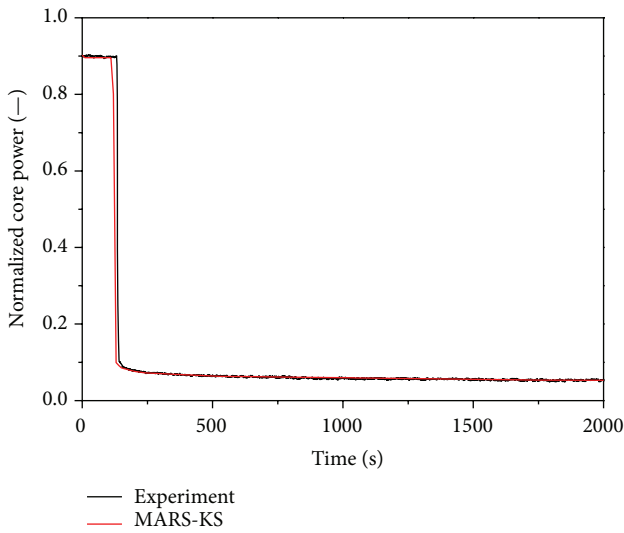


FIGURE 9: Comparison of calculation results with the test data: core power.

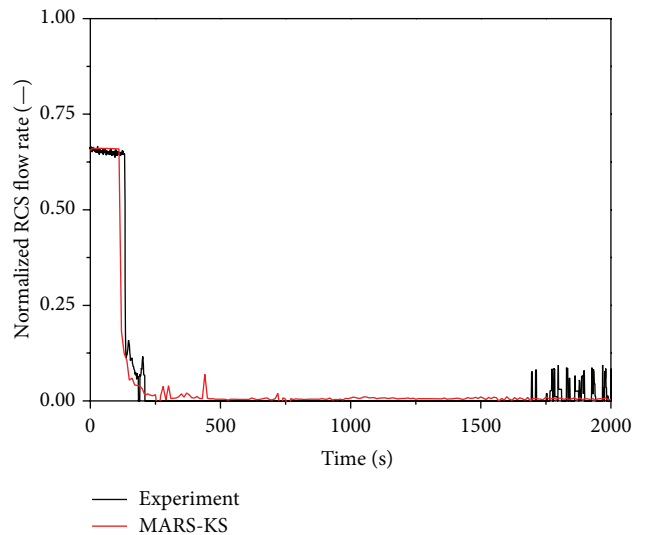


FIGURE 11: Comparison of calculation results with the test data: RCS flow rate.

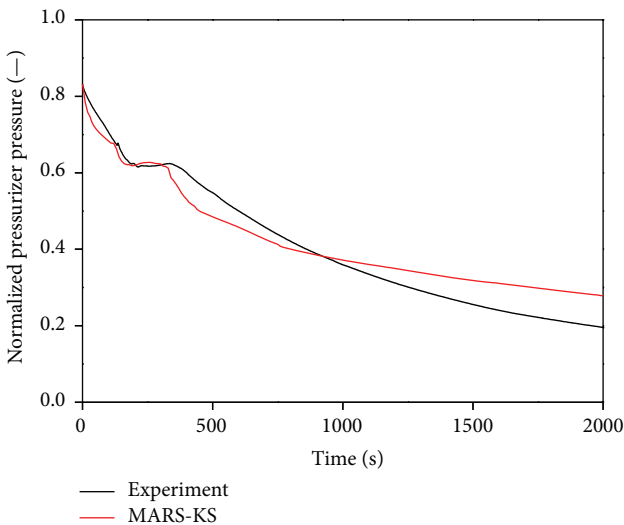


FIGURE 10: Comparison of calculation results with the test data: pressurizer pressure.

the simulation than that in the experiment. The slow pressure decrease during the later period seems to be due to the high amount of heat structure in the small-scale integral effect test facility of VISTA-ITL.

The simulated RCS flow rate was in good agreement with the test data during the considered period of about 2,000 s, as shown in Figure 11. In the present simulation, a discharge coefficient of 0.6 was used to match the initial break flow rate of the SB-SCS-04 test. A typical trend of the break flow rate consists of three periods: single-phase water, two-phase mixture, and single-phase steam. As shown in Figure 12, the plateau region in the simulation seemed to be similar to that in the test. Figure 13 shows a comparison of the calculation results with the test data of the RPV level. In the earlier region, the RPV level decreases faster in the simulation than in the test. It is considered that a small amount of pressurizer inventory is held up in the pressurizer bottom and surge line.

As shown in Figure 14, the primary temperatures measured in the inlet and outlet of the steam generator decreased steadily for the whole simulation time because the decay heat

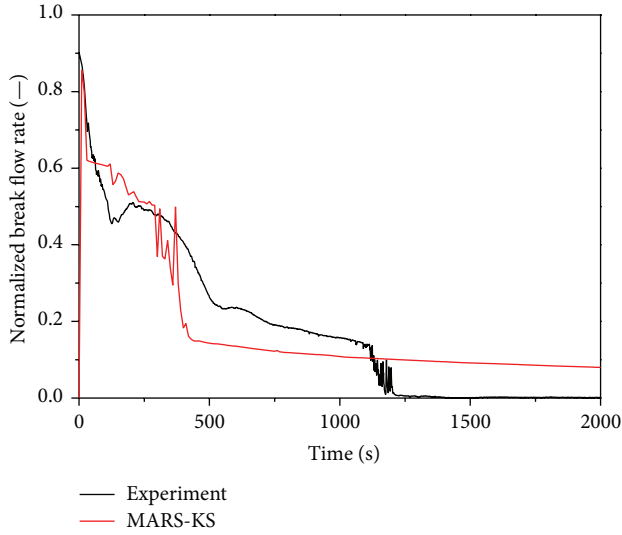


FIGURE 12: Comparison of calculation results with the test data: break flow rate.

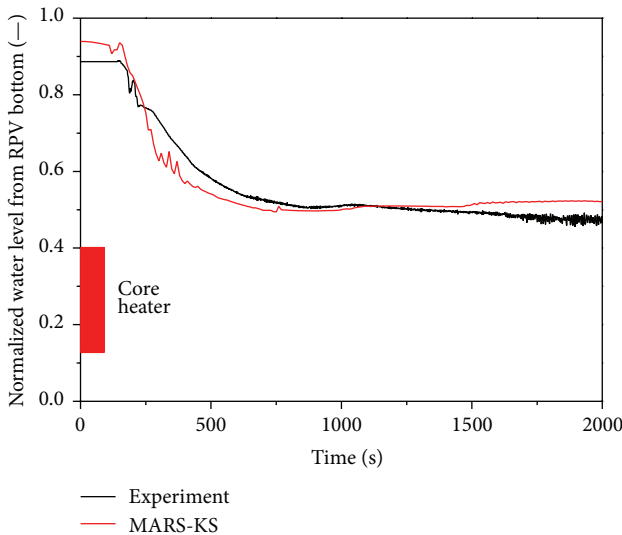


FIGURE 13: Comparison of calculation results with the test data: RPV level.

of the primary side could be removed by the PRHRS. This means that the PRHRS was operated well during both the test and the simulation. The trends of the simulated primary temperatures were in good agreement with the test data during the initial period but they become different during the later period. In the MARS-KS code, a slow natural circulation flow is formed in the primary system, but in the test both regions of the heater (source) and steam generator (sink) became separated. Figure 15 shows the typical secondary flow rate behaviors. The initial flow rate decreases as the PRHRS is operated. The MARS-KS code overestimates the experimental data during the initial period, but it matches well with the experimental data 500 seconds after the test start.

In the present simulation, the similarity between the VISTA-ITL data and its simulation results was good for the

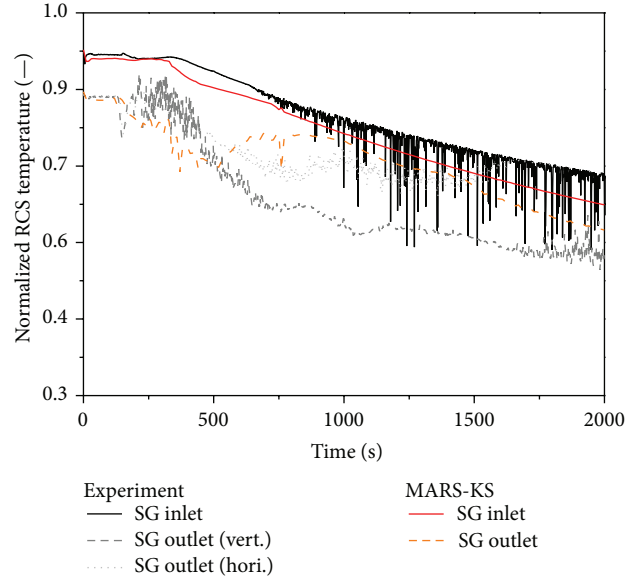


FIGURE 14: Comparison of the calculation results with the test data: primary temperature.

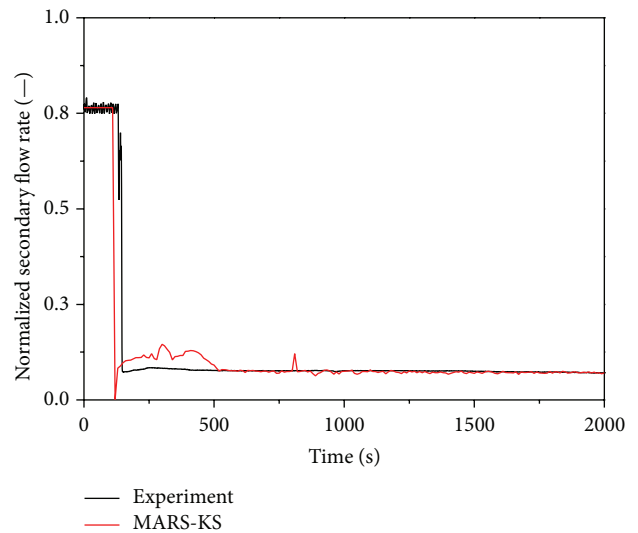


FIGURE 15: Comparison of calculation results with the test data: secondary flow rate.

major thermal-hydraulic parameters, as described in Figures 9–15.

### 5. Summary and Conclusions

A thermal-hydraulic integral effect test facility, VISTA-ITL, was introduced for the SMART design with a discussion of its scientific design characteristics; the similarity between the SMART design and the VISTA-ITL facility was analyzed using the MARS-KS code; and the VISTA-ITL test program was briefly introduced. The VISTA-ITL is a small-scale integral effect test facility and has the following characteristics: 1/2.77-height, 1/1310-volume, and full pressure

and temperature simulation of SMART. Several tests on the SBLOCA, CLOF, and PRHRS performance were conducted using the VISTA-ITL facility in support of the SMART design verification. The VISTA-ITL program contributed to the SMART design licensing by providing proper test data for validating the system analysis code.

A typical SBLOCA scenario of the safety injection line break accident was analyzed using the MARS-KS code to ascertain the thermal-hydraulic similarity between the SMART design and the VISTA-ITL facility, and the similarity analysis results provided good insight into the unique design features of the VISTA-ITL and the thermal-hydraulic characteristics of the SMART design. In addition, a SBLOCA test for the shutdown cooling system line break was performed, and the test was simulated with the MARS-KS code, to assess its simulation capability for the SBLOCA scenario of the SMART design. The SBLOCA scenario in the SMART design was well reproduced using the VISTA-ITL facility, and the measured thermal-hydraulic data were properly simulated with the MARS-KS code. The present SBLOCA test and analysis results can provide a comprehensive understanding on the thermal-hydraulic characteristics of the SBLOCA behavior of the SMART design.

The VISTA-ITL facility could be used for further understanding of the full-power thermal-hydraulic behaviors for the SMART design together with the FESTA facility [12], which is a full-height integral effect test facility having the capability of simulating the multidimensional and multitrain effects for the SMART design.

## Nomenclature

ATLAS:	Advanced thermal-hydraulic test loop for accident simulation (facility)
BMS:	Break measuring system
BSS:	Break simulation system
FWST:	Feed water supply tank
IET:	Integral effect test
ITL:	Integral test loop
KAERI:	Korea Atomic Energy Research Institute
LPP:	Low pressure pressurizer
MARS-KS:	A best-estimate, multidimensional, thermal-hydraulics system code
MCP:	Main coolant pump
MV:	Measuring vessel
PRHRS:	Passive residual heat removal system
PSV:	Pressurizer safety valve
RCS:	Reactor coolant system
RPV:	Reactor pressure vessel
RWT:	Refueling water tank
SBLOCA:	Small-break loss of coolant accident
SCS:	Shutdown cooling system
SIP:	Safety injection pump
SIS:	Safety injection system
SMART:	System-integrated modular advanced reactor (plant)
SMART-P:	SMART-Pilot (plant)
SV:	Separating vessel

TASS/SMR-S:	Transient and set point simulation/small and medium reactor (computer code)
VISTA:	Experimental verification by integral simulation of transients and accidents (facility)
VISTA-ITL:	VISTA integral test loop (facility).

## Conflict of Interests

The authors declare that there is no conflict of interests regarding the publication of this paper.

## Acknowledgments

This work was supported by the National Research Foundation of Korea (NRF) Grant funded by the Korea government (MSIP) (no. 2013M2B9A1020039). Also the authors would like to thank Dr. Y. J. Chung, Dr. W. J. Lee (KAERI), Mr. D. H. Kang, and Dr. J. S. Suh (SEnTech, Co.) for their support and discussion during the pretest analysis by using the MARS-KS code.

## References

- [1] S. J. Yi, H. S. Park, K. Y. Choi et al., "Basic design of the high temperature/high pressure thermal-hydraulic test facility," KAERI Internal Report, KAERI, 2001.
- [2] K. K. Kim, W. Lee, S. Choi et al., "SMART: the first licensed advanced integral reactor," *Journal of Energy and Power Engineering*, vol. 8, pp. 94–102, 2014.
- [3] Y. J. Chung, K.S. Hyoung, K. S. Darl et al., "TASS/SMR code topical report for SMART plant, Vol. I: code structure, system models, and solution methods," KAERI/TR-3640/2008, 2008.
- [4] B. D. Chung, S. W. Bae, J. J. Jeong et al., "Development and assessment of multi-dimensional flow models in the thermal-hydraulic system analysis code MARS," KAERI/TR-3011/2005, 2005.
- [5] Y.-G. Lee, I.-W. Park, and G.-C. Park, "SBLOCA and LOFW experiments in a scaled-down IET facility of rex-10 reactor," *Nuclear Engineering and Technology*, vol. 45, no. 3, pp. 347–360, 2013.
- [6] Y.-G. Lee and G.-C. Park, "TAPINS: a thermal-hydraulic system code for transient analysis of a fully-passive integral PWR," *Nuclear Engineering and Technology*, vol. 45, no. 4, pp. 439–458, 2013.
- [7] S. J. Yi, H. S. Park, T. S. Kwon et al., "Major results of thermal-hydraulic validation tests for the SMART design licensing," in *Proceedings of the 15th International Topical Meeting on Nuclear Reactor Thermal Hydraulics (NURETH '13)*, Pisa, Italy, May 2013.
- [8] K. Y. Choi, H. S. Park, H.S. Cho et al., "Parametric studies on thermal hydraulic characteristics for transient operations of an integral type reactor," *Nuclear Engineering and Technology*, vol. 38, no. 2, pp. 185–194, 2006.
- [9] H.-S. Park, K.-Y. Choi, S. Cho, S.-J. Yi, C.-K. Park, and M.-K. Chung, "Experiments on the performance sensitivity of the passive residual heat removal system of an advanced integral type reactor," *Nuclear Engineering and Technology*, vol. 41, no. 1, pp. 53–62, 2009.

- [10] W.-P. Baek, C.-H. Song, B.-J. Yun, T.-S. Kwon, S.-K. Moon, and S.-J. Lee, "Kaeri integral effect test program and the ATLAS design," *Nuclear Technology*, vol. 152, no. 2, pp. 183–195, 2005.
- [11] M. Ishii and I. Kataoka, "Similarity analysis and scaling criteria for LWRs under single-phase and two-phase natural circulation," NUREG/CR-3267, ANL-83-32, 1983.
- [12] H. S. Park, S. J. Yi, C. H. Song et al., "SMR accident simulation in experimental test loop," *Nuclear Engineering International*, pp. 12–15, 2013.

## Research Article

# Experimental Research on Passive Residual Heat Removal System of Chinese Advanced PWR

Zhuo Wenbin, Huang Yanping, Xiao Zejun, Peng Chuanxin, and Lu Sansan

*CNNC Key Laboratory on Nuclear Reactor Thermal Hydraulics Technology, Nuclear Power Institute of China, Chengdu 610041, China*

Correspondence should be addressed to Zhuo Wenbin; [npic011371@163.com](mailto:npic011371@163.com)

Received 6 December 2013; Accepted 24 February 2014; Published 5 June 2014

Academic Editor: Shengqiang Li

Copyright © 2014 Zhuo Wenbin et al. This is an open access article distributed under the Creative Commons Attribution License, which permits unrestricted use, distribution, and reproduction in any medium, provided the original work is properly cited.

Passive residual heat removal system (PRHRS) for the secondary loop is one of the important features for Chinese advanced pressurized water reactor (CAPWR). To prove the safety characteristics of CAPWR, series of experiments have been done on special designed PRHRS test facility in the former stage. The test facility was built up following the scaling laws to preserve the similarity to CAPWR. A total of more than 300 tests have been performed on the test facility, including 90% steady state cases and 10% transient cases. A semiempirical model was generated for passive heat removal functions based on the experimental results of steady state cases. The dynamic capability characteristics and reliability of passive safety system for CAPWR were evidently proved by transient cases. A new simulation code, MISAP2.0, has been developed and calibrated by experimental results. It will be applied in future design evaluation and optimization works.

## 1. Introduction

The passive safety feature is one important essential requirement for both integral type reactors and large scale multiloop type reactors. The steam generators (SGs) have been considered as passive safety cooling devices to provide primary loop decay heat removal capacity. There is no additional power supply needed for SGs cooling features. It is specially fit for nonloss of coolant accident applications. The steam released from SGs will be condensed in an accessory heat exchanger, which is located in a tank and submerged in low temperature coolant. To enhance the passive safety function and provide a redundant heat removal path, the secondary side passive cooling system will be necessary for advanced reactors.

In order to improve the security and reliability of reactor, some evolutionary and innovative reactors, such as AP600/1000, WWER640/407, APR+, SBWR, and SMART, employ passive residual heat removal systems [1]. But most of these systems are primary passive cooling systems, except for WWER640/407 and APR+. The passive heat removal system for the WWER640/407 reactor is located at the secondary side of SG. In case of non-LOCAs the decay heat is removed by coolant natural circulation to steam generator boiler water. The steam generated comes into the passive heat removal

system where steam is condensed on the internal surface of the tubes that are cooled on the outside surface by the water stored in the demineralized water tank outside the containment. The water inventory in this tank is sufficient for the long-term heat removal (at least 24 hours) and can be replenished if necessary from an external source [2].

The APR+ is a Generation III+ nuclear power plant being developed in Korea. The passive auxiliary feedwater system (SG secondary side passive residual heat removal system) is one of the advanced safety features being adopted in the APR+. It cools down the secondary side of the steam generator and eventually removes the decay heat from the reactor core by adopting a natural circulation mechanism, that is, condensing steam in the nearly horizontal passive condensation heat exchanger tubes submerged inside the passive condensation cooling tank [3].

The SG secondary side passive residual heat removal system (PRHRS), which removes the residual heat when station blackout occurs, is considered in Chinese advanced PWR. The passive residual heat removal system eliminates a great deal of water in the condensation tank, which is cooled by air natural circulation in the chimney. Only a small quantity of water in the emergency feedwater tank is needed for absorption of residual heat at the initial period of accident.

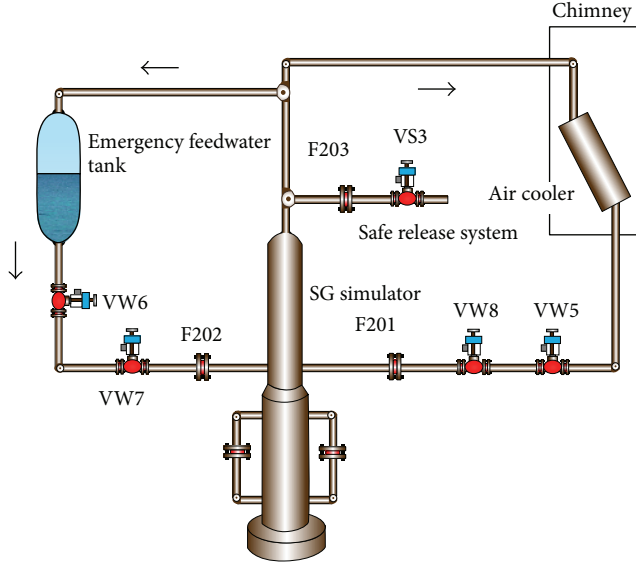


FIGURE 1: Schematic diagram of PRHRS test facility.

In order to assess the ability of PRHRS, experimental research had been done at advanced PWR PRHRS test facility in Nuclear Power Institute of China; in the meantime, the computer code MISAP2.0 has been developed and verified.

## 2. Test Facility

The test facility has been built according to two-phase natural circulation scaling methodology laws. The geometrical similarity, friction number, density ratio, Froude number, phase change number, and drift-flux number are the important similarity groups. And it is composed of steam-water circulation loop, emergency feedwater loop, air natural circulation loop, and safe release system. The main components include steam generator, air cooler, emergency feedwater tank (EFWT), and chimney. It has a geometrical scaling ratio of 1/390 in volume, and the total height from the top of the height-adjustable chimney to the bottom of SG is about 23 m. The maximal pressure of facility is 8.6 MPa, and the core decay heat is simulated by electric heaters with a capacity of 400 kW (DC). Figure 1 shows its schematic diagram.

The work principle of test facility is as follows. When station blackout or other accidents occur, the isolation valves located at the outlet pipe of emergency tank are opened by a low-low water signal for the SG, so that the emergency water tank provides water to the secondary side of SG driven by gravity and maintains the water level. The water in the SG absorbs the residual heat when the water evaporates. The steam rises and passes through the air cooler where the steam is condensed into water; simultaneously, the heat is transferred into the air through the air natural circulation composed of chimney and atmosphere. Then, the condensed water returns to the SG loop driven by gravity; thereby, a continuous natural circulation flow is established.

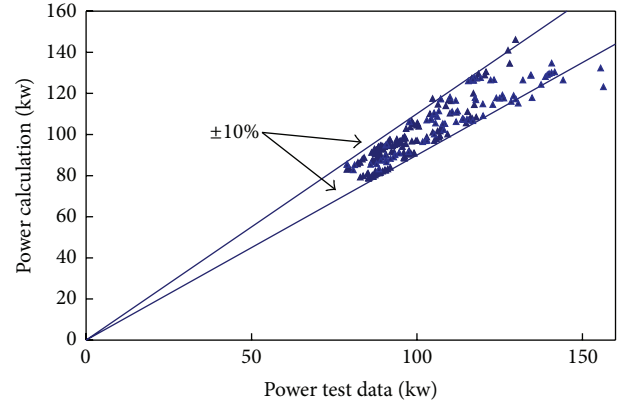


FIGURE 2: Power comparison between test and calculation.

## 3. Test Matrix and Startup Modes

A total of 280 sets of experimental data at steady state have been obtained and the main influence factors on heat removal capability were identified. The main operation parameters are the height of chimney, the hydraulic resistance, and the initial pressure.

More than 30 transient tests had been performed while the residual heat drops from 8% full power to 2% full power (Figure 2). In addition the influence factors on flow instability were identified.

## 4. Test Results and Analysis

**4.1. Steady Test.** The natural circulation is influenced by many parameters, such as the height of chimney, the hydraulic resistance, and the initial pressure. Several tests are implemented to investigate the effect of these parameters on the passive residual heat removal system. In addition a semiempirical model was generated for predicting the natural circulation behavior of Chinese advance pressurized water reactor.

The equation of momentum for passive residual heat removal loop is

$$(\rho_w L_w - \rho_s L_s - \rho_{sg} L_{sg}) g = \frac{k_w w^2}{2\rho_w A_w^2} + \frac{k_s w^2}{2\rho_s A_s^2}, \quad (1)$$

where the subscripts  $w$ ,  $s$ , and  $sg$  are water in the down pipe, steam in the rise pipe, and SG respectively.

Equation of momentum for air loop is

$$(\rho_y - \rho_{yi}) g L_y = \frac{k_y w_a^2}{2\rho_y A_y^2}, \quad (2)$$

where the subscripts  $y$  and  $yi$  are outlet and inlet of chimney, respectively.

The air cooler heat transfer equation is

$$Q = KF\Delta T_m. \quad (3)$$

In steam side of the cooler,

$$Q = W(H_s - H_w). \quad (4)$$

TABLE 1: Effect of the height of chimney.

Number	Height of chimney (m)	Test			Calculation		
		Natural circulation flow rate (kg/h)	Temp. of condensate (°C)	Power (kW)	Natural circulation flow rate (kg/h)	Temp. of condensate (°C)	Power (kW)
1	9.7	204.4	280.2	86.7	210.3	277.09	90.8
2	14.1	226.4	279.6	96.5	236.7	278.66	101.7
3	14.8	230.9	280.9	97.2	235.6	273.87	102.8
4	21.1	238.5	263.1	107.4	249.5	256.16	115.1
5	27.1	249.0	243.7	119.1	259.3	237.96	125.8

The height between air cooler and SG is 14.5 m, the hydraulic resistance is 105, the water in SG is 5.1 m, the pressure is 6.4 MPa, and the temperature at the inlet is 20°C.

TABLE 2: Effect of the hydraulic resistance.

Number	Hydraulic resistance (m)	Test		Calculation	
		Natural circulation flow rate (kg/h)	Power (kW)	Natural circulation flow rate (kg/h)	Power (kW)
1	86	215.6	89.4	227	92.7
2	122	211.0	88.5	221	91.9
3	153	210.1	88.2	220	92.7
4	157	209.4	87.9	219	92.5
5	171	206.7	87.6	217	91.7

The height between air cooler and SG is 14.5 m, the height of chimney is 10.5, the water in SG is 5.1 m, the pressure is 6.4 MPa, and the temperature at the inlet is 20°C.

In air side of the cooler,

$$Q = W_a (H_y - H_{yi}), \quad (5)$$

where  $K$  is heat transfer coefficient,  $F$  is heat transfer area,  $\Delta T_m$  is mean temperature difference, and  $W_a$  is the air flow rate.

Coupling with (1)–(5), a semiempirical correlation has been built up for total PRHR system heat transfer estimation based on the test results. In this case, when system pressure, water level in SG, friction coefficient, and the height between SG and air cooler are given, the ability of heat removal can be calculated. Consider

$$Q = 268 \times \frac{(0.98 - Lth/30)^{-0.05} \times (0.8 \ln H + 1.2)}{(7.06 - 1.23 \ln P) e^{(0.05/100)K} \times t_{in}^{0.2}}. \quad (6)$$

Sensitivity studies on different structure parameters have been made. The results will be described in detail as follows.

**4.1.1. Effect of the Height of Chimney.** The effect of the height of chimney in the passive residual heat removal system has been identified at the initial height of chimney of 9.7 m and 27.1 m. In this group of sensitive studies, the hydraulic resistance hardly keeps the same value under different condition, which is maintained at less than 10%. And the temperature of air at the inlet of chimney and pressure are unchanged values with only the height being allowed to change to find the effect.

Table 1 shows the experimental data and calculation of the natural circulation flow rate, power, and temperature of condensate, respectively. As the height of chimney increases, the natural circulation flow rate of air loop and power of air cooler rise. Then, the temperature of condensate decreases.

When the height between air cooler and SG and hydraulic resistance is constant, the reduced density of condensate causes the increase of natural circulation flow rate. In addition the calculation shows good agreement with experimental data.

**4.1.2. Effect of the Hydraulic Resistance.** The effects of the hydraulic resistance (frictional resistance and local resistance) in the passive residual heat removal system are performed in this study (Table 2). Other parameters are kept at a constant value. The hydraulic resistance is varied from 86 to 171. We can see that the resistance increases more than 100%, but the natural circulation flow rate and power decrease rarely. Therefore, the hydraulic resistance has little influence on the passive residual heat removal system.

**4.1.3. Effect of the Initial Pressure on the Passive Residual Heat Removal System.** The initial pressure in the passive residual heat removal system changes from 3.53 MPa to 7.30 MPa, and other parameters are fixed except for the hydraulic resistance with a 10 percent deviation. As the pressure ascends, the increase of power and natural circulation flow rate is 22.3% and 25%, respectively (Table 3).

**4.2. Transient Test.** When the station blackout accident happens in the Chinese advance pressurized water reactor, it adopts the passive residual heat removal system to mitigate consequences of accidents. The passive residual heat removal system startup modes include warm and cold patterns when the emergency feedwater is on or off, respectively. If there is a tiny flow rate to keep a little natural circulation in both steam-water circulation loop and air natural circulation loop

TABLE 3: Effect of the initial pressure.

Number	Pressure (MPa)	Test		Calculation	
		Natural circulation flow rate (kg/h)	Power (kW)	Natural circulation flow rate (kg/h)	Power (kW)
1	3.53	151.0	76.1	153.2	74.7
2	4.51	160.2	80.8	161.6	80.2
3	6.82	170.3	88.0	163.0	86.2
4	7.80	188.3	93.6	176.7	89.5

The height between air cooler and SG is 14.5 m, the height of chimney is 12.8, the water in SG is 5.1 m, the hydraulic resistance is 105, and the temperature at the inlet is 33°C.

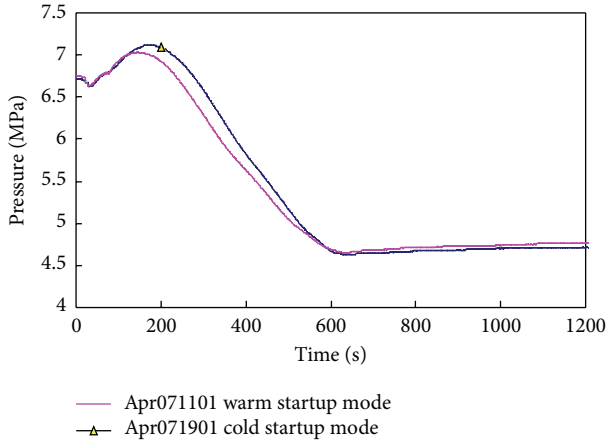


FIGURE 3: The pressure of cold and warm startup mode.

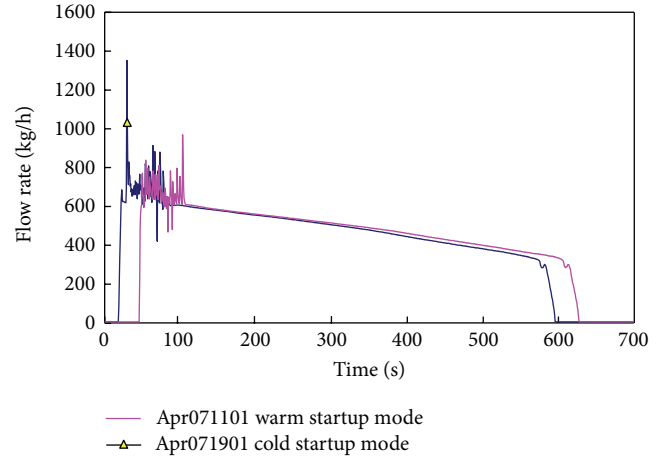


FIGURE 5: The feedwater flow rate.

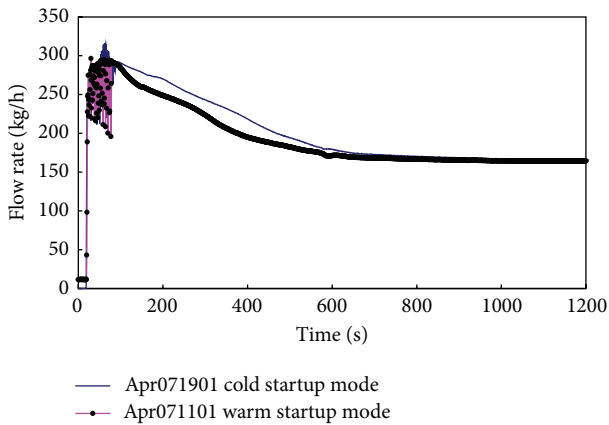


FIGURE 4: The natural circulation flow rate.

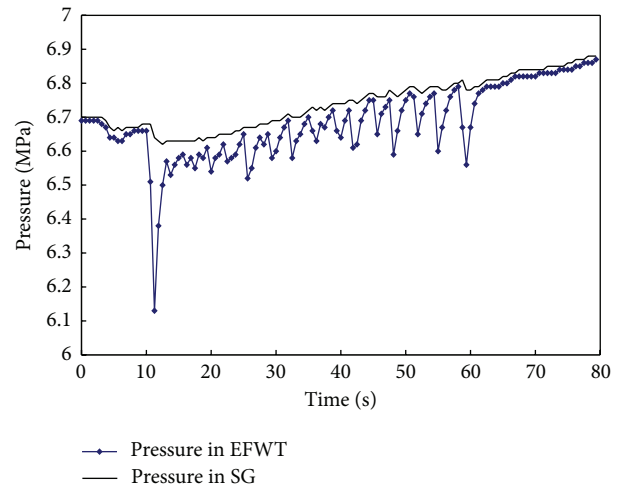


FIGURE 6: The pressure fluctuation when water hammer occurs.

before the startup of transient test, this type of startup mode is defined as warm startup. On the other hand, if the initial condition is cold, or there is no flow in both steam-water circulation loop and air natural circulation loop, this type of startup mode is defined as cold startup.

The typical results of cold and warm startup tests with emergency feedwater are shown in Figures 3–6. The pressure increases before the air natural circulation is established when the residual heat is larger than that absorbed by cold water in air cooler and EFWT. But the pressure begins to drop not only because of the residual heat decay but also

because the air flow rate reaches its maximum. As shown in Figure 3, there is no remarkable difference between cold and warm startup. Figure 4 shows the natural circulation. As the isolation valve is open, the natural circulation is established between SG and air cooler. The flow rate rises to 300 kg/h. The flow instability happens at the beginning of natural circulation, which is caused by the water hammer that occurs in emergency feedwater tank. The water hammer also results in flow instability of injection from emergency feedwater tank

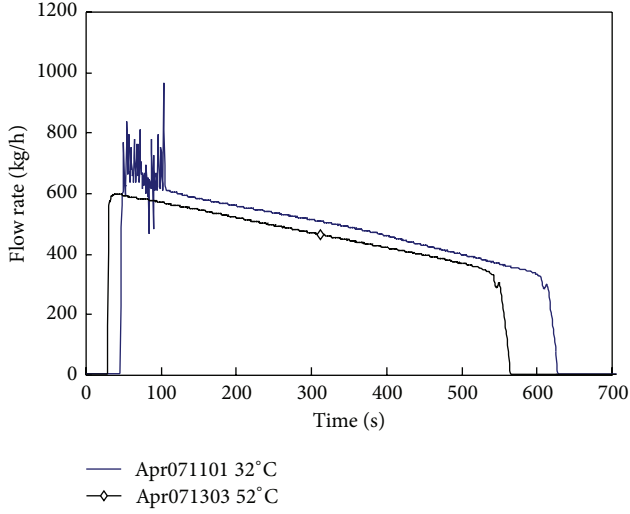


FIGURE 7: Water hammer influenced by feedwater temperature.

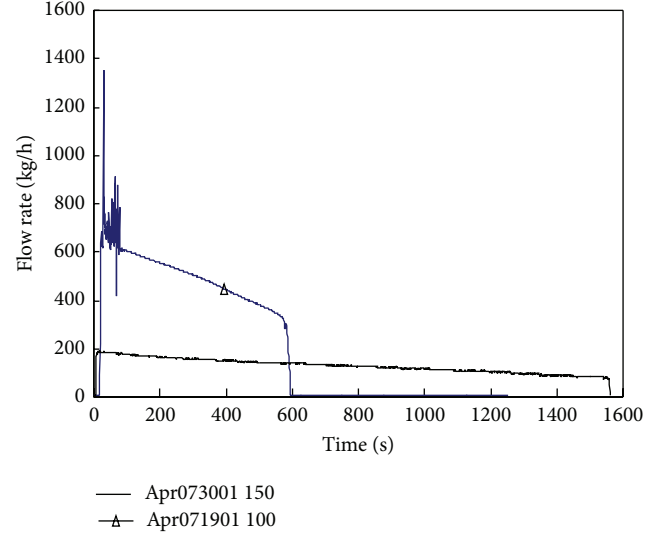


FIGURE 8: Water hammer influenced by resistance of feedwater loop.

as shown in Figure 5. The water hammer occurs in emergency feedwater tank when a great deal of steam, which is rushing into emergency feedwater tank through the pressure balance pipe after the feedwater valve is opened, condenses quickly. The pressure fluctuates in the emergency feedwater tank when the water hammer happens as shown in Figure 6. Some tests have been performed to avoid water hammer's appearance.

**4.2.1. Effect of Temperature of Feedwater.** The effect of temperature of feedwater in the passive residual heat removal system has been identified at the initial temperatures of 32°C and 52°C and the other parameters are kept at a constant value. The results are shown in Figure 7. When the temperature of feedwater in the emergency feedwater tank is 52°C, the water hammer does not happen because the direct contact condensation is related to the temperature of fluid.

**4.2.2. Effect of Resistance of Feedwater Loop.** In this group of case studies, the resistance of feedwater loop is changed by +50% of the reference case, and the other parameters are the same. The results are shown in Figure 8. As the resistance of feedwater loop increases, the feedwater flow rate and steam flow rate decrease accordingly. As a result there is not flow instability.

## 5. Code Development and Verification

MISAP2.0 code is a typical code that is used to analyze steady and transient performance of the secondary passive residual heat removal system.

**5.1. Mathematical Model.** A basic assumption is that one-dimensional approach is used.

**5.1.1. Single-Phase Conservative Equations.** Equation of continuity is

$$\frac{\partial \rho}{\partial \tau} + \frac{1}{A} \frac{dW}{dZ} = 0, \quad (7)$$

where  $W$  is flow rate and  $\rho$  is density.

Equation of momentum is

$$\frac{\partial W}{\partial \tau} = -A \frac{\partial P}{\partial Z} - \frac{\partial}{\partial Z} \left( \frac{W^2}{\rho A} \right) - \rho g A - U_h f \frac{W^2}{2\rho A^2}, \quad (8)$$

where  $A$  is the cross-sectional area of the flow channel;  $P$  is pressure;  $U_h$  is wetted perimeter;  $f$  is friction coefficient;  $g$  is the gravitational acceleration.

Equation of energy is

$$\begin{aligned} & \frac{\partial}{\partial \tau} \left[ \rho \left( u + \frac{V^2}{2} \right) \right] + \frac{\partial}{\partial Z} \left[ \rho \left( u + \frac{V^2}{2} \right) V \right] \\ & = \frac{qU_k}{A} + \frac{1}{A} \int_A q_V dA - \frac{\partial}{\partial Z} (VP) - \rho g V, \end{aligned} \quad (9)$$

where  $h$  is enthalpy;  $V$  is velocity;  $q_V$  is heat generation rate of the fluid;  $U_k$  is heated perimeter. The gravitational work and the work related to the kinetic energy variation can be neglected and the heat generation of the fluid is ignored; the equation can be simplified as follows:

$$\rho \frac{\partial h}{\partial \tau} + \frac{W}{A} \frac{\partial h}{\partial Z} = \frac{qU_h}{A} + \frac{\partial P}{\partial t}. \quad (10)$$

**5.1.2. Two-Phase Mixture Conservative Equations.** Equation of continuity is

$$\frac{\partial}{\partial t} [\alpha \rho_g + (1 - \alpha) \rho_f] + \frac{1}{A} \frac{\partial W}{\partial Z} = 0, \quad (11)$$

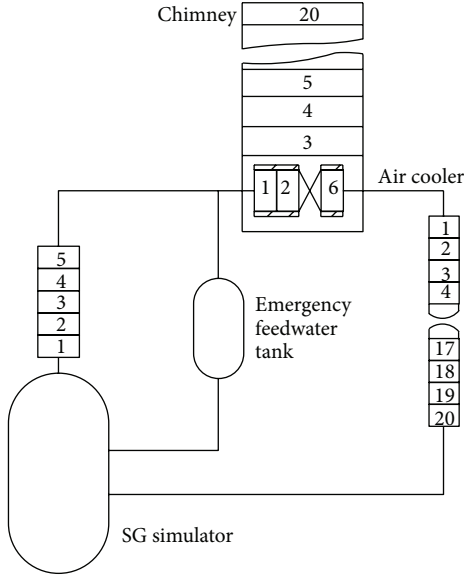


FIGURE 9: MASAP nodalization diagram of the test facility.

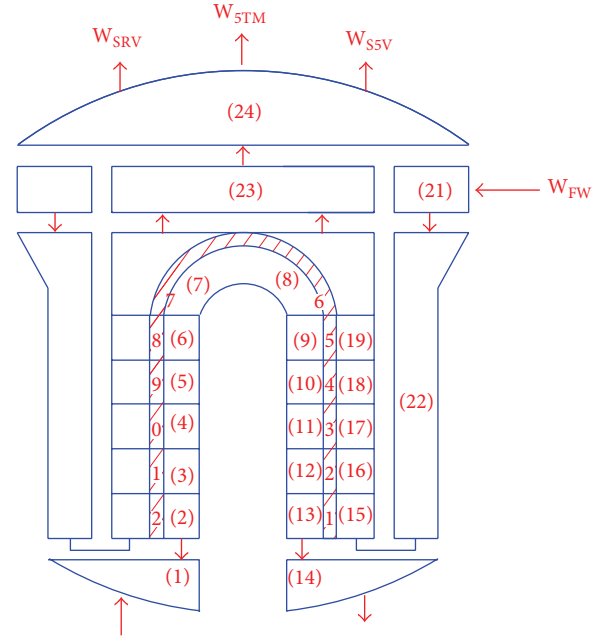


FIGURE 10: MASAP nodalization diagram of SG.

where  $\alpha$  is void fraction; subscripts  $g$  and  $f$  stand for steam and saturated liquid, respectively.

Equation of momentum is

$$\frac{\partial}{\partial \tau} (\rho V) + \frac{\partial}{\partial Z} (\rho V^2) = -\frac{\partial P}{\partial Z} - \frac{1}{A} \int_U \tau_f dU - \rho g. \quad (12)$$

Equation of energy is

$$\frac{\partial}{\partial t} [(1 - \alpha) \rho_f h_f + \alpha \rho_g h_g] + \frac{1}{A} \frac{\partial}{\partial Z} [Wh] = \frac{qU_h}{A} + \frac{\partial P}{\partial t}. \quad (13)$$

5.1.3. *Emergency Feedwater Tank.* Consider

$$W_{\text{tank}} = \sqrt{\frac{2g\Delta H}{\xi}} \rho A_{\text{tank}}. \quad (14)$$

5.1.4. *Air Loop.* Momentum equation is

$$\begin{aligned} \frac{\partial W_a}{\partial \tau} \int_0^{Ly} \frac{1}{A} dz = & - \int_0^{Ly} \frac{\partial P}{\partial Z} dz - \int_0^{Ly} \frac{1}{A} \cdot \frac{\partial}{\partial z} \left( \frac{W_a^2}{\rho A} \right) dz \\ & - \int_0^{Ly} \rho g dz - W_a^2 \int_0^{Ly} \frac{U_h}{A} f \frac{1}{2\rho A^2} dz, \end{aligned} \quad (15)$$

where  $Ly$  is the chimney height.

5.2. *Numerical Model.* In view of the fact that two loops closely couple with each other due to energy and momentum interactions, the two loops are solved together. Figures 9 and 10 show MASIP2.0 nodalization diagram of test facility and SG. After the discretization of the spatial derivative terms in

the equations, the following ordinary differential equations are obtained:

$$\begin{aligned} \frac{d\vec{y}}{dt} &= \vec{f}(t, \vec{y}, \vec{y}'), \\ \vec{y}(t_0) &= \vec{y}_0. \end{aligned} \quad (16)$$

Therefore, the whole system dynamic simulation can be solved as an initial value problem. For the stiff system of differential equations, Gear's algorithm is used traditionally.

5.3. *Steady State Calculation.* During the steady state calculation, several parameters, such as natural circulation flow rate, flow rate of air, temperature of condensate, and air at outlet of chimney, are calculated. And the calculations of MASIP2.0 are compared with the experimental data shown in Table 4. It shows that the error between calculation and experimental data is less than 10%.

5.4. *Transient State Calculation.* The transient calculation results of cold startup model test are compared with experimental data in Figures 11 and 12. Figure 11 shows the pressure comparison between calculation and test. The pressure increases before the air natural circulation is established when the residual heat is larger than that absorbed by cold water in air cooler and EFWT. MISAP2.0 code predicts the pressure well. However, the quantitative description is poor in the initial period of the transient. The reason is that there is no direct contact condensation model in the code. Then, the calculated flow rate of feedwater is less than experimental data, as shown in Figure 12. As a result the calculation of pressure is higher than that in the tests. As for the absence of direct contact condensation model, the water hammer is not observed.

TABLE 4: Comparison between the calculation of MISAP2.0 and experimental data.

Number	Test				Calculation of MISAP2.0			
	Natural circulation flow rate (kg/h)	Temp. of condensate (°C)	Flow rate of air (kg/s)	Temp. of air at outlet (°C)	Natural circulation flow rate (kg/h)	Temp. of condensate (°C)	Flow rate of air (kg/s)	Temp. of air at outlet (°C)
1	184.0	218.5	0.581	184.3	194.6	218.3	0.600	184.1
2	165.8	194.9	0.582	185.5	183.4	216.9	0.595	177.6
3	198.8	255.2	0.579	181.2	219.9	249.6	0.609	202.1
4	164.6	229.3	0.515	193.0	180.6	246.3	0.550	188.6

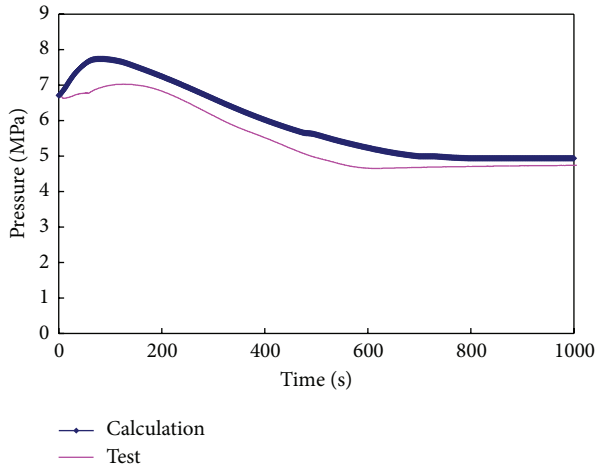


FIGURE 11: The pressure comparison between calculation and test.

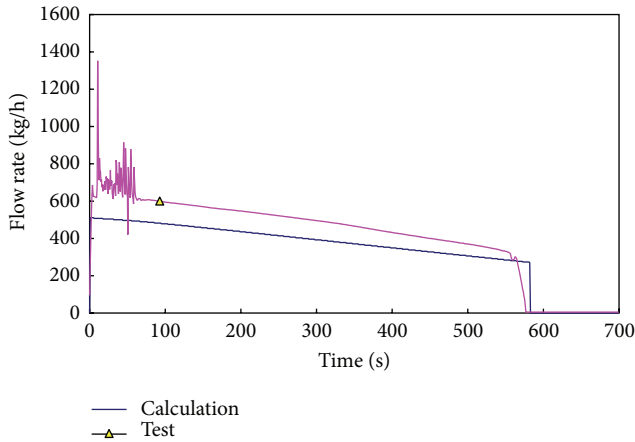


FIGURE 12: The flow rate comparison between calculation and test.

## 6. Conclusion

The passive residual heat removal system (PRHRS) characteristics of Chinese advance pressurized water reactor (CAPWR) have been experimentally investigated. Based on the investigations, the following conclusions are drawn.

- (1) A total of 280 sets of tests at steady state have been implemented to investigate the effect of some parameters on the passive residual heat removal system.

The result shows that the height of chimney has great influence on natural circulation flow rate. And the effect of the initial pressure and hydraulic resistance is small or negligible.

- (2) Based on the experiments, semiempirical model for analyzing passive residual heat removal system is established, and the calculation shows good agreement with experimental data. It can be applied to system arrangement design for PRHRS of Chinese advanced PWR.
- (3) In case of station blackout accident, the transient characteristics of passive residual heat removal system were studied. The natural circulation and injection of feedwater are very useful for removal of decay heat.
- (4) The increase of feedwater's initial temperature and resistance of feedwater loop is useful to avoid the water hammer.
- (5) A code MISAP2.0 has been developed, and the transient tests are used to verify the prediction of MISAP2.0. The calculated parameter variation trend is reasonable. However, the flow fluctuation and water hammer cannot be simulated by MISAP2.0. Now the direct contact condensation is under development for next version of MISAP.

## Nomenclature

- $A$ : Flow area ( $m^2$ )
- $f$ : Friction factor
- $g$ : Gravity acceleration ( $m/s^2$ )
- $h$ : Specific enthalpy ( $J/kg$ )
- $K$ : Loss coefficient
- $H$ : Emergency feedwater tank water lever (m)
- $P$ : Pressure (Pa)
- $q$ : Heat flux ( $W/m^2$ )
- $t$ : Time (s)
- $U$ : Heated perimeter (m)
- $U_e$ : Wetted perimeter (m)
- $W$ : Mass flow rate (kg/s)
- $z$ : Special coordinate (m)
- $\alpha$ : Void fraction
- $\rho$ : Density ( $kg/m^3$ ).

## Conflict of Interests

The authors declare that there is no conflict of interests regarding the publication of this paper.

## References

- [1] “Passive safety systems and natural circulation in water cooled nuclear power plants,” IAEA-TECDOC-1624, IAEA, Vienna, Austria, 2009.
- [2] “Status of advanced light water reactor designs 2004,” IAEA-TECDOC-1391, IAEA, Vienna, Austria, 2004.
- [3] S. Kim, B. Byoung-Uhn, C. Yun-Je, P. Yu-Sun, K. Kyoung-Ho, and Y. Byong-Jo, “An experimental study on the validation of cooling capability for the passive auxiliary feedwater system (PAFS) condensation heat exchanger,” *Nuclear Engineering and Design*, vol. 260, pp. 54–63, 2013.

## Research Article

# Some Movement Mechanisms and Characteristics in Pebble Bed Reactor

Xingtuan Yang,<sup>1</sup> Yu Li,<sup>1</sup> Nan Gui,<sup>1</sup> Xinlong Jia,<sup>1</sup> Jiyuan Tu,<sup>1,2</sup> and Shengyao Jiang<sup>1</sup>

<sup>1</sup> Institute of Nuclear and New Energy Technology of Tsinghua University and the Key Laboratory of Advanced Reactor Engineering and Safety, Ministry of Education, Beijing 100084, China

<sup>2</sup> School of Aerospace, Mechanical & Manufacturing Engineering, RMIT University, Melbourne, VIC 3083, Australia

Correspondence should be addressed to Shengyao Jiang; [jiangshy2012@sina.com](mailto:jiangshy2012@sina.com)

Received 16 November 2013; Accepted 4 May 2014; Published 1 June 2014

Academic Editor: Yanping Huang

Copyright © 2014 Xingtuan Yang et al. This is an open access article distributed under the Creative Commons Attribution License, which permits unrestricted use, distribution, and reproduction in any medium, provided the original work is properly cited.

The pebblebed-type high temperature gas-cooled reactor is considered to be one of the promising solutions for generation IV advanced reactors, and the two-region arranged reactor core can enhance its advantages by flattening neutron flux. However, this application is held back by the existence of mixing zone between central and peripheral regions, which results from pebbles' dispersion motions. In this study, experiments have been carried out to study the dispersion phenomenon, and the variation of dispersion region and radial distribution of pebbles in the specifically shaped flow field are shown. Most importantly, the standard deviation of pebbles' radial positions in dispersion region, as a quantitative index to describe the size of dispersion region, is gotten through statistical analysis. Besides, discrete element method has been utilized to analyze the parameter influence on dispersion region, and this practice offers some strategies to eliminate or reduce mixing zone in practical reactors.

## 1. Introduction

The high-temperature gas-cooled reactor (HTGR) [1] is generally recognized as a probable solution for the generation IV advanced reactors [2, 3] for its advantages of security, environmental applicability, high efficiency, and industrial-process heat applied in producing hydrogen. A pebble bed-type reactor core is one of the mainstream types for HTGRs, which has been adopted in many tests or demonstration reactors such as HTR-10 [4–6] in China, PBMR [7, 8] in South Africa, and their prototype reactor known as AVR [9–11] early in Germany. Compared with conventional reactors, a pebble-bed reactor is formed with spherical coated fuel pebbles and graphite pebbles instead of fixed fuel assemblies. Pebbles descend along the core under gravity, whose movements are determined by pebble flow. Pebble-bed HTGR runs in a recirculating way, in which fuel pebbles are drained out from discharge hole at the bottom of the core and loaded into the core from the top. When pebble bed reaches equilibrium state, the number of pebbles in the core approximately remains constant.

The two-region arranged reactor core is expected as a promising technique for pebble bed HTGRs [12]. In this concept, the reactor core is divided into two distinct regions, a central column region consisting of graphite pebbles (called graphite region) and an outer annular region consisting of fuel pebbles (called fuel region). In running circumstances, at the top of the core, graphite pebbles are inserted into the core from a single central spot and fuel pebbles are loaded from several positions in the annular periphery of the core. All the pebbles are discharged from the base hole. The two-region arrangement brings numerous advantages. It flattens the neutron flux and consequently allows a significantly higher power output without reducing safety margin. The decay heat also transfers a shorter distance from the core to outside during accidents [13].

It was found that a stable two-region arrangement could be formed under experimental conditions [14, 15]. There is still a crucial issue remained to be verified. As the two-region arrangement formed, a mixing interface appeared between the fuel-pebble region and the graphite-pebble region as a result of the pebble dispersion. Figure 1 depicts the sketch

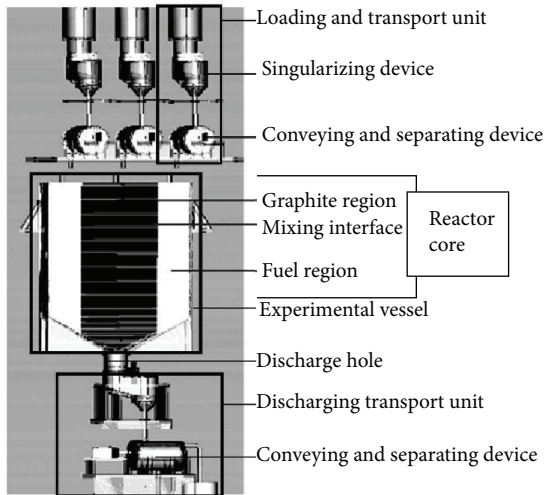


FIGURE 1: Experimental installation at INET of Tsinghua University and sketch of the two-region arranged reactor core.

map of the two-region arranged reactor core. The mixing interface is limited within several diameters of pebbles, which approximately has no impact on the stability of two-region arrangement. However, neutron moderation in the mixing interface is enhanced, which leads to more intensive reactions as well as more heat. Obviously, the temperature in mixing interface is higher and the fuel pebbles are easier to be damaged. In other words, in order to meet the requirements of reactor security, the mixing interface should be small enough. To some extent, the feasibility of two-region depends on the size of mixing interface which is directly related to the dispersion of pebble flow.

Dispersion of pebble flow is investigated through experiments and numerical simulations. Some fundamental mechanisms underlying pebble flow remain unknown, and the experimental way is still a principal approach to study it. The phenomenological method [15] is widely accepted to study experimental phenomena of pebble flow, which is an approach to study the dense pebble flow by means of investigating the interface features of different areas composed of differently colored pebbles. Several representative experimental facilities related to their own HTGRs have been built, including the installation developed by INET, Tsinghua University, according to the HTR-PM in China. Modeling of pebble flow which can be called granular flow in a broader term began during 1960s. Over the past 50 years, a number of theoretical approaches have been proposed for granular flow. Models based on continuum assumption are derived from other science branches, which fail to predict the dispersion of pebble flow and can only be applied into two extreme forms: quasistatic flow and rapid flow [16]. Some other models, such as the void model [17, 18] and spot model [19], provide different ideas for dense pebble flow and achieve certain agreements with the process of pebble motion but lead to some unexpected problems. Among these models, discrete element method [20, 21] is recognized to be more appropriate

TABLE 1: Main parameters of experimental facility.

Experiment vessel (width $\times$ height $\times$ thickness)	800 $\times$ 1000 $\times$ 120 mm; 800 $\times$ 2200 $\times$ 120 mm (higher vessel)
Base cone angle	30°
Diameter of discharge hole	120 mm
Diameter of particle	12 mm
Number of particle	70,000; 150,000 (higher vessel)

and its qualitative accuracy has been verified. The DEM simulation has been utilized to investigate the influence of some key parameters on pebble flow.

## 2. Experimental Installation

The experimental installation (Figure 1) is designed on the basis of the two-region pebble bed reactor with the scale of 1:5. The 2-dimensional experimental vessel is equivalent to an axial central cut piece of the 3-dimensional cylinder with the same ratio. The geometries of the vessel, including the base angle and the discharge-hole diameter, are supposed to have great effect on pebble flow. Experimental vessels for various combinations of bed and pebble parameters are planned to be set up to determine the parameter influences on the characteristics of pebble flow. Experiments discussed in this paper are for one combination of these parameters. More details can be found in [15]. Table 1 shows the main design parameters.

As a 2-dimensional model, the pebble flow in the experimental pebble bed is not fully the same as the one in practical reactor core. However, important geometries and pebble parameters are in accord with similarity theory, including base angle, discharge-hole diameter, and pebble size. Therefore, the studies still have an important practical meaning of guidance, whose conclusions can also be considered as general rules of the pebble flow in a reactor core.

In addition, the DEM methods used for comparative study and its application in pebble flows can be found in recently published papers of our group.

## 3. Experimental Results

**3.1. Experimental Observation.** Experiments were designed to investigate the establishment of the two-region arrangement and the mixing interface between the two regions. Experimental vessel was first filled with about 70,000 colorless pebbles to form the initial state of random pebble packing. During the recirculating procedure, black pebbles were loaded from the central inlet tube while colorless pebbles were loaded from the two-side inlet tubes. Meanwhile, pebbles were discharged from the bottom outlet tube at a reasonable rate to keep summation of pebbles constant. After a period of time, black pebbles were expected to form the central region (representing the graphite region) of the two-region arrangement by replacing initial colorless pebbles.

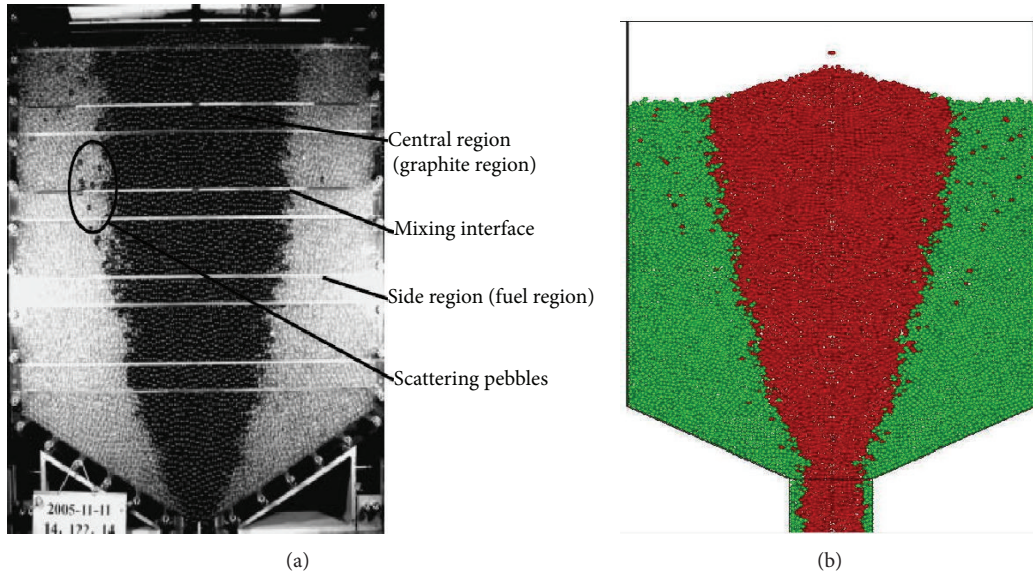


FIGURE 2: Equilibrium state of the two-region arrangement after about 7.5 h (a) and the counterpart obtained by DEM simulation (b).

Likewise, loaded colorless pebbles were expected to form the side regions (representing the fuel region). Different states of the development of two-region arrangement were recorded by snapshots at intervals. Figure 2 depicts the equilibrium state of two-region arrangement.

It is shown that two-region arrangement reached an equilibrium state after a period of running. Obviously, there was a quite rough boundary between central region and side region, which is the mixing interface. The maximum size of the mixing interface was about 4 to 5 times of pebble diameter. In addition, the appearance of some scattering pebbles results from the pebbles which are bounced away when they were loaded at the top of vessel, which is not caused by dispersion.

Thus, the existence of mixing interface is evident, and the size of mixing interface is finite. According to the physical calculations for the PBMR reactor, the size of mixing interface should be less than 5.5 times of pebble diameter to meet security requirements [12]. It seems that the mixing interface obtained from the experiment agrees with practical application, but the safety margin is not large enough.

Mixing interface depends on the pebble’s dispersion. In the recirculating mode of the two-region pebble bed reactor, the motion of individual pebble determines the two-region arrangement as well as the mixing interface. For the purpose of exploring the characteristics of pebble motion, statistical investigations have been undertaken.

**3.2. Study on Pebble Tracks.** The pebble motions were recorded at intervals by tracing the tagged pebbles, when they descended with the overall downward movement of pebble flow. At the beginning, the experimental vessel was filled with colorless pebbles. Then, the pebbles tagged with different color were distributed uniformly along the radial length and pairwise symmetrized against the central axis of the vessel. When the installation ran, positions of each tagged pebble at

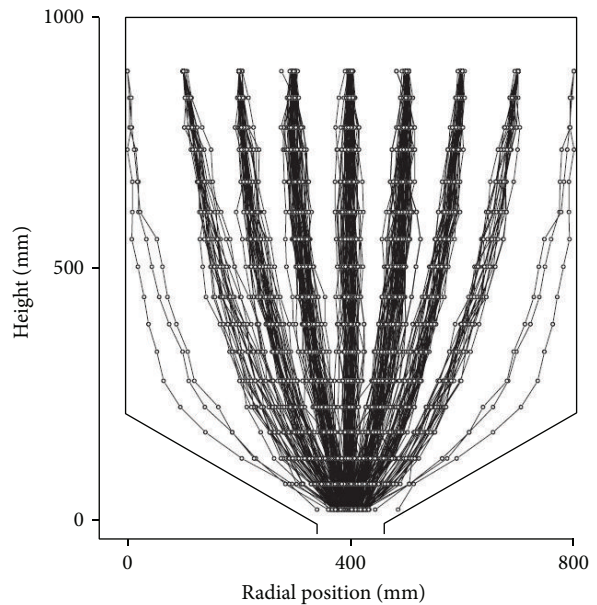


FIGURE 3: Descending tracks of tagged pebbles.

particular moments were visually detected. In this way, tracks of tagged pebbles were determined and they are found to be generally like “streamline” form, while these tracks are not as smooth as those of common fluids.

The above experimental procedure was repeated for numerous times. Each tagged pebble was placed at the same starting point repeatedly and a bunch of tracks for each tagged pebble were obtained. The motion characteristics of individual pebble are analyzed statistically based on the tracks of tagged pebbles and visual observation. Figure 3 plots all tracks for each tagged pebble.

As seen in Figure 3, the tracks of tagged pebbles located at the same initial position are different, but the differences between them are small. It is recognized that pebbles in the pebble bed move randomly to a small extent, and tracks of pebbles can only be statistically determined. The movements of pebbles are greatly confined by their neighbors, which makes dispersion among pebbles limited and is totally different from general flows. Therefore, the two-region arrangement is capable to be established without breaking the configuration during running, and consequently the mixing interface can be constrained to a small size.

Some characteristics of pebble dispersion can be concluded preliminarily. Due to randomness of pebble flow, it can be considered that the descending track of a pebble is not a single “stream line” but a statistical “stream tube” consisted of a bunch of “stream lines” starting from the same point. The diameters of “stream tubes,” which indicate the extent of dispersion, are varied in the vertical and horizontal directions. Specifically, dispersion of each pebble increases to the maximum at the midvessel and then decreases according to the specific geometry of bottom vessel. The decrease of dispersion at the bottom of vessel results from the small discharging hole which forces pebbles to move more compactly. In addition, pebbles staying away from the central axis have a tendency of larger dispersion through the visual stream lines in Figure 3.

After adequate experimental observations and statistical analysis, a common view on the behavior of individual pebble has been obtained. Individual pebbles in the same initial position at the top of the vessel move downward within a limited region and rarely exceed the slim region. To put it simply, these pebbles flow in the pebble bed like flowing in a stream tube, which is mentioned above. In other words, pebbles’ random movements have been restricted by their surrounding pebbles, which lead to a finite dispersion constrained in a tube-like region. Next, the distribution of pebbles in the tube-like region is going to be discussed, as the mixing interface in two-region arrangement is actually a tube-like region located at a particular radial position. Features of mixing interface, such as size and shape, are determined by the behaviors of a series of pebbles flowing in a specific tube-like region.

### 3.3. Radial Distribution of Pebbles in Dispersion Region.

After a period of stable running, attentions are paid to the distribution of pebbles within a tube-like region which have same starting-point at a particular height by getting enough pebble tracks. The tube-like region is a dispersion region of a series of pebbles. At a particular height, the dispersion region is divided into several equal intervals, and the number of pebble tracks within each interval is calculated, as shown in Figure 4 (the upper inset). The tagged pebbles are located inside certain intervals according to their initial positions of mass center. For instance, pebble A belongs to interval 6 and pebble B belongs to interval 10.

In Figure 3, it is easy to find that most tracks lie near the center of the dispersing region, and track numbers near the border of dispersion region are much less. Figure 4 (the lower

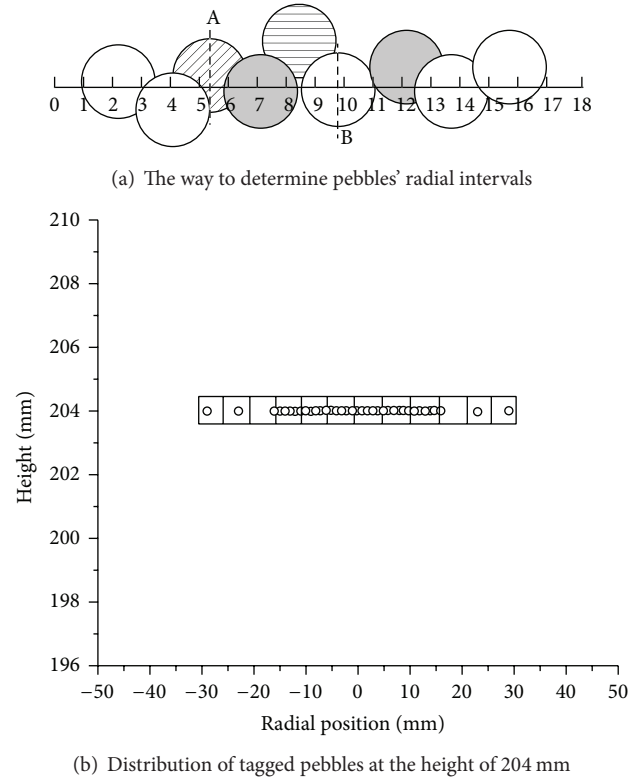


FIGURE 4: The method to illustrate radial distribution of pebbles.

inset) also demonstrates the phenomenon that most tagged pebbles are concentrated in the central intervals. All the tagged pebbles start from the radial position of 0, and their radial positions are recorded at the height of 204 mm to form the radial distribution.

In order to study the distribution at a particular height statistically, the probability density of radial distribution is defined as quantity fraction of pebbles in each interval divided by the length of interval (5 mm). In this way, the curve of probability density of radial distribution at the height of 204 mm (Figure 4) is gotten and shown in Figure 5. Several features of the curve should be noticed. The curve has a decent symmetry whose shape is high in the middle and low in both sides, which looks quite similar to the Gaussian distribution.

The relevance of the probability density curve to Gaussian distribution has been investigated through curve fitting based on the experimental data. The obtained fitting curve agrees with those data points on probability density to a large extent, as is shown in Figure 5. The radial position of symmetry axis of the Gaussian fitting curve, 0.4 mm, is close to the mean value of radial positions of these data points, -0.2 mm. Therefore, at least the radial distribution at the height of 204 mm of such pebbles which start from the specific radial position, 0 mm, accords with Gaussian distribution.

According to the uniform characters of pebble flow in experiments, it is supposed that the radial distributions located at different heights of pebbles starting from different radial positions accord with Gaussian distribution, which has been justified by the coincidences between experimental

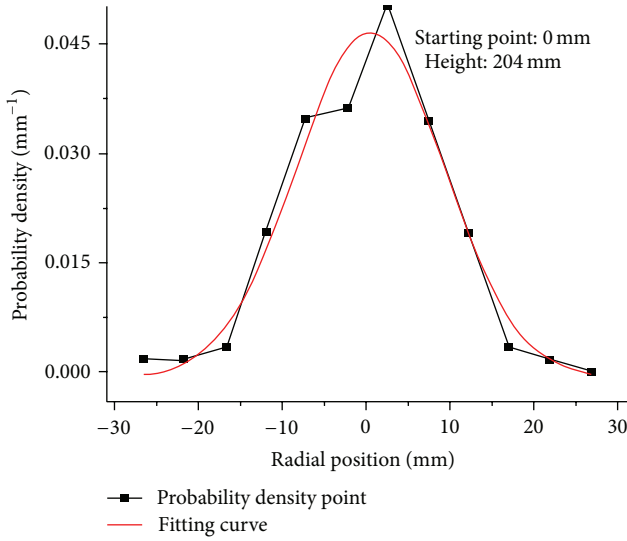


FIGURE 5: Gaussian fitting curve on probability density of radial distribution.

data and fitting curves (Figure 6). Therefore, in the entire pebble flow field, it can be generally recognized that radial distribution of pebbles which have the same starting point agrees with Gaussian distribution at a particular height in dispersion region.

If a random variable  $x$  obeys the Gaussian distribution whose expectation and deviation are  $\mu$  and  $\sigma$ , the probability density of  $x$  accords with the following formula:

$$f(x; \mu, \sigma) = \frac{1}{\sigma\sqrt{2\pi}} \exp\left(-\frac{(x-\mu)^2}{2\sigma^2}\right), \quad (1)$$

where  $\mu$  determines the location of Gaussian curve and  $\sigma$  determines the range of distribution. The characteristics of Gaussian distribution define that the area surrounded by the curve and horizontal axis is 1. When the selected region ranges from  $-\sigma$  to  $\sigma$  by the sides of mean value ( $\mu$ ), the surrounded area is 0.9545.

When the law of Gaussian distribution is applied to the dispersion region, a statistical conclusion can be obtained. It is not difficult to find agreements between Figures 3 and 6. The slim part of dispersion region in Figure 3 corresponds with the “tall” and “thin” distribution in Figure 6, and similarly the bulky part of dispersion region relates to the “dumpy” distribution. A small standard deviation means a concentrative distribution, which represents a small dispersion region. Therefore, one of the parameters in Gaussian distribution, namely, the standard deviation  $\sigma$ , indicates the size of dispersion region.

We investigate standard deviations of radial positions at different heights and radial positions, in order to find the variation trend of standard deviations along the descending path. Figure 7 shows tracks starting from different radial positions. The tracks and variation trends of standard deviations are got through calculating the mean value of radial coordinates at different heights. Actually, there are essential resemblances between Figures 3 and 7, and identical conclusions can also be

drawn from Figure 7. Four curves in Figure 7 reveal that the standard deviations increase to the maximum at the height of about 300 mm and then begin to decrease, which is like the variation trend of sizes of dispersion regions. Besides, the curve of id3 has relatively large values, for pebbles represented by id3 stay far away from the central axis, which can also be observed in Figure 3 that pebbles in side region have larger dispersion.

The value of standard deviation is in proportion to the size of dispersion region. Virtually, the concept of dispersion region is also statistical, since it is only realistic for the region to comprise a majority of pebbles instead of all of them. For instance, the dispersion region can comprise 95.45% pebbles if radiuses of this region are set to be 2 times of standard deviations at different heights. To some extent, it is acceptable to regard 2 or 3 times of standard deviation as radius of dispersion region in engineering. In conclusion, quantity and variation trend of standard deviation display the features of dispersion region well, and it is applicable to treat standard deviation as a quantitative index of dispersion region.

**3.4. Experiment in Heightened Vessel.** Inherent safety of HTGR in china is insured by its fuel characteristics and passive safety system, which is attributed to the specific design of small radius of reactor core to some extent. Small radius allows the decay heat to transfer from the inner core to the outside more easily because of a shorter distance, so that passive approaches like radiation heat transfer and heat convection can meet the requirements of heat-transfer capacity during accidents. On the other hand, in terms of the total power, such design restricts the output due to the size of the core. Thus, enlarging the height of the core is the adoptive way, which can drive up the total power and maintain the passive safety capacity at the same time.

As mentioned in the section of experimental installation, the height of the experimental vessel can be heightened to a height of 2.2 m. Similar experiments have been conducted in the heightened vessel so as to study whether there would be differences or not.

Figure 8 shows the tracks in the heightened vessel. The tracks in the heightened vessel are also smoothly varied and symmetric which is similar to those in 1 m vessel. As a result of the cone-shaped bottom and the small discharging hole, tracks bend towards the axis and flow more compactly. There is a region in the upper vessel where the tracks are uniformly straight, and these tracks do not bend until they reach the bottom vessel. In terms of tracks, there is not an essential link between the upper and bottom regions. The flow field below 1 m in heightened vessel shares many features with that in standard vessel.

The standard deviation in heightened vessel depicted in Figure 8 reveals more characteristics. The curve of id4 is based on relatively limited data, and it perhaps cannot represent the physical law well. Compared with the results in the last section shown in Figure 7, several differences are concluded. In general, pebble flow in heightened vessel has larger dispersion regions, because standard deviations in Figure 8 reach maximums above 20 mm, whereas they

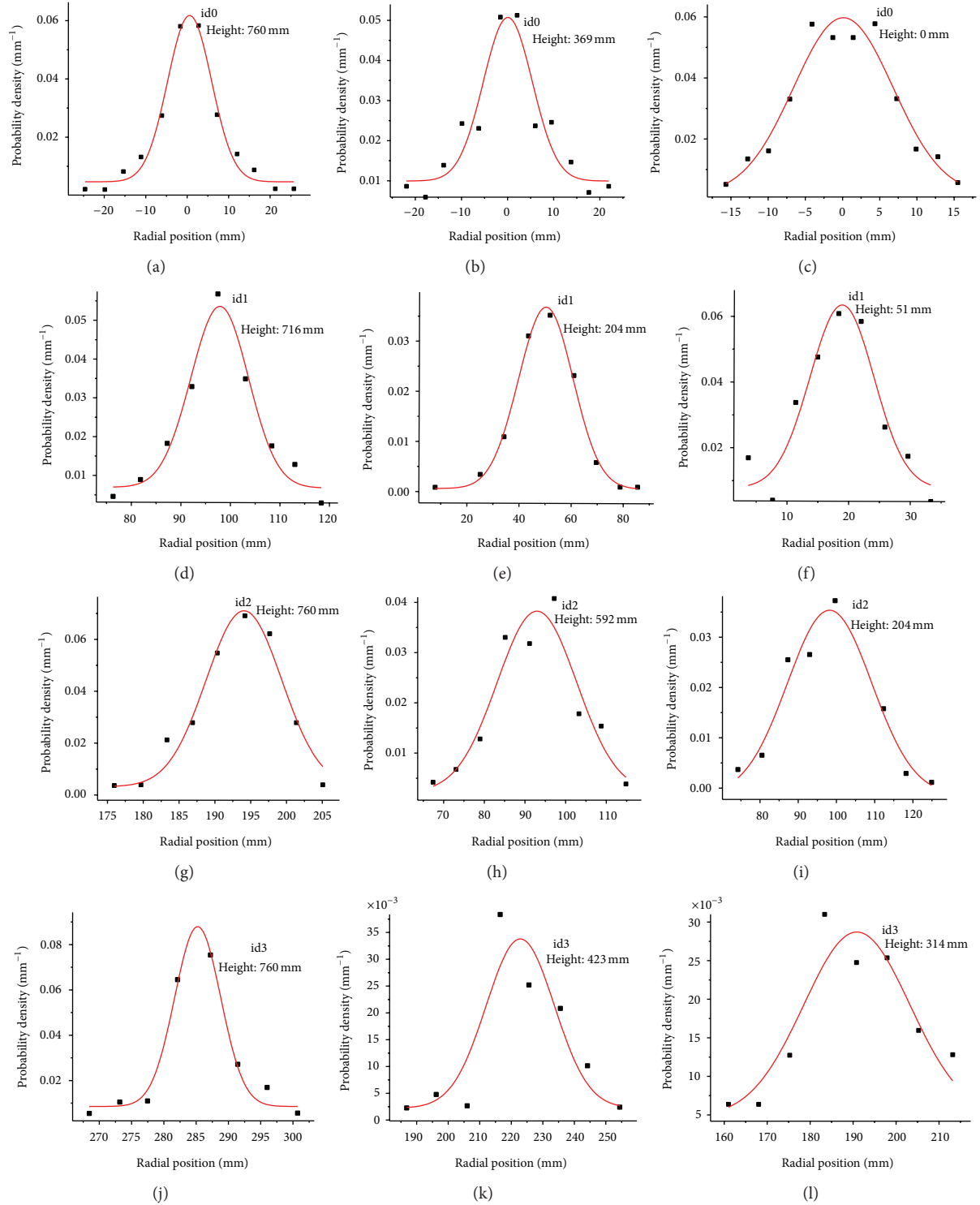


FIGURE 6: Coincidences between probability density points and fitting curve at different heights and radial positions.

are about 12 mm in Figure 7. What is more, apart from id4, curves do not split until they reach the depth of 1000 mm, which refers to the uniform flow region in upper vessel. Of course, several laws are justified again. The standard

deviations increase to maximums at the middle vessel and then decrease. Pebbles staying far from axis have larger dispersion, which can be illustrated by the curve of id3. At last, from the perspective of engineering, the most important

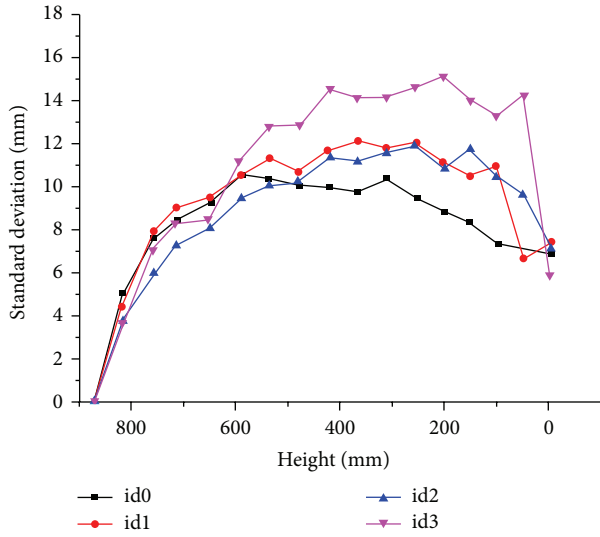


FIGURE 7: The variation trend of standard deviations of tracks.

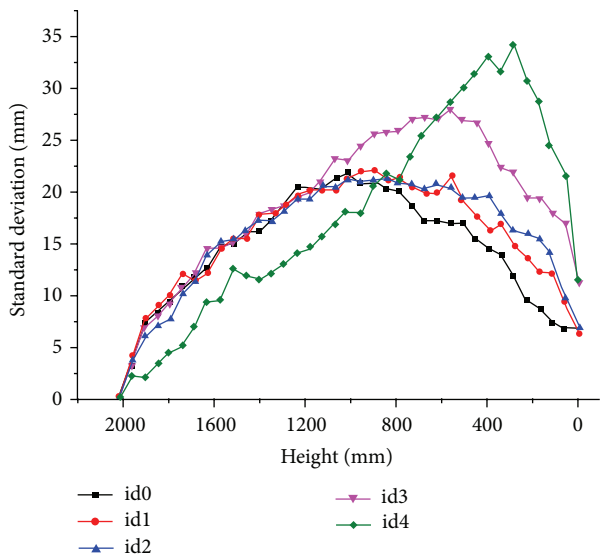


FIGURE 8: The standard deviations of tracks in the heightened vessel.

issue that we should be concerned about is that heightening reactor core will bring larger dispersion region, which is not expected.

#### 4. Discussions

The main factors that determine the phenomenon of dispersion still remain unknown. It is generally accepted that the qualitative accuracy of DEM has been verified. DEM simulation has been adopted to discuss principal parameters' influence on dispersion. The standard deviation at a particular height, as a quantitative index to show the size of the dispersion region, will be investigated with the change of other parameters.

**4.1. Radial Velocity.** It is natural to associate dispersion with radial velocity which can be detected in DEM simulation. Figure 9 illustrates variation trend of standard deviation as well as radial velocity both in 1m vessel and heightened vessel. The unit of radial velocity (d/s) means diameter per second and the data were drawn from those pebbles starting at half-radius position. In Figure 9, the size of dispersion region does not correlate well with radial velocity, since the standard deviation has a sharp increase whereas the radial velocity remains stable at a low level in the upper vessel. The overall correlations have been proved weak, with the Pearson correlation coefficients of 0.0823 and 0.19725, respectively.

In Figure 10, which set radial velocity as abscissa axis, correlation between these two parameters is illustrated more obviously. When radial velocity is less than 0.005 (d/s), standard deviation has a wide range and is not affected by radial velocity. Due to the majority of spots standing at low velocity, the overall correlation is not apparent. However, when radial velocity is larger than 0.005 (d/s), a much more significant correlation appears, with Pearson correlation coefficients of  $-0.9618$  in 1m vessel and  $-0.9648$  in heightened vessel, respectively. It means that there is a critical value of radial velocity, above which the size of dispersion region drops with the rise of radial velocity.

Enlarging radial velocity seems to help in dispersion control as shown in the above figures, if this rule can be applied in practice. Nevertheless, the pebble flow in experimental vessel as well as in practical reactor belongs to quasistatic flow, so velocity of most pebbles is under the critical value (appropriate 0.005 d/s). Only in bottom vessel larger radial velocity can be realized, and the size of dispersion region declines to some extent. Additionally, we cannot focus on the growth of radial velocity to announce that it directly leads to the decrease of dispersion region, because radial velocity rises at the result of specific bottom geometry which may also exerts impact on dispersion.

**4.2. Base Cone Angle and Friction Coefficient.** The vessel geometry impacts the overall pebble flow dramatically. To say specifically, the base cone angle in bottom vessel plays an important role in developing the main features of pebble flow, including the dispersion region. The base cone angle of experimental vessel can be adjusted from 30 to 60 degrees, and corresponding DEM simulations are carried out as well.

As shown in Figure 11, dispersion regions in vessels whose cone angles are 30 and 45 degrees are nearly matched, which means that this change has little impact on the size of dispersion region. However, with angle changing from 45 to 60 degrees, the maximum size of dispersion region has a significant drop. Therefore, geometry influences the phenomenon in a nonlinear way. Perhaps there is also a particular angle or a specific geometry that can minimize the dispersion. Moreover, the standard deviation does not show differences until they reach the middle vessel, which means the bottom geometry fails to influence flow pattern in the upper vessel. This enables simplified researches of heightened vessel, and we can concentrate on the bottom flow field on some occasions.

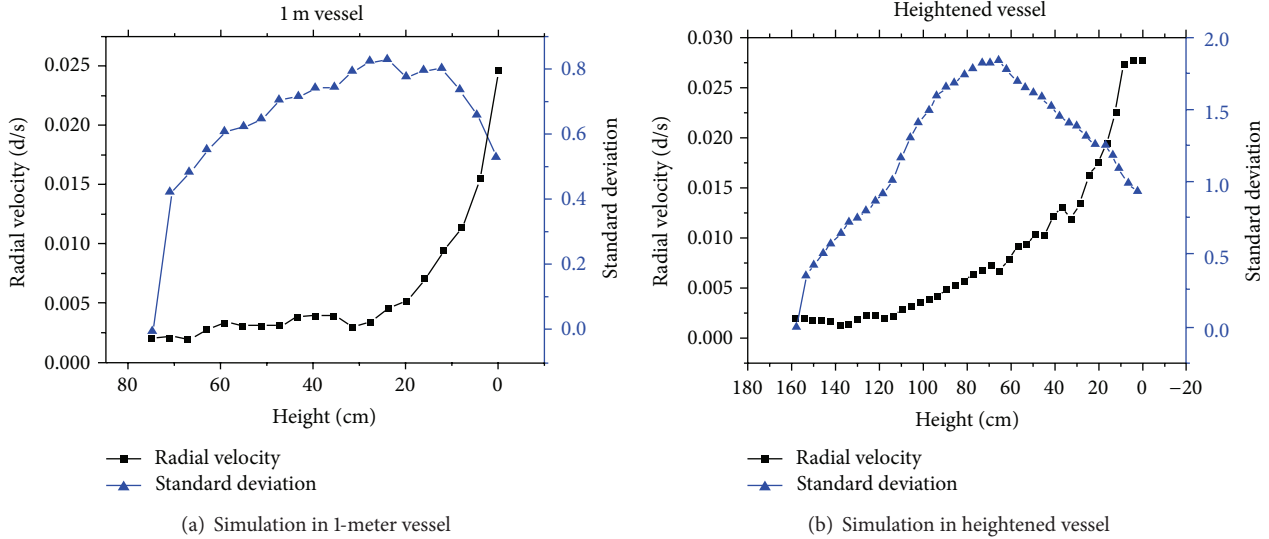


FIGURE 9: DEM simulations on standard deviation and radial velocity in 1-meter and heightened vessels.

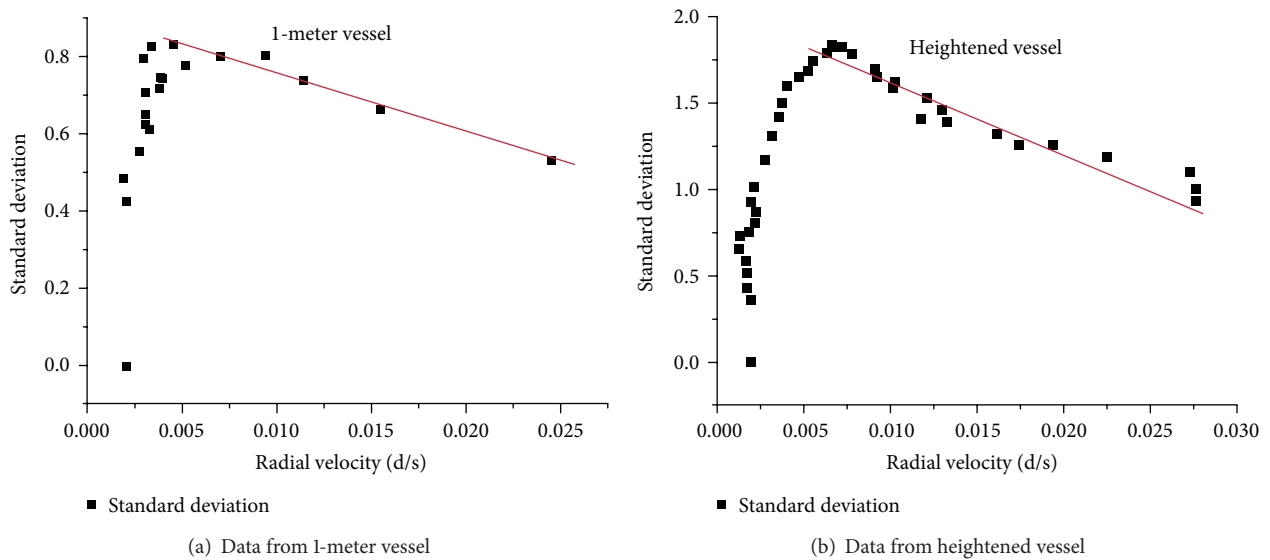


FIGURE 10: Correlation between standard deviation and radial velocity in 1-meter and heightened vessels.

Friction coefficient is determined by physical property of individual pebble. Apart from gravity, the friction is an important force of driving or resisting. It is natural to suppose that a larger friction restricts the behavior of pebbles. Then, the dispersion would be reduced to some extent. In fact, the friction resulting from surrounding pebbles also acts as driving force which may push pebbles away from its original path and bring about more obvious dispersion. As a result, we believe that there is a competitive mechanism between driving and resisting effects produced by friction. This hypothesis is demonstrated by Figure 12. It is hard to predict variation trend of dispersion by changing the friction coefficient, because the relation between them is not consistent in different friction scopes. Bottom pebbles in the heightened vessel suffer more pressure from above

pebbles and competition between the driving and resistance forces is more intense. As a consequence, the size of dispersion approximately remains stable when friction coefficient changes from 0.2 to 0.4, for resistance force as well as driving force increases to some extent.

## 5. Summary

Through the above analysis, we can summarize the following.

In our experiment, the stable two-region arrangement in pebble bed reactor can be established with a definite and finite mixing interface. The dispersion happened in mixing interface results from pebbles' random motion behavior. Pebbles with the same starting point flow downward in a "tube-like" region and rarely get out statistically. This region

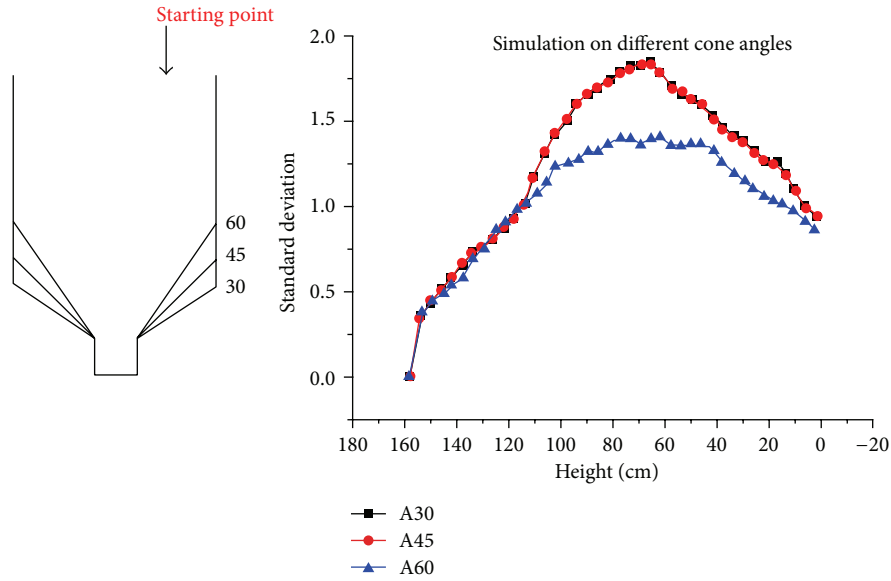


FIGURE 11: Simulation on different base cone angles.

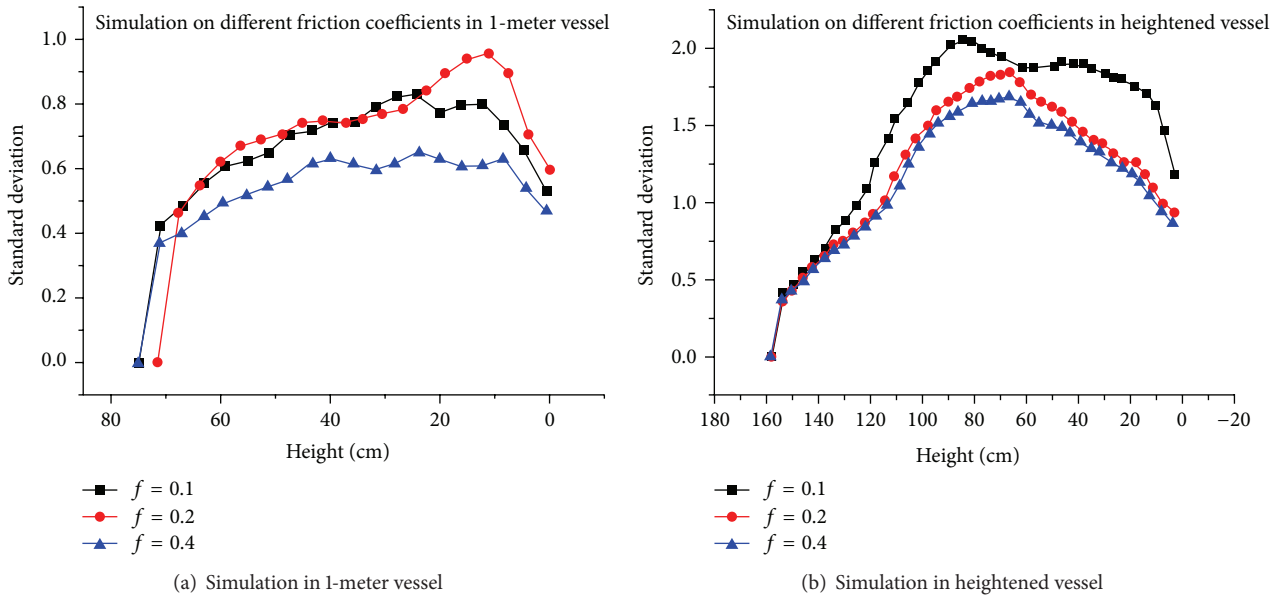


FIGURE 12: Simulations on different friction coefficients in 1-meter and heightened vessels.

is called the dispersion region which directly relates to the size of mixing interface. The side or peripheral dispersion regions have larger diameters compared with central ones, and, for each region, it usually reaches the maximum size in the middle of vessel. In dispersion region, the radial distribution of pebbles at a particular height accords with Gaussian distribution and the standard deviation determines the size of dispersion as a quantitative index.

In the heightened vessel, apart from the uniform flow field in the upper vessel, pebble flow has a more obvious dispersion. There is a critical value of radial velocity (approximately 0.005 diameter/s) that determines the influence on

dispersion. The rise of radial velocity larger than the critical value can reduce the size of dispersion linearly.

Enlarging base cone angle helps in the control of dispersion. The impact of friction on dispersion region is complicated, because friction is related to driving as well as resistance force of dispersion and the competitive mechanism between them remains unknown.

### Conflict of Interests

The authors declare that there is no conflict of interests regarding the publication of this paper.

## Acknowledgments

The authors are grateful for the support of this research by the National Natural Science Foundations of China (Grant nos. 11072131 and 51106180) and the research funds of Tsinghua University (no. 2010Z02275).

## References

- [1] A. J. Goodjohn, "Summary of Gas-Cooled reactor programs," *Energy*, vol. 16, no. 1-2, pp. 79–106, 1991.
- [2] W. Magwood, "Roadmap to the Next Generation Nuclear Power Systems: A Vision for a Powerful Future, Nuclear News," American Nuclear Society, 2000.
- [3] J. Ryskamp, "Next Generation Nuclear Plant: High-Level Functions and Requirements," Tech. Rep. INEEL/EXT-03-01163, Idaho National Engineering and Environmental Laboratory, 2003.
- [4] D. Z. Wang and Y. Y. Lu, "Roles and prospect of nuclear power in China's energy supply strategy," *Nuclear Engineering and Design*, vol. 218, pp. 3–12, 2002.
- [5] Y. H. Xu and Y. L. Sun, "Status of the HTR programme in China, IAEA TCM on High Temperature Gas Cooled Reactor Application and Future Prospects ECN," Petten, The Netherlands, 1997.
- [6] Z. Y. Zhang, Z. X. Wu, Y. H. Xu, Y. L. Sun, and F. Li, "Design of Chinese modular high-temperature gas-cooled reactor HTR-PM," in *Proceedings of the 2nd International Topical Meeting on High Temperature Reactor Technology*, Beijing, China, 2004.
- [7] A. Koster, H. D. Matzner, and D. R. Nicholisi, "PBMR design for the future," *Nuclear Engineering and Design*, vol. 222, no. 2-3, pp. 231–245, 2003.
- [8] W. K. Terry, H. D. Gougar, and A. M. Ougouag, "Novel method for the deterministic design, analysis, and optimization of the in-core fuel cycle of a recirculating pebble-bed reactor," *Annals of Nuclear Energy*, vol. 29, pp. 1345–1364, 2001.
- [9] R. Schulten, "Pebble bed HTRs," *Annals of Nuclear Energy*, vol. 5, no. 8–10, pp. 357–374, 1978.
- [10] H. Frewer, W. Keller, and R. Pruschek, "The modular high-temperature reactor," *Nuclear Science and Engineering*, vol. 90, no. 4, pp. 411–426, 1985.
- [11] G. H. Lohnert and H. Reutler, "The modular HTR—a new design of high temperature pebble-bed reactor," *Nuclear Energy*, vol. 22, no. 3, pp. 197–201, 1982.
- [12] International Atomic Energy Agency, "Current status and future development of modular high temperature gas cooled reactor technology," IAEA TEDOC-1223, Vienna, Austria, 2001.
- [13] Pebble Bed Modular Reactor (Pty) Limited, "PBMR safety analysis report," Document 001929-207/4, 2002.
- [14] X. T. Yang, W. P. Hu, and S. Y. Jiang, "Experimental Investigation on feasibility of two-region-designed pebble-bed high-temperature gas-cooled reactor," *Journal of Nuclear Science and Technology*, vol. 46, no. 4, pp. 374–381, 2009.
- [15] X. T. Yang, W. P. Hu, S. Y. Jiang, K. K. L. Wong, and J. Y. Tu, "Mechanism analysis of quasi-static dense pebble flow in pebble bed reactor using phenomenological approach," *Nuclear Engineering and Design*, vol. 250, pp. 247–259, 2012.
- [16] C. S. Campbell, "Granular material flows—an overview," *Powder Technology*, vol. 162, no. 3, pp. 208–229, 2006.
- [17] W. W. Mullins, "Stochastic theory of particle flow under gravity," *Journal of Applied Physics*, vol. 43, no. 2, pp. 665–678, 1972.
- [18] H. Caram and D. C. Hong, "Random-walk approach to granular flows," *Physical Review Letters*, vol. 67, no. 7, pp. 828–831, 1991.
- [19] M. Z. Bazant, "The spot model for random-packing dynamics," *Mechanics of Materials*, vol. 38, no. 8–10, pp. 717–731, 2006.
- [20] N. Gui, X. T. Yang, J. Y. Tu, and S. Y. Jiang, "A simple geometrical model for analyzing particle dispersion in a gravity-driven monolayer granular bed," *Powder Technology*, vol. 254, pp. 432–438, 2014.
- [21] N. Gui, X. T. Yang, J. Y. Tu, and S. Y. Jiang, "Effect of bed configuration on pebble flow uniformity and stagnation in the pebble bed reactor," *Nuclear Engineering and Design*, vol. 270, pp. 295–301, 2014.

## Research Article

# Experimental and Numerical Study of Stagnant Zones in Pebble Bed

Xinlong Jia,<sup>1</sup> Xingtuan Yang,<sup>1</sup> Nan Gui,<sup>1</sup> Yu Li,<sup>1</sup> Jiyuan Tu,<sup>1,2</sup> and Shengyao Jiang<sup>1</sup>

<sup>1</sup> Institute of Nuclear and New Energy Technology of Tsinghua University and the Key Laboratory of Advanced Reactor Engineering and Safety, Ministry of Education, Beijing 100084, China

<sup>2</sup> School of Aerospace, Mechanical & Manufacturing Engineering, RMIT University, Melbourne, VIC 3083, Australia

Correspondence should be addressed to Shengyao Jiang; [jiangshy2012@sina.com](mailto:jiangshy2012@sina.com)

Received 17 December 2013; Accepted 11 April 2014; Published 18 May 2014

Academic Editor: Shengqiang Li

Copyright © 2014 Xinlong Jia et al. This is an open access article distributed under the Creative Commons Attribution License, which permits unrestricted use, distribution, and reproduction in any medium, provided the original work is properly cited.

The experimental method (side area method) and DEM simulation have been carried out to analyse the stagnant zone in the quasi-two-dimensional silos. The side area method is a phenomenological method by means of investigating the interface features of different areas composed of different coloured pebbles. Two methods have been discussed to define the stagnant zone. In particular, the area of the stagnant zone has been calculated with the mean-streamline method, and the tracking time of different marking pebbles has been investigated with the stagnant time method to explore the kinematics characteristics of the pebbles. The stagnant zone is crucial for the safety of the pebble-bed reactor, and the practical reactor core must avoid the existence of the stagnant zone. Furthermore, this paper also analyses the effects of bed configuration (the bed height, the base angle, and the friction coefficient) on stagnant zone with the two methods mentioned above. In detail, the bed height shows little impact on the stagnant zones when the bed height exceeds a certain limit, while the base angle has negative prominent correlation with the stagnant zone. The friction coefficient effect seems complicated and presents the great nonlinearity, which deserves to be deeply investigated.

## 1. Introduction

It is generally known that the high temperature gas-cooled nuclear reactor is regarded as one potential solution for generation IV advanced reactor [1]. The Institute of Nuclear and New Energy Technology (INET) at Tsinghua University has developed the HTR-PM [2], which has been authorized to be one of the National Special Grand Science-Technology Projects of China.

In addition, the mechanisms and characteristics of the pebble-bed reactor have received more attention. Some countries, such as South Africa [3] and the United States [4], develop their own test and demonstration reactors (PBMR and MPBR, resp.) and their prototype reactor, for example, the AVR early in Germany, and so forth [5].

The geometric and physical design of pebble-bed reactor core is based on the flow characteristics of the spherical fuel elements in the pebble bed. The pebble flow (or named granular flow) is an attractively simple and yet surprisingly complex area of research [6]. Fast, dilute flows are generally

dominated by classical hydrodynamics (with inelastic collisions), while slow, dense flows seem full of challenge, because of many-body interactions and nonthermal fluctuations. Such flows are meaningful for not only the fundamental scientific research, but also the engineering applications [7]. For instance, the degree of mixing in very slow granular drainage (<1 pebble per min) determines the efficiency and safety of the new pebble-bed nuclear reactors [8].

Currently, the information about the dense pebble flow provided by experiments is limited, but important. Numerous experiments of the drainage flows in quasi-two-dimensional silos have been conducted. The motion information of the particles is tracked accurately at a transparent wall [9–13]. The technology, such as the magnetic resonance imaging [14], confocal microscopy [15], index matching with an interstitial fluid [16], and diffusing-wave spectroscopy [17], has been applied in particle tracking in some 3D granular materials and colloids. However, there are obvious distinctions between the experiment equipment and the practical pebble-bed reactor core. The porosity distribution of static packing of

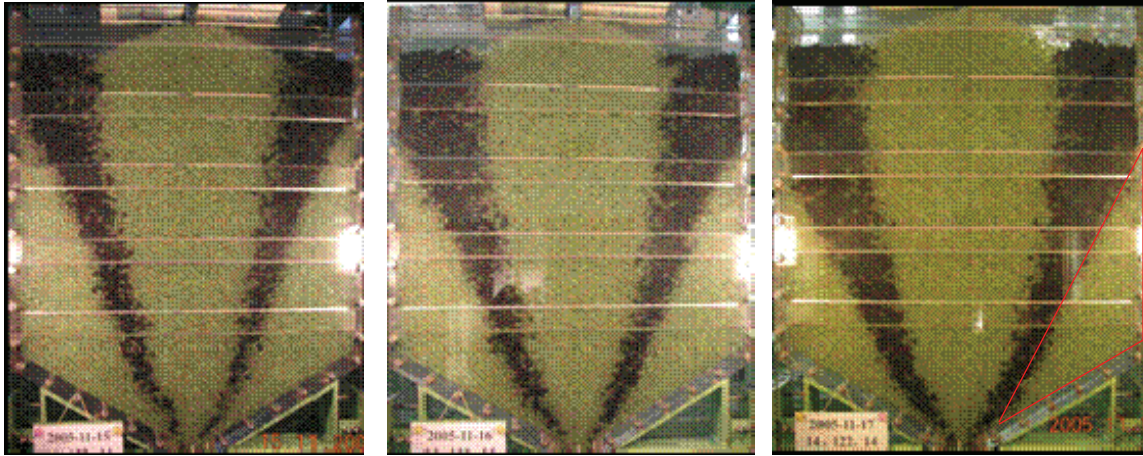


FIGURE 1: Sketch of the stagnant zone of different time with the side area method in experiment.

spheres [18] has drawn more attention in the experiment about the realistic geometries for PBR, because it affects helium gas flow through the core [19].

Moreover, the past 50 years witnessed the developing of the mathematical models of the pebble flow, including the continuum approach [20], void model [21], spot model [22], and discrete element method [23] (DEM). However, a generally accepted theoretical model has not been found yet. Among them, DEM with its qualitative accuracy might be the most applicable approach for dense granular flow investigation [24].

There are some features concerning the quasi-static dense pebble flow in the pebble-bed reactor. First of all, the pebbles are always undergoing the transition from static state to dynamic state, and then back to static state with small disturbance, which are only driven by the gravity. Additionally, this shows that the falling pebbles in the pebble packing swiftly reach their own equilibrium state with almost no collision effects [24], and the equilibrium state time is larger than the dynamic state time. As mentioned above, the quasi-static dense pebble flow in the pebble-bed reactor is quite different from the normal dilute flow, which needs to be explored.

Stagnant zone can be found in the low corners, or at the bottom of the cone angle of the experimental vessels near the wall under some conditions [24]. Figures 1 and 2 display the sectional sketch map of the stagnant zone marked with the red outline in the experimental vessel. A stagnant zone in the pebble bed probably occurs under the specific design of a reactor core. Pebbles in the stagnant region will move extremely slowly or even remain static. The fuel pebbles which stay in the stagnant zone and spend much more time than their design parameter may cause the severe irradiation and thermal damage with possible fission product escaping. So stagnant region is not allowed to exist in practical reactors, and the strategy to eliminate the stagnant zone should be discussed.

Investigation on parameter effects of pebble flow and the stagnant zone in the dense pebble flow is meaningful and significant to understand the physical mechanism of

quasi-static dense flow. However, the study of the field of pebble flow of pebble-bed reactor is not sufficient by now, and only few literatures were published. For example, MIT's scientists have ever reported their research results under the operation mode of free drainage of pebbles [4, 25].

Motivated by this consideration, the experiment and the discrete element method (DEM) simulation will be carried out to investigate the stagnant zone forming in the lower corners of the vessel. More motion behaviors and characteristics of the dense pebble flow will be observed. Furthermore, we try some quantitative methods to calculate and analyze the stagnant zone in the dense pebble flow, and parameter effects of the stagnant zone will be discussed. All the work may help us have a more profound understanding of the characteristics of the dense pebble flow in the pebble-bed reactor.

## 2. Experimental Setup and Numerical Method

**2.1. Experimental Setup.** The experimental vessel is a 2D structure with smaller size, shown in Figure 1, which is designed to simulate a real pebble-bed reactor at the scale of 1:5. This experiment facility runs in a way of recirculation mode; that is to say, the pebbles discharged from the outlet will be carried back to the inlet tube.

The experiment facility has the dimensions 3000 \* 3000 \* 6000 mm in total length, width, and height, respectively [4]. The main three parts make up the whole experimental setup. Firstly, the vessel (Figure 1) is made up of the plexiglass, with the dimensions 800 \* 1000(2000) \* 120 mm in width, height (after being increased), and thickness, respectively. It is a quasi-two-dimensional setup. The bottom of the vessel has a steep hill of 30 degrees. The pebbles in the vessel are made up of glass, with the numbers 70000 and 150000 (after being increased). Moreover, there are three inlet tubes over the vessel, and the pebbles from the inlet tubes will be falling in the left, center, and right zones in the upper surface of the packing pebbles in the vessel. The discharge hole is in the bottom of the vessel, with the diameter of 120 mm and length of 200 mm.

2.2. *Numerical Method.* Discrete element method (DEM) is usually applied in the research about the discontinuous media. The calculated zones are covered by collections of unique “discrete elements”. Every element has its own independent properties and motion parameters. One hypothesis of the DEM indicates that the contacting interactions of elements with each other are proportional to the relative displacement between them. The equations of motion of the elements will be established based on Newton’s laws.

The following equations described the translational and rotational motions of element “ $i$ ” in a system at time  $t$ , determined by Newton’s second law:

$$\begin{aligned} m_i \frac{dV_i}{dt} &= \sum_{j=1}^n F_{ji}^c + F_i^g, \\ I_i \frac{dw_i}{dt} &= \sum_{j=1}^n (r_{ij} \times F_{ji}^c) + M_i^e. \end{aligned} \quad (1)$$

In the equations above,  $m_i$ ,  $I_i$ ,  $V_i$ , and  $w_i$  represent the mass, moment of inertia, and translational and rotational velocities of particle “ $i$ ”;  $F_i^g$  is the gravitational force;  $r_{ij}$  is the vector pointing from element “ $i$ ” to “ $j$ ”.

The contact force  $F_{ji}^c$  includes two parts: normal contact force  $F_{ji}^{cn}$  and tangential force  $F_{ji}^{cs}$ , and they are shown as follows:

$$\begin{aligned} F_{ji}^{cn} &= -k_n \cdot \Delta u_{ij}^n + \beta_n \cdot V_{ji}^n, \\ F_{ji}^{cs} &= -k_s \cdot \Delta u_{ij}^s + \beta_s \cdot V_{ji}^s, \\ |F_{ji}^{cs}|_{\max} &\leq \mu |F_{ji}^{cn}|, \end{aligned} \quad (2)$$

where  $k$  and  $\beta$  represent the stiffness and damping coefficients, respectively, and  $n$  and  $s$  represent the normal and tangential directions, respectively.  $\mu$  is the friction coefficient;  $\Delta u_{ij}^n$  and  $\Delta u_{ij}^s$  delegate the normal and tangential deformations; and  $\Delta V_{ij}^n$  and  $\Delta V_{ij}^s$  are the normal and tangential relative velocities of two contacted particles.

The DEM simulation is carried out in a quasi-two-dimensional condition too, according to the experimental setup for comparative study. Moreover, the interaction model in DEM is called the “spring-dashpot” model. It is suitable for present simulation since the particle material is plexiglass where the collision between the particles is considered as incomplete elastic because of the damping effect of the material.

### 3. Results and Discussions

#### 3.1. Observation of Stagnant Zone

3.1.1. *Experimental Observation.* Side area method (Figure 1) can be designed to investigate the stagnant zone in the lower corners of the vessel, which focuses on the characteristics of the interface between different color pebbles.

The experiment begins with the random packing by prefilling the colorless pebbles in the vessel. Then, colorless

pebbles were falling from the middle inlet tube, and black pebbles were falling from both sides of inlet tubes, with the ratio of 14 : 122 : 14. At the same time, pebbles were flowing from the discharge hole with 150 pebbles per minute. The stagnant zone is most possible to occur in both corners of the vessel. The initially filled pebbles which still remained in the vessel are surrounded by the inserted black pebbles and seem more conspicuous, as shown in Figure 1.

As is illustrated in Figure 1, the black pebbles area and the sides and bases of the vessel enclose up the two stagnant zones, where the initially filled pebbles still remained in the vessel. After about 22 h of operation, the stagnant zone still remained with about 2.8 times of the total number recirculated. However, the pebbles in stagnant zone were not completely static. It is obvious that the size of the stagnant zone decreased with the recirculation continuing. Figure 1 shows the size of the stagnant zones after 22 h, 40 h, and 60 h, respectively, but finally the stagnant zone stayed with a stable size and did not change any more, which illustrates that the stagnant zone exists under the experimental conditions. This is apparently unacceptable in practical reactor core.

3.1.2. *Simulation Observation.* Similarly, the forming of stagnant zone has been carried out with the DEM simulation. The parameters of the simulation are the same with the above experiment. Firstly, green pebbles were prefilled to form the initial random packing state; then, green pebbles were falling from the middle inlet tube, and red pebbles were falling from both sides of inlet tubes, with the ratio of 14 : 122 : 14.

Figure 2 shows the DEM simulation results. By comparing Figure 1 with Figure 2, it indicates that DEM simulation is remarkably in agreement with experiment results, where the friction coefficient of both particle-particle and particle-wall is 0.2 and cone angle is 30°.

3.2. *Stagnant Zone Definition.* The movement information, such as the mean-streamline and the mean stagnant time, of the marking pebbles in different radial position could reflect the statistical characteristics of the movement of the pebbles when there is plenty of statistical data. This paper shows two different methods to define the stagnant zone in order to analyze the effects of the bed configuration on the shape, size, and other mechanical mechanisms and characteristics of the stagnant zone.

The mean-streamline method to define the stagnant zone is mainly based on the section about the experimental observation of the stagnant zone with the side area method. As shown in Figure 1, the obvious interface of the experiment between the white pebbles and black pebbles will finally remain stable as time went on; that is to say, the size of the white pebble zone and the black pebble zone will not change any more. The scope of the small mixing zone (Figure 4) between the white and black pebble zones is limited; that is to say, the curved surface  $S$  exists which is made up of the mean-streamlines of the mixing zone. If the time-average flux of the pebble flow through the interface between the different color pebbles is not equal to zero, then the smooth, stable interface will not exist. In summary, the curved surface  $S$  and

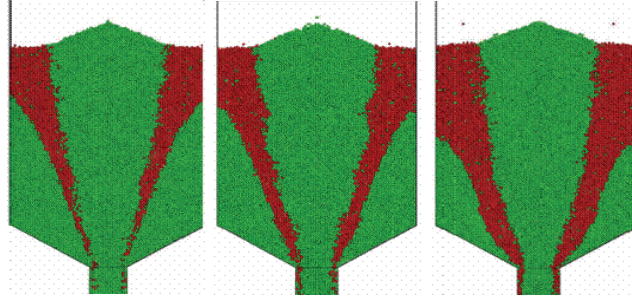


FIGURE 2: Sketch of the stagnant zone of different time with the side area method with DEM method.

the interface of the two zones coincide with each other, when the central zone and the side zone stay stable.

The mean stagnant time method to define the stagnant zone is mainly based on the marking pebble method. As shown in Figure 5, the stagnant time of the marking pebbles from the upper surface to the outlet hole in the vessel will be recorded, which will be meaningful for analyzing the pebble flow when the data is enough. This method can also get the information about the mean-streamline.

**3.2.1. Mean-Streamline.** In the experiment with  $h = 1$  m, the mean-streamlines of the pebbles after  $t = 60$  h in the pebble bed are smooth and symmetrical. The base cone lacks the arc transition, which causes the existence of the very slow flow zone.

As easily inferred, when the pebbles fall through the cylinder vessel where the outlet tube or orifice has the same diameter of the main body, that is to say, when the pebbles are regarded as a whole body, they are only affected by the gravity and the friction with the wall. The streamlines of the pebbles are almost vertically downward, and the stagnant zone will disappear resulting from the changing of the vessel shape.

Considering the influence of the geometric factor, the size of stagnant zone can be defined as follows: the stagnant zone is the area in the corner of the cone-base section between mean-streamline in the side area method where pebble is nestling against the wall of the vessel at initial time and the outline of the wall of the vessel which is the green zone in Figure 3, when the region shape remains a dynamic equilibrium or time stationary. Then, the area of the stagnant zone  $A_s$  can be calculated.

A mixing zone exists between the stagnant zone and the central zone illustrated in Figure 4 which makes the stagnant zone have a blurry boundary. The mixing zone is crucial and is required to be small enough in the real pebble-bed reactor. One way to minimize the mixing zone is to insert plates [24] in the separating surfaces between the central region and the side region at the top section of the vessel. In addition, the competency of the guide ring in a practical reactor needs more theoretical analysis and experimental verifications. The bad influence of the mixing zone on defining the size of the stagnant zone will be reduced when using the mean-streamline method from the statistical point of view.

To analyze the relationship of the size of the stagnant zone and the whole pebble bed, it is necessary to define the

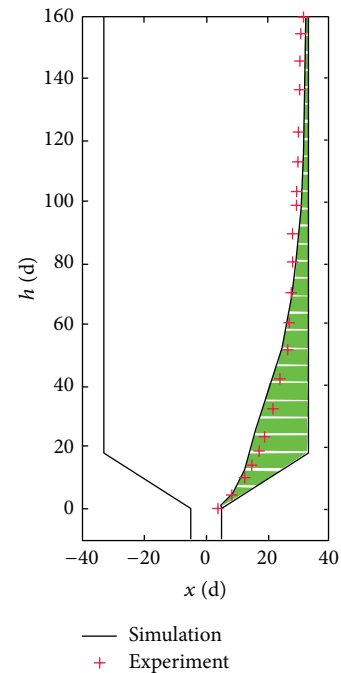


FIGURE 3: The mean-streamline method of the definition of stagnant zone ( $f = 0.2$ ,  $A = 30^\circ$ , and  $h = 160$  d).

stagnant zone area fraction  $\alpha_s$  which is the ratio of the area of stagnant zone  $A_s$  to the whole zone  $A_w$  which is filled with the pebbles in the pebble bed.

**3.2.2. Mean Stagnant Time.** Figure 5 shows the distribution of the mean stagnant time of the pebbles in the experiment ( $h = 1$  m). Because the stagnant time is related to the load and drainage rate of the pebbles, the critical stagnant time hardly takes effect about the stagnant zone definition actually. It is more reasonable to describe the characteristics of the pebble flow when the mean stagnant time is replaced by the drainage pebble rate. That is to say, paying more attention to the number of the drainage pebbles before the marking pebble flows out of the orifice is more meaningful. But the experimental data in this paper is received in the regular or fixed drainage pebble rate, so there is much comparability in the mean stagnant time of different pebbles in the experiment installation.

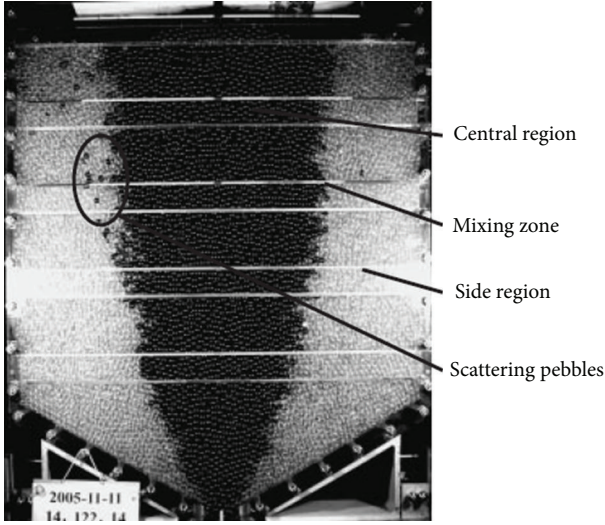


FIGURE 4: Establishment of the two-region arrangement in experiment without guide plates.

The stagnant zone can be defined as follows: the stagnant zone is the area where the data of the mean stagnant time of pebbles or the element balls in the pebble bed exceed the limit or design value. The pebbles in the stagnant zone are not critically static, although they cannot flow out of the orifice in a certain time.

The mean stagnant time method is diverse from the mean-streamline method in defining the stagnant zone in the following aspects. Firstly, the mean stagnant time method is usually effective when used to describe the change of the size of the stagnant zone dynamically. On the contrary, the mean-streamline method focuses on the stagnant zone when it gets its steady state. Meanwhile, the mean-streamlines are basically unchanged. Secondly, the mean-streamline method describes the stagnant zone in space, but the mean stagnant time method focuses on time. Thirdly, the data must be enough for the mean stagnant time method to show the meaningful statistical information, while it is not necessary for the mean-streamline method. The mean-streamline method has more advantages than the mean stagnant time method in attaining the pebble flow information in 3D experiments. But the results of the mean stagnant time seem more direct and visual and show more quantification. Also, in the nuclear reactor, the stagnant zone is the area where the burnup fraction of the fuel element can reach a certain value after which it goes through the reactor core one time in the pebble flow. This method is complicated because it is related to the thermal reactor physics and needs much more data, such as the velocity and the route of the movement of the pebbles.

In this paper, we do not use the burnup fraction method because it cannot give a precise definition of the stagnant zone. The size of the stagnant zone is changing with time and finally becomes fixed. In this paper, we mainly use the mean-streamline method and the mean stagnant time method.

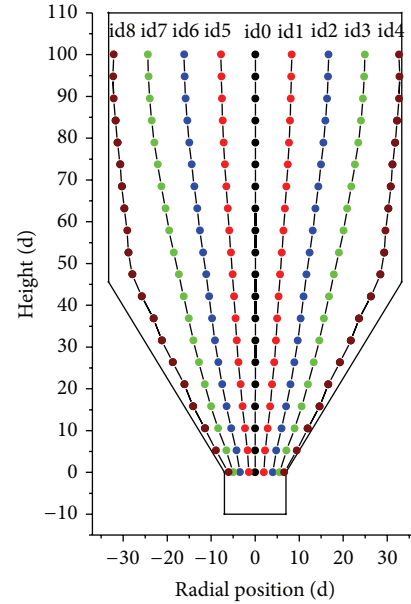


FIGURE 5: Distribution of the mean stagnant time and the streamline of the marking pebbles in the experiment ( $h = 75 d$ ).

3.3. *Effects of Bed Configuration on Stagnant Zone.* Investigation on parameter effects of pebble flow is meaningful and significant to understand the physical mechanism of quasi-static pebble flow and to explore how to minimize the stagnant zone.

In this section, we will provide some information of parameter effect on the pebble packing under recirculation operation mode, including different height of the experiment installation, different friction coefficient, and different base cone angle. In order to facilitate the comparison, only one parameter was altered in one case; the rest such as operation mode, rate of discharging, and ratio of loading were unchanged.

Geometric design plays the most important part in the pebble flow, including configuration of vessel, height, width, discharging hole diameter, pebble diameter, and base cone angle, on which some important dimensionless numbers have been derived. We only investigate the height; base cone angle influences the pebble flow under our experiment conditions here.

3.3.1. *The Bed Height Effect.* The simulation and experiment have been carried out to analyze the stagnant zone in the pebble-bed reactor. Figure 6 shows the results of DEM simulation on different bed heights from  $h = 75 d$  to  $h = 160 d$  on the base cone angle  $30^\circ$  under  $f = 0.2$ . The ratio of loading pebbles was set to be 14 : 122 : 14; discharging pebble was 150 pebbles per minute. Snapshots were taken under the side-inserting pebble manner at intervals to record the changing of the size of the stagnant zone. Only a part of them were presented here.

The DEM simulation of the changing process of the stagnant zone on different bed height demonstrates the following: the changing process of the size of the stagnant

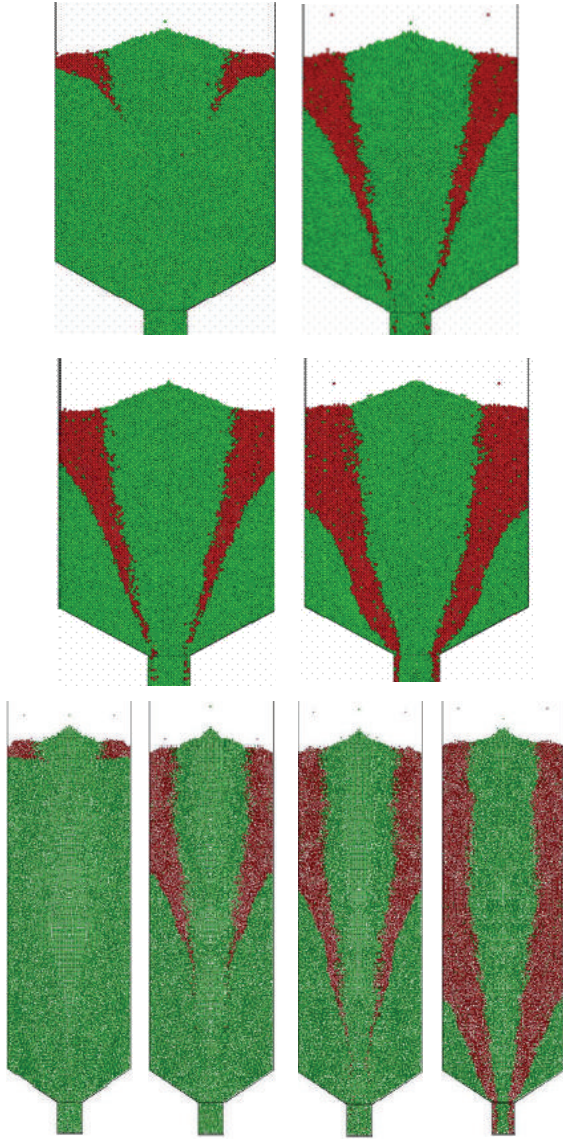


FIGURE 6: DEM simulation of stagnant zone on different bed height from  $h = 75$  d to  $h = 160$  d ( $f = 0.2$ ,  $A = 30^\circ$ ).

zone can be affected by the pebble-bed height. This change is related to the fact that more time will be needed for the pebbles to flow through the pebble bed with the height of 160 d under the same discharging rate. That is to say, pebbles with the same velocity require more flow time for transferring a longer distance. The changing of the height of the pebble bed almost has an impact on the pebbles in the lower corner of the pebble bed initially. Meanwhile, the lateral or radial diffusion of the pebbles tends to become more intensive with the more space and time provided on the condition of  $h = 160$  d.

Figures 5 and 7 show the final results about the distribution of the mean-streamlines of the marking pebbles from id0 to id8 in the experiments with  $h = 75$  d and  $h = 160$  d on the base cone angle  $30^\circ$  under  $f = 0.2$  with the same loading and discharging rate. The position of the pebbles from id0 to id8 presents a symmetrical distribution.

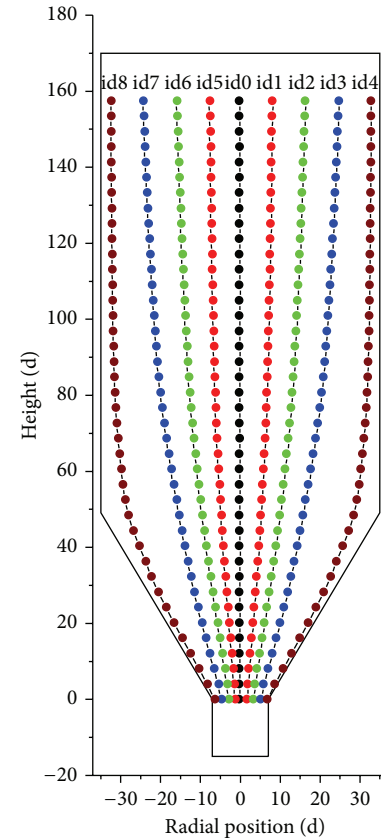


FIGURE 7: Distribution of the mean stagnant time and streamline of the marking pebbles in the experiment ( $h = 160$  d).

The experiment results of the mean-streamlines with different bed height denote the following.

The streamlines of the marking pebbles in the pebble bed are almost smooth and symmetrical. Pebbles in the lower corner of the pebble bed flow more slowly, and this zone may have a significant influence on the pebble flow which makes the streamline of id4 unable to adapt to the shape of the wall. Then, a triangle zone exists between the streamline and the wall named the stagnant zone. The pebbles in the stagnant zone are almost static which squeeze the central pebbles intensively and cause the flow irregularity in the pebble bed; as a result, the bend of the streamline exists much earlier than that of the wall of the pebble bed. As shown in Figure 7, about experiment results of the distribution of the mean-streamlines of the experiment with  $h = 160$  d, the mean-streamlines in the upper zone of the pebble bed are almost vertical, which are different from those in the lower zone. From the perspective of the streamlines, the upper zone of the pebble bed may have a particularly small impact on the lower zone of the pebble bed. In other words, the streamlines in the lower zone of the experiment with  $h = 160$  d may have an identical shape with those in the experiment with the height  $h = 75$  d.

As mentioned above, the streamlines of the upper zone of the pebble bed with height  $h = 160$  d may have little influence on the size of the stagnant zone with the mean-streamline

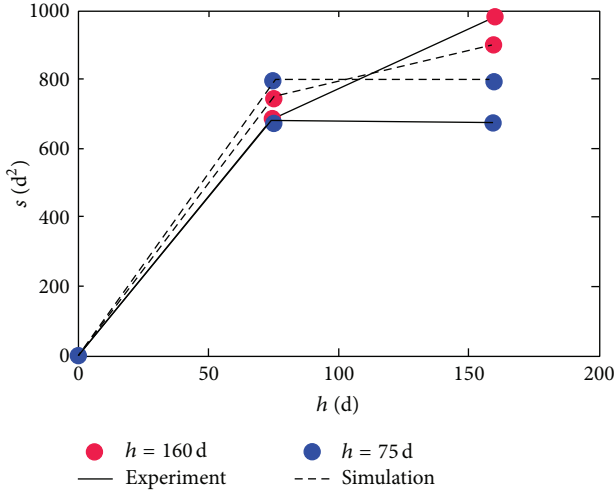


FIGURE 8: The relationship between the height of the pebble bed and the area of the stagnant zone about the experimental and simulation results.

definition method. To verify this consideration, the area of the stagnant zone  $A_s$  on the core angle  $30^\circ$  under  $f = 0.2$  has been calculated in the experiments with  $h = 75$  d and  $h = 160$  d with the data of the experiment and simulation given in Figure 8.

The relationship between the height of the pebble bed and the area of the stagnant zone in Figure 8 can be illustrated as follows.

- (1) The  $A_s$  of  $h = 160$  d is larger than that of  $h = 75$  d, which may show that the bed of pebbles is higher and the area of the stagnant zone is larger. However, the area of the lower zone with the height 75 d in the pebble bed  $h = 160$  d holds the great majority of the whole stagnant zone. It shows that the pebble flow in the lower zone plays a significant role in the formation of the stagnant zone.
- (2) Moreover, the area of the lower zone with the height 75 d in the pebble bed  $h = 160$  d is almost the same as the area of the stagnant zone of  $h = 75$  d. This fact indicates that the upper zone of the pebble bed has less impact on the mean-streamlines of the lower zone when the height is beyond a certain limit.
- (3) The differences exist between the results of simulation and those of the experiment. The DEM may have its own disadvantages when calculating the area of the stagnant zone quantitatively, but it can be more useful for analyzing qualitatively.

Figure 9 shows the results about the distribution of the mean stagnant time of the experiments with  $h = 75$  d and  $h = 160$  d with the same loading and discharging rate as above. The physical time in simulation was determined by means of counting the discharged pebbles.

In the experiment with  $h = 75$  d, the stagnant time of the marking pebble id4 is more than ten times that of the marking pebble id0. The pebble id4 is against the cylinder wall, and the

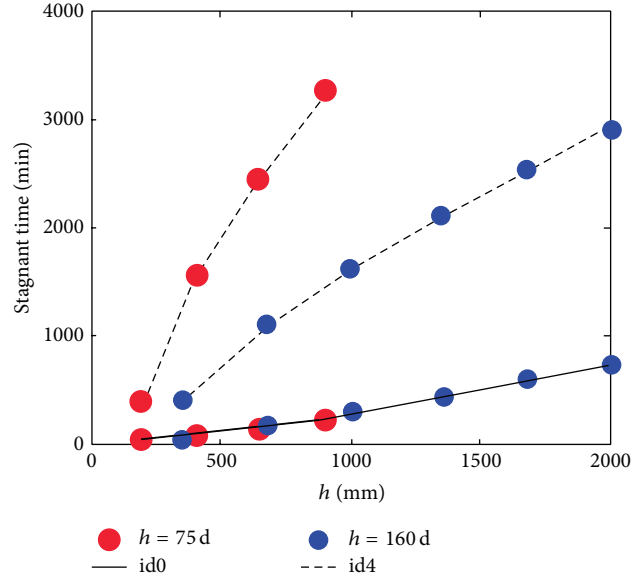


FIGURE 9: Experiment results of stagnant time of the id0, id4 and the stagnant time ratio id2/id0, id4/id0, of the experiment installation with  $h = 75$  d and  $h = 160$  d.

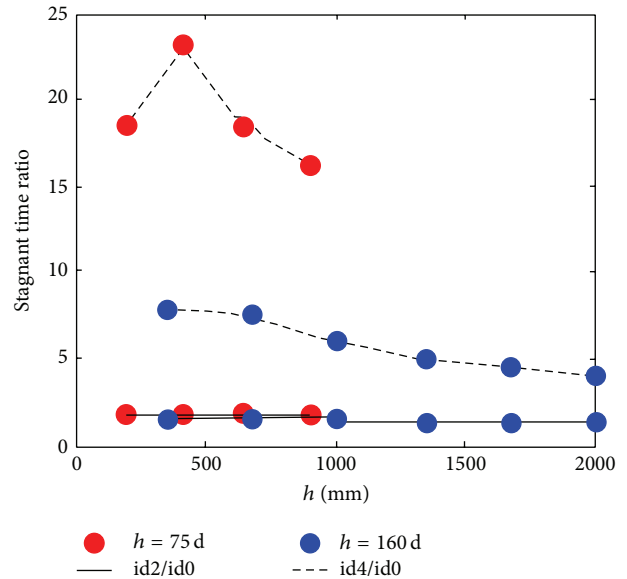


FIGURE 10: Experiment results of stagnant time ratio id2/id0, id4/id0, of the experiment installation with  $h = 75$  d and  $h = 160$  d.

id0 is in the central region, as shown in Figure 5. In order to explore the height's impact on stagnant time, Figures 9 and 10 show the experiment's impact results of stagnant time of the id0, id4 and the stagnant time ratio id2/id0, id4/id0, of the experiment installation with  $h = 75$  d and  $h = 160$  d.

The experiment shows that the stagnant time ratio id4/id0 of the experiment installation with  $h = 160$  d is much smaller than that with  $h = 75$  d. The number of the ratio id1/id0, id2/id0, id3/id0 in the upper zone of the experiment with  $h = 160$  d is similar to that of the experiment with  $h = 1$  m at the

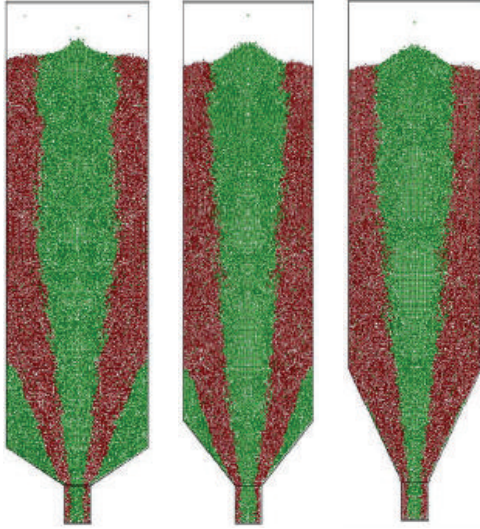


FIGURE 11: The result of the DEM simulation of the stagnant zone on the cone angles 30°, 45°, and 60° ( $f = 0.2$ ,  $h = 160$  d).

same height. The pebble flow in the upper region has impact on the lower region, but the impact is not very large. However, the position of id4 against the cylinder wall is special. In the experiment with  $h = 75$  d, the id4 is close to the cylinder wall, but in the experiment with  $h = 160$  d, at height 1 m, the trace of id4 deviates from the cylinder wall. That is the reason why the ratio of stagnant time id4/id0 of the experiment  $h = 75$  d is much larger than that of the experiment with  $h = 160$  d. This is significant for us to find the way to avoid the stagnant zone.

**3.3.2. Base Angle Effect.** Figures 11 and 12 show the result of the DEM simulation of the stagnant zone on the cone angles 30°, 45°, and 60° under  $f = 0.2$  with pebble bed  $h = 160$  d.

We can find that the base cone angle is larger, and the stagnant zone is smaller, which plays a significant role in the flow field. When the base cone angle is not large enough, the slow zone exists. The pebbles in the stagnant zone are easier to move on a more inclined base slope, because the more inclined slope provides the larger driving force along the slope. That is why the increasing cone angle can decrease the scale of stagnant zone, and it almost disappears in the case of 60° cone angle. In the case of 90° cone angle, the whole pebbles are forced by the gravity and the friction with the wall, and the streamlines are almost vertical; then, the stagnant zone will disappear totally. So we can infer that the existence of the inclines of the wall plays a leading role in the forming of the stagnant zone.

Figures 13 and 14 indicate the simulation results about the mean stagnant time of the marking pebbles id0, id2, and id4 and the stagnant time ratio of id2, id4 to id0 in different height on the cone angles 30°, 45°, and 60° under  $f = 0.2$  on condition that the total height is 160 d. The information can be inferred as follows.

(1) The stagnant time of the marking pebbles id0 and id2 is almost the same at different heights on the angles

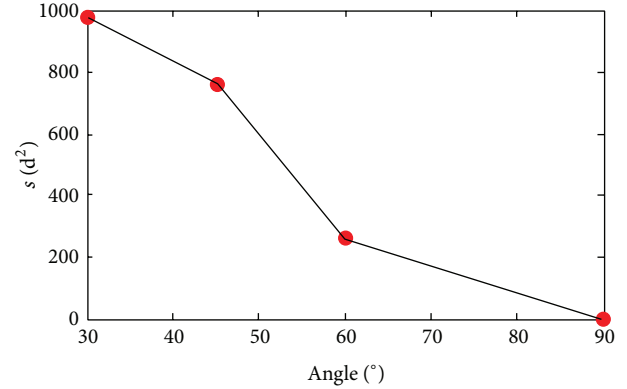


FIGURE 12: The simulation results about the cone angle and the stagnant zone size ( $f = 0.2$ ,  $h = 160$  d).

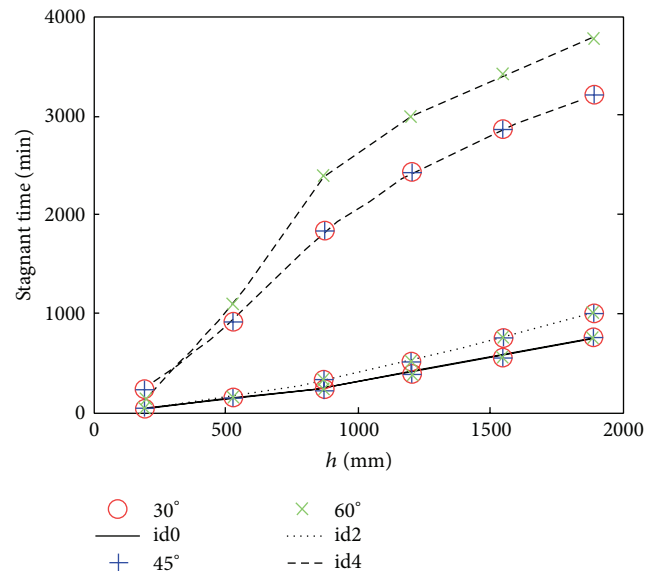


FIGURE 13: Simulation results about the mean stagnant time of the marking pebbles id0, id2, and id4, on the cone angles 30°, 45°, and 60° ( $f = 0.2$ ,  $h = 160$  d).

30°, 45°, and 60°. Meanwhile, the pebbles id0 and id2 which are in the central zone of the pebble bed initially have passed the same vertical displacement, so we can infer that the changing of the cone angle has less impact on the size of the mean vertical velocity of the pebbles in the central zone with the same discharging and loading rate.

- (2) The stagnant time of the pebble id4 against the wall is much larger than that of id0 and id2 in the central zone when the height of the pebble bed ranges from 200 mm to 1900 mm on different cone angles. Based on the consideration above, the existence of the inclines of the wall may be the main reason for the longer stagnant time of the pebbles against the wall.
- (3) The stagnant time of id4 does not change much on different cone angles. But the stagnant time of id4 on

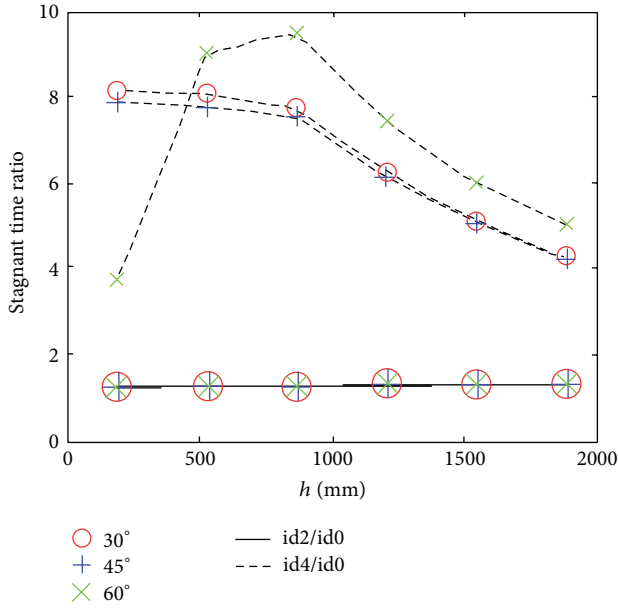


FIGURE 14: Simulation results about stagnant time ratio of id2, id4 to id0 in different height on the cone angles 30°, 45°, and 60° ( $f = 0.2$ ,  $h = 160$  d).

cone angle 60° is larger than that on the angles 30° and 45°, while the stagnant time of id4 on angles 30° and 45° is almost the same. As we can see in Figure 13, the pebble id4 transferring from  $h = 1000$  mm to  $h = 500$  mm takes up longer time than the other two angles. It may relate with the fact that the mean-streamline of id4 on 60° is much closer to the wall than the other two cone angles. This fact must be paid attention to while designing the reactor core.

**3.3.3. Friction Coefficient Effect.** The friction coefficient offers more complicated influence on pebble flow and presents a strong nonlinearity. The related work was yet very insufficient. The simulation results of the stagnant zone shape and size have been shown in Figure 15 under  $f = 0.1$ ,  $f = 0.2$ , and  $f = 0.4$  on the base cone angle 30° with  $h = 75$  d.

As is shown in Figure 16, when the friction coefficient is small enough, for example,  $f = 0.1$ , the stagnant zone decreases but has not yet disappeared due to being far away from the drainage hole. However, this kind of change of the size of stagnant zone is not linear.

The driving force and resistance force influence the existence, shape, and size of the stagnant zone. The stagnant zone receives not only the resistance from the base wall but also the driving force from the outer flowing pebbles. When friction coefficient increases from 0.1 to 0.2, the stagnant zone tends to increase by a large margin because the resistance force between the stagnant zone and the base wall plays a more important role than the driving force between stagnant zone and the outer flowing pebbles. Meanwhile, when the friction coefficient becomes from 0.2 to 0.4, the stagnant zone tends not to increase obviously due to the increase of the driving force from outer neighbor pebbles.

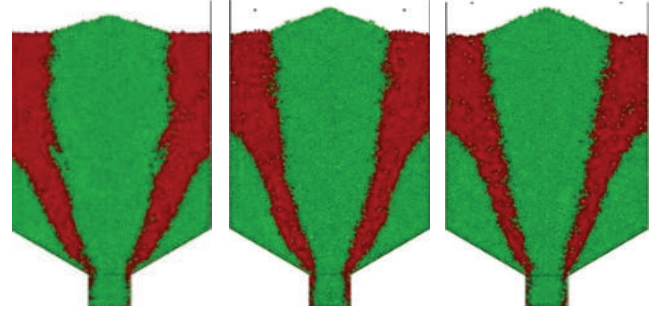


FIGURE 15: The result of the DEM simulation of the stagnant zone on the friction coefficients 0.1, 0.2, and 0.4 ( $A = 30^\circ$ ,  $h = 160$  d).

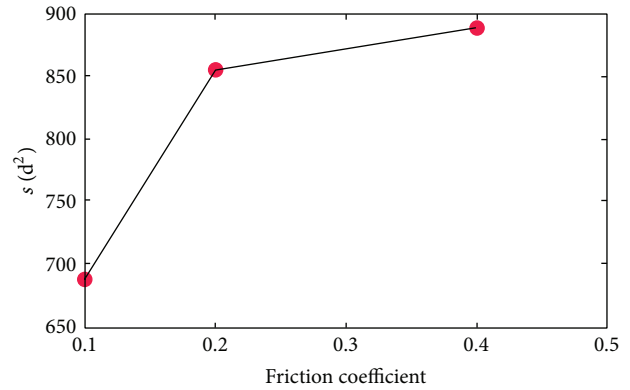


FIGURE 16: The simulation results about the friction coefficient and the stagnant zone size ( $f = 0.2$ ,  $h = 160$  d).

## 4. Conclusion

In this paper, the stagnant zone in the gravity-driven pebble bed has been analyzed via the experimental method (side area method) and DEM simulation. The mean-streamline method to define stagnant zone and to calculate the proportion of this has been proposed with considering the undesirable effect of the mixing zone. Meanwhile, the stagnant time method with tracking the time of the marking balls until they are discharged from the orifice has been applied to explore the kinematics characteristics of the pebbles with different coordination in the quasi-static pebble flow field. We also discussed the effects of bed configuration on stagnant zone including the bed height effect, base angle effect, and the friction coefficient effect and can summarize as follows.

- (1) The pebble flow in the lower zone plays a significant role in the formation of the stagnant zone. The upper zone of the pebble bed has less impact on the mean-streamlines of the lower zone when the height is beyond a certain limit. Bed height affects the stagnant zone slightly when exceeding a certain height.
- (2) The base angle has negative prominent correlation with the stagnant zone; the angle is larger, and the area of the stagnant zone is smaller. The existence of the inclines of the wall plays a leading role in the formation of the stagnant zone.

- (3) The area of the stagnant zone increases more rapidly with the friction coefficient from 0.1 to 0.2 than that with the friction coefficient from 0.2 to 0.4. The mechanism about how the friction influences the area of the stagnant zone and the overall flow field deserves to be deeply investigated.
- (4) Thus, it could be suggested that smooth transition from bases to sides, larger base cone angle or discharge hole, and less width of the vessel will be favorable to avoid the stagnant region.

## Disclosure

This paper has been approved by all authors; none of the material presented in the paper is submitted or published elsewhere; and the paper does not contain any information with restricted access or proprietary content.

## Conflict of Interests

The authors declare that there is no conflict of interests regarding the publication of this paper.

## Acknowledgments

The authors are grateful for the support of this research by the National Natural Science Foundation of China (Grants nos. 11072131 and 51106180) and China Postdoctoral Science Foundation (2013M540964).

## References

- [1] W. Magwood, "Roadmap to the next generation nuclear power systems: a vision for a powerful future," *Nuclear News*, vol. 43, pp. 35–37, 2000.
- [2] Z. Y. Zhang, Z. X. Wu, Y. H. Xu, Y. L. Sun, and F. Li, "Design of Chinese modular high-temperature gas-cooled reactor HTR-PM," in *Proceedings of the 2nd International Topical Meeting on High Temperature Reactor Rechnology*, Beijing, China, September 2004.
- [3] A. Koster, H. D. Matzner, and D. R. Nicholsi, "PBMR design for the future," *Nuclear Engineering and Design*, vol. 222, no. 2-3, pp. 231–245, 2003.
- [4] A. C. Kadak and M. V. Berte, "Modularity in design of the MIT pebble bed reactor," in *Proceedings of the American Nuclear Society Meeting*, Reno, Nev, USA, November 2001.
- [5] R. Schulten, "Pebble bed HTRs," *Annals of Nuclear Energy*, vol. 5, no. 8–10, pp. 357–374, 1978.
- [6] H. M. Jaeger, S. R. Naegel, and R. P. Behringer, "Granular solids, liquids and gases," *Reviews of Modern Physics*, vol. 68, no. 4, pp. 1259–1273, 1996.
- [7] J. M. Ottino and D. V. Khakhar, "Mixing and segregation of granular materials," *Annual Review of Fluid Mechanics*, vol. 32, pp. 55–91, 2000.
- [8] D. Talbot, "The next nuclear plant," *Technology Review*, vol. 105, no. 1, pp. 54–59, 2002.
- [9] J. Choi, A. Kudrolli, and M. Z. Bazant, "Velocity profile of granular flows inside silos and hoppers," *Journal of Physics Condensed Matter*, vol. 17, no. 24, pp. S2533–S2548, 2005.
- [10] S. B. Rochal, V.P. Dmitriev, V. L. Lorman, and P. Tolédano, "Local mechanism for crystal-quasicrystal transformations," *Physics Letters A*, vol. 220, no. 1–3, pp. 111–116, 1996.
- [11] A. Samadani, A. Pradhan, and A. Kudrolli, "Size segregation of granular matter in silo discharges," *Physical Review E*, vol. 60, no. 6, pp. 7203–7209, 1999.
- [12] J. Choi, A. Kudrolli, R. R. Rosales, and M. Z. Bazant, "Diffusion and mixing in gravity-driven dense granular flows," *Physical Review Letters*, vol. 92, no. 17, Article ID 174301, 2004.
- [13] A. Medina, J. Andrade, and C. Treviño, "Experimental study of the tracer in the granular flow in a 2D silo," *Physics Letters A*, vol. 249, no. 1-2, pp. 63–68, 1998.
- [14] D. M. Mueth, G. F. Debregeas, G. S. Karczmar, P. J. Eng, S. R. Nagel, and H. M. Jaeger, "Signatures of granular microstructure in dense shear flows," *Nature*, vol. 406, no. 6794, pp. 385–389, 2000.
- [15] E. R. Weeks, J. C. Crocker, A. C. Levitt, A. Schofield, and D. A. Weitz, "Three-dimensional direct imaging of structural relaxation near the colloidal glass transition," *Science*, vol. 287, no. 5453, pp. 627–631, 2000.
- [16] J.-C. Tsai and J. P. Gollub, "Slowly sheared dense granular flows: crystallization and nonunique final states," *Physical Review E*, vol. 70, no. 3, Article ID 031303, 2004.
- [17] M. Menon and D. J. Durian, "Diffusing-wave spectroscopy of dynamics in a three-dimensional granular flow," *Science*, vol. 275, no. 5308, pp. 1920–1922.
- [18] J. S. Goodling, R. I. Vachon, W. S. Stelpflug, and S. J. Ying, "Radial porosity distribution in cylindrical beds packed with spheres," *Powder Technology*, vol. 35, no. 1, pp. 23–29, 1983.
- [19] Y. Cohen and A. B. Metzner, "Wall effects in laminar flow of fluids through packed beds," *AIChE Journal*, vol. 27, no. 5, pp. 705–715, 1981.
- [20] R. M. Nedderman and U. Tüzün, "A kinematic model for the flow of granular materials," *Powder Technology*, vol. 22, no. 2, pp. 243–253, 1979.
- [21] W. W. Mullins, "Stochastic theory of particle flow under gravity," *Journal of Applied Physics*, vol. 43, no. 2, pp. 665–678, 1972.
- [22] M. Z. Bazant, "The Spot model for random-packing dynamics," *Mechanics of Materials*, vol. 38, no. 8–10, pp. 717–731, 2006.
- [23] P. A. Cundall and O. D. L. Strack, "A discrete numerical model for granular assemblies," *Géotechnique*, vol. 29, no. 1, pp. 47–65, 1979.
- [24] X. T. Yang, W. P. Hu, S. Y. Jiang, K. K. L. Wong, and J. Y. Tu, "Mechanism analysis of quasi-static dense pebble flow in pebble bed reactor using phenomenological approach," *Nuclear Engineering and Design*, vol. 250, pp. 247–259, 2012.
- [25] C. H. Rycroft, G. S. Grest, J. W. Landry, and M. Z. Bazant, "Analysis of granular flow in a pebble-bed nuclear reactor," *Physical Review E*, vol. 74, no. 2, Article ID 021306, 2006.

## Research Article

# Study on Thermal-Hydraulic Behavior of an Integral Type Reactor under Heaving Condition

Beibei Feng,<sup>1</sup> Xingtuan Yang,<sup>1</sup> Shengqiang Li,<sup>1</sup> Yanfei Sun,<sup>1</sup>  
Jiyuan Tu,<sup>1,2</sup> and Shengyao Jiang<sup>1</sup>

<sup>1</sup> Key Laboratory of Advanced Reactor Engineering and Safety, Ministry of Education of China,  
Institute of Nuclear and New Energy Technology, Tsinghua University, Beijing 100084, China

<sup>2</sup> School of Aerospace, Mechanical & Manufacturing Engineering, RMIT University, Plenty Road, Bundoora, VIC 3083, Australia

Correspondence should be addressed to Shengyao Jiang; [jiangshy@tsinghua.edu.cn](mailto:jiangshy@tsinghua.edu.cn)

Received 5 November 2013; Revised 20 February 2014; Accepted 20 February 2014; Published 8 April 2014

Academic Editor: Luciano Burgazzi

Copyright © 2014 Beibei Feng et al. This is an open access article distributed under the Creative Commons Attribution License, which permits unrestricted use, distribution, and reproduction in any medium, provided the original work is properly cited.

A self-developed program was used to study the thermal-hydraulic behavior of an integral type reactor under heaving condition. Comparison of calculated results with the data of experiments performed on a natural circulation loop designed with reference to an integral type reactor of Tsinghua University in inclination, heaving, and rolling motions was carried out. Characteristics of natural circulation in heaving motion and effect of motion parameters on natural circulation were investigated. Results indicated that: (1) long-period heaving motion would lead to more significant influence than inclination and rolling motion; (2) it was an alternating force field which consisted of gravity and an additional force that decided the flow temperature and density difference of natural circulation; (3) effect of strength  $k$  and cycle  $T$  of heaving motion on flow fluctuation of natural circulation and condensate depression of heating section outlet was performed.

## 1. Introduction

Integral type reactor with its coolant system components in reactor vessel has wide applications due to its passive safety property. 5 MW experimental low temperature nuclear heating reactor (NHR) of Tsinghua University is a low-power integral type reactor with modular and self-stabilization which has been applied to the engineering fields of heat supply and seawater desalination [1, 2]. As part of the studies responding to the application of NHR as ship power, Institute of Nuclear and New Energy Technology (INET) of Tsinghua University built an experimental loop with reference to NHR to investigate the effect of rolling motion and inclination motion (two typical oceanic movements) on natural circulation [3–5]. A program was also developed to provide a tool for investigating the effect of heaving motion (the third typical oceanic movement) on natural circulation which could not realized through the experimental loop.

On land, successful operation of NHR has proved the feasibility of its technical solutions. Under oceanic conditions,

it needs revalidation through experiments resulting from the effect of oceanic environment on thermal-hydraulic behavior of natural circulation due to the additional movements caused by oceanic motions, such as rolling, heaving, and inclination. So, INET built a rolling experimental apparatus with reference to NHR to simulate oceanic motions, which consisted of a symmetrical two-circuit test loop and auxiliary equipment [6, 7]. Geometric parameters of experimental rolling apparatus was designed completely the same as NHR to investigate the effect of same strength of oceanic motion on natural circulation, and operation parameters were arranged the same as NHR. Due to the restriction of experimental rolling apparatus, effect of heaving motion on thermal-hydraulic behavior of natural circulation could not be investigated experimentally and a self-developed program was accordingly developed to accomplish this work. The aim of the present paper was to describe our comprehensive analysis results concerning natural circulation under heaving motion and effect of motion parameters on natural circulation obtained using the self-developed program. Comparison

of effect of inclination motion and rolling motion on natural circulation between calculation and experimental data was conducted to validate the self-developed program. A heaving strength parameter  $k$  was proposed to describe heaving motion in alternating force field. Flow rate and condensate depression of natural circulation under heaving motion with various cycle  $T$  and strength  $k$  were investigated in detail.

## 2. Experimental System

*2.1. Similarity Analysis.* For two similar physical phenomena, parameters describing the law of the phenomena should be proportionable. Similarity analysis is carried out for catching the dynamics of the coupled physics. In order to guarantee a more clear and comparable comprehension to NHR, mathematical equations of experimental system should have the same solution as NHR. Criteria numbers deduced from momentum equation, energy equation, and thermal boundary condition could be obtained as follows:

$$\begin{aligned} S_t &= \frac{L}{V \cdot t}, & F_r &= \frac{V^2}{g \cdot L}, \\ E_u &= \frac{P}{\rho \cdot V^2}, & R_e &= \frac{\rho V L}{\mu}, \\ P_e &= \frac{\rho c V L}{\lambda}, \\ N_u &= \frac{\partial L}{\lambda}. \end{aligned} \quad (1)$$

For the issue of single-phase flow and heat transfer process, the experimental apparatus and NHR are equivalent when the above criteria numbers are the same. For the heat exchange process of natural circulation, density difference induced by flow temperature and height difference drive the natural circulation. So, Grashof number should be introduced:

$$G_r = \frac{g \beta \Delta T L^3}{\nu^2}. \quad (2)$$

*2.2. Experimental Apparatus.* The experimental setup is made up of three loops (as shown in Figure 1(a)). Test section in experiments is a symmetrical two-circuit loop (primary loop) which is designed exactly based on NHR's structure provided with the same height and width. Primary loop equals to a cut from NHR in the diameter direction, as shown in Figure 1(b). Experimental condition parameters are arranged the same as NHR to simulate the actual environment and achieve high comparative accuracy.

Primary loop consisted of heating section, upper plenum, steam generator, downcomer, and lower plenum. A rolling test bench is built to fix primary loop and oceanic motions, such as rolling and inclination, could be achieved through the movement of the test bench driven by two motors. Three electric heaters (EH) located at the shared part of the two circuits supply the heat source with outlet temperature

220°C. To meet the requirement of heating power, heater tubes are divided into two groups of eight tubes each with 75 V DC operating voltage and 3.7 Kw single-robust power would be achieved. The arrangement of heater tubes and electrifying mode is shown in Figure 1(c). Two double-pipe heat interchangers located on the upper part of each circuit were used, but the amount of heat exchange tubes was reduced proportionality to ensure same heat load on heat exchange area as NHR. The primary loop was mounted on a ship motions simulation platform and could achieve rolling motion with maximum angles of 45° and 20° in  $x$  direction and in  $y$  direction, respectively. The working fluid of the primary loop was demineralized water with a pressure of 4.0 MPa.

The secondary loop consisted of a pump, a heat exchanger, two mixers, and a pressurizer. The coolant for the secondary loop was water driven by a pump rather than natural circulation. The mixer and control valves were used to equally set the coolant temperature and flow rates of the two circuits in order to avoid an unbalanced load. The secondary loop was kept at high pressure (4.0 MPa) to prevent the occurrence of two-phase flow due to the simplicity of the equipment. The pressurizer was filled with high-pressure nitrogen gas in order to adjust and maintain the pressure. The main equipment for the third loop was the cooling tower, through which heat input from the secondary loop was finally emitted into the environment with the coolant circulation.

Main shape and operation parameters are listed in Table 1. Compared with public experimental studies, testing section in this work is designed with following characteristics.

- (a) A symmetrical two-circuit loop which simulate natural circulation of an actual reactor under oceanic motions is more reasonable.
- (b) Same height and width of primary loop as NHR will reflect the real strength of rolling motion.
- (c) Operation parameters of primary loop are arranged the same as NHR to simulate NHR's operation.

## 3. Calculation Model and Validation

*3.1. Mathematical Model.* Mathematical model based on the analysis of experimental system was built first [8–10]. To simplify handling natural circulation in heaving condition, coordinate system was established on the experimental apparatus. It was mathematically an issue in noninertial reference frame of natural circulation under heaving condition. An inertia force was brought into the fluid particle momentum equation in heaving condition resulting from the additional force of oceanic motions.

Continuity equation is as follows:

$$\frac{\partial \rho}{\partial t} + \nabla \cdot (\rho \vec{V}) = 0. \quad (3)$$

Momentum equation is as follows:

$$\frac{D\vec{V}}{Dt} = \vec{f} - \frac{1}{\rho} \nabla P + \frac{1}{\rho} \nabla \cdot (2\mu S). \quad (4)$$

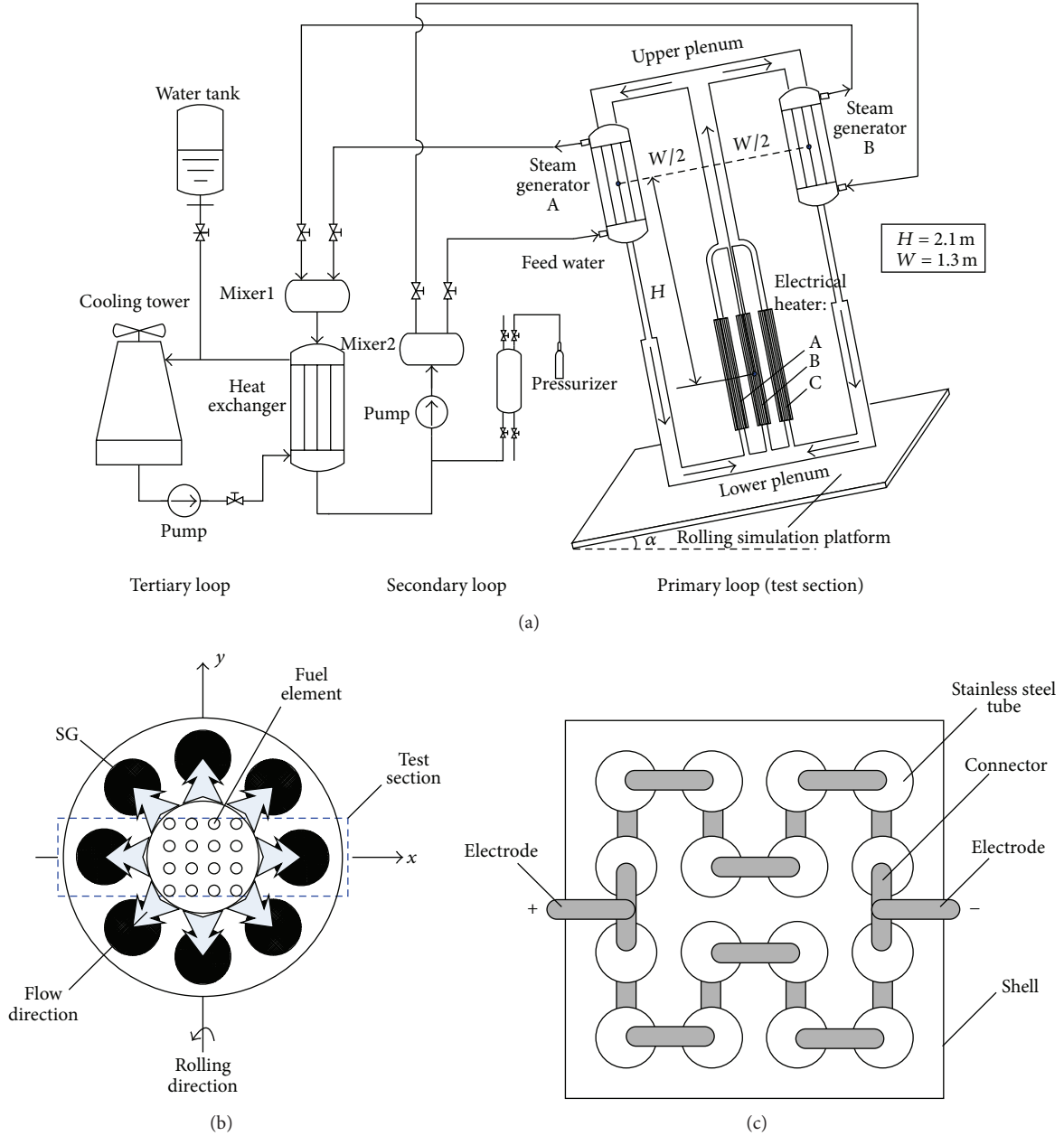


FIGURE 1: Experimental apparatus [6].

Energy equation is as follows:

$$\rho C \frac{DT}{Dt} = \nabla \cdot (\lambda \nabla T), \quad (5)$$

where  $\rho$ ,  $f$ ,  $\mu$ , and  $\lambda$  were the density, mass force, viscosity, and thermal conductivity of the fluid and  $S$  was rate of strain tensor.

$$\vec{f} = \vec{g} - \vec{a}_o - \vec{\omega} \times \vec{r} - \vec{\omega} \times (\vec{\omega} \times \vec{r}) - 2\vec{\omega} \times \vec{V}_r, \quad (6)$$

where  $g$  was acceleration of gravity and  $\vec{a}_o = d^2\vec{r}_o/dt^2$  as an additional force induced by the translational motion of experimental apparatus in  $x$ ,  $y$ , and  $z$  direction.  $\vec{a}_t = \vec{\omega} \times \vec{r}$

was tangential force;  $\vec{a}_n = \vec{\omega} \times (\vec{\omega} \times \vec{r})$  was normal force; and  $\vec{a}_c = 2\vec{\omega} \times \vec{V}_r$  was Coriolis force.

In the case of one-dimensional flow, the Coriolis force was negligible. Assume that  $a_{oz} = kg \cdot \sin(w_d \cdot t)$ ; thus  $g - a_{oz} = (1 - k \sin(w_d \cdot t)) \cdot g$ .

Heaving motion was the vertical translational motion which was in the same direction of gravity. So,  $(g - a_{oz})$  could be treated as alternating gravitational field which was viewed as the product of acceleration of gravity  $g$  and a time-varying coefficient  $(1 - k \sin(w_d \cdot t))$ .

Relative velocity of natural circulation to experimental apparatus was used to describe natural circulation in the above formulas. Symmetric double circulation of primary

TABLE I: Comparison of operation parameters of experimental apparatus and NHR.

	Power (Kw)	Pressure bearing capacity (MPa)	Inlet/outlet temperature of heating section ( $^{\circ}\text{C}$ )
Experimental apparatus			
Operation value	163.054	5.0	179.8/210.1
Design value	164	5.0	180/211
NHR	$3 \times 10^4$	5.0	180/211
	Temperature difference between inlet and outlet of heating section ( $^{\circ}\text{C}$ )	Average temperature of heating section ( $^{\circ}\text{C}$ )	Outlet velocity of heating section ( $\text{m}\cdot\text{s}^{-1}$ )
Experimental apparatus			
Operation value	30.4	194.95	0.3619
Design value	31	195.5	0.37321
NHR	31	195.5	/
	Outlet velocity of heat exchanger ( $\text{m}\cdot\text{s}^{-1}$ )	Natural circulation flow ( $\text{kg}\cdot\text{s}^{-1}$ )	Amount of fuel rod
Experimental apparatus			
Operation value	0.4292	1.2062	48
Design value	0.4318	1.2404	/
NHR	/	227	8784
	Amount of heat exchangers	Type of heat exchanger	Experimental apparatus/NHR ratio
Experimental apparatus			
Operation value	2	Telescopic	1/183
Design value	/	/	/
NHR	18	Telescopic	/

loop that consisted of two inner circuits, one outer circuit, and three mediate channels was observed, as shown in Figure 2. F101, F102, and F103 were used to mark the right heating section, the mediate heating section and the left heating section of primary loop, respectively, and F104, F105 were used to mark the two-side heat exchangers.

**3.2. Program Verification.** Verification of the developed program was carried out through comparison between calculation results and the data of experiments on land and in rolling, inclination conditions. For one-dimensional natural circulation, the key factor was whether the calculated flow resistance was consistent with the experimental results. So, calculated flow resistance would be modified through experiments to make sure of the correction of program. Then, use this program to calculate natural circulation in heaving condition.

Figures 3 and 4 plotted the comparison of experimental results and calculated results of rolling motion with swing angle  $\psi_m = 22.5^{\circ}$  and rolling cycle  $T = 13$  s in zero-power condition and in hot state, respectively. It can be inferred that curves of calculated results were almost the same as that of experimental results of rolling motion with swing angle  $\psi_m = 22.5^{\circ}$  and rolling cycle  $T = 13$  s in zero-power condition and of rolling motion with swing angle  $\psi_m = 45^{\circ}$  and rolling cycle  $T = 18$  s in full-power condition.

## 4. Results and Discussion

**4.1. Characteristics of Natural Circulation in Heaving Motion.** Reference [8] has reported the experimental verification of natural circulation of an actual reactor on land. The program has been proved to be correct through the comparison with experimental data. Comparison of flow characteristics of natural circulation on land with heaving motion was conducted to study the effect of heaving motion on natural circulation.

The additional force induced by heaving motion was acting on natural circulation in a parallel field of force. Effect of heaving motion exhibited a symmetry property for a symmetrical natural circulation loop. Figure 5 plotted the flow and condensate depression of channel outlet of the left and the intermediate heating section in heaving motion with strength  $(g - a_{oz}) = 0.4g$  and cycle  $T = 13$  s. Dotted line in Figure 5 was the dynamic time-average value in steady heaving motion. Figure 6 plotted the flux of primary side of heat exchanger and condensate depression of outlet of secondary side.

Experimental results indicated the following.

- (1) Flux of natural circulation, outlet temperature of heating section, and temperature of secondary side of the heat exchanger will rise and fall in the same period as heaving motion. The value of fluctuate cycle was about 13 s as shown in Figures 5 and 6.

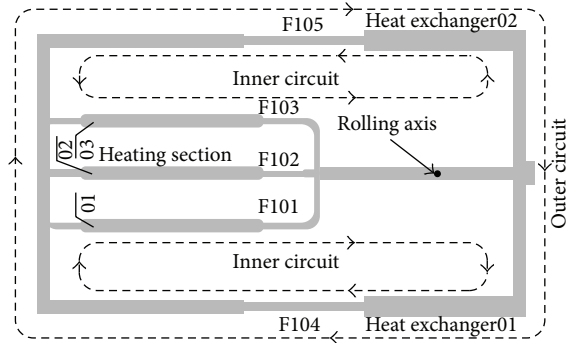


FIGURE 2: Structure of primary loop consisted of inner circuit and outer circuit.

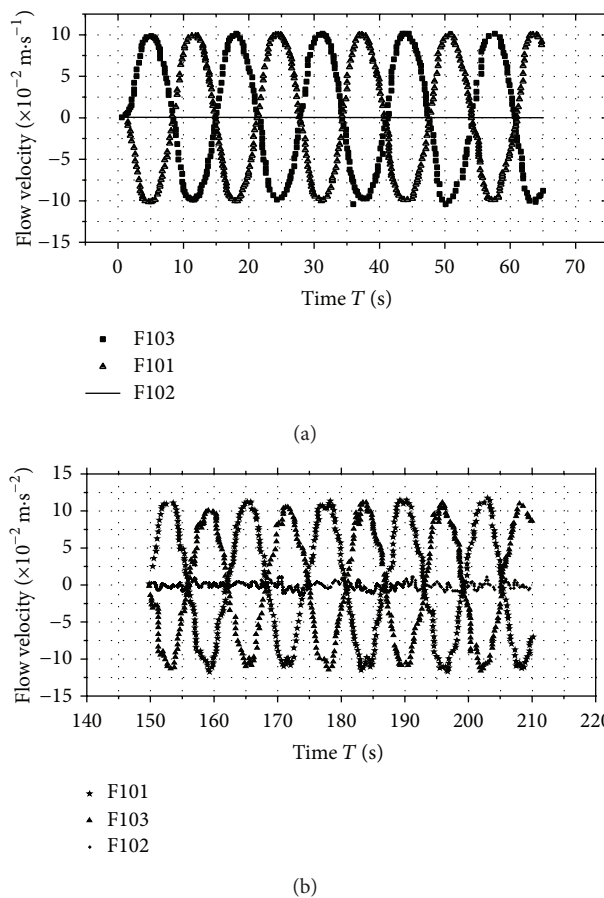


FIGURE 3: Comparison of experimental results and calculated results of rolling motion with swing angle  $\psi_m = 22.5^\circ$  and rolling cycle  $T = 13$  s in zero-power condition: (a) calculated result; (b) experimental result.

- (2) The flux and flow temperature of left heating section were the same as that of the intermediate heating section which indicated that the uniform distribution of flow was realized on the bottom of reactor core. Slight difference of flux and temperature were generated from the resistance of channel bend.
- (3) In heaving motion, time-average value of relative flux of heating section and the part of heat exchangers was

both less than 1 which indicated a decreased capability of natural circulation of the primary loop. The amount of reduction was about 5% in heaving motion with strength  $(g - a_{oz}) = 0.4 g$  and cycle  $T = 13$  s.

4.2. Mechanism of Natural Circulation in Heaving Motion. Heaving motion of the experimental apparatus would result in an additional force acting on the natural circulation which

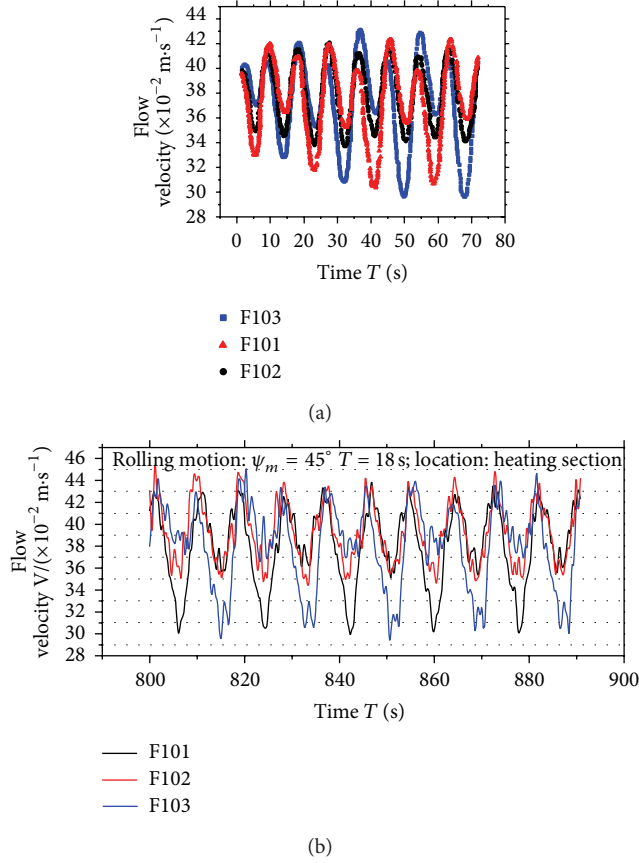


FIGURE 4: Comparison of experimental results and calculated results of rolling motion with swing angle  $\psi_m = 45^\circ$  and rolling cycle  $T = 18$  s in full power condition: (a) calculated result; (b) experimental results.

was parallel to gravity. Fixing the coordinate system on the experimental apparatus, natural circulation in heaving motion could be the issue in the noninertia coordinate system and treated as natural circulation under alternating vertical force field which could be calculated through the following formula:

$$g - a_{oz} = (1 - k \sin(w_d \cdot t)) \cdot g. \quad (7)$$

The driving force of natural circulation could be expressed as

$$\Delta P_d = \Delta \rho(t) (1 - k \sin(w_d \cdot t)), \quad (8)$$

where  $\Delta \rho(t)$  was the time-varying density difference between the hot fluid and the cold fluid. The driving force of natural circulation in heaving motion included the gravity and an additional force resulting from the heaving motion. Slight flow density difference in the primary loop could be achieved in the case of low level of temperature fluctuation caused by heaving motion. If the above factor was ignored, flow rate of natural circulation in heaving motion could be equal to the superposition of the steady flow and the additional flow resulting from the heaving motion. Gravity and the induced force were independent and the effect on natural circulation

could be superposed of the two above force directly. In the case of stronger flow temperature difference resulting from heaving motion, the former superposition was not correct in this case any more. Compared with the steady natural circulation on land, flow fluctuation in heaving motion would result in flow density difference. Simultaneously, flow density difference affects the driving force of natural circulation. Consequently, natural circulation in strong heaving motion was a result of alternating force field and flow density field.

Figure 7 plotted the relationship chain of factors affecting natural circulation in heaving motion: the alternating field which consisted of gravity and additional force would drive natural circulation. Flow fluctuation resulting from the alternating field would cause the flow temperature fluctuation which resulted in flow density difference. Further, density difference simultaneously affected the driving force of natural circulation. Accordingly, flux of natural circulation changed. Relationship of the factors affecting natural circulation was illustrated in Figure 7.

**4.3. Effect of Heaving Cycle and Heaving Strength on Natural Circulation.** Considering the effect of heaving motion on natural circulation, a heaving item  $a_{oz} = k \cdot g \cdot \sin(w_d \cdot t)$  was imported into the momentum equation, where  $w_d = 2\pi/T$ .

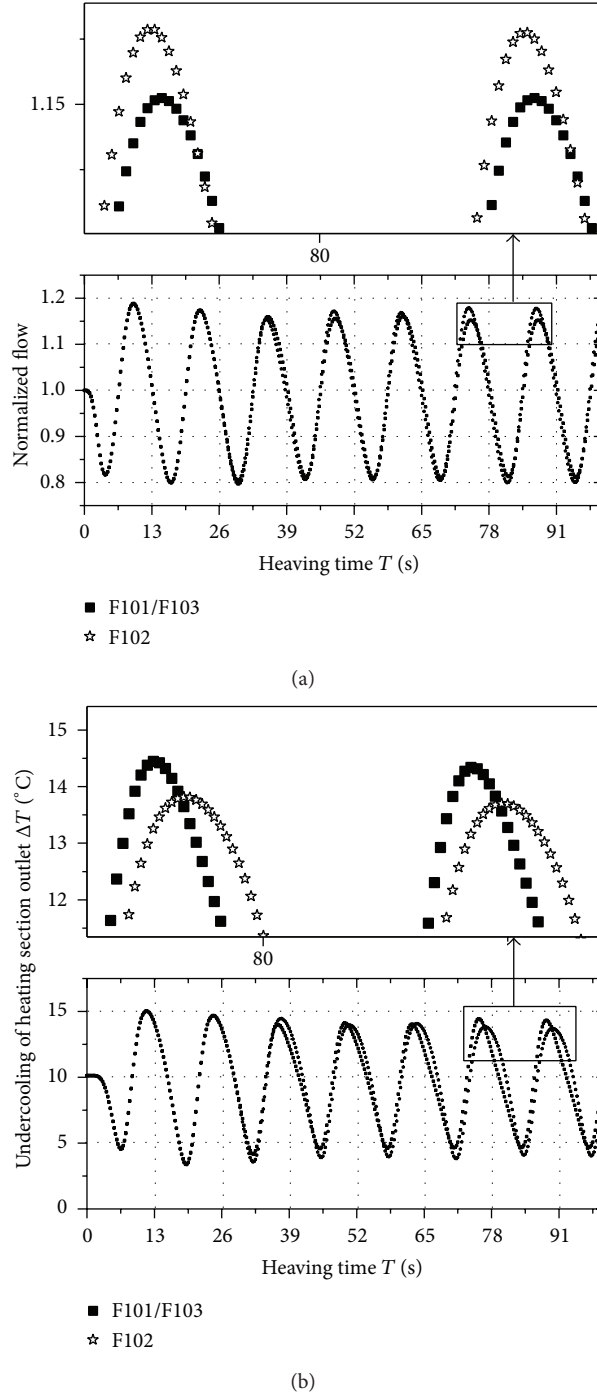


FIGURE 5: Flow and condensate depression of channel outlet of the left and the intermediate heating section in heaving motion with strength  $(g - a_{oz}) = 0.4$  g and cycle  $T = 13$  s: (a) normalized flow; (b) condensate depression.

So, flow velocity and displacement would be calculated through the following equations:

$$\begin{aligned}
 V_{oz} &= -\frac{kg}{\bar{w}_d} \cdot k \cdot g \cdot \cos(\bar{w}_d \cdot t), \\
 A_{oz} &= -\frac{kg}{\bar{w}_d} \cdot k \cdot g \cdot \sin(\bar{w}_d \cdot t).
 \end{aligned}
 \tag{9}$$

It can be inferred that phase of displacement of heaving motion was inverted to acceleration and the amplitude was proportional to frequency squared. The parameter  $k$  was proposed to describe the strength of heaving motion.

Figure 8 plotted the flux of natural circulation, condensate depression of heating section's outlet, and the secondary side of heat exchanger under heaving motion with cycle

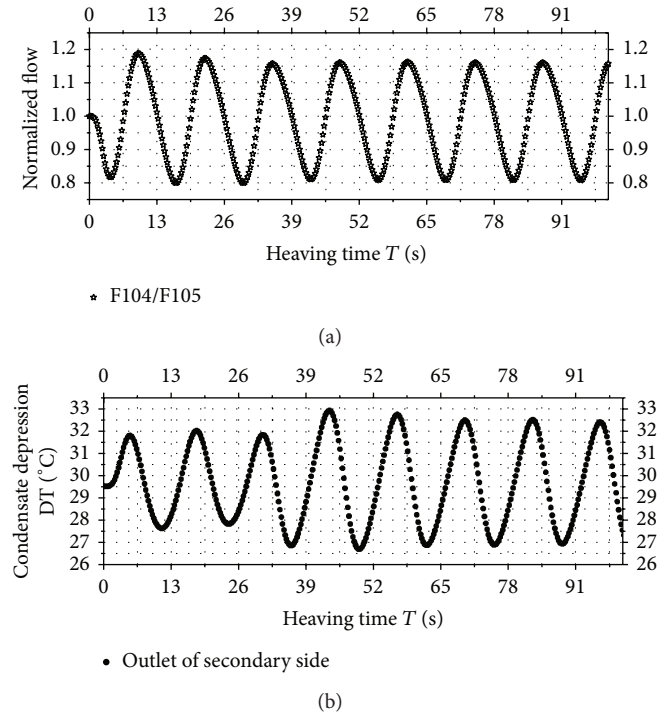


FIGURE 6: Flux of primary side of heat exchanger and condensate depression of outlet of secondary side: (a) normalized flow; (b) condensate depression.

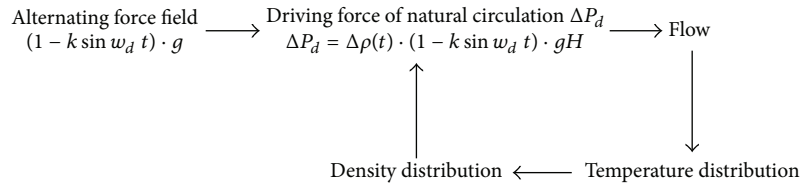


FIGURE 7: Relationship chain of factors affecting natural circulation in heaving motion.

$T = 3$  s and  $k = 0.2, 0.4, 0.6$ , respectively. Results indicated the following.

- (1) Fluctuation of flux and temperature would be stronger with the increasing heaving strength. When heaving strength  $(g - a_{oz}) = 0.6g$  and cycle  $T = 3$  s, fluctuation of flux was up to 17%.
- (2) Changes of the condensate depression of heating section's outlet exhibited regular fluctuation along with the heaving motion experiencing several heaving motion cycles with the start of steady state on land, as shown in Figure 8(b). In the initial stage, the inlet temperature of heating section kept constant while about 17% flow fluctuation was observed in the process of fluid flowing into heating section channel from the down comer. Accordingly, condensate depression of heating section's outlet exhibited serious fluctuation in the first heaving cycle. Weaker temperature fluctuation of heating section's outlet and the secondary side of heat exchanger was achieved in the later transitory stage. This was because the

temperature of heating section's outlet was decided by inlet temperature and flux fluctuation which would go weaker with the end of transitory stage.

While  $k$  was constant, the flow and temperature of natural circulation would exhibit similar fluctuation with the variational cycles of heaving motion. In Figure 9, the peak and valley of natural circulation were given. Flow fluctuation would rise nonlinearly with the heaving cycle  $T$  changing from 3 s to 8 s when heaving strength  $k$  was constant. Longer heaving cycle meant that the additional force generating from heaving motion would act on natural circulation in a longer period of time which led to bigger flow change and thermal saturation, or even boiling. Figure 10 plotted the calculated results of condensate depression of heating section outlet in heaving motion with strength  $k = 0.6$  and cycle  $T = 3$  s, 8 s, 13 s, 18 s, and 23 s, respectively. Results indicated an obvious fluctuation of temperature with heaving cycle changing from 3 s to 8 s. When heaving cycle  $T = 8$  s, the temperature difference from peak to valley was about  $16^\circ\text{C}$ . The critical point of heaving cycle was  $T = 13$  s when heaving strength

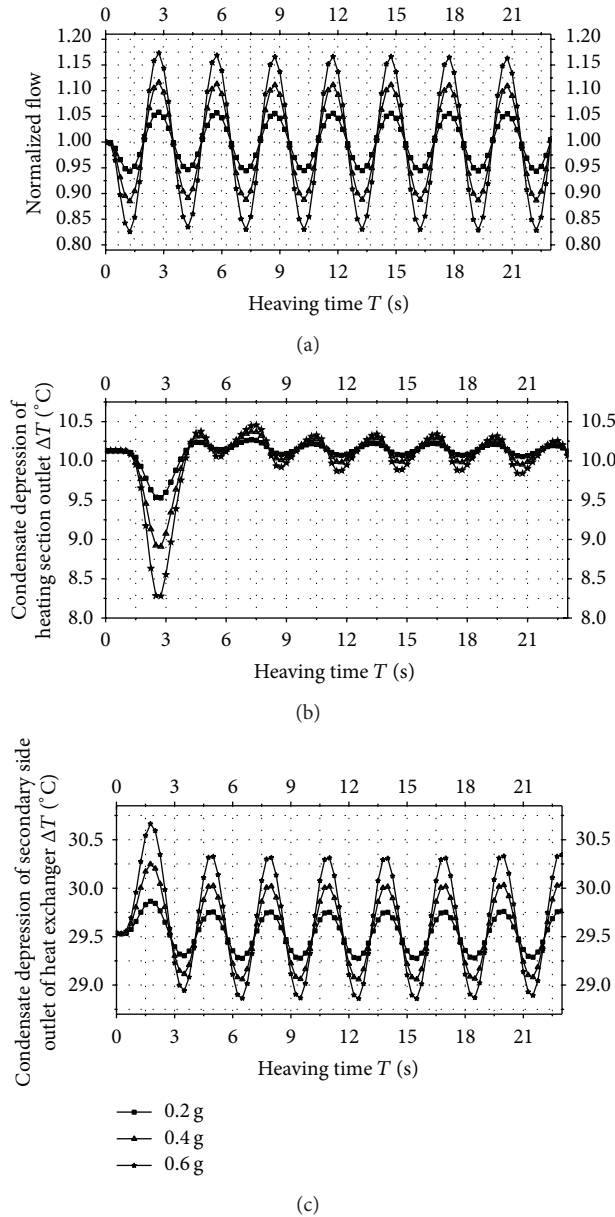


FIGURE 8: Flux of natural circulation, condensate depression of heating section's outlet, and the secondary side of heat exchanger under heaving motion with cycle  $T = 3$  s and  $k = 0.2, 0.4,$  and  $0.6$ : (a) flux of natural circulation; (b) condensate depression of heating section's outlet; (c) secondary side of heat exchanger.

$k = 0.6$ : there was no thermal saturation when  $T < 13$  s, but thermal saturation when  $T > 13$  s.

Little effect of short -cycle heaving motion (for instance  $T = 3$  s) on natural circulation was observed, while significant effect, or even serious accident, would occur under heaving motion with long cycle.

4.4. Comparison of Characteristics of Natural Circulation in Heaving, Inclination, and Rolling Motions. Effect of basic oceanic movements, such as heaving motion, inclination, and rolling motion on natural circulation was investigated through the program and experiments. Comparison of

experimental results and simulation results of natural circulation under inclination was carried out, as shown in Figure 11. Total amount of natural circulation decreased slightly, while the flow going through one heat exchanger would increase, but another would decrease under inclination condition, which was related to the resistance characteristics, geometric parameters, and facility arrangement of the experimental apparatus. Under inclination with tilt angle  $45^\circ$ , 12% reduction of the total amount of natural circulation was achieved. From Figure 12, little effect of inclination on natural circulation was observed through comparison of calculated results with experimental data.

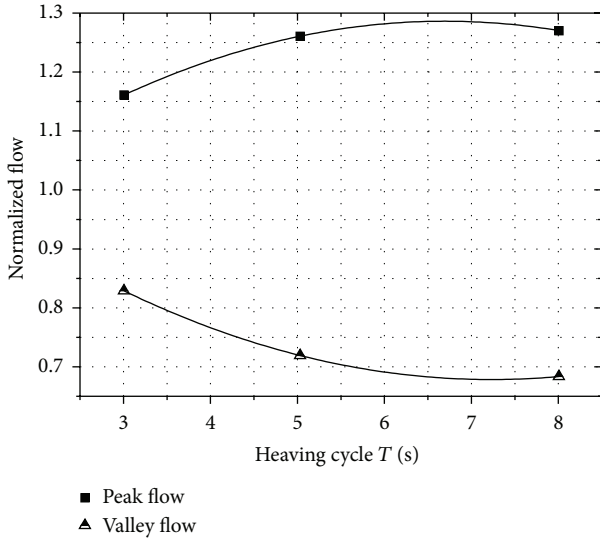


FIGURE 9: Peak and valley of flow changes of natural circulation with variable heaving cycle  $T$  when heaving strength  $k = 0.6$ .

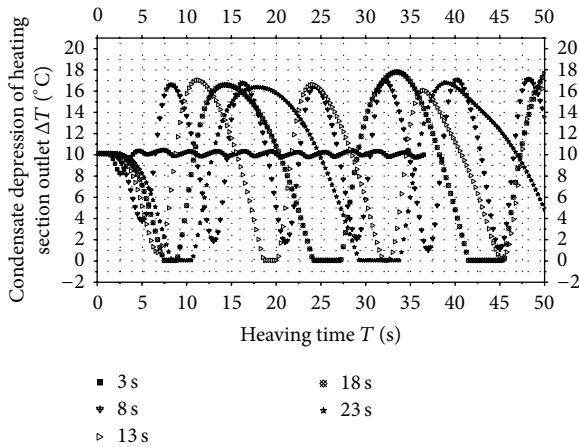


FIGURE 10: Calculated results of condensate depression of heating section outlet in heaving motion with strength  $k = 0.6$  and cycle  $T = 3$  s, 8 s, 13 s, 18 s, and 23 s.

Effect of heaving motion with strength 0.6 g and cycle 8 s, vertical rolling with swing angle  $22.5^\circ$  and cycle 8 s, compound motions which consisted of the above two movements, heaving motion with strength 0.6 g and cycle 8 s, transverse rolling with swing angle  $22.5^\circ$  and cycle 13 s, and compound motion which consisted of the above two movements on the normalized flow of natural circulation was shown in Figure 12. Rolling motion along the axis parallel to this page was defined as vertical rolling motion, and rolling motion along the axis perpendicular to this page was defined as transverse rolling motion. An increase of flow fluctuation was observed compared heaving motion 0.6 g, 8 s with vertical rolling 13 s,  $22.5^\circ$ . And, stronger effect of the compound motion consisted of the mentioned heaving motion and rolling motion on natural circulation was confirmed. Due to the identical cycle of vertical rolling motion and heaving

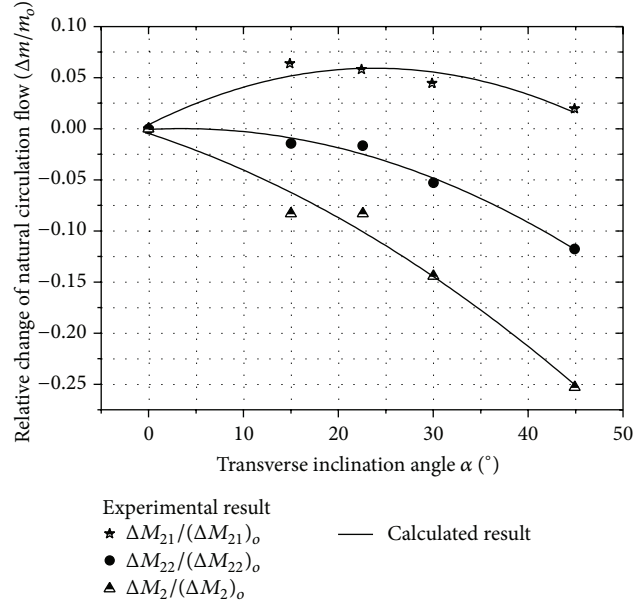


FIGURE 11: Comparison of experimental results and simulation results of natural circulation in inclination condition with different angles.

motion, cycle of natural circulation in the combination of the above two movements was synchronous. Considering the effect of heaving motion and transverse rolling, much stronger fluctuation of natural circulation in heaving motion with strength 0.6 g and cycle 8 s was observed than in transverse rolling motion with swing angle  $22.5^\circ$  and cycle 13 s. Stronger fluctuation could be predicted in heaving motion with cycle 13 s. A complex flow waveform resulting from the motion of heaving together with transverse rolling was observed and the heaving component was considered the main driving factor. Same flow fluctuation cycle was observed as the cycle of heaving component, and magnitude of flow fluctuation would be affected by the transverse component.

For large-scale ships, oceanic low frequency motion would lead to significant effect on natural circulation. Long-period rolling motion took slight effect on natural circulation due to small amount of the induced additional force which inclination could be treated as a special type of rolling motion with infinite cycle. But long-period heaving motion would lead to significant effect on natural circulation. Through the comparison, we could find out that long-period heaving motion may lead to the worst effect on natural circulation than inclination and rolling motion.

### 5. Conclusion

The comparison of calculated results with experimental data on a natural circulation loop designed with reference to 5 MW experimental low temperature nuclear heating reactor of Tsinghua University in inclination, heaving, and rolling motions was carried out. Flow characteristics and effect of motion parameters on natural circulation in heaving motion

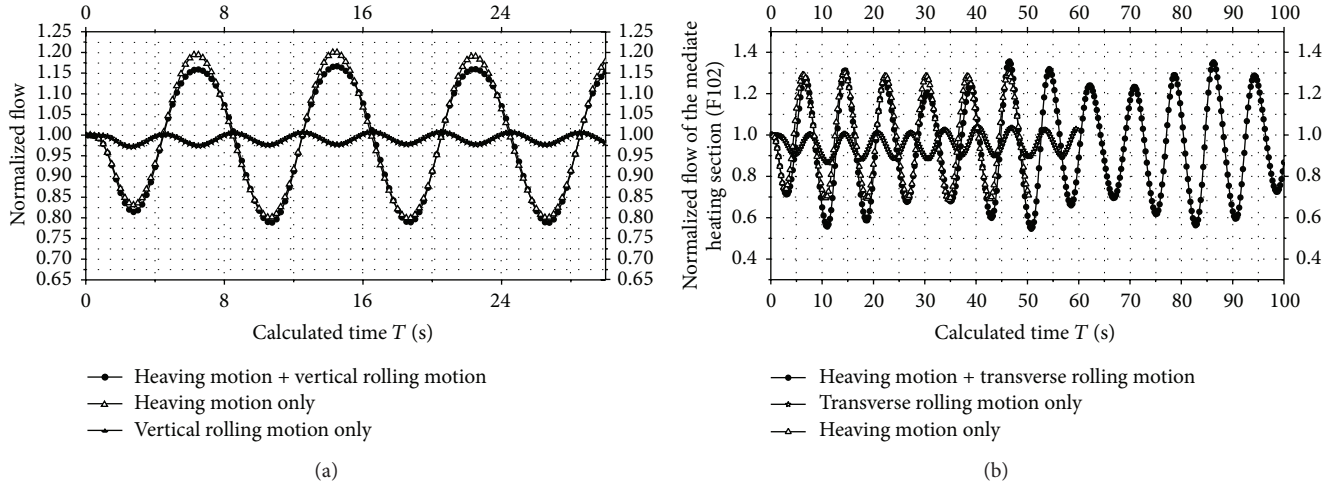


FIGURE 12: Effect of heaving motion with strength 0.6 g and cycle 8 s, vertical rolling with swing angle 22.5° and cycle 8 s, and compound motions consisted of the above two movements on the normalized flow of natural circulation.

were investigated and mechanism of natural circulation in heaving motion was stated. Results indicated the following.

- (1) Significant effect of heaving motion on natural circulation was observed. Flow fluctuation would become stronger in heaving motion with long period and high strength.
- (2) Slight effect of short-period heaving motion on natural circulation was verified.
- (3) Relationship chain of factors affecting natural circulation in heaving motion was given, the alternating field consisted of gravity and additional force, and flow density difference would result in the flow fluctuation of natural circulation.
- (4) Long-period heaving motion would lead to more significant influence than inclination and rolling motion and may cause serious accident.

**Symbols**

- $k$ : Strength of heaving motion
- $T$ : Cycle of motion
- $\rho$ : The density of fluid
- $f$ : Mass force of fluid
- $\mu$ : Flow viscosity
- $\lambda$ : Thermal conductivity of the fluid
- $S$ : Rate of strain tensor
- $g$ : Acceleration of gravity
- $\vec{f}$ : Unit mass force of the fluid
- $a_o$ : The acceleration of the additional force induced by the translational motion
- $a_t$ : The tangential force of fluid
- $a_n$ : The normal force of fluid
- $\psi_m$ : Swing angle of the rolling motion
- $\omega_d$ : Angular velocity of the periodic heaving motion
- $\Delta P_d$ : Driving force of natural circulation

- $\Delta\rho(t)$ : Time-varying density difference between the hot fluid and the cold fluid
- $V_{oz}$ : Velocity of fluid in z direction
- $A_{oz}$ : Displacement of fluid in z direction.

**Conflict of Interests**

The authors declare that there is no conflict of interests regarding the publication of this paper.

**Acknowledgments**

This work was supported by Project 11072131 of National Natural Science Foundation of China (NSFC) and the Tribology Science Fund of State Key Laboratory of Tribology (Grant no. SKLTKF12B16).

**References**

- [1] D. Duo and Z. Zhensheng, “5MW Test low-temperature heating reactor put into operation,” *Chinese Science Bulletin*, vol. 36, pp. 177–182, 1991.
- [2] W. Dazhong, D. Dou, and Z. Wenxiang, “Development of the 5WM experimental low temperature nuclear heating reactor and its operational features,” *Journal of Tsinghua University*, vol. 31, pp. 1–11, 1991.
- [3] Y. Zhang, D. Zhang, and D. Dong, “Analysis of seawater desalination with NHR-200,” *Nuclear Energy*, vol. 38, no. 1, pp. 21–29, 1999.
- [4] Z. Wenxiang and W. Dazhong, “NHR-200 nuclear energy system and its possible applications,” *Progress in Nuclear Energy*, vol. 29, pp. 193–200, 1995.
- [5] W. Li, Y. Zhang, and W. Zheng, “Investigation on three seawater desalination process coupled with NHR-200,” *Desalination*, vol. 298, pp. 93–98, 2012.
- [6] H. Zhu, X. Yang, H. Gong et al., “Theoretical and experimental study on single phase natural circulation under inclined condition,” *Journal of Nuclear Science and Technology*, vol. 50, pp. 304–313, 2013.

- [7] G. Houjun, Y. Xingtuan, H. Yanping et al., "Study on flow characteristics of integral reactor test facility under rolling motion without heating," *Nuclear Power Engineering*, vol. 34, pp. 77–81, 2013.
- [8] G. Houjun, Y. Xingtuan, and J. Shengyao, "Reactor natural circulation model for a reactor experiencing motion," *Journal of Tsinghua University*, vol. 53, no. 4, pp. 432–436, 2013.
- [9] H.-J. Gong, X.-T. Yang, S.-Y. Jiang, and Z.-Y. Liu, "Theoretical analysis of effect of ocean condition on natural circulation flow," *Nuclear Power Engineering*, vol. 31, no. 4, pp. 52–56, 2010.
- [10] S.-Y. Jiang, X.-T. Yang, H.-J. Gong et al., "Mechanism of natural circulation taking account into heaving movement," *Atomic Energy Science and Technology*, vol. 43, no. 1, pp. 92–96, 2009.

## Research Article

# Study on the Behaviors of a Conceptual Passive Containment Cooling System

Jianjun Wang, Xueqing Guo, Shengzhi Yu, Baowei Cai, Zhongning Sun, and Changqi Yan

*National Defense Key Laboratory for Nuclear Safety and Simulation Technology, Harbin Engineering University, Harbin 150001, China*

Correspondence should be addressed to Jianjun Wang; wangjianjunheu@163.com

Received 19 November 2013; Revised 11 February 2014; Accepted 12 February 2014; Published 26 March 2014

Academic Editor: Li Shengqiang

Copyright © 2014 Jianjun Wang et al. This is an open access article distributed under the Creative Commons Attribution License, which permits unrestricted use, distribution, and reproduction in any medium, provided the original work is properly cited.

The containment is an ultimate and important barrier to mitigate the consequences after the release of mass and energy during such scenarios as loss of coolant accident (LOCA) or main steam line break (MSLB). In this investigation, a passive containment cooling system (PCCS) concept is proposed for a large dry concrete containment. The system is composed of series of heat exchangers, long connecting pipes with relatively large diameter, valves, and a water tank, which is located at the top of the system and serves as the final heat sink. The performance of the system is numerically studied in detail under different conditions. In addition, the influences of condensation heat transfer conditions and containment environment temperature conditions are also studied on the behaviors of the system. The results reveal that four distinct operating stages could be experienced as follows: startup stage, single phase quasisteady stage, flashing speed-up transient stage, and flashing dominated quasisteady operating stage. Furthermore, the mechanisms of system behaviors are thus analyzed. Moreover, the feasibility of the system is also discussed to meet the design purpose for the containment integrity requirement. Considering the passive feature and the compactness of the system, the proposed PCCS is promising for the advanced integral type reactor.

## 1. Introduction

In order to prevent the radioactive species escaping to atmosphere, high integrity containment has been one of the most active design focuses in recent years. Under the internal effects of such design basis accidents scenarios as loss of coolant (LOCA) and main steam line break (MSLB), the expansion and transport of high mass/energy releases into the containment free volume will make the pressure and the temperature increase (Tills et al. [1]). In conventional nuclear power plant, the sprays and/or fan coolers are employed to control the containment peak pressure and temperature for ensuring the integrity of the containment. However, either sprays or fan coolers are dependent on the power supply, which is unreliable if LOCA or MSLB scenarios are coupled with the loss of power supply. Moreover, if there is no effective way to transfer the energy, the pressure and the temperature in the containment may exceed the allowed value. Therefore, there may be potential risks for the containment integrity. Till now, there have been worldwide efforts to develop promising passive containment cooling systems which are much safer,

more reliable, and possibly simpler than traditional designs as spray and/or fan cooler systems.

There are several conceptual candidate passive containment cooling systems which have been proposed and studied to date for either steel or dry double-wall concrete containment configuration of interest. For example, passive containment cooling by natural circulation and air convection and thermal radiation has been proposed for AP600 (Tower et al. [2]) and API1000 (Schulz [3]) reactors. Gavrilas et al. [4] proposed a containment design concept, in which heat rejection through the steel shell was enhanced by using an air-convection annulus on the upper portion and an external moat on the lower portion.

However, as compared to steel containment design for AP600 or API1000, it may be more difficult to remove the energy released in the accidents from a concrete containment due to the lower thermal conductivity of the concrete than steel.

Thus, a passive containment cooling system may be preferable and essential for the safety of containment in harsh postaccident conditions, which is completely independent of

mechanical, electrical, instrumentation, and control system. There are several conceptual candidate passive containment cooling systems which have been proposed and studied to date for the large dry double-wall concrete containment configuration of interest. Ahmad et al. [5] raised a heat pipe design concept for a passive containment heat removal system. Forsberg and Conklin [6] presented a so-called temperature-initiated passive cooling system. A thermosyphon loop concept for double-shell concrete containment was developed by ENEL. Similarly, Leiendecker et al. [7] had investigated another thermosyphon type conceptual containment cooling system. On the basis of thermosyphon type design schemes, Byun et al. [8] raised an internal evaporator-only (IEO) concept and the performance of the system was then investigated with the GOTHIC computer code. They concluded that four IEO loops could be utilized to meet design criteria for severe accident scenarios. In 2000, Liu et al. [9] performed an experimental investigation for a passive IEO cooling unit, in which the condensation heat transfer coefficients are thoroughly studied.

Enlightened by IEO design concept, we present an open-loop passive containment cooling system (OLPCCS) concept, which is composed of heat exchangers located in the containment, long connecting pipes with relatively large diameter, valves, and one water tank located outside the containment. The proposed system may operate by natural circulation means and free of pumps or other power supplies. The OLPCCS is designed to serve as the accidental consequence mitigation for the large dry containments of conventional PWRs. The OLPCCS is designed to control the pressure and the temperature in the containment after some accidents. As such, the operating pressure of the proposed system must be lower than permitted pressure in the containment due to heat transfer requirement, which means the OLPCCS is a system with very low pressure (near to atmosphere pressure). At present, most investigations on the behaviors of the natural circulation under low-pressure conditions were contributing to the studies of either start-up procedures to cross the instability region (Jiang et al. [10], van der Hagen and Stekelenburg [11], Manera et al. [12], and Kuran et al. [13]) or two-phase flow instabilities (Aguirre et al. [14], Aritomi et al. [15], Van Bragt and van der Hagen [16], Guanghui et al. [17], etc.) for the boiling water reactors (BWRs). Among these studies, the authors were dealing with the performance of closed loop natural circulation system which was rather different from OLPCCS. Furthermore, several codes were developed to study the flow instabilities which may occur in those natural circulation systems in time domain or frequency domain (Inada et al. [18] and Van Bragt et al. [19]). Even though thermal-hydraulic codes had been used for the numerical simulations of natural circulation with lower pressure (Tiselj and Černe [20], Kozmenkov et al. [21], and Mangal et al. [22]), it is still debatable for the validation of those codes in this field.

Thus, it is clear that there is not proper code for the simulation of operating behaviors of such a natural circulation system as OLPCCS. Therefore, this paper addresses the model on the basis of HEM formulation for two-phase flow. The model allows for the thermal properties change, which is

calculated with open code package named WASPCN, along the flow path both in single phase and two-phase zone. The one-dimensional computational code is developed by incorporating the above-mentioned model in order to numerically investigate the operation characteristics of the OLPCCS. With the code, transient flow behaviors are simulated from startup to quasisteady state and from single phase flow to two-phase flow. Besides, the heat removal capabilities of the system are also analyzed.

## 2. OLPCCS

The schematic of OLPCCS design and the structure of the heat exchangers are shown in Figure 1. The heat exchanger inside the containment is supposed to be located along the containment perimeter. With the consideration of components arrangement inside the containment, the heat exchangers of OLPCCS are designed to locate above the ring lifting. In order to eliminate the influence between the bundles during condensation, the heat exchanger can be designed as single row configuration. The heat exchanger is connected to the water tank through pipes with valves.

Some of the design parameters of the OLPCCS are listed in Table 1.

As shown in Figure 1, in the event of a LOCA or MSLB, the coolant released from the reactor vessel or steam line will be flashing into the containment because of the sudden decrease of the pressure. Afterwards, the mixture composed of steam and air may be cooled through the heat exchangers located inside the containment. Meanwhile, the fluid in the tubes of the heat exchangers will be heated up, which will supply the original driving force for the natural circulation of OLPCCS.

## 3. Model Setup

In this paper, the following conditions are assumed.

- (1) The heat can only be exchanged via the heat exchangers, which means the connecting pipes are adiabatic.
- (2) The OLPCCS is isothermal when it is standing by.
- (3) The heat transfer coefficient remains constant along the tubes except in phase change scenario.
- (4) When the OLPCCS is activated, the temperature in the containment steps to and remains some specific value.
- (5) Both steam and the liquid in the system are incompressible.

The homogeneous two-phase flow model is used in this paper. The main conservation equations are listed as follows. Mass conservation equation:

$$\frac{\partial W_m}{\partial z} = 0. \quad (1)$$

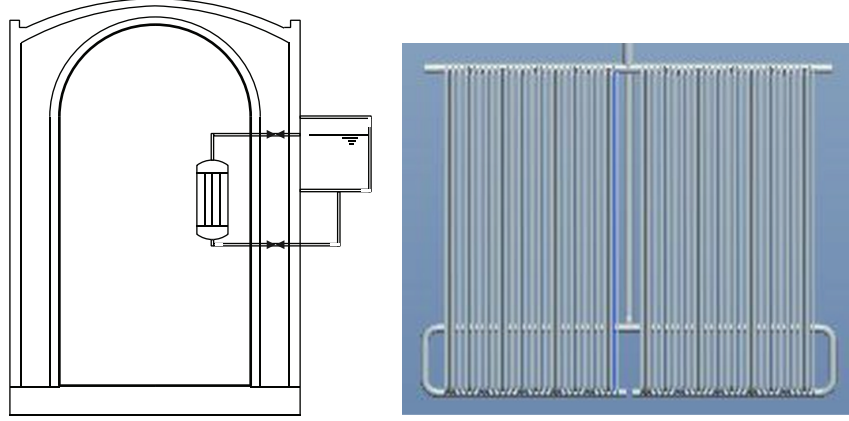


FIGURE 1: Schematic of OLPCCS (not to scale).

TABLE 1: Parameters of OLPCCS unit.

Parameter	Value
Height of heat exchanger/m	5.0
Height difference between the in-containment heat exchanger and water tank/m	10
Area of one heat exchanger/m <sup>2</sup>	300
Initial water temperature/°C	30~70
Condensation heat transfer coefficient/(W/(m <sup>2</sup> K))	500~1000

Momentum conservation equation:

$$\frac{\partial W_m}{\partial t} + \frac{\partial (W_m^2 / (A \rho_m))}{\partial z} = -\frac{dp}{dz} + \left(\frac{dp}{dz}\right)_f + \left(\frac{dp}{dz}\right)_g + \left(\frac{dp}{dz}\right)_i \quad (2)$$

Energy conservation equation:

$$A \frac{\partial (h_m \rho_m)}{\partial t} + \frac{\partial (W_m h_m)}{\partial z} = q_l, \quad (3)$$

where  $W_m$  is the mass flow rate, kg/s;  $A$  is flow area, m<sup>2</sup>;  $\rho_m$  is the average density of the mixture, kg/m<sup>3</sup>;  $h_m$  is the enthalpy of mixture, kJ/kg;  $q_l$  denotes the linear power, W/m.

The main constitutive relationships used in the paper are as follows, which include the pressure drop and heat transfer calculation expression:

$$\Delta p_{f,sp} = f \frac{L}{d_i} \frac{\rho u^2}{2}, \quad (4)$$

where

$$f = \begin{cases} \frac{64}{Re} & Re \leq 2000 \\ 0.3164 Re^{-0.25} & 2000 < Re \leq 3.0 \times 10^4 \\ 0.184 Re^{-0.2} & 3.0 \times 10^4 < Re \leq 2.1 \times 10^6 \\ 0.01 & Re > 2.1 \times 10^6, \end{cases} \quad (5)$$

$$\Delta p_{f,tp} = \phi_{l0}^2 f \frac{L}{d_i} \frac{\rho u^2}{2}. \quad (6)$$

In (6),  $\phi_{l0}^2$  denotes the two-phase friction multiplier, which can be expressed as follows:

$$\phi_{l0}^2 = \left[ 1 + x \left( \frac{\rho_l}{\rho_g} - 1 \right) \right], \quad (7)$$

or Baroczy method is used for the calculation of  $\phi_{l0}^2$ .

If the convection heat transfer is in single liquid phase, then

$$Nu = \begin{cases} 3.66 & Re \leq 2000 \\ 0.023 Re^{0.8} Pr^{0.4} & Re > 2000, \end{cases} \quad (8)$$

where  $Nu = h_{sp} d_i / k$ .

The boiling heat transfer coefficient is calculated with the correlations recommended by Shah [23]:

$$h_{tp} = h_{sp} (h_{BL} + h_{CL}), \quad (9)$$

where  $h_{tp}$  is the boiling heat transfer coefficient, W/(m<sup>2</sup>K):

$$h_{BL} = \begin{cases} 230 Bo^{0.5} & Bo > 0.0003 \\ 1 + 46 Bo^{0.5} & Bo < 0.0003; \end{cases} \quad (10)$$

$$h_{CL} = \frac{1.8}{C_0^{0.8}}.$$

PCCSTS (passive containment cooling system transient simulation) code is developed with the finite difference method (FDM) based on the models. The schematic of the control volumes of main parts of the system is shown in Figure 2. The numerical simulation of behaviors of the OLPCCS is performed with PCCSTS code. In the current study, the time step for the transient analysis is set to 0.01 s and the converging criteria of the calculations are set to less than  $1.0e - 6$  in terms of relative error.

## 4. Results and Discussions

**4.1. Overall Operating Behaviors of OLPCCS.** From the conservation point of view, it is supposed that the temperature

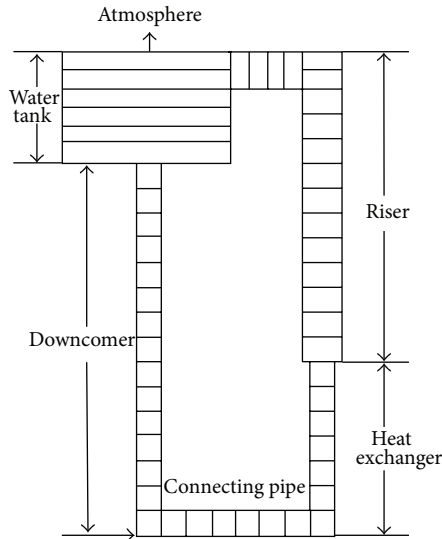


FIGURE 2: Schematic of the nodalization.

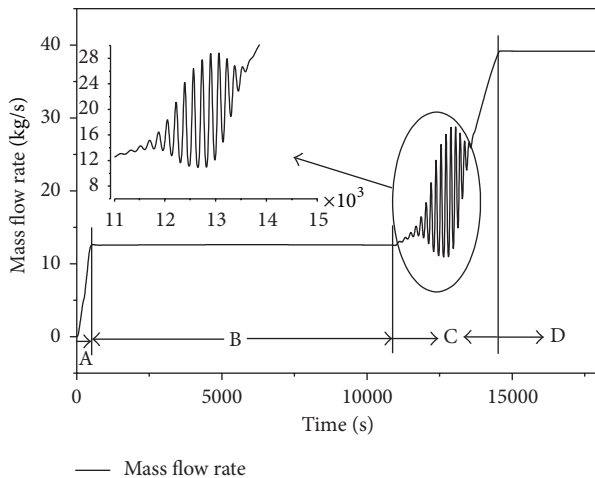


FIGURE 3: Mass flow rate evolution after OLPCCS being activated.

inside the containment steps from the same value as that inside water tank to some value and remains afterward. Firstly, such case is studied that the OLPCCS remains standing by with the water tank temperature of  $50^{\circ}\text{C}$  and is activated and the temperature inside the containment steps to  $150^{\circ}\text{C}$  since then. According to the study of Liu et al. [9] the condensation heat transfer coefficient of steam in the presence of incondensable air changes from about  $500\text{ W}/(\text{m}^2\text{K})$  to almost  $2500\text{ W}/(\text{m}^2\text{K})$ . From conservation point of view, the heat transfer coefficient is set to  $500\text{ W}/(\text{m}^2\text{K})$  in this case. Furthermore, the height difference between the water tank and the heat exchanger is 10. Figure 3 depicts the mass flow rate evolution of the OLPCCS in time after being activated.

It can be found that the mass flow rate will increase quickly after the system is activated. With the temperature inside the containment suddenly increasing from  $50^{\circ}\text{C}$  to  $150^{\circ}\text{C}$ , the fluid in the heat exchanger will be heated up simultaneously and its temperature gradually increases, which will

make the density difference of the fluid between downward pipe and the riser pipes. Therefore, the force generating from the density difference drives the fluid to move along the loop. During the early stage in startup process, denoted as A in Figure 3, the velocity grows faster and faster, which is because the flow enhances the heat transfer capacity of the heat exchanger and the driving force increases consequently. After the OLPCCS fully starts up, the system operates in single phase mode and the mass flow rate remains barely constant for a relatively long time as shown in Figure 3 with B. Therefore, the period of operation is named as single phase quasisteady stage. During single phase quasisteady operating stage, the fluid that flows through the heat exchangers maintains single phase along all the pipes, even if the system is heated up gradually. Moreover, the fluid temperature difference between inlet and outlet of the heat exchangers changes very slowly. Therefore, the driving force and the mass flow rate of the system are almost changeless. With the increase of the fluid temperature inside the water tank, the temperature increases at the exit of the heat exchangers and reaches saturation point at the outlet of the riser. This causes the flashing of the fluid and then results in the sharp increase of driving force for natural circulation of the system. Thus, the mass flow rate of the system begins to increase when the flashing occurs in the riser. Along with the development of the flashing downward, the system is being speeded up more and more. However, the speeding up process will not continue all the time because the quick increasing velocity may have the effects in two aspects: (1) it will help enhance the heat transfer capability of the heat exchanger; (2) it also may result in the decrease of outlet temperature because of high mass flow rate. Furthermore, the coupling and the lag effect between heat transfer and fluid flow result in the oscillation occurrence. Under given conditions, the oscillation of the mass flow rate will vanish when the temperature of the fluid inside the water tank reaches  $90^{\circ}\text{C}$  as shown in Figure 4. After that, the natural circulation capability will be enhanced continuously until the fluid reaches the saturate temperature inside the water tank. This transient process denoted as C in Figure 3 is named as flashing speed-up transient stage. Finally, the system operates in two-phase quasisteady mode and is dominated by flashing which supplies the main driving head for the system. This stage is marked as D in Figure 3.

According to the description of the operating stages for OLPCCS, it can be concluded that there are two transient phases and two quasisteady phases from A to D. From system design point of view, quasisteady operating stages, marked with B and D, make sense as far as the long-term cooling is concerned in single phase and two-phase mode, respectively. Hence, the flow characteristics of both single phase and flashing dominated two-phase quasisteady stages are studied in the following parts.

**4.2. Mass Flow Rate in Single Phase Quasisteady Stage of OLPCCS.** Figure 5 shows the mass flow rate in single phase quasisteady stage of OLPCCS under different conditions, which include different condensation heat transfer coefficients and different containment temperatures.

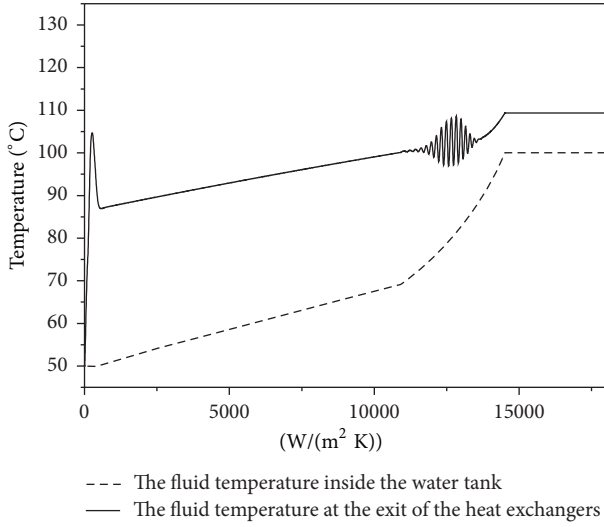


FIGURE 4: The temperature evolution at typical position after OLPCCS being activated.

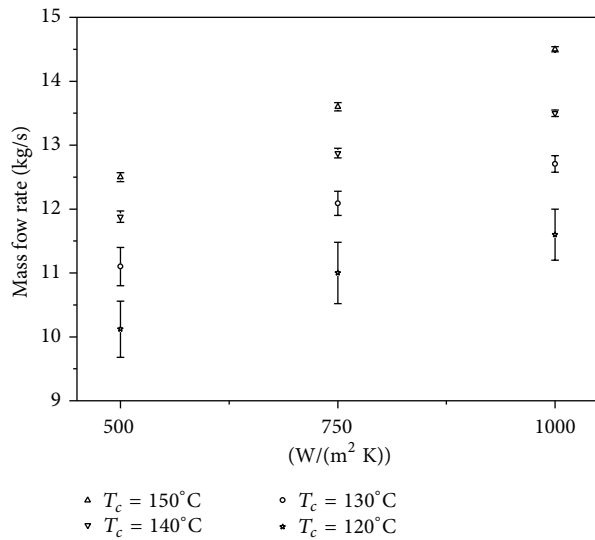


FIGURE 5: Mass flow rate in single phase quasisteady stage under different conditions.

It can be found in Figure 5 that the maximum relative error of the mass flow rate, which is defined as the ratio of the maximum over the average mass flow rate during single phase quasisteady operating stage, is not more than 5%. In addition, with the increase of either condensation heat transfer coefficient or the containment temperature, it is easy to understand that the mass flow rate of the system may increase for single phase quasisteady operating stage. Furthermore, it is interesting that the larger the mass flow rate is, the less variation the flow shows in single phase quasisteady operating stage. This is helpful for the passive cooling of the containment because of the good adaptability.

4.3. Mass Flow Rate in Two-Phase Quasisteady Stage of OLPCCS. Figure 6 presents the mass flow rate of OLPCCS

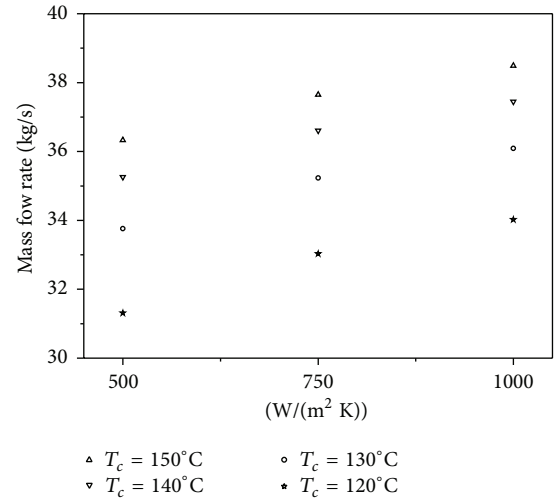


FIGURE 6: Mass flow rate in two-phase quasisteady stage under different conditions.

under different conditions when the system operates in two-phase quasisteady stage. The two-phase frictional pressure drop is calculated based on homogeneous model in this figure.

As stated before, the OLPCCS will not operate in two-phase quasisteady stage until the water inside the water tank reaches the saturation condition at atmosphere pressure. Afterwards, the flashing two-phase fluid drained from riser will not heat the water inside the tank any more, which is the reason why the system can operate in quasisteady state. The results shown in Figure 6 reveal that the OLPCCS mass flow rate increases with the increase of condensation heat transfer coefficient at given containment temperature condition or the OLPCCS mass flow rate increases with the increase of containment temperature at specified condensation heat transfer coefficient if the OLPCCS operates in two-phase quasisteady phase. With the consideration of the coupling relationship between fluid flow and heat transfer, it can also be concluded that the OLPCCS exhibits good adaptability to the containment thermal conditions in two-phase operating stage. It needs to be noticed that the flow behavior of OLPCCS in two-phase quasisteady stage is quite important for the long-term cooling and integrity insurance of the containment during LOCA or MSLB scenario.

4.4. The Influence of Different Frictional Two-Phase Pressure Drop Models. Commonly, the correlations for the evaluation of frictional pressure drop in two-phase flow can be categorized into such two typical branches as homogeneous model and separated flow model based methods. The former is proper for bubble flow pattern and the latter is suitable for the annular flow pattern. In this paper, the influence of different frictional two-phase pressure drop models on the mass flow rate in quasisteady operating phase for OLPCCS is also discussed. As shown in Figure 7, (7) based on homogeneous model and Baroczy method are used for the evaluation of

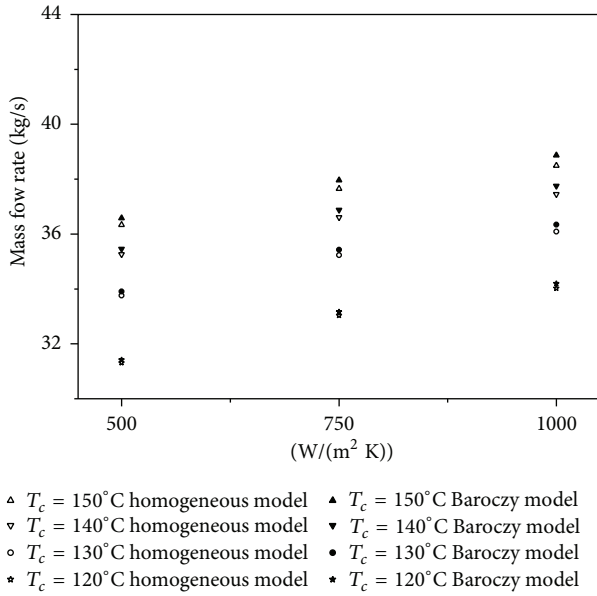


FIGURE 7: Mass flow rate evaluated based on different two-phase frictional pressure drop models.

mass flow rate of OLPCCS during two-phase quasisteady operating stage.

From the results shown in Figure 7, the predicted mass flow rate of OLPCCS may change a little under different two-phase frictional pressure drop models. The maximum relative error of mass flow rate is under 1%. Therefore, the prediction of the performance of OLPCCS is not sensible for the model selection of two-phase frictional pressure drop.

**4.5. The Long-Term Heat Removal Capability of OLPCCS Unit.** In order to assess the feasibility of the OLPCCS to the mitigation of LOCA or MSLB consequences, the long-term heat removal capability, which means the system operates in two-phase quasisteady stage, of the OLPCCS is also simulated with the codes and the results are shown in Figure 8.

It can be found that at given containment temperature and condensation heat transfer coefficient condition, the results of long-term heat removal capability are almost the same for different two-phase frictional pressure drop models. For the large dry concrete containment, the design pressure limit is mostly less than 0.52 MPa and the requirement of the containment temperature is less than about 150°C. To match the requirement on the temperature after accidents, the proposed OLPCCS may provide over 1.3 MW heat removal capability per unit if the condensation heat transfer coefficient is not less than 500 W/(m<sup>2</sup>K). Actually, during LOCA or MSLB scenario, the condensation heat transfer coefficient onto the stainless pipes will vary and be larger than 500 W/(m<sup>2</sup>K) in most cases. Furthermore, the actual heat removal capability of OLPCCS is higher than long-term heat removal capacity in calculated cases because of the large temperature difference and relative small condensation heat transfer coefficient as compared to the conduction through pipes and convection inside the pipes. Therefore, the

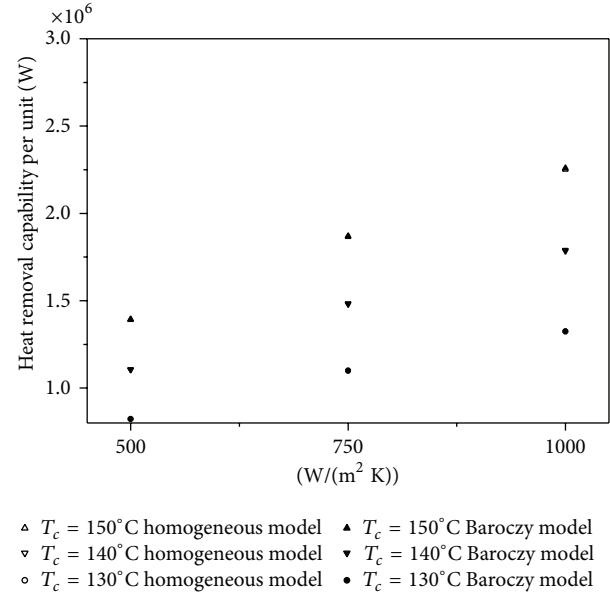


FIGURE 8: The heat removal capability per OLPCCS unit under different conditions.

proposed OLPCCS is promising for the containment integrity after such accidents as LOCA or MSLB.

## 5. Summary and Conclusions

In order to ensure the integrity of the containment after typical accidents, the conceptual OLPCCS is proposed and the PCCSTS code is developed to simulate the behavior of OLPCCS. The performances of the system under relative conservative conditions, such as low condensation heat transfer coefficient and high standing-by water temperature, are numerically studied. Analysis of simulation results and the comparison of different models lead to following conclusions.

Based on the PCCSTS code developed by ourselves, the conceptual open loop passive containment cooling system behaviors and the influence of different in-containment conditions are simulated and analyzed. From the results, the following can be concluded.

- (1) The proposed OLPCCS shows good self-adaptability to the in-containment conditions, which means the more steam is drained into containment, the more heat can be transferred to the final heat sink.
- (2) The OLPCCS is a fully passive system and can be used in the advanced integral type reactor design because of its simplicity and compactness.
- (3) The OLPCCS can experience such four different operating stages as startup, single phase quasisteady state stage before flashing occurring, transient process, and long-term two-phase quasisteady state operating stage. Even if instability may occur in the OLPCCS during transient process, there is very little impact on the heat removal capability of the system.

- (4) The proposed OLPCCS is a system dominated by flashing regarding the long-term cooling of the containment after typical accidents.

## 6. Future Work

The new model for the evaluation of onset condition of flashing should be developed to account for the thermal inequilibrium effect in the future.

## Nomenclature

$A$ :	Flow area $m^2$
$d_i$ :	Inner diameter $m$
$f$ :	Frictional resistance coefficient
$h_m$ :	Enthalpy of mixture $kJ/kg$
$h_{sp}$ :	Single phase heat transfer coefficient $W/(m^2K)$
$h_{tp}$ :	Two-phase heat transfer coefficient $W/(m^2K)$
$k$ :	Thermal conductivity
$L$ :	Pipe length $m$
$Nu$ :	Nusselt number
$p$ :	Pressure $Pa$
$Pr$ :	Prandtl number
$q_l$ :	Linear power $W/m$
$Re$ :	Reynolds number
$u$ :	Velocity $m/s$
$W_m$ :	Mass flow rate $kg/s$
$x$ :	Quality
$\Delta p_{f,sp}$ :	Single phase pressure drop $Pa$
$\Delta p_{f,tp}$ :	Two-phase pressure drop $Pa$
$\rho_l$ :	Density of liquid phase $kg/m^3$
$\rho_g$ :	Density of gas phase $kg/m^3$
$\rho_m$ :	Density of mixture $kg/m^3$
$\phi_{10}^2$ :	Two-phase multiplier.

## Conflict of Interests

The authors declare that there is no conflict of interests regarding the publication of this paper.

## Acknowledgment

The authors are gratefully thankful for the support of the Projects (HEUFT07091 and HEUFN1307) of National Defense Key Laboratory for Nuclear Safety and Simulation Technology in Harbin Engineering University.

## References

- [1] J. Tills, A. Notarfrancesco, and J. Phillips, "Application of the MELCOR code to design basis PWR large dry containment analysis," SANDIA Report 2009-2858, 2009.
- [2] S. N. Tower, T. L. Schulz, and R. P. Vijuk, "Passive and simplified system features for the advanced westinghouse 600 MWe PWR," *Nuclear Engineering and Design*, vol. 109, no. 1-2, pp. 147-154, 1988.
- [3] T. L. Schulz, "Westinghouse AP1000 advanced passive plant," *Nuclear Engineering and Design*, vol. 236, no. 14-16, pp. 1547-1557, 2006.
- [4] M. Gavrilas, N. E. Todreas, and M. J. Driscoll, "Containment passive-cooling design concepts," *Progress in Nuclear Energy*, vol. 32, no. 3-4, pp. 647-655, 1998.
- [5] A. Ahmad, I. Catton, M. Cuesta-Gonzalez, F. Gazzillo, W. Kastenber, and R. Wong, "PWR severe accident delineation and assessment," NUREG/CR-2666 UCLA-ENG-8284, 1983.
- [6] C. W. Forsberg and J. C. Conklin, *Use of Temperature-Initiated Passive Cooling System (TIPACS) for Modular High-Temperature Gas-Cooled Reactor Cavity Cooling System*, Oak Ridge National Laboratory, ORNL, Oak Ridge, Tenn, USA, 1994.
- [7] M. Leiendecker, N. E. Todreas, M. J. Driscoll, and A. Hurtado, "Design and numerical simulation of a two-phase thermosiphon loop as a passive containment cooling system for PWRs," Tech. Rep. MIT-ANP-TR-053, 1997.
- [8] C. S. Byun, D. W. Jerng, N. E. Todreas, and M. J. Driscoll, "Conceptual design and analysis of a semi-passive containment cooling system for a large concrete containment," *Nuclear Engineering and Design*, vol. 199, no. 3, pp. 227-242, 2000.
- [9] H. Liu, N. E. Todreas, and M. J. Driscoll, "Experimental investigation of a passive cooling unit for nuclear plant containment," *Nuclear Engineering and Design*, vol. 199, no. 3, pp. 243-255, 2000.
- [10] S. Y. Jiang, M. S. Yao, J. H. Bo, and S. R. Wu, "Experimental simulation study on start-up of the 5 MW nuclear heating reactor," *Nuclear Engineering and Design*, vol. 158, no. 1, pp. 111-123, 1995.
- [11] T. H. J. van der Hagen and A. J. C. Stekelenburg, "The low-power low-pressure flow resonance in a natural circulation cooled boiling water reactor," *Nuclear Engineering and Design*, vol. 177, no. 1-3, pp. 229-238, 1997.
- [12] A. Manera, U. Rohde, H.-M. Prasser, and T. H. J. van der Hagen, "Modeling of flashing-induced instabilities in the start-up phase of natural-circulation BWRs using the two-phase flow code FLOCAL," *Nuclear Engineering and Design*, vol. 235, no. 14, pp. 1517-1535, 2005.
- [13] S. Kuran, Y. Xu, X. Sun et al., "Startup transient simulation for natural circulation boiling water reactors in PUMA facility," *Nuclear Engineering and Design*, vol. 236, no. 22, pp. 2365-2375, 2006.
- [14] C. Aguirre, D. Caruge, F. Castrillo et al., "Natural circulation and stability performance of BWRs (NACUSP)," *Nuclear Engineering and Design*, vol. 235, no. 2-4, pp. 401-409, 2005.
- [15] M. Aritomi, J. H. Chiang, T. Nakahashi, M. Wataru, and M. Mori, "Fundamental study on thermo-hydraulics during start-up in natural circulation boiling water reactors, (I). Thermo-hydraulic instabilities," *Journal of Nuclear Science and Technology*, vol. 29, no. 7, pp. 631-641, 1992.
- [16] D. D. B. Van Bragt and T. H. J. van der Hagen, "Stability of natural circulation boiling water reactors: part I—description stability model and theoretical analysis in terms of dimensionless groups," *Nuclear Technology*, vol. 121, no. 1, pp. 40-51, 1998.
- [17] S. Guanghai, J. Dounan, K. Fukuda, and G. Yujun, "Theoretical and experimental study on density wave oscillation of two-phase natural circulation of low equilibrium quality," *Nuclear Engineering and Design*, vol. 215, no. 3, pp. 187-198, 2002.
- [18] F. Inada, M. Furuya, and A. Yasuo, "Thermo-hydraulic instability of boiling natural circulation loop induced by flashing (analytical consideration)," *Nuclear Engineering and Design*, vol. 200, no. 1, pp. 187-199, 2000.

- [19] D. D. B. Van Bragt, W. J. M. De Kruijf, A. Manera, T. H. J. J. van der Hagen, and H. Van Dam, "Analytical modeling of flashing-induced instabilities in a natural circulation cooled boiling water reactor," *Nuclear Engineering and Design*, vol. 215, no. 1-2, pp. 87-98, 2002.
- [20] I. Tiselj and G. Černe, "Some comments on the behavior of the RELAP5 numerical scheme at very small time steps," *Nuclear Science and Engineering*, vol. 134, no. 3, pp. 306-311, 2000.
- [21] Y. Kozmenkov, U. Rohde, and A. Manera, "Validation of the RELAP5 code for the modeling of flashing-induced instabilities under natural-circulation conditions using experimental data from the CIRCUS test facility," *Nuclear Engineering and Design*, vol. 243, pp. 168-175, 2012.
- [22] A. Mangal, V. Jain, and A. K. Nayak, "Capability of the RELAP5 code to simulate natural circulation behavior in the test facilities," *Progress in Nuclear Energy*, vol. 61, pp. 1-16, 2012.
- [23] M. M. Shah, "A new correlation for heat transfer during boiling flow through pipes," *ASHRAE Transactions*, vol. 82, no. 2, pp. 66-86, 1976.

## Research Article

# Operation of Shared Systems via a Common Control System in a Multi-Modular Plant

**Jia Qianqian, Huang Xiaojin, and Zhang Liangju**

*Institute of Nuclear and New Energy Technology of Tsinghua University, The Key Laboratory of Advanced Reactor Engineering and Safety, Ministry of Education, Beijing 100084, China*

Correspondence should be addressed to Jia Qianqian; [jqq@tsinghua.edu.cn](mailto:jqq@tsinghua.edu.cn)

Received 2 December 2013; Revised 31 January 2014; Accepted 31 January 2014; Published 20 March 2014

Academic Editor: Luciano Burgazzi

Copyright © 2014 Jia Qianqian et al. This is an open access article distributed under the Creative Commons Attribution License, which permits unrestricted use, distribution, and reproduction in any medium, provided the original work is properly cited.

Integral type reactors may need to be grouped to produce as much energy as a utility demands due to the small electrical output of an individual reactor. Sharing of systems among modules at a nuclear plant site is economically beneficial. Operation of systems shared between modules in a multi-modular plant is an issue never met in current NPPs, which may impact human performance. A design of operation of the shared systems via a common control system is presented as a technical approach to solve the problem. Modules and shared systems are controlled in independent network domains, respectively. Different from current NPPs, a limitation of operation authorities corresponding to certain modules and shared systems is defined to minimize the operation confusion between modules by one operator and to minimize the operation confusion of shared systems by different operators. Different characteristics of the shared system are analyzed, and different operation and control strategies are presented. An example is given as an application of the operation strategies. The operation design of the multi-modular system is in the preliminary stage, and, as a concept design, more verification and validation is needed in further works.

## 1. Introduction

Integral type reactor is a promising solution to meet future energy needs. Due to the design aspects of the integral type reactor, the electrical output of an individual reactor is relatively small compared to that of a typical commercial nuclear power plant. However, reactors can be grouped to produce as much energy as a utility demands due to the economic benefits [1], which form a nuclear energy system with multiple modules. To further reduce the cost, many designers of the small modular reactors [2, 3] provide for creation of multi-module plants with certain shared components and infrastructure [4]. The sharing of systems between modules means that only one system needs to be built rather than two [5]. It is a reduction of overall construction time and outlay for equipment, materials, and structures.

The configuration of a multi-modular plant is different from current NPPs, and the differences include the layout of the infrastructure, integral placement of primary coolant system component, and shared systems or resources among modules. The sharing among modules may include the minor

support or auxiliary systems, such as circulating water, instrument air, and AC and DC electric power [6], and some major primary or secondary systems, such as turbine generators coupled with two or more modules [7]. Besides, the control system of the multi-modular plant is another aspect shared between modules. The control considerations of the shared aspects are uncommon in nuclear power operational experience, as presented by Clayton and Wood [8].

Due to the differences of the multi-modular plant and current NPPs, the U.S. Nuclear Regulatory Commission (NRC) conducted research to examine the human factors engineering (HFE) and the operational aspects of small modular reactors (SMRs). The research identified some potential human performance issues that should be considered in NRC's reviews of small modular reactor designs and in future research activities [9]. These issues include multi-unit operations and teamwork, staffing mode and staffing level, control room configuration and workstation design, HSI design for multi-unit monitoring and control, and operational impact of control systems for shared aspects of SMRs.

TABLE 1: Operation differences of multi-modular plants and current NPPs.

	Multi-modular plants	Current NPPs
Number of modules operated via one control room	Multiple	Single
Number of modules (units) operated by one operator (crew)	Multiple	Single
Staffing level	Unknown	4-5
Number of control rooms	One or more	One
Shared system	Some	None

However, there is no operating experience from predecessor plants for the multi-modular plant, especially for the systems shared between modules. The operations of shared systems are related to many aspects, such as control system design [10–12], human factor engineering [13, 14], team work, and operator training. In order to provide a technical approach to solve the problem, this paper presents a design strategy of the operation for shared systems via a common control system of a multi-modular plant.

In the design, a digital control system is used to realize the monitoring and control of multiple modules and each individual module is controlled via an independent network domain. The HSI (human-system interface) network connects all control network domains on an upper level, which enables monitoring and control of the whole plant through the operator workstation. Different operation and control strategies are considered for different types of shared systems. Control procedures are developed, and an example of the shared system control design in HTR-PM is presented.

## 2. Issues of Control and Operation of Shared Systems

*2.1. Shared Systems.* The shared systems refer to the resources and components that are shared among modules. The sharing of systems cannot impair the ability of the systems to perform their safety functions. Thus, an important objective of sharing systems is to reduce cost while maintaining safety. For many designs of multi-modular plants, safety functions are not shared. In this paper, the shared systems mainly include the process systems and control systems, which are all non-safety systems. Infrastructures are not included, such as buildings and structures mentioned in [4, 8], because they need no controls.

According to the degree of the sharing, the shared systems can range from minor support or auxiliary systems to major primary or secondary systems. The minor support and auxiliary systems include systems for circulating water, instrument air, service-water cooling, and AC and DC electric power. These systems supply working medium for modules simultaneously or in turn. As important auxiliary systems, the failure of shared process system may result in abnormal situation of one module or more. The turbine generator coupled with two or more modules of HTR-PM [15] is an example of the major systems shared among modules. The steam generated by the two NSSS (nuclear steam supply system) modules, respectively, feeds one steam turbine to generate electricity. The turbine generator may be the biggest system shared among modules.

At the view of control, the shared systems can be categorized into two types. The first type is the systems capable of connecting with all modules simultaneously, such as the turbine shared among modules, or the device-cooling water systems. The second type is the system connecting with one module at a time, which is an independent system with full capacity for one module that can be cross-connected to support the other module if necessary. An example of this type of sharing is the standby coolant supply system that provides the capability to cross-connect selected portions of the residual heat removal (RHR) systems between units [5].

In order to realize the integrated monitoring and control, the common control system should be employed, which is another shared aspect. According to the I&C (instrument and control) design of current NPPs, all processes are monitored and controlled in an integrated fashion, and one control room is used. For the multi-modular plant, all modules may be monitored and controlled via a common control system, similarly to current NPPs.

*2.2. Differences with Current NPPs.* Operation of multi-modular plant is different with current NPPs, as shown in Table 1. These differences may have the potential to impact human performance.

For current NPPs, one control room is used to realize the monitoring and control of a single unit, and four or five operators are responsible for operation of reactor, turbine, and balance of plant (BOP), respectively. All systems involved are serving for one unit; there is no concept of “sharing.”

For a multi-modular plant, one control room may be used to realize the monitoring and control, and multiple modules may be operated by one operator (crew). The challenge to the operator lies in monitoring such a control system to confirm that individual modules and shared system are performing properly and that there are not degradations of the I&C system.

*2.3. Operation of Shared Systems.* The operational impact of control systems for shared aspects is identified as one of the potential human performance issues that should be considered in the US Nuclear Regulatory Commission’s reviews of SMR designs [9]. The integrated control of multiple modules and their shared systems can be an operational challenge, as well as an I&C (instrument and control) one.

For the multi-modular system, the concept of operations is in the preliminary stages and control room and HSI designs are all in conceptual phase. However, no matter what is the control room or HSI like, the control system of shared aspects

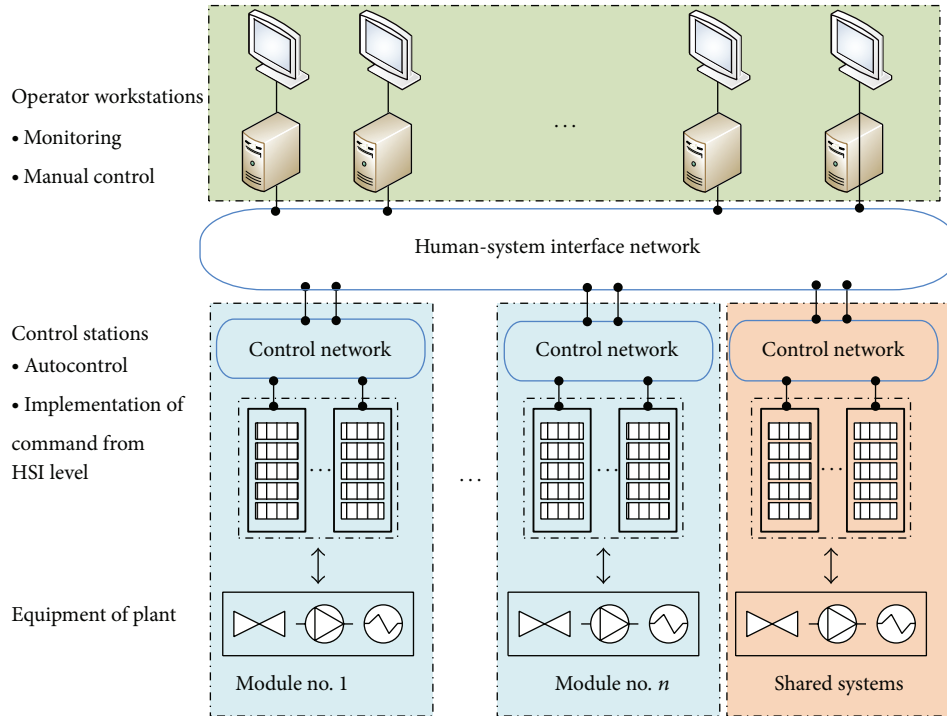


FIGURE 1: Control system of the multi-modular plant.

is an important issue to be solved, which may include some special problems.

- (1) How can the operators monitor and control the multiple modules and shared systems?
- (2) How are the controls of multiple modules and shared systems to be implemented at operator workstations?
- (3) Can different operators at different workstations monitor different modules and shared systems?
- (4) Are the shared systems to be operated by more than one operator?
- (5) How to control the shared system by more than one operator?
- (6) Are there increased opportunities for wrong operation?

The problems above are to be solved through two technical approaches in this paper: control system design and operation strategy.

### 3. A Design of Control System for a Multi-Modular Plant

It is a trend for the nuclear industry to employ a digital I&C system. For the modular reactors designed recently, most of them employ the digital I&C, such as SMART [16] in Korea and mPower [17] in America.

Control room designs are in the conceptual phase for many types of modular reactors. Configuration of the HSI and staffing level [18] are developed as prototypes and not

finally determined. However, some design characteristics of the control system can be determined based on the monitoring and control function of the multi-modular system without consideration of the control room design.

**3.1. System Architecture.** A control system should be employed to realize the integrated monitoring and control for the multi-modular system, as shown in Figure 1.

Similar to current digital control systems, the system consists of devices divided into three levels: the first level is the equipment of the plant, the second level is the control station, and the third level is human-system interface (HSI) device. The HSI devices supply information and controls, where the operator monitors and controls the plant; the control stations execute the commands from HSI level and automation of the equipment is executed here, too.

Considering the characteristics of the multi-modular system, the network is designed a little different. Control stations for a single module are designed to be connected in an independent network domain. Here, the independent network domain refers to a domain without direct network connection to the other domain on the control network level, and each network domain has its own network switches to the HSI network level. The control stations in an independent domain are dedicated to control the process for a single module. Similarly, control stations dedicated for shared systems are connected by another independent network domain.

The HSI network connects the control network of each module and shared systems on an upper level, and the data of every module and every shared system can be accessed

and viewed by any VDU (visual display unit) at the operator workstation.

### 3.2. System Characteristics

3.2.1. *Advantages.* The system architecture may have many advantages, including the following.

- (1) The control system design enables integrated monitoring and control from one control room or two separate control rooms, which supplies flexibility for control room design and HSI design.
- (2) Failure of one individual control network domain cannot affect other control network domains, which ensures the normal operation of other modules and shared systems and minimizes the risk of control failures of all modules due to a network common-cause failure.
- (3) Failure of HSI network may not affect the automation of the plant executed in the control station on the control network level.
- (4) The design enables adding new module controls to the system with less impact on current modules.
- (5) The design also enables the authority definition according to the network domain. Different control authorities can be defined based on the network position of the control system.

3.2.2. *Possible Drawback.* Failures of HSI network will cause loss of the monitoring and manual operation of the whole plant via the control system. Diversities should be provided, such as direct hardwire connection from plant equipment to the control room and safety monitoring and controls (not included in Figure 1). The hardwire connection and safety controls are not aspects shared among modules and not the focus of this paper.

### 3.3. Authority Design

3.3.1. *Necessity of Authority Limitation.* For current NPPs, there are few concepts of authority. The plant is controlled by the operator according to the operating procedures. Every operator has his own responsibility; the reactor operator is in charge of the reactor control and the turbine operator is in charge of the turbine control.

For a plant with multiple modules, if there is no authority limitation, control of shared system may cause confusion between operators especially for the system operated by different operators at the same time. Therefore, the operation authority of a certain operator should be limited. In order to solve the problem, three different types of authorities are defined: monitoring authority, operation authority, and allocation authority.

3.3.2. *Monitoring Authority.* Monitoring authority here refers to the access to displays at the operator workstation. HSI of the operator workstation is the most important way to share

information and support teamwork, and any operator logged in the system should have the authority to view all displays. The control system architecture enables that, because every operator workstation has the same function as a node of the network.

3.3.3. *Operation Authority.* Operation authority refers to the authorization of an operator to operate the plant equipment via VDUs. According to design aspects of the control system, different types of operation authority can be defined. Figure 2 gives an illustration of the operation authority design. Operation authority can be divided into two types: individual module operation and individual shared system operation.

Control authority corresponding to the first network domain refers to the operation authority of the equipment dedicated for module no. 1. Operators with operation authority of network domain of module no. 1 can operate the equipment of module no. 1 through operator workstation. Similarly, operators with operation authority in control network domain of shared systems can operate the equipment of the shared systems.

An operator may have the authorities of more than one domain or system according to the task he should accomplish. The equipment in a certain system can be operated by anyone who owns the corresponding authority. The authority of one system can be assigned to more than one operator. Here, operators with different authorities are identified by the user name and password when they log in the HSI system.

3.3.4. *Allocation Authority to the Operator.* Besides the basic operation of the real equipment in the plant, there is another kind of authority, which is designed to be implemented by the senior operator, such as the supervisor. This kind of authority enables the supervisor to allocate operation authority to a certain operator, according to the situation of the plant.

Some of the modules are shut down due to the need of the electrical power grid, and the responsibility of the operator who is in charge of these modules may be changed and the operation authority also needs to be changed. Here, the allocation of the control authority makes the sense. The operation authority can be changed at the supervisor workstation through VDUs.

The design of allocation authority supplies flexibility in operation authority configuration according to the plant situation of multiple modules.

3.3.5. *Advantages of Authority Limitation.* This operation authority design enables one module to be operated by a certain operator as well as one operator to operate some certain modules. It is designed to minimize the opportunity for wrong operation between modules and the control confusion of the shared system by different operators at different workstations. If, according to the task analysis, an operator is in charge of only one module, he should not operate the equipment of other modules to avoid confusion between modules. The authority design is a technical approach to minimize human mistakes.

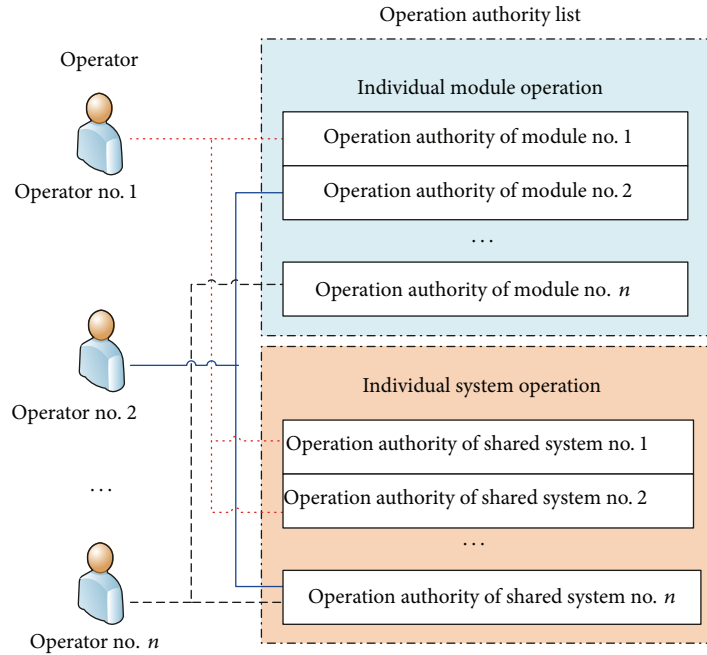


FIGURE 2: Operation authority design.

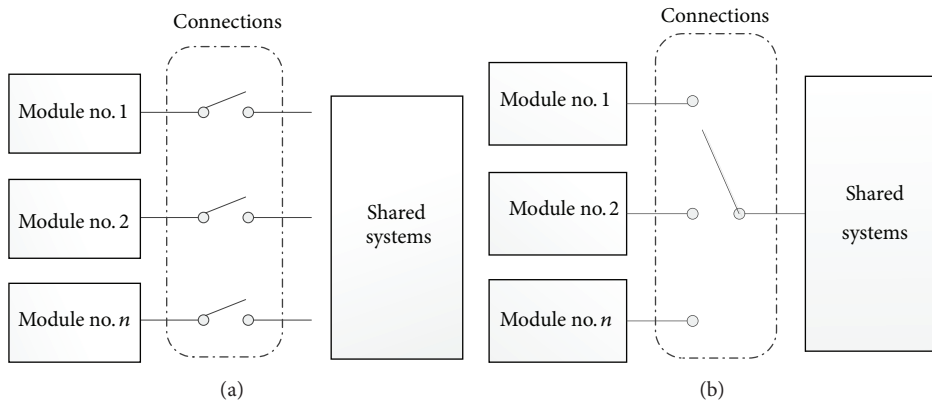


FIGURE 3: Differences of the two types of shared systems.

#### 4. Operation Strategies of Shared Systems

The shared systems may include small auxiliary systems and big primary or secondary systems. However, at the view of control, the systems shared among modules can be divided into two types: the systems capable of connecting with all modules simultaneously and the systems connecting with one module at a time.

The differences of two types are shown in Figure 3, in which the connections between systems are represented by different types of electrical switches.

For system capable of connecting with all modules simultaneously, there is no need of switchover function from one module to another. The connection can be switched on or off according to the operation requirement of each module with little interaction effect on other modules.

For systems connecting with one module at a time, the switchover function is needed. Switchover between modules

is complicated, because the switchover may impact the states of the two modules before and after the switchover. Some special strategies should be considered.

*4.1. System Capable of Connecting with All Modules Simultaneously.* For the shared systems capable of connecting all modules simultaneously, the operation authority can be allocated to one certain operator by the supervisor for the first time and not changed most of the time.

No matter whether the system shared is small or big, the control strategies are similar. The cooling water system supplies water for all modules at the same time, and control of this system may be authorized to a certain operator, who is responsible for monitoring and controlling the water supply for all modules. Control of turbine generator shared among modules is similar, and operator who is in charge of turbine control should have the authority to control the related components.

TABLE 2: States of the shared system.

System state definition	Representation
0	The system is idle, not connecting with any module
1	The system is connecting with module no. 1
2	The system is connecting with module no. 2
$n (n \neq 0)$	The system is connecting with module no. $n$

The operation authority for a certain operator is not changed most of the time. However, if the operation mode of the plant is changed due to some reason, such as the scheduled inspection outage, the tasks of the operator in charge of the module and the shared systems may be changed. The supervisor can allocate the operation authority of shared systems to other operators.

**4.2. Systems Connecting with One Module at a Time.** According to the switchover requirement, the states of shared system should be defined, as shown in Table 2.

Different states of the system can be defined through some status of the system, such as the combination states of some valves, system temperatures, and system pressures.

**4.2.1. Switchover Controlled by Automation.** For the system connecting with one module at a time, according to the frequency of the system switchover between modules, the control function is assigned to the automation or operator. If the switchover between modules is frequent and need not the permission of operator, the switchover function can be assigned to the automation.

Figure 4 shows the switchover controlled by automation.

**4.2.2. Switchover Controlled by Operator.** If the shared system serves the modules in turn and cannot be operated automatically due to the importance of the system, special design is considered to solve the problem.

The operation authority of the shared system is allocated to all module operators who need the system. The shared system can be used by only one module at the same time. Therefore, a preemptive algorithm is applied to the control logic of the shared system. The algorithm is shown in Figure 5.

- (1) If the system state is 0, any module can use the system through the automation process or manual operation by the operator.
- (2) If the system state is not 0, which is 1, that means the system is used by module no. 1, and the system state cannot be set to other numbers by other operators except the operator of module no. 1. If the system is needed by other modules, the operator in charge of module no. 1 should “release” the system and then the system state is set to 0.
- (3) When the shared system is used by one module and is needed by other modules, the coordination between modules is needed, such as communication between operators and judgment of situation after system switchover to other modules.

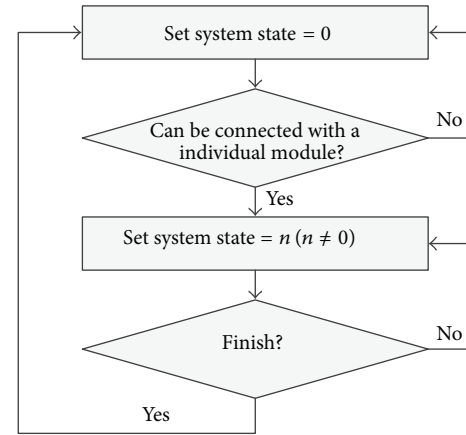


FIGURE 4: System switchover controlled by automation.

**4.3. Corporation between Operators.** The operation of multiple modules and shared systems relies on high levels of automation and team work. Corporation between different operators is more complicated than it is in current NPPs.

**4.3.1. Mode of Corporation.** According to the characteristics of different systems shared (switchover between modules or not), the corporation modes between operators are different.

The operator corporation for the control of the system capable of connecting with all modules simultaneously is similar to the corporation in current NPPs, because the system shared is related to whole plant, and control of the shared system is related to all operators. The corporation of the control for the system switchover between modules is different, because it is related to only two modules, and other modules and operators may not be included in the switchover corporation.

**4.3.2. HSI Consideration.** In order to support the corporation between different operators, the human-system interface should supply information necessary, including the following.

- (1) All displays can be viewed by any operator at any workstation in the control room, no matter whether the operator has the operation authority of the system or not.
- (2) The in-use and idle state of the shared system (whether system state is 0 or not) should be clearly shown on the display where the shared system is needed.
- (3) If the system is used by any module, which module is served for (the number of the system state) should be clearly shown on the display.

## 5. Example and Application

**5.1. Example.** The control of shared system for a multi-modular system is in preliminary stage. And there is an example of control design of the some shared systems in HTR-PM.

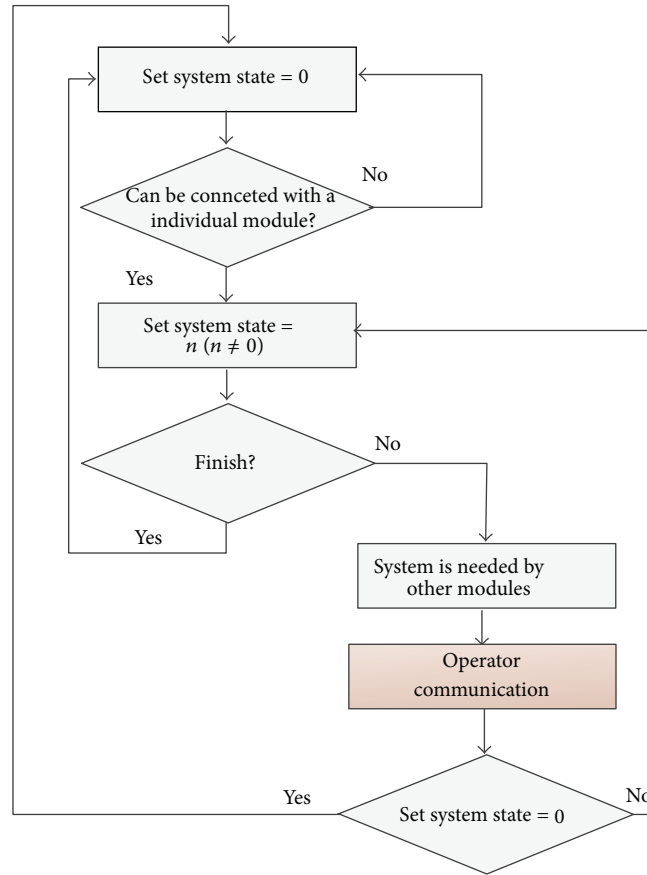


FIGURE 5: System switchover controlled by operators.

HTR-PM is the demonstration construction of the Chinese design [15] of the MHTGR (modular high-temperature gas-cooled reactor). The HTR-PM plant consists of two nuclear steam supply systems (NSSSs), which are the modules. Each module includes a single zone 250 MW<sub>th</sub> pebble-bed modular reactor and a steam generator. The steam generated by the two NSSSs, respectively, feeds one steam turbine generating an electric power of 210 MW.

In HTR-PM, the turbine generator is the biggest sharing which connects with two modules simultaneously. There are some other auxiliary systems shared between the two modules, as shown in Figure 6.

In the two-modular HTR-PM, one control room is used to realize the monitoring and control of the whole plant. A DCS (distributed control system) is employed [19]. There are four operators in the control room, including two reactor operators, one turbine operator, and one supervisor. The two reactor operators (ROs) are in charge of the two NSSS modules operations, respectively, and turbine operator (TO) is in charge of turbine generator operation. The basic operation authorities of one RO include the operation of one NSSS module and some shared systems. RO no. 1 cannot operate the equipment of NSSS no. 2 and the turbine generator, and RO no. 2 cannot operate the equipment of NSSS no. 1 and the turbine generator. The responsibility of each operator is not changed most of the time.

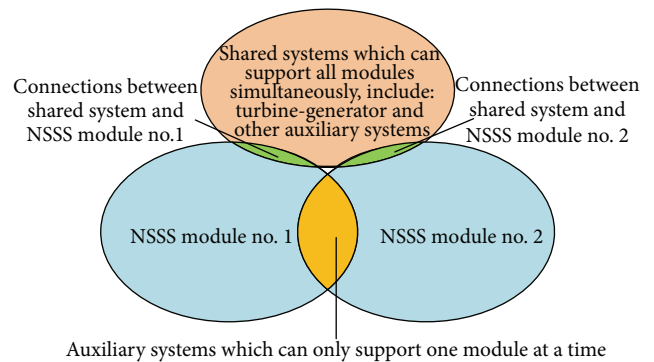


FIGURE 6: Relationship between shared systems and modules in HTR-PM.

The switchover of the shared systems between two modules is considered as follows. If one subsystem is needed by module no. 2 while it is supporting module no. 1, RO no. 2 should communicate with RO no. 1 and supervisor. If the supervisor and RO no. 1 determine that the switchover will not impact the situation of module no. 1, RO no. 1 should “release” the shared system through an operation via VDU, and then RO no. 2 can use the shared system for reactor no. 2.

The communication and corporation between the two ROs can be presented by the flow chart shown in Figure 7(a).

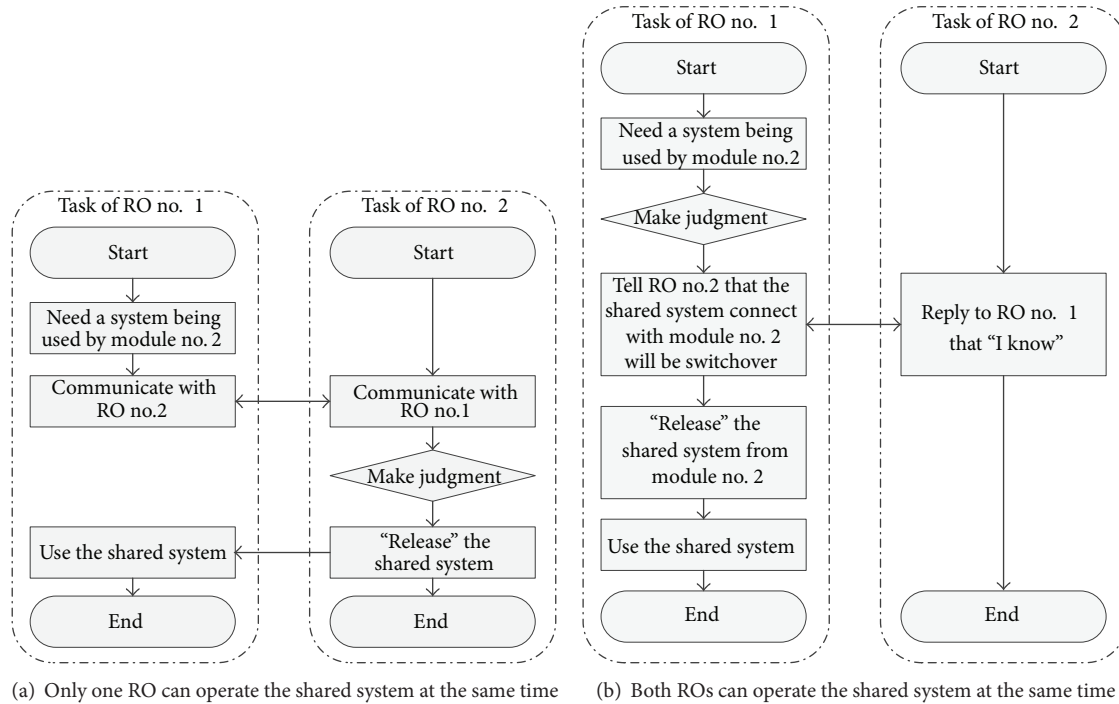


FIGURE 7: Comparison of corporation of two ROs on the shared system switchover between modules.

It is clear that if corporation fails, the shared system cannot be used by the other module. The operation design forces different operators to communicate with each other on switchover of the shared system in order to ensure that both ROs keep the situation awareness of the shared system.

**5.2. Comparison and Analysis.** There should be another design of the switchover operation of the shared system, as shown in Figure 7(b). If the two ROs can operate the shared system at the same time, the time elapsed may be shortened, but the communication and corporation between two ROs are weakened, and RO no. 2 may possibly neglect the switchover of the shared system to the other module. The design in Figure 7(a) may need more operation time than the design of Figure 7(b) but supply better communication and situation awareness of the shared system.

## 6. Conclusion

A design of operation of shared systems via a common control system for a multi-modular plant is presented. Without consideration of the workstation configuration and staffing level of the control room design, this paper focuses on the control and operation of the shared systems. A control system and its control network configuration are designed. Each module is controlled via an independent network domain, and failures of one independent network domain may not affect other modules. Displays of all modules can be viewed at any operator workstation under the structure of the control system. In order to minimize the human error of operation between modules and control confusion of shared system between operators, different operation authorities

corresponding to network domain are defined. An allocation authority is also defined to supply flexibility for configuration of operation authorities of operators under different plant situations.

According to the characteristics of different shared systems, the shared system can be categorized into two types: the system capable of connecting with all modules simultaneously and the system connecting with one module at a time. Different control strategies are developed for the shared systems. The preemptive algorithm of the system switchover is designed to force the operators to communicate with each other on the shared system. An example in HTR-PM of a shared system control is shown as an application of the design strategy.

The design of I&C system for the multi-modular plant is in the preliminary stage, and there are many other issues to be discussed. The control and operation presented in this paper need further verification and validation to prove that it is good for human performance.

## Conflict of Interests

The authors declare that there is no conflict of interests regarding the publication of this paper.

## Acknowledgments

This work has been supported by the National S&T Major Project (Grant no. ZX06901) and Tsinghua University Initiative Scientific Research Program (no. 20131089232).

## References

- [1] International Atomic Energy Agency, “Innovative small and medium sized reactors: design features, safety approaches and R&D trends,” IAEA-TECDOC-1451, 2005.
- [2] J. Vujić, R. M. Bergmann, R. Škoda, and M. Miletić, “Small modular reactors: simpler, safer, cheaper?” *Energy*, vol. 45, no. 1, pp. 288–295, 2012.
- [3] Z. Liu and J. Fan, “Technology readiness assessment of Small Modular Reactor (SMR) designs,” *Progress in Nuclear Energy*, vol. 70, pp. 20–28, 2013.
- [4] V. Kuznetsov, “Options for small and medium sized reactors (SMRs) to overcome loss of economies of scale and incorporate increased proliferation resistance and energy security,” *Progress in Nuclear Energy*, vol. 50, no. 2–6, pp. 242–250, 2008.
- [5] M. D. Muhlheim and R. T. Wood, “Design strategies and evaluation for sharing systems at multi-unit plants,” ORNL/LTR/INERI-BRAZIL/06-01, Oak Ridge National Laboratory, 2007.
- [6] W. S. Jung, J.-E. Yang, and J. Ha, “A new method to evaluate alternate AC power source effects in multi-unit nuclear power plants,” *Reliability Engineering & System Safety*, vol. 82, no. 2, pp. 165–172, 2003.
- [7] S. R. P. Perillo, B. R. Upadhyaya, and F. Li, “Control and instrumentation strategies for multi-modular integral nuclear reactor systems,” *IEEE Transactions on Nuclear Science*, vol. 58, no. 5, part 2, pp. 2442–2451, 2011.
- [8] D. Clayton and R. Wood, “The role of instrumentation and control technology in enabling deployment of small modular reactors,” in *Proceedings of the 7th International Topical Meeting on Nuclear Plant Instrumentation, Control, and Human-Machine Interface Technologies (NPIC-HMIT '10)*, pp. 140–152, American Nuclear Society, Las Vegas, Nev, USA, November 2010.
- [9] J. O’Hara and J. Higgins, “NRC reviewer aid for evaluating the human factors engineering aspects of small modular reactors,” BNL-96809-2012, 2012.
- [10] C. Weaver, K. Harris, and S. Blomgren, “Developing the human system interface (HSI) and the supporting instrumentation control (IC) architecture for a multi-module control room,” in *Proceedings of the 7th International Topical Meeting on Nuclear Plant Instrumentation, Control, and Human-Machine Interface Technologies (NPIC-HMIT '10)*, pp. 348–356, Las Vegas, Nev, USA, November 2010.
- [11] T. V. Nguyen, K. D. Leidy, D. P. Keene, and B. K. Arnholt, “Key design challenges in next generation instrumentation control (IC) systems for small modular reactor nuclear power plants,” in *Proceedings of the 8th International Topical Meeting on Nuclear Plant Instrumentation, Control, and Human-Machine Interface Technologies (NPIC-HMIT '12)*, Enabling the Future of Nuclear Energy, American Nuclear Society, San Diego, Calif, USA, 2012.
- [12] B. Lu, M. Memmott, and A. Harkness, “Small Modular Reactor (SMR) instrumentation control (IC) functional and structural requirements considerations,” in *Proceedings of the 8th International Topical Meeting on Nuclear Plant Instrumentation, Control, and Human-Machine Interface Technologies (NPIC-HMIT '12)*, Enabling the Future of Nuclear Energy, American Nuclear Society, San Diego, Calif, USA, 2012.
- [13] J. O’Hara, J. Higgins, R. Deem, J. Xing, and A. D’Agostino, “Human factors aspects of operating small modular reactors,” in *Proceedings of the 7th International Topical Meeting on Nuclear Plant Instrumentation, Control, and Human-Machine Interface Technologies (NPIC-HMIT '10)*, pp. 1780–1791, American Nuclear Society, Las Vegas, Nev, USA, November 2010.
- [14] T. Q. Tran, H. Garcia, R. L. Boring, J. C. Joe, and B. P. Hallbert, “Human factors issues for multi-modular reactor units,” in *Proceedings of the 8th IEEE Conference on Human Factor and Power Plants and HPRCT*, pp. 347–352, Institute of Electrical and Electronics Engineers, Monterey, Calif, USA, August 2007.
- [15] Z. Zhang, Z. Wu, D. Wang et al., “Current status and technical description of Chinese  $2 \times 250 \text{ MW}_{th}$  HTR-PM demonstration plant,” *Nuclear Engineering and Design*, vol. 239, no. 7, pp. 1212–1219, 2009.
- [16] I. S. Koo, Technical Features of the I&C System Design and Technology of SMART, <http://www.iaea.org/NuclearPower/Downloadable/Meetings/2013/2013-05-21-05-24-TM-NPTD/day-2/20.smart-koo.pdf>.
- [17] B. K. Arnholt, The B&W mPower™ Small Modular Reactor I&C Design, Architecture and Challenges, <http://www.iaea.org/NuclearPower/Downloadable/Meetings/2013/2013-05-21-05-24-TM-NPTD/day-3/23.mpower-arnholt.pdf>.
- [18] J. Smith and R. Moore, “Small modular reactor issue identification and ranking program control room staffing—final report,” in *Proceedings of the 8th International Topical Meeting on Nuclear Plant Instrumentation, Control, and Human-Machine Interface Technologies (NPIC-HMIT '12)*, Enabling the Future of Nuclear Energy, American Nuclear Society, San Diego, Calif, USA, 2012.
- [19] International Atomic Energy Agency, Status report 96—High Temperature Gas Cooled Reactor—Pebble-Bed Module, 2011.

## Research Article

# The Effect of Beam Intensity on Temperature Distribution in ADS Windowless Lead-Bismuth Eutectic Spallation Target

Jie Liu, Lei Gao, and Wen-qiang Lu

University of Chinese Academy of Sciences, Beijing 100049, China

Correspondence should be addressed to Jie Liu; [nauty@ucas.ac.cn](mailto:nauty@ucas.ac.cn)

Received 25 November 2013; Accepted 28 January 2014; Published 19 March 2014

Academic Editor: Li Shengqiang

Copyright © 2014 Jie Liu et al. This is an open access article distributed under the Creative Commons Attribution License, which permits unrestricted use, distribution, and reproduction in any medium, provided the original work is properly cited.

The spallation target is the component coupling the accelerator and the reactor and is regarded as the “heart” of the accelerator driven system (ADS). Heavy liquid metal lead-bismuth eutectic (LBE) is served as core coolant and spallation material to carry away heat deposition of spallation reaction and produce high flux neutron. So it is very important to study the heat transfer process in the target. In this paper, the steady-state flow pattern has been numerically obtained and taken as the input for the nuclear physics calculation, and then the distribution of the extreme large power density of the heat load is imported back to the computational fluid dynamics as the source term in the energy equation. Through the coupling, the transient and steady-state temperature distribution in the windowless spallation target is obtained and analyzed based on the flow process and heat transfer. Comparison of the temperature distribution with the different beam intensity shows that its shape is the same as broken wing of the butterfly. Nevertheless, the maximum temperature as well as the temperature gradient is different. The results play an important role and can be applied to the further design and optimization of the ADS windowless spallation target.

## 1. Introduction

At present, China's nuclear power industry is expanding rapidly and more nuclear power plants are being built to solve air pollution and energy need. Naturally, it will lead to the severe problem of nuclear waste disposal. The accelerator driven system (ADS), shown in Figure 1 [1], aiming at the management and disposal of high level nuclear wastes, is of high cleanliness and safety. So the construction of ADS has been included in the large science and technology fundamental facilities in the twelfth five-year plan of the National Development and Reform Commission (NDRC) of China. The study of ADS has already been carried out systematically for decades in Europe. In earlier designs, a window exists between the proton beam and the target to ensure the accelerator is safe. But the window needs to sustain high-energy proton irradiation and corrosion by the flowing heavy liquid metal in very high temperature and no suitable materials can be used for a long time at present. Therefore, the windowless design is more desirable for it is able to avoid the problems of materials [2].

The thermal hydraulics design of the target is a challenging task, as the space available is very limited and the maximum heat load is about  $300 \text{ W/cm}^3$  and the total heat deposit reaches 2.1 MW [1]. Previous works focus on the heat transfer in the spallation target with a window. For example, Nema [3] introduced the Indian roadmap and activities under ADS programme. Mantha et al. [4] proposed an experimental LBE loop for simulating the window thermal load by a high power plasma torch and conjugate heat transfer analysis has been carried out for various window materials, geometry, and flow configuration to determine cooling capability of LBE. Borgohain et al. [5] carried out steady-state natural circulation experimental studies and transient studies for start-up of natural circulation in the loop, loss of heat sink, and step power change. Cho et al. [6] proposed a numerical design study to obtain the optimal design parameters for a 20 MW spallation target for a 1000 MWth ADS and a dual injection tube for a reduction of the LBE flow rate at the target channel. Zanini et al. [7] performed the research of the thermal hydraulics behavior from the neutronic and nuclear aspects during the irradiation in the MEGAPIE

target at the SINQ Facility of the Paul Scherrer Institute. Vanderhaegen et al. [8] simulated the flow inside the vessel in the MYRRHA project using the renormalization group  $k$ - $\epsilon$  turbulence model by the computational fluid dynamics software FLUENT. Su et al. [9, 10] built the water experiment to study the free surface behavior and flow patterns which means the respective distribution of the liquid and vapor phases in the flow channel.

The studies mentioned above are all based on the window spallation target because the heat transfer is relatively easy to carry out as the single phase flow in it. However, the beam intensity will be stronger and stronger with the development of the accelerator in the windowless design as there is no limit to window materials, so it is necessary to carry out the research of heat transfer in ADS windowless spallation target as well as different results with various intensity beams to catch up with the development of the accelerator. Roelofs et al. [11] reviewed the development of ADS windowless spallation target in the experiment and the numerical simulation. But the heat transfer in the heavy liquid metal LBE in the windowless spallation target has not been published as far as authors' knowledge is concerned because of the high difficulty caused by the complicated two-phase flow and its interaction with the proton beam. In this paper, the heat transfer calculation is performed and steady-state and transient temperature distribution is obtained which is very important in the further design and optimization of the ADS windowless spallation target in China.

## 2. Numerical Model

During EUROTRANS the design of the windowless target has been evolved substantially so that the latest design (V0.10, Figure 1) conforms to specifications [1].

The flow is considered to be viscous, incompressible, and turbulent. The dimensionless equations governing the axisymmetric mean flow [12–14] are as follows.

Continuity equation

$$\frac{1}{x^j} \frac{\partial}{\partial x} (x^j u) + \frac{\partial v}{\partial y} = 0, \quad (1)$$

momentum equation

$$\begin{aligned} \frac{\partial u}{\partial \tau} + \left[ u \frac{\partial u}{\partial x} + v \frac{\partial u}{\partial y} \right] &= -\frac{\partial p}{\partial x} \\ &+ \frac{1}{x^j} \frac{1}{\text{Re}} \left[ \frac{\partial}{\partial x} \left( x^j \nu_{\text{eff}} \frac{\partial u}{\partial x} \right) \right. \\ &\quad \left. + \frac{\partial}{\partial y} \left( x^j \nu_{\text{eff}} \frac{\partial u}{\partial y} \right) \right] + S_u, \end{aligned}$$

$$\frac{\partial v}{\partial \tau} + \left[ u \frac{\partial v}{\partial x} + v \frac{\partial v}{\partial y} \right] = -\frac{\partial p}{\partial y}$$

$$\begin{aligned} &+ \frac{1}{x^j} \frac{1}{\text{Re}} \left[ \frac{\partial}{\partial x} \left( x^j \nu_{\text{eff}} \frac{\partial v}{\partial x} \right) \right. \\ &\quad \left. + \frac{\partial}{\partial y} \left( x^j \nu_{\text{eff}} \frac{\partial v}{\partial y} \right) \right] + S_v, \end{aligned} \quad (2)$$

where

$$\begin{aligned} S_u &= \frac{1}{x^j} \frac{1}{\text{Re}} \left[ \frac{\partial}{\partial x} \left( x^j \nu_{\text{eff}} \frac{\partial u}{\partial x} \right) + \frac{\partial}{\partial y} \left( x^j \nu_{\text{eff}} \frac{\partial v}{\partial x} \right) - 2j \nu_{\text{eff}} \frac{u}{x} \right], \\ S_v &= \frac{1}{x^j} \frac{1}{\text{Re}} \left[ \frac{\partial}{\partial x} \left( x^j \nu_{\text{eff}} \frac{\partial u}{\partial y} \right) + \frac{\partial}{\partial y} \left( x^j \nu_{\text{eff}} \frac{\partial v}{\partial y} \right) \right], \end{aligned} \quad (3)$$

where  $p$  is the pressure,  $v$  is velocity, and  $(u, v)$  are the radial and axial mean velocity components. The effective turbulent viscosity  $\nu_{\text{eff}}$  ( $= 1 + \nu_{t,n}$ ) is calculated using the  $k$ - $\epsilon$  model of turbulence:

$$\nu_{\text{eff}} = 1 + c_\mu \text{Re} \frac{k_n^2}{\epsilon_n}. \quad (4)$$

Transfer of the turbulent kinetic energy  $k_n$ , its dissipation rate  $\epsilon_n$ , and the temperature distribution  $\theta$  are modeled as follows.

$k$ -equation

$$\begin{aligned} \frac{\partial k_n}{\partial \tau} + u \frac{\partial k_n}{\partial x} + v \frac{\partial k_n}{\partial y} &= \frac{1}{x^j} \frac{1}{\text{Re}} \left[ \frac{\partial}{\partial x} \left( x^j \frac{\nu_{t,n}}{\sigma_k} \frac{\partial k_n}{\partial x} \right) \right. \\ &\quad \left. + \frac{\partial}{\partial y} \left( x^j \frac{\nu_{t,n}}{\sigma_k} \frac{\partial k_n}{\partial y} \right) \right] \\ &+ G_n - \epsilon_n, \end{aligned} \quad (5)$$

$\epsilon$ -equation

$$\begin{aligned} \frac{\partial \epsilon_n}{\partial \tau} + u \frac{\partial \epsilon_n}{\partial x} + v \frac{\partial \epsilon_n}{\partial y} &= \frac{1}{x^j} \frac{1}{\text{Re}} \left[ \frac{\partial}{\partial x} \left( x^j \frac{\nu_{t,n}}{\sigma_\epsilon} \frac{\partial \epsilon_n}{\partial x} \right) \right. \\ &\quad \left. + \frac{\partial}{\partial y} \left( x^j \frac{\nu_{t,n}}{\sigma_\epsilon} \frac{\partial \epsilon_n}{\partial y} \right) \right] \\ &+ \frac{\epsilon_n}{k_n} (C_{1\epsilon} G_n - C_{2\epsilon} \epsilon_n), \end{aligned} \quad (6)$$

energy equation

$$\frac{\partial \theta}{\partial \tau} + u \frac{\partial \theta}{\partial x} + v \frac{\partial \theta}{\partial y} = \frac{1}{x^j} \frac{1}{\text{RePr}} \left[ \frac{\partial}{\partial x} \left\{ x^j (1 + \alpha_{t,n}) \frac{\partial \theta}{\partial y} \right\} + S_\theta \right], \quad (7)$$

where  $S_\theta$  is the heat source term.

Production

$$\begin{aligned} G_n &= \frac{\nu_{t,n}}{\text{Re}} \left[ 2 \left\{ \left( \frac{\partial u}{\partial x} \right)^2 + \left( \frac{\partial v}{\partial y} \right)^2 + j \left( \frac{u}{x} \right)^2 \right\} \right. \\ &\quad \left. + \left( \frac{\partial u}{\partial y} + \frac{\partial v}{\partial x} \right)^2 \right], \end{aligned} \quad (8)$$

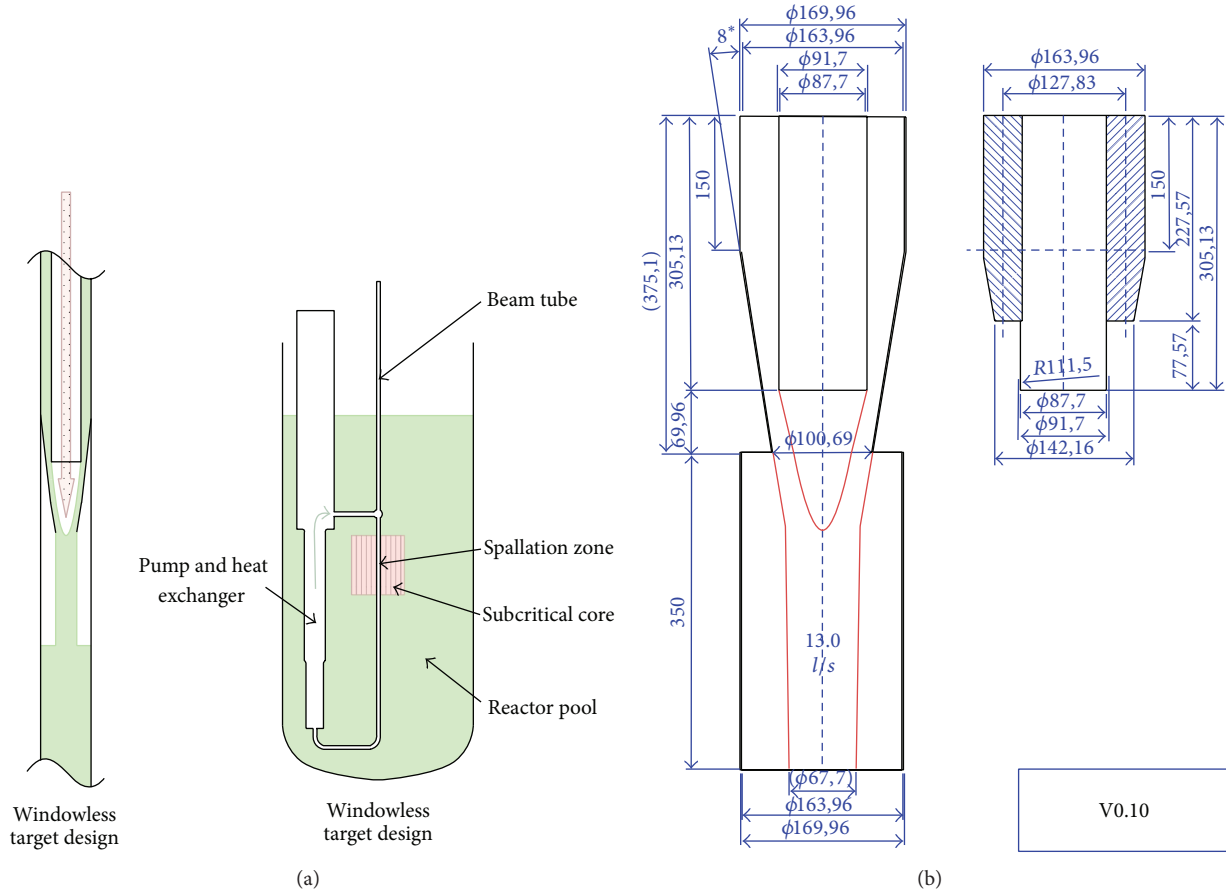


FIGURE 1: Schematic view of spallation target in the ADS (a) and construction of target (b) [1].

where  $G_n$  is the production term. Finally,  $v_{t,n}$  and  $\alpha_{t,n}$  can be written as follows:

$$v_{t,n} = C_\mu \text{Re} \frac{k_n^2}{\epsilon_n}; \quad \alpha_{t,n} = C_\mu \text{Re} \frac{\text{Pr} k_n^2}{\sigma_t \epsilon_n}. \quad (9)$$

Here,  $C_\mu = 0.09$ ,  $\sigma_k = 1.0$ ,  $\sigma_\epsilon = 1.3$ ,  $\sigma_t = 0.9$ ,  $C_{1\epsilon} = 1.44$ , and  $C_{2\epsilon} = 1.92$ .

According to the work by Batta and Class [15], volume of fluid (VOF) [16] combining with the cavitation is an appropriate numerical model to capture the free surface between the LBE liquid and LBE vapor. Therefore, the  $k$ - $\epsilon$  turbulence model, the VOF method, and the cavitation model are used to simulate the flow in the target. With correct physical parameters of LBE and appropriate boundary condition, the steady-state flow pattern of the LBE liquid and vapor has been captured by the authors [17–19] and shown in Figure 2. LBE liquid flows downwards through an annular feeder line surrounding the beam tube and will form a conical free surface which is subjected to the proton beam in early structure. Then, the use of wider guide tubes will result in a detachment zone near the guide tube and the second free surface forms. According to the design for the MYRRHA proton beam [20], the proton beam is circular and energy and maximum intensity are equal to 600 MeV and 4 mA in continuous wave mode, respectively. The spallation reaction

between the LBE and the proton beam is simulated using Monte Carlo radiation transport code that tracks particles.

To obtain heat deposition, the steady-state flow pattern and the nuclear cross section data libraries are introduced into nuclear physics simulation and the result is shown in Figure 3. Then, the initial temperature of the whole domain is set to be 723 K and the boundary conditions are given (Figure 4). Finally, the heat deposition is introduced into the energy equation in the CFD in order to gain the temperature distribution in the ADS windowless spallation target.

### 3. Numerical Results

**3.1. Temperature Distribution.** As larger beam intensity may cause boiling of LBE or other instable phenomena, smaller beam intensity is preferred in obtaining different temperature distribution with different beam intensity and 3 mA is chosen to compare with 4 mA. Figure 5 shows the temperature distribution at the initial time. The temperature distribution is the same as the shape of the heat deposition after taking logarithm calculation. So the heat deposition calculated from the nuclear physics simulation is correctly introduced into the CFD calculation. What is more, maximum temperature occurs near the initial contact surface of proton beam and LBE. It can be inferred that the heat deposition plays a leading

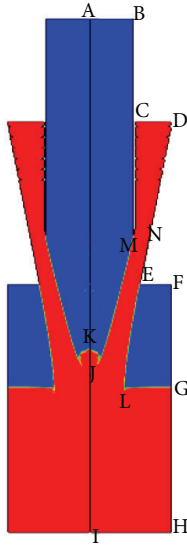


FIGURE 2: Steady-state flow pattern (red: LBE liquid; blue: LBE vapor).

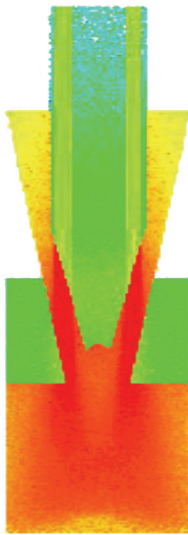


FIGURE 3: Schematic of the heat deposition in the LBE.

role in the forming of the temperature distribution at the very beginning instead of the flow of liquid metal LBE because the characteristic time scale of the spallation reaction is several magnitudes smaller than that of fluid flow and heat transfer by flow should be omitted. Therefore, the heat deposition can be regarded as the constant volumetric heat sources in the simulation of the flow process and heat transfer.

The temperature distribution varying with time while the spallation reaction takes place and fluid flows is shown in Figure 6. As can be seen, the maximum heat load at the contact surface is transferred to the downstream and then the temperature on the two-side free surface near the wall rises because of the flow of the LBE vapor. The temperature is higher near the free surface compared to other area. While the temperature of the LBE liquid at the outlet is very low near

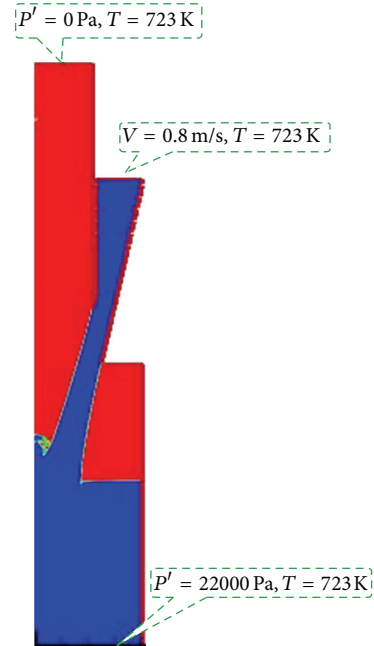


FIGURE 4: The initial temperature and boundary conditions.

the wall. Finally, the maximum temperature which occurs in the LBE liquid under the two-side free surfaces rises to about 815 K and the distribution is like the shape of broken wings of the butterfly.

**3.2. Physical Analysis.** The formation of the steady-state temperature distribution is the result of the heat deposition combined with the flow of the heavy liquid metal liquid and vapor, shown in Figure 7. As mentioned before, the distribution of heat deposition (Figure 7(b)) is formed according to the steady-state flow pattern (Figure 7(a)). It is one of the main reasons of the formation of such a temperature distribution that the area of high temperature in the steady-state temperature distribution (Figure 7(c)) just corresponds to the area of a relatively large intensity of the heat deposition on the basis of the comparison between the heat deposition and the steady-state temperature distribution (Figure 7(b)). In addition, another reason is the effect of fluid flow shown in the distribution of streamline (Figure 7(d)) and absolute magnitude of axial velocity (Figure 7(e)). It is illustrated that there is a clockwise vortex in the left side and an anticlockwise vortex in the right side of the streamline (Figure 7(d)) so that the large intensity of the heat deposition (Figure 7(c)) near to the free surface will transfer toward the area of high temperature in the steady-state temperature distribution. So the high temperature area distributes on the free surface on both sides and the temperature distribution is just like Figure 7(c) shown eventually.

**3.3. Comparison between 3 mA and 4 mA.** The authors [18] have calculated the temperature distribution while the beam intensity is 4 mA. Compared with that, the different temperature distribution at the initial time is shown in Figure 8. It can

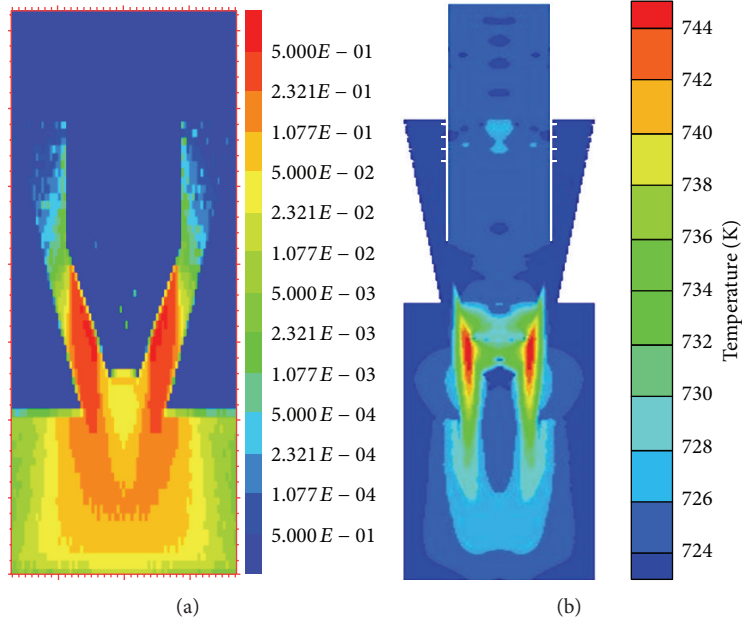


FIGURE 5: The heat deposition (a) and temperature distribution at the initial time ( $t = 0.1$  s) (b).

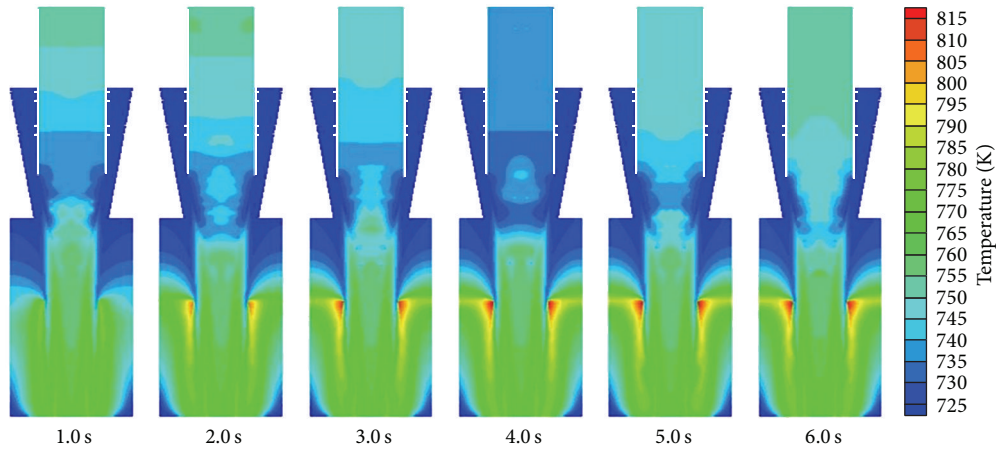


FIGURE 6: Temperature distribution varies with the time in 3 mA.

be seen that the shape of the distribution is the same while the maximum temperature at 3 mA is a little lower than that at 4 mA. To figure out how the temperature distribution of different beam intensity varies with time, the comparison at the time of 3 s and 6 s is given in Figure 9, respectively. Just like that at the initial time, the shape is almost the same. However, the maximum temperature is about 35 K higher while the beam intensity is 4 mA compared to 3 mA. Besides, the temperature distribution in the area of vapor is different as well (Figure 10). It is concluded that stronger beam intensity will lead to larger area of high temperature in the area of vapor located at the top of the target (zone “1” in Figure 10). Furthermore, it shows that the temperature gradient at 3 mA is smaller in the area of the vapor on the free surface (zone “2” in Figure 10). These results confirm the conclusion that the beam intensity has no effect on the shape of the temperature distribution while making a big difference to the temperature

value and stronger beam intensity leads to higher temperature and temperature gradient.

**3.4. Maximum Temperature.** Figure 11 shows the maximum temperature varying with the different beam intensity. It indicates that the maximum temperature at 3 mA is always lower than that at 4 mA at the same time. What is interesting is that the variation of maximum temperature at 3 mA is gentler while that at 4 mA has a steady state from the very beginning while that at 4 mA has a steady state from the very beginning to about 1 s and then the maximum temperature starts to rise. It is inferred that the very large heat deposition loaded plays a leading role compared with fluid flow at the beginning and it results in the initial variation at 4 mA. Afterwards, the temperature distribution will result from the common effect between heat deposition and fluid flow. When it refers to the variation at 3 mA, the heat deposition and fluid flow have an effect on the heat transfer in the windowless

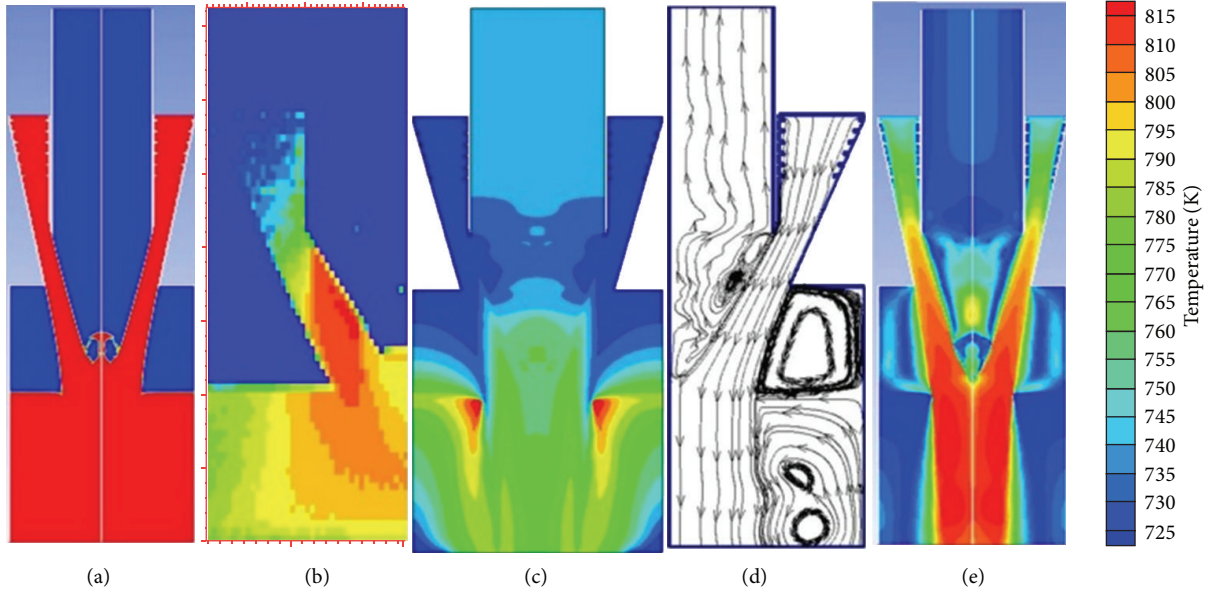


FIGURE 7: Distributions from left to right: (a) flow pattern; (b) heat deposition; (c) steady-state temperature distribution; (d) streamline; (e) absolute magnitude of axial velocity.

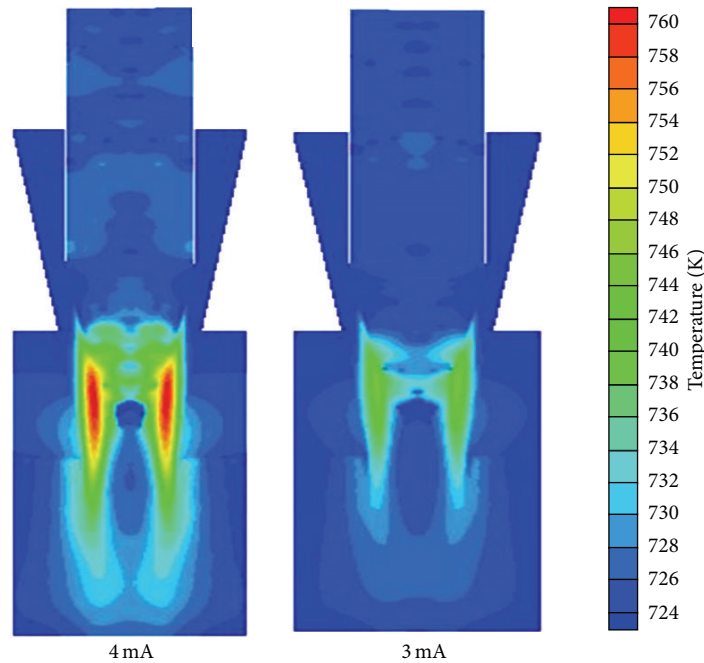


FIGURE 8: Initial temperature distribution varies with the beam intensity ( $t = 0.1$  s).

spallation target together all the time as the heat deposition is smaller. When it reaches the steady state, the maximum temperature at 3 mA is about 815 K while at 4 mA it is 848 K. The beam intensity is identified as follows:

$$N \times q_p = I \times t, \quad (10)$$

where  $N$  and  $q_p$  are the number and charge of the proton particles, respectively,  $t$  is time, and  $I$  is beam intensity. The stronger the intensity in the same period of time, the more

the energy of spallation reaction and higher temperature is caused by larger number of the proton particles. So the maximum temperature is always smaller while the beam intensity is 3 mA.

#### 4. Conclusions

The paper employs computational fluid dynamics and nuclear physics simulation and obtains the different temperature

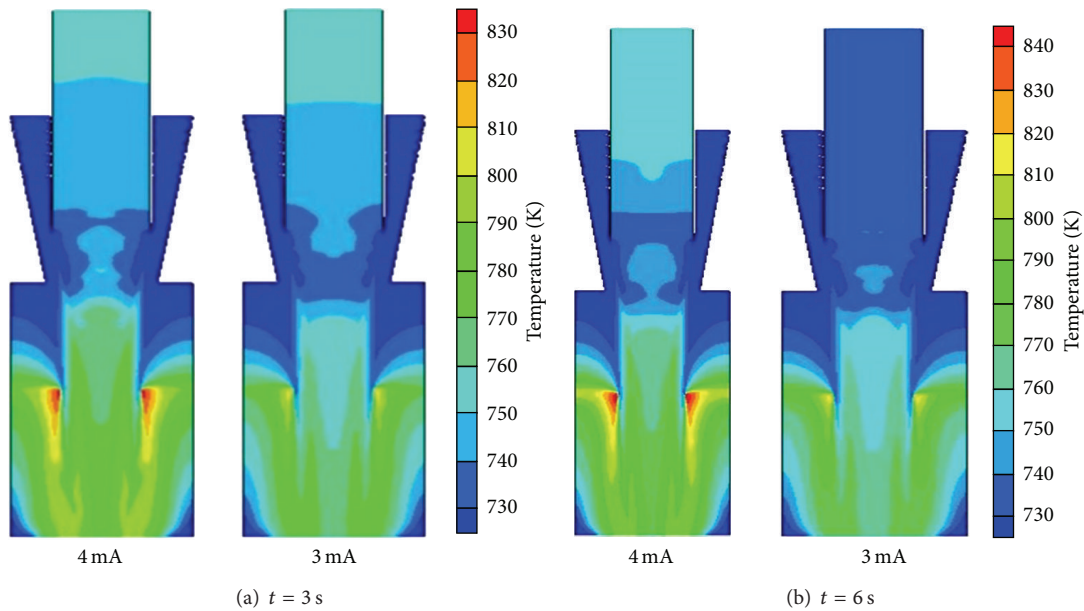


FIGURE 9: Transient temperature distribution varies with different beam intensity at  $t = 3$  s and 6 s.

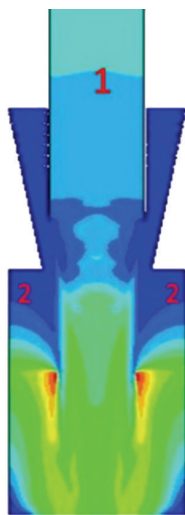


FIGURE 10: Two zones are depicted in the area of the vapor.

distribution in the ADS spallation target while the two values of beam intensity are set.

The CFD provides the phase flow pattern for the nuclear physics simulation and the result provides the heat load for the CFD. The heat load calculated from the nuclear physics simulation is correctly introduced into the CFD calculation and the temperature distribution is obtained finally.

Different beam intensity has little effect on the shape of the temperature distribution while making a big difference to the temperature value. The stronger the intensity is, the larger the temperature gradient is in the area of the vapor.

The maximum temperature varies with different intensity. When the beam intensity is 3 mA, the variation trend is gentler and the maximum temperature eventually reaches about 815 K. On the other hand, while the intensity is 4 mA,

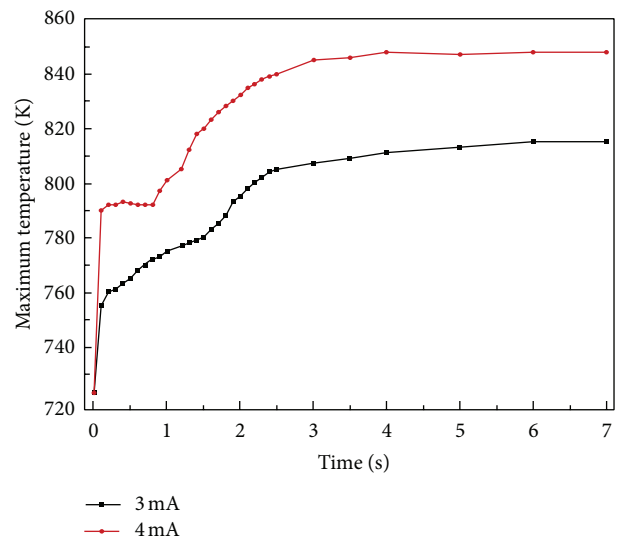


FIGURE 11: Maximum temperature varies with the beam intensity.

the maximum temperature will remain stable for a short time at the beginning and then will rise steadily to about 848 K. It can be inferred that the temperature varies by 4% per milliamper.

In the future, different proton beam spatial distribution as well as energy can be conducted to provide more complete results and references for the design and optimization of the ADS windowless spallation target.

### Conflict of Interests

The authors declare that there is no conflict of interests regarding the publication of this paper.

## Acknowledgments

The authors would like to thank Dr. Tian-jiao Liang and Dr. Song-lin Wang of the CAS Institute of High Energy Physics for their great help and support in nuclear physics calculation. This work is financially supported by the National Natural Science Foundation of China (Grant nos. 50936006 and 51276190).

## References

- [1] A. G. Class, D. Angeli, A. Batta et al., "XT-ADS Windowless spallation target thermohydraulic design & experimental setup," *Journal of Nuclear Materials*, vol. 415, no. 3, pp. 378–384, 2011.
- [2] F. Bianchi, R. Ferri, and V. Moreau, "Thermo-hydraulic analysis of the windowless target system," *Nuclear Engineering and Design*, vol. 238, no. 8, pp. 2135–2145, 2008.
- [3] P. K. Nema, "Application of accelerators for nuclear systems: accelerator Driven System (ADS)," *Energy Procedia*, vol. 7, pp. 597–608, 2011.
- [4] V. Mantha, R. Chaudhary, S. Pal et al., "Intense heat simulation studies on window of high density liquid metal spallation target module for accelerator driven systems," *International Journal of Heat and Mass Transfer*, vol. 49, no. 19–20, pp. 3728–3745, 2006.
- [5] A. Borgohain, B. K. Jaiswal, N. K. Maheshwari, P. K. Vijayan, D. Saha, and R. K. Sinha, "Natural circulation studies in a lead bismuth eutectic loop," *Progress in Nuclear Energy*, vol. 53, no. 4, pp. 308–319, 2011.
- [6] C. Cho, Y. Kim, T. Y. Song, and Y. Lee, "Numerical design of a 20 MW lead-bismuth spallation target with an injection tube," *Nuclear Engineering and Design*, vol. 238, no. 1, pp. 90–101, 2008.
- [7] L. Zanini, S. Dementjev, F. Gröschel et al., "Experience from the post-test analysis of MEGAPIE," *Journal of Nuclear Materials*, vol. 415, no. 3, pp. 367–377, 2011.
- [8] M. Vanderhaegen, J. Vierendeels, and B. Arien, "CFD analysis of the MYRRHA primary cooling system," *Nuclear Engineering and Design*, vol. 241, no. 3, pp. 775–784, 2011.
- [9] G. Y. Su, H. Y. Gu, and X. Cheng, "Experimental and numerical studies on free surface flow of windowless target," *Annals of Nuclear Energy*, vol. 43, pp. 142–149, 2012.
- [10] G. Su, X. Chai, H. Gu, and X. Cheng, "Studies on unsteady characteristics of free surface flow in ADS windowless target," *Journal of Engineering Thermophysics*, vol. 32, no. 9, pp. 1509–1512, 2011.
- [11] F. Roelofs, N. B. Siccama, H. Jeanmart, K. V. Tichelen, M. Dierckx, and P. Schuurmans, "Application of a controlled swirl in the XT-ADS spallation target," in *Proceeding of the International Conference on Advances in Nuclear Power Plants (ICAPP '08)*, Paper 8003, pp. 643–648, Anaheim, Calif, USA, June 2008.
- [12] J. N. Reddy and D. K. Gartling, *The Finite Element Method in Heat Transfer and Fluid Dynamics*, CRC Press, Boca Raton, Fla, USA, 1994.
- [13] R. L. Lewis, P. Nithiarasu, and K. N. Seetharamu, *Fundamentals of the Finite Element Method for Heat and Fluid Flow*, John Wiley and Sons, Chichester, UK, 2004.
- [14] K. Arul Prakash, G. Biswas, and B. V. Rathish Kumar, "Thermal hydraulics of the spallation target module of an accelerator driven sub-critical system: a numerical study," *International Journal of Heat and Mass Transfer*, vol. 49, no. 23–24, pp. 4633–4652, 2006.
- [15] A. Batta and A. Class, "Free surface modeling and simulation of the water experiment for the XT ADS spallation target," in *Proceedings of the International Congress on Advances in Nuclear Power Plants (ICAPP '08)*, pp. 1779–1786, Anaheim, Calif, USA, June 2008.
- [16] T. Wang, C. G. Gu, B. Yang et al., "PISO algorithm for unsteady flow field," *Journal of Hydrodynamics*, vol. 18, pp. 233–239, 2003.
- [17] J. Liu, B. Q. Liu, X. Z. Zhang et al., "Flow and phase change process of LBE liquid and vapor in the ADS windowless spallation target," *Journal of Engineering Thermophysics*, vol. 34, no. 9, pp. 1683–1686, 2013.
- [18] J. Liu, L. Gao, H. Chen et al., "Two-way coupling simulation of heat transfer in ADS windowless spallation target," in *Proceeding of the 21st International Conference on Nuclear Engineering (ICONE '13)*, vol. 3 of Paper No. ICONE21-15903, Chengdu, China, July 2013.
- [19] J. Liu, L. Gao, and W. Q. Lu, "The influence of adding swirl velocity on height of the recirculation region in ADS windowless spallation target," *Journal of Engineering Thermophysics*. In press.
- [20] <http://myrrha.sckcen.be/en/Engineering/Accelerator/Beam-specifications>.

## Research Article

# The Stress and Reliability Analysis of HTR's Graphite Component

**Xiang Fang, Haitao Wang, and Suyuan Yu**

*Institute of Nuclear and New Energy Technology, Tsinghua University, Beijing 100084, China*

Correspondence should be addressed to Xiang Fang; [fangxiang@tsinghua.edu.cn](mailto:fangxiang@tsinghua.edu.cn)

Received 15 November 2013; Revised 6 February 2014; Accepted 7 February 2014; Published 18 March 2014

Academic Editor: Luciano Burgazzi

Copyright © 2014 Xiang Fang et al. This is an open access article distributed under the Creative Commons Attribution License, which permits unrestricted use, distribution, and reproduction in any medium, provided the original work is properly cited.

The high temperature gas cooled reactor (HTR) is developing rapidly toward a modular, compact, and integral direction. As the main structure material, graphite plays a very important role in HTR engineering, and the reliability of graphite component has a close relationship with the integrity of reactor core. The graphite components are subjected to high temperature and fast neutron irradiation simultaneously during normal operation of the reactor. With the stress accumulation induced by high temperature and irradiation, the failure risk of graphite components increases constantly. Therefore it is necessary to study and simulate the mechanical behavior of graphite component under in-core working conditions and forecast the internal stress accumulation history and the variation of reliability. The work of this paper focuses on the mechanical analysis of pebble-bed type HTR's graphite brick. The analysis process is comprised of two procedures, stress analysis and reliability analysis. Three different creep models and two different reliability models are reviewed and taken into account in simulation. The stress and failure probability calculation results are obtained and discussed. The results gained with various models are highly consistent, and the discrepancies are acceptable.

## 1. Introduction

The high temperature gas cooled reactor is one of the candidate reactor types of the fourth generation advanced nuclear reactor [1]. At present, the development of pebble-bed type HTR technology is oriented to modularization, miniaturization, and integration. The side reflector of the reactor core is piled up by a large number of graphite bricks. The reliability of side reflector graphite component impacts the integrity and safety of reactor core directly. This paper mainly focuses on the analysis and study of graphite component's mechanical behaviors under in-core working conditions. The graphite components are subjected to high temperature load and fast neutron irradiation load simultaneously when the reactor operates. High temperature and irradiation not only create significant internal stresses, but also change the physical properties of graphite in evidence. The graphite component might deteriorate into failure if the internal stress accumulates to a certain extent. Most of graphite properties significantly change in high temperature and neutron irradiation conditions, and the changing of properties makes the behavior of graphite component more

complex [2]. Meanwhile, creep also plays a decisive role in the process. The majority of internal stresses can be relaxed by creep [3].

The mechanical analysis procedure of graphite component is sketched in Figure 1. The process consists of two steps. The first is stress analysis. The parameters of graphite (including Young's modulus, Poisson's ratio, the coefficient of thermal expanding, the irradiation-induced deformation, and the thermal conductivity), the geometric parameters (as the geometric model of graphite brick and finite element meshing), and the environment parameters (i.e., the boundary conditions for calculation, including temperature distribution and neutron dose distribution) are used as input data. Stress distribution and development history can be obtained after finite element analysis (FEA) calculation. Establishing a practical constitutive law is the key for this step. The thermal strain, irradiation-induced strain, and creep strain must be considered in the constitutive law. The second step is reliability analysis. In this step, the stress distribution gained in the first step is used as source data, and the reliability is estimated by form of failure probability or service life of graphite component [4]. Both deterministic and probabilistic methods

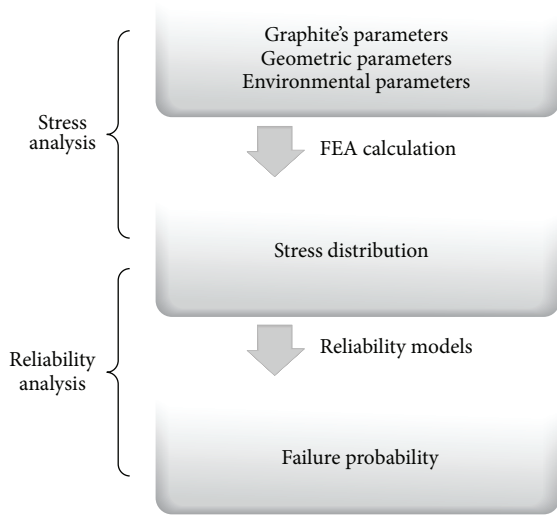


FIGURE 1: Mechanical analysis procedures of graphite component.

have been accepted in engineering standards and codes, but the probabilistic method is commonly regarded as the more suitable tool to evaluate the mechanical behaviors of brittle materials like graphite, due to the failure of brittle materials usually occurring within a certain range of stress rather than a specific stress value (i.e., the intensity value) [5, 6]. Two kinds of probabilistic reliability models, the Weibull model and the Burchell model, are reviewed in the present paper.

A MSC.MARC based finite element code INET-GRA3D has been established in INET, Tsinghua University, to numerically study the mechanical behavior of graphite component in HTRs [7]. A candidate design of pebble-type HTR's graphite brick is selected to develop a three-dimensional finite element geometric model. Both analysis steps are implemented in the code. Various creep models and reliability models are contained in order to compare the results. In Section 2 of this paper, the constitutive law and creep models are reviewed and the main formulae of three graphite creep models are introduced. In Section 3, both Weibull model and Burchell model are reviewed in detail. In Section 4, the geometric model, boundary conditions, and initial data are summarized. Two kinds of graphite, ATR-2E and H-451, are selected as demonstration materials for HTR side reflector since their calculation-required original data are comprehensive. The results of different graphite types are calculated with different models. The results, analysis, and model assessment are given in Section 5. Stress distributions, stress history, and the corresponding failure probabilities are calculated and compared. In Section 6, there are the conclusions.

## 2. Review of Constitutive Law and Creep Models

*2.1. The Constitutive Law.* The constitutive law of nuclear graphite is [8]

$$\sigma = D(T, \gamma) \varepsilon^E = D(T, \gamma) (\varepsilon - \varepsilon^T - \varepsilon^R - \varepsilon^C), \quad (1)$$

where  $\sigma$  is the stress tensor and  $D(T, \gamma)$  is the elastic matrix as a function of temperature  $T$  and neutron dose  $\gamma$ . The total strain tensor  $\varepsilon$  is composed of the elastic strain  $\varepsilon^E$ , the thermal strain  $\varepsilon^T$ , the irradiation-induced strain  $\varepsilon^R$ , and the creep strain  $\varepsilon^C$ . The incremental form of (1) is

$$d\sigma = D(T, \gamma) \cdot (d\varepsilon - d\varepsilon^T - d\varepsilon^R - d\varepsilon^C) + \varepsilon^E \cdot dD(T, \gamma), \quad (2)$$

and  $d\varepsilon^T$  is simplified and expressed as  $\alpha(T, \gamma)dT$  in calculation, where  $\alpha$  is the coefficient of thermal expansion (CTE) depending on  $T$  and  $\gamma$ .  $d\varepsilon^R$  is obtained by experimental data of dimensional change rate. Equation (2) is used in finite element calculation.

*2.2. Creep Models.* The creep phenomenon greatly impacts the behavior of graphite under high temperature and neutron irradiation conditions. With the accumulation of neutron irradiation dose, the internal stresses of graphite component grow rapidly, making the failure probability increase significantly. However, most of the internal stress can be released by the action of creep. In the past few decades, researchers set up several mechanical models to describe creep behavior. Some models are based on fitting experimental data (as the linear viscoelastic model and the M2 model), some are approximation or correction of some other model (as the UKAEA model and the Kennedy model), and others are set up with microscopic theory (as the Kelly-Burchell model) [3]. In the present paper, the linear viscoelastic model, the UKAEA model, and the Kennedy model are reviewed, applied in simulation, and assessed.

*2.2.1. Linear Viscoelastic Model.* The creep behavior is always divided into two stages: the primary creep with strain  $\varepsilon^{PC}$  and the secondary creep with strain  $\varepsilon^{SC}$ .  $\varepsilon^{PC}$  is transient creep strain, following a law of exponential growth. The secondary creep is a steady stage with a constant creep strain  $\varepsilon^{SC}$ . The total creep strain  $\varepsilon^C$  in (1) is

$$\varepsilon^C = \varepsilon^{PC} + \varepsilon^{SC} = \frac{a\sigma}{E_0} [1 - \exp(-b\gamma)] + k\sigma\gamma, \quad (3)$$

where  $a$  and  $b$  are constants. The saturated value of  $\varepsilon^{PC}$  is always same with elastic strain  $\varepsilon^E$ ; this indicates  $a = 1$  [9].  $k$  is the secondary creep coefficient, which is related to  $T$  and  $\gamma$ . Equation (3) is the expression of linear viscoelastic creep model; "linear" denotes that there is a linear relationship between  $\varepsilon^{SC}$  and  $\gamma$ . In order to simplify the calculation, the true creep strain is represented as

$$\varepsilon^C = \varepsilon^{PC} + \varepsilon^{SC} = \frac{\sigma}{E_0} + k\sigma\gamma. \quad (4)$$

It has been shown that (4) is consistent with experimental stress-strain curve [10]. The experimental data of  $k$  is required in the viscoelastic model. The data is limited, which means the linear viscoelastic model is applicable only to a few types of graphite. However, in any case, the linear viscoelastic model is always the most intuitive method to reflect the experimental results.

**2.2.2. UKAEA Model.** Both the UKAEA model (or called the UK model for short) and the Kennedy model use other parameters instead of  $k$ , in order to solve the problem that  $k$ 's experiment data is insufficient. The viscoelastic model is adapted by the UKAEA model and the Kennedy model in two different ways: the UKAEA model by modifying  $k$  with Young's modulus and the Kennedy model by using the percentage volume change. Some experimental results show that Young's modulus  $E$  and  $k$  have approximate inversely proportional relation. The secondary creep coefficient  $k$  at a neutron dose  $\gamma$  can be given by

$$k(T, \gamma) = k_p \left[ \frac{E_p}{E(T, \gamma)} \right] = \frac{k_p}{S(T, \gamma)}. \quad (5)$$

$E_p$  and  $k_p$  are Young's modulus and creep coefficient in some specific region, respectively [11]. Their possible values are selected at neutron dose point  $1 \times 10^{21} \text{ n}\cdot\text{cm}^{-2}$  (EDN).  $S(T, \gamma)$  is Young's modulus structure factor given by  $E(T, \gamma)/E_p$ . Equation (4) can be rewritten as

$$\varepsilon^C = \varepsilon^{PC} + \varepsilon^{SC} = \frac{\sigma}{E_0} + k_p \int_0^\gamma \frac{\sigma}{S(T, \gamma)} d\gamma. \quad (6)$$

**2.2.3. Kennedy Model.** The percentage volume change  $\Delta V/V$  of graphite is used as the substitution parameter in the Kennedy model [12].  $k$  is given as

$$k(T, \gamma) = k_p \left[ 1 - \mu \frac{(\Delta V/V)(T, \gamma)}{(\Delta V/V)_m} \right]. \quad (7)$$

Under fast neutron irradiation, the volume of graphite shrinks first and expands later.  $(\Delta V/V)_m$  in (7) stands for the maximum volume shrinking.  $\mu$  is an empirical constant and varies with graphite grade. In this paper,  $\mu = 0.75$  [3]. Equation (4) can be rewritten as

$$\varepsilon^C = \varepsilon^{PC} + \varepsilon^{SC} = \frac{\sigma}{E_0} + k_p \int_0^\gamma \left[ 1 - \mu \frac{(\Delta V/V)(T, \gamma)}{(\Delta V/V)_m} \right] \cdot \sigma d\gamma. \quad (8)$$

### 3. Review of Reliability Models

The failure probability is usually used to express the reliability of graphite component. A graphite brick is divided into many integration points in the FEM calculation, and the total failure probability is a summation of all integration points' failure probabilities. There are mainly two completely different ideas to study the failure behavior of graphite: one is based on fitting experimental results of unirradiated graphite specimens (as the Weibull model), and the other proceeds from the microscopic mechanism of graphite rupture and connects the microcrack of crystal lattice with macrofailure (as the Burchell model).

The destructive testing of graphite specimen shows that there is an S-shape relationship between the failure probability and the tensile stress. Figure 2 is the tensile destruction curve of H-451 graphite, an extrusion forming nuclear

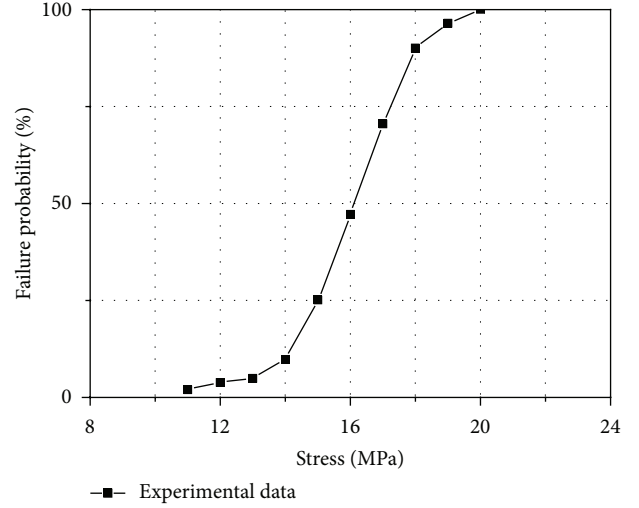


FIGURE 2: Tensile destruction curve of H-451 graphite.

graphite. The failure probability increases from 0 to 100% when the stress rises from 10 MPa to 20 MPa. The stress corresponding to 50% failure probability, ~16 MPa, is always defined as the mean strength point.

**3.1. Weibull Model.** The fitting curve method is used in Weibull model. The failure probability  $P_i$  at number  $i$  integration point of graphite brick can be designated as

$$P_i = 1 - \exp \left[ - \left( \frac{\sigma}{S_c} \right)^m \right], \quad (9)$$

where  $m$  and  $S_c$  are two Weibull parameters.  $m$  is a shape parameter and  $S_c$  is the characteristic strength value. Both parameters arise from the fitting experimental curves like Figure 2. With logarithmic transformation, (9) changes into the form of

$$\ln(-\ln(1 - P_i)) = -m \cdot \ln \sigma + m \cdot \ln S_c, \quad (10)$$

corresponding to the straight line equation  $y(x) = ax + b$ .  $1 - P_i$  indicates the survival probability of graphite specimen. Thus, the parameters  $(m, S_c)$  can be obtained by fitting experimental data  $(\sigma, P_i)$ .

The survival probability of the graphite component is

$$P_s = \exp \left\{ - \sum_i \left[ \left( \frac{\sigma}{S_c} \right)^m \times \frac{V_i}{V} \right] \right\}, \quad (11)$$

where  $V_i$  is the representative volume of integration point  $i$  and  $V$  is the volume of graphite component;  $V = \sum_i V_i$ . The failure probability of the graphite component is then expressed as [13]

$$P_{\text{tot}} = 1 - P_s = 1 - \exp \left\{ - \sum_i \left[ \left( \frac{\sigma}{S_c} \right)^m \times \frac{V_i}{V} \right] \right\}. \quad (12)$$

As the two parameters  $m$  and  $S_c$  are contained, (12) is known as the two-parameter Weibull model, which is used

in the German HTR code draft KTA-3232 [14] to generate a value of failure probability for graphite components in HTRs. Another Weibull model, called three-parameter Weibull model, has been proposed in ASME code 2010, HHA-II-3000 [15]. The failure probability  $P_i$  in (9) is modified as

$$P_i = 1 - \exp \left[ - \left( \frac{\sigma - S_0}{S_c - S_0} \right)^m \right], \quad (13)$$

where the third parameter  $S_0$  is called the threshold parameter, representing the stress value corresponding to low failure probability in Figure 2. The failure probability of the graphite component is

$$P_{\text{tot}} = 1 - P_s = 1 - \exp \left\{ - \sum_i \left[ \left( \frac{\sigma - S_0}{S_c - S_0} \right)^m \times \frac{V_i}{V} \right] \right\}. \quad (14)$$

However, only two-parameter Weibull model will be used in this paper's calculation because of the lack of  $S_0$ 's experimental data.

**3.2. Burchell Model.** The Burchell model, which is founded from the microfracture mechanism of graphite, is an evolution of the Rose and Tucker fracture model which was developed in the 1970s [5]. It has been verified that the Burchell model is able to simulate the tensile test results in Figure 2 very well [13].

Each integration point of graphite FEM model is regarded as comprising of a pile of graphite particles with magnitude mm or even less. The particle is so small that the anisotropy of graphite's microstructure is expressed. Each particle contains a so-called "weakness plane" which parallels the  $a$ -axis of the particle (parallel to the layer of carbon atoms) and is oriented at angle  $\theta$  to the fracture exposure. The starting points of microstructural fracture, a great deal of pores, are randomly distributed in the graphite particle matrix. Cracks extend by tearing the particles on their way along with the weakness planes. A graphite particle matrix which contains particles and pores is shown in Figure 3.  $a$  and  $c$  are the mean filler particle size and pore radius, respectively. When stressed at a level  $\sigma$ , a particle's fracture probability along the weakness plane is [16]

$$P_i = \frac{4}{\pi} \cos^{-1} \left( \frac{K_{Ic}}{K_I} \right)^{1/3}, \quad (15)$$

where  $K_{Ic}$  is known as the critical stress intensity factor which reflects the resistance capacity of a particle against cracks.  $K_I$  is a stress intensity factor associated with a pore.  $K_I$  is defined as

$$K_I = \sigma \sqrt{\pi c}. \quad (16)$$

The limits of particle fracture probability in (15) must be defined as follows: when  $K_I \leq K_{Ic}$ ,  $P_i = 0$ , the particle cannot be broken; when  $K_I \geq 2\sqrt{2}K_{Ic}$ ,  $P_i = 1$ , the particle will certainly break; when  $K_{Ic} \leq K_I \leq 2\sqrt{2}K_{Ic}$ , the corresponding probability of fracture is  $P_i$ .

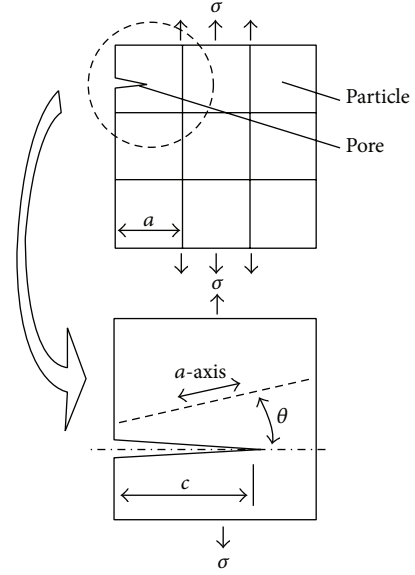


FIGURE 3: A graphite particle matrix containing particles and pores.

If there are  $n$  particles along the crack width row (or depth for Figure 3), the failure probability of the row is

$$P_n = (P_i)^n = \left[ \frac{4}{\pi} \cos^{-1} \left( \frac{K_{Ic}}{\sigma \sqrt{\pi c}} \right)^{1/3} \right]^n, \quad (17)$$

where  $n$  can be regarded as  $n = b/a$  and  $b$  is the representative size of integration point. Equation (17) indicates the chance for the crack to move forward a length  $a$ . The crack will extend only if each particle along the way of extending is torn. With the crack propagating, the crack size will increase from  $c$  to  $c + ia$ ,  $i = 1, 2, 3, \dots$ . The probability of crack extending  $i$  rows of particles can be derived as

$$P_n = \prod_{i=0}^n \left[ \frac{4}{\pi} \cos^{-1} \left( \frac{K_{Ic}}{\sigma \sqrt{\pi (c + ia)}} \right)^{1/3} \right]^{b/a}, \quad (18)$$

where  $a$  and  $K_{Ic}$  are constants for a particular kind of graphite, but  $c$  inevitably is distribution data. There exist many initial pores in unirradiated graphite. The pores are considered to be the origin of cracks. In order to characterize the dispersion characterization of pore size, a probability function  $f(c)$  is defined as

$$f(c) = \text{const} \cdot \exp \left[ - \frac{1}{2} \left( \frac{\ln 2c - \ln S_0}{\ln S_d} \right)^2 \right], \quad (19)$$

where  $S_0$  is the mean pore size and  $S_d$  is a statistical parameter reflecting the spread of  $c$ 's distribution. The probability that the size of a pore falls between  $c$  and  $c + dc$  is  $f(c)dc$ . The chance that a single pore tears an integration point under stress  $\sigma$  is

$$P_{fc} = \int_0^{\infty} f(c) \cdot P_n(\sigma, c) dc. \quad (20)$$

TABLE I: Graphite type and model selection.

	Graphite type	
	ATR-2E	H-451
Models selected for stress analysis	(1) Linear viscoelastic model (2) UKAEA model (3) Kennedy model	(1) Kennedy model
Models selected for reliability analysis	(1) Two-parameter Weibull model	(1) Two-parameter Weibull model (2) Burchell model

The survival probability of the integration point is

$$P_{fs} = (1 - P_{fc})^2 = \left[ 1 - \int_0^{\infty} f(c) \cdot P_n(\sigma, c) dc \right]^2. \quad (21)$$

As each pore has two sides, there is a square in the right side of (21). If  $N$  is defined as the number of pores per unit volume and  $V$  is the volume of integration point,  $NV$  is the amount of pores in the integration point. The total fracture probability of the part is

$$P_{ftot} = 1 - P_s^{NV} = 1 - \left[ 1 - \int_0^{\infty} f(c) \cdot P_n(\sigma, c) dc \right]^{2NV}. \quad (22)$$

The graphite component possesses many integral parts whose volumes and stress levels are different. Therefore, the survival probability of the component can be derived by multiplying principle [17]:

$$P_s = \prod_j \left[ 1 - \int_0^{\infty} f(c) \cdot P_n(\sigma(j), c) dc \right]^{2NV(j)}. \quad (23)$$

And the total failure probability of the graphite brick is

$$P_{tot} = 1 - P_s = 1 - \prod_j \left[ 1 - \int_0^{\infty} f(c) \cdot P_n(\sigma(j), c) dc \right]^{2NV(j)}. \quad (24)$$

Nine graphite parameters are required when calculating the reliability of graphite components with Burchell model, most of which are microparameters. The initial data of H-451 graphite will be given in Section 4.

#### 4. Finite Element Calculation

The finite element modeling of graphite brick, the boundary conditions, and some initial data of graphite will be described in this section. A three-dimensional finite element model is established according to a candidate design of the pebble-bed HTR graphite side reflector. The FEM geometric model is simplified to a certain extent in order to reduce the amount of calculation.

*4.1. FEM Model and Boundary Conditions.* A symmetric FEM geometric model is shown in Figure 4, as well as the boundary condition of temperature distribution at the end

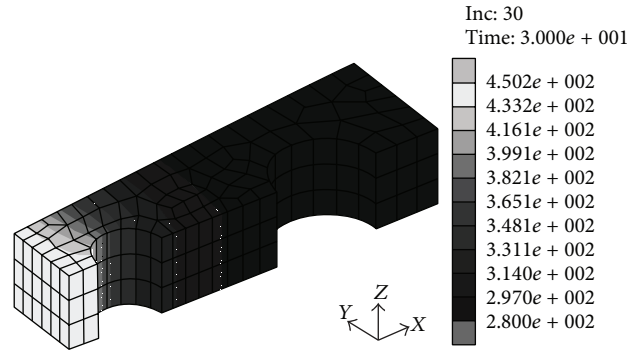


FIGURE 4: FEM model of graphite brick and temperature distribution at EOL (unit: °C).

of 30 full power years' service life (EOL). The left side of the brick neighbors reactor core while the right side neighbors peripheral carbon bricks. The inner hole is for the control rod and the other hole serves as helium path. The temperature of the core side is 450°C while the outer side is 280°C. Another boundary condition, the neutron dose, is also distributed nonuniformly. The maximum fast neutron dose at the core side reaches  $1 \times 10^{22} \text{ n} \cdot \text{cm}^{-2}$  (EDN) at EOL and decreases in radial direction of the core towards the outside, following an exponential law. The neutron dose unit EDN is the abbreviation of equivalent DIDO nickel dose. EDN has a transformation relation with another neutron dose unit dpa (displacement per atom) [3]:

$$1 \times 10^{22} \text{ n} \cdot \text{cm}^{-2} \text{ (EDN)} \cong 13 \text{ dpa}. \quad (25)$$

*4.2. Model Selection and Parameter Values.* Two types of graphite, ATR-2E and H-451, are selected in this paper to simulate the behavior of graphite and validate the models. As different types of irradiation experiments have been carried out for various types of graphite, the resource data of different types of graphite is not the same. That indicates that not every kind of graphite can be simulated with all models. For example, it is unable to simulate the irradiation creep behavior of H-451 graphite brick with the viscoelastic model due to the lack of  $k$ 's experimental data of H-451 graphite. The graphite types and corresponding calculation models are listed in Table I. The calculation of ATR-2E graphite focuses on the comparison of three different creep models, while the calculation of H-451 graphite focuses on the comparison of two different reliability models. The calculation results and model comparisons are summarized in Section 5.

TABLE 2: Weibull parameters of ATR-2E and H-451 graphite.

	Graphite type	
	ATR-2E	H-451
Weibull parameter, $m$	9.0	9.97
Weibull parameter, $S_c$ (MPa)	18.5	16.86

TABLE 3: Burchell parameters of H-451 graphite.

Parameter	Value
Mean particle size, $a$ ( $\mu\text{m}$ )	500
Bulk density, $\rho$ ( $\text{g}/\text{cm}^3$ )	1.79
Mean pore size, $S_0$ ( $\mu\text{m}$ )	42
Statistical parameter, $S_d$	1.9
Mean pore area, $P_a$ ( $\mu\text{m}^2$ )	700
Number of pores per $\text{m}^3$ , $N$ ( $\text{m}^{-3}$ )	$2.97 \times 10^8$
Integration point volume, $V$ ( $\text{m}^3$ )	Real-time computed
Specimen breadth, $b$ (mm)	Real-time computed
Particle critical stress intensity factor, $K_{Ic}$ ( $\text{MPa}\cdot\text{m}^{1/2}$ )	0.285

The two Weibull parameters of graphite are obtained by tensile test. The values for ATR-2E and H-451 are shown in Table 2.

The Burchell parameters of H-451 graphite are shown in Table 3, including all nine parameters required. Some of the parameter values change after neutron irradiation, and the variation and new values are induced in [16]. It is worth noting that the value of  $K_{Ic}$  rises to  $0.42 \text{ MPa}\cdot\text{m}^{1/2}$  at a low dose level  $10^{20} \text{ n}\cdot\text{cm}^{-2}$  (EDN).

## 5. Results and Comparisons

The internal stress distribution of graphite brick at EOL is shown in Figure 5 as an example. The result shown in Figure 5 is obtained with ATR-2E graphite and the linear viscoelastic model. The stress distribution and concentration areas gained by other cases are the same. The stress concentrates in two areas in each case, and the stress concentrative points A and B are selected to analyze the stress history.

**5.1. Results of ATR-2E Graphite.** The stress history of points A and B is shown in Figure 6. The stress development processes of two stress concentrative points are completely different. The stress on point A slightly increases and then decreases to initial value in the first 15 years and rises rapidly thereafter. The maximum stress value appears at EOL and reaches about 6 MPa. Although various kinds of raw data are used in different creep model calculations, the stress results are very close to each other. It is hard to tell which stress value among the three ones is higher from stress diagram of point A.

On point B, the stress increases continually in most of graphite brick's service time but declined slightly near EOL. The peak value reaches 8-9 MPa, 30% higher than peak value on point A. The curves of various models do not intersect each other. It is quite clear that the Kennedy model gives

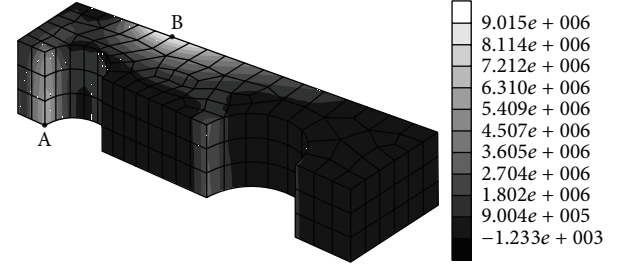


FIGURE 5: Stress distribution at EOL (unit: Pa).

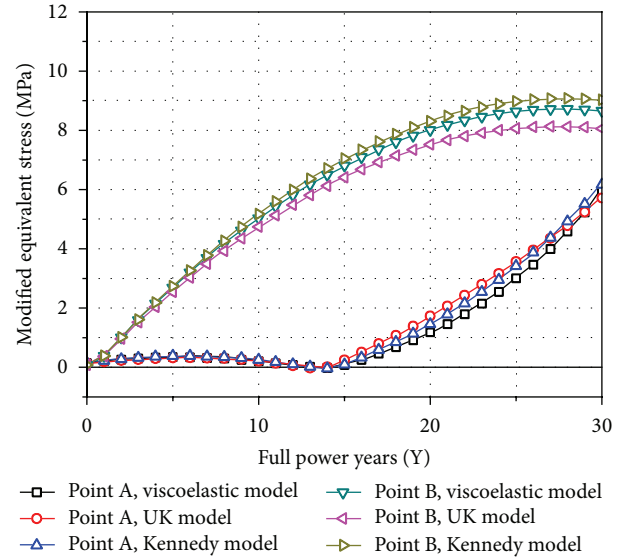


FIGURE 6: Stress history in service life of ATR-2E graphite brick.

the highest stress, while the UKAEA model gives the lowest. However, the model error is no more than 10%, which will not negative the validity of any creep model.

Figure 7 shows the reliability analysis results of ATR-2E graphite brick. The failure probability rapidly grows in the first 20 years, followed by a decline near EOL. The failure probability calculated by the Kennedy model is the highest with peak value exceeding  $10^{-7}$ , while the failure probability by the UKAEA model is the lowest with peak value  $4.5 \times 10^{-8}$ . Different creep models not only give exactly the same failure probability change trend, but also present very close results. This means that each creep is effective and competent for engineering design. In addition, if one feels like getting the most conservative design, selecting the Kennedy creep model is recommended.

**5.2. Results of H-451 Graphite.** It is shown in the previous calculation that each of the three selected creep models is valid for design. Therefore, only the Kennedy creep model is adopted in the calculation of H-451 graphite brick's mechanical behavior. The points A and B's internal stress development curves of H-451 graphite brick are shown in Figure 8. The changing process of stress on point A is very similar with that of ATR-2E graphite. The peak value is also  $\sim 6$  MPa,

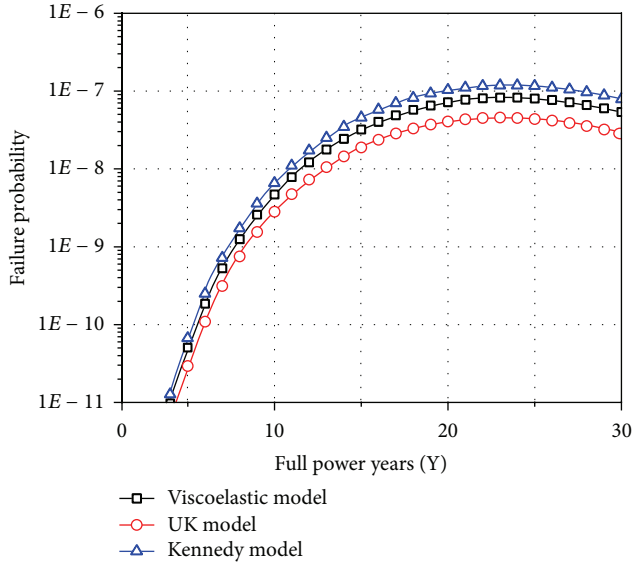


FIGURE 7: Failure probability history of ATR-2E graphite brick.

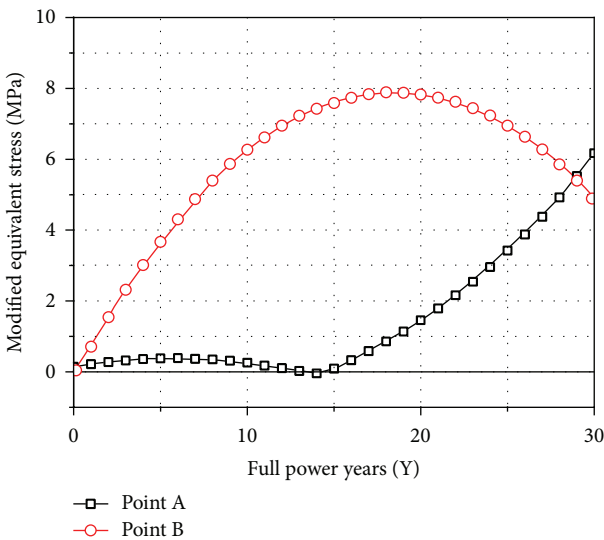


FIGURE 8: Stress history in service life of H-451 graphite brick.

presenting at EOL. On point B, the stress peak value appears near 20 years' service time and reaches 8 MPa. The stress begins to fall since, and only 5 MPa is left at EOL.

The subsequent reliability analysis' results are shown in Figure 9. The results of two-parameter Weibull model are very close to that of ATR-2E graphite. This means that the two kinds of graphite have almost the same reliability level. Although the establishing mechanisms of the two reliability models are completely different, their obtained results are pretty similar. Compared with the results of Weibull model, the failure probability obtained by Burchell model changes much faster. That indicates that the Burchell model is much more sensitive to stress (or neutron dose) than the Weibull model. The Burchell model's result is much lower in the beginning, but rises fast, and exceeds the Weibull model's

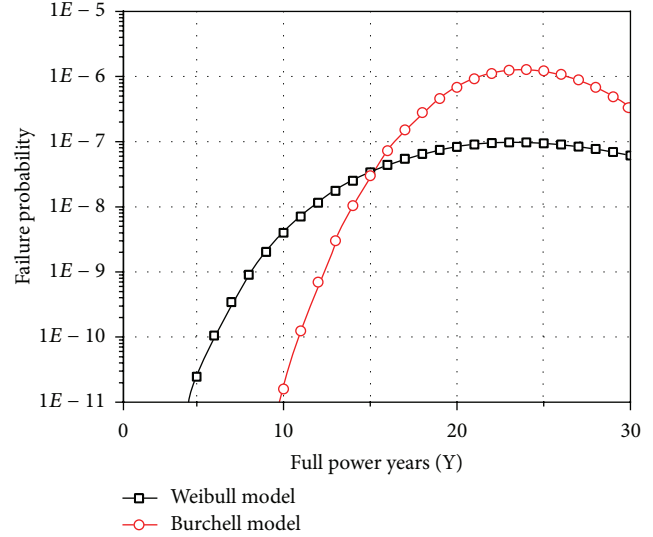


FIGURE 9: Failure probability history of H-451 graphite brick.

result at 15 years' service time. The peak value reaches  $10^{-6}$ , still far from the threshold value  $10^{-4}$  which is determined in [15].

## 6. Conclusions

Along with the advance of technology, the HTR is oriented to modularization, miniaturization, integration, and other new development direction. The safety of reactor structural components is one of the most important focuses in the meantime. The reliability of graphite component is directly related to the integrity of the reactor core and affects the safety of the entire reactor. When the reactor is on operation, the graphite components are exposed to high temperature and fast neutron irradiation. The temperature and irradiation load will not only create an accumulation of stresses, but also dramatically change the nature of graphite. Creep will also influence the whole process of mechanics at the same time. A comprehensively constitutive model calculation, including elastic behavior, thermal strain, irradiation deformation, and creep phenomenon, must be established in order to properly simulate the mechanical behavior of graphite component and predict the internal stresses and failure probability.

Three creep models and two reliability models are reviewed, applied, and compared in the present paper. Two types of graphite, ATR-2E and H-451, are selected as the demonstration material for calculation. The main conclusions of graphite component's mechanical analysis and model comparisons are provided. It is shown in the stress analysis procedure that all three creep models can be used for stress prediction and engineering design. The Kennedy model is the most conservative one. In the reliability analysis procedure, the results obtained by both reliability models are in satisfactory agreement and both much lower than the threshold value  $10^{-4}$ . The discrepancies on the specific values indicate that the Burchell model leads to the failure probability more sensitive to stress (or neutron dose) than that of the Weibull model.

In addition, more models have been established but still lack for engineering design experience, as the Kelly-Burchell creep model and M2 creep model for stress analysis and the three-parameter Weibull model for reliability analysis. Other practical models are still being established as well. There is still much further work that can be carried out in terms of model application and assessment.

### Conflict of Interests

The authors declare that there is no conflict of interests regarding the publication of this paper.

### Acknowledgments

This project is supported by the Tsinghua University Initiative Scientific Research Program (no. 20111080959) and the Specialized Research Fund for the Doctoral Program of Higher Education (no. 20120002120010).

### References

- [1] T. Abram and S. Ion, "Generation-IV nuclear power: a review of the state of the science," *Energy Policy*, vol. 36, no. 12, pp. 4323–4330, 2008.
- [2] B. T. Kelly and T. D. Burchell, "The analysis of irradiation creep experiments on nuclear reactor graphite," *Carbon*, vol. 32, no. 1, pp. 119–125, 1994.
- [3] T. D. Burchell, K. L. Murty, and J. Eapen, "Irradiation induced creep of graphite," *JOM*, vol. 62, no. 9, pp. 93–99, 2010.
- [4] T. Oku and M. Ishihara, "Lifetime evaluation of graphite components for HTGRs," *Nuclear Engineering and Design*, vol. 227, no. 2, pp. 209–217, 2004.
- [5] A. P. G. Rose and M. O. Tucker, "A fracture criterion for nuclear graphite," *Journal of Nuclear Materials*, vol. 110, no. 2-3, pp. 186–195, 1982.
- [6] T. Burchell, T. Yahr, and R. Battiste, "Modeling the multiaxial strength of H-451 nuclear grade graphite," *Carbon*, vol. 45, no. 13, pp. 2570–2583, 2007.
- [7] H. Wang and S. Yu, "Uncertainties of creep model in stress analysis and life prediction of graphite component," *Nuclear Engineering and Design*, vol. 238, no. 9, pp. 2256–2260, 2008.
- [8] D. K. L. Tsang and B. J. Marsden, "Constitutive material model for the prediction of stresses in irradiated anisotropic graphite components," *Journal of Nuclear Materials*, vol. 381, no. 1-2, pp. 129–136, 2008.
- [9] T. D. Burchell, "Irradiation induced creep behavior of H-451 graphite," *Journal of Nuclear Materials*, vol. 381, no. 1-2, pp. 46–54, 2008.
- [10] X. Fang, H. Wang, S. Yu, and C. Li, "The various creep models for irradiation behavior of nuclear graphite," *Nuclear Engineering and Design*, vol. 242, pp. 19–25, 2012.
- [11] B. T. Kelly and J. E. Brocklehurst, "UKAEA reactor group studies of irradiation-induced creep in graphite," *Journal of Nuclear Materials*, vol. 65, no. 1, pp. 79–85, 1977.
- [12] C. R. Kennedy, W. P. Eatherly, and R. L. Senn, "Compressive creep characteristics of graphite under irradiation," in *Proceedings of the 33rd Pacific Coast Regional Meeting of the American Ceramic Society*, San Francisco, Calif, USA, October 1980.
- [13] S. Y. Yu, X. Fang, H. T. Wang, and C. F. Li, "Failure probability study of HTR graphite component using microstructure-based model," *Nuclear Engineering and Design*, vol. 253, pp. 192–199, 2012.
- [14] KTA-3232, "Keramische Einbauten in HTR-Reaktordruckbehältern," Sicherheitstechnische Regel des KTA, 1992.
- [15] HHA-II-3000, "Rules for construction of nuclear facility components," ASME boiler and pressure vessel code, III, Division 5, 2010.
- [16] T. D. Burchell, "A microstructurally based fracture model for polygranular graphites," *Carbon*, vol. 34, no. 3, pp. 297–316, 1996.
- [17] M. Ishihara, T. Takahashi, and S. Hanawa, "Applicability of Advanced Design Method of Graphite Components by Microstructure-Based Brittle Fracture Model," SmiRT 16, Washington DC. Paper #1920, 2001.